

*Thermodynamic Modeling and Experimental Investigation of the
Mg-Cu-Ni-Y Quaternary System*

Md. Mezbahul Islam

A Thesis

In

The Department

Of

Mechanical and Industrial Engineering

Presented in Partial Fulfillment of the Requirements for the Degree of Doctorate in
Philosophy (Mechanical Engineering) at
Concordia University
Montreal, Quebec, Canada

September 2013

© Md. Mezbahul Islam, 2013

CONCORDIA UNIVERSITY
SCHOOL OF GRADUATE STUDIES

This is to certify that the thesis prepared

By: Md. Mezbahul Islam

Entitled: Thermodynamic Modeling and Experimental
Investigation of the Mg-Cu-Ni-Y Quaternary

and submitted in partial fulfillment of the requirements for the degree of

Doctorate in Philosophy

complies with the regulations of the University and meets the accepted standards with respect to originality and quality.

Signed by the final examining committee:

Dr. Rabin Raut Chair

Dr. Mathieu Brochu External Examiner

Dr. Michelle Nokken External to Program

Dr. Martin Pugh Examiner

Dr. Van Suong Hoa Examiner

Dr. Mamoun Medraj Thesis Supervisor

ABSTRACT

Thermodynamic Modeling and Experimental Investigation of the Mg-Cu-Ni-Y Quaternary System

Md. Mezbahul Islam, Ph.D.
Concordia University, 2013

In this work, a self-consistent thermodynamic database for the Mg-Cu-Ni-Y system has been constructed by combining the thermodynamic descriptions of the constituent binary and ternary sub-systems. The modified quasichemical model has been used to describe the liquid phase in this system, for the first time, which accounts for the short range ordering. Isothermal sections of the Mg-Cu-Y and Mg-Ni-Y systems at 673 K and Cu-Ni-Y system at 973 K have been constructed experimentally. Diffusion couples and key samples have been employed for establishing the phase equilibria. Microstructural characterizations using scanning electron microscopy (SEM), and phase identification using x-ray diffraction (XRD) and wave dispersive x-ray spectrometer (WDS) have been carried out. Twelve ternary intermetallic compounds have been identified in the Mg-Ni-Y system. Crystallographic prototypes of two of these compounds; τ_1 (MgNiY_4) and τ_2 (MgNi_2Y_2) have been found and their lattice parameters have been determined using Rietveld analysis of the XRD patterns. Also, ternary solubility of τ_3 (MgNi_4Y) has been found to be from 9.2 to 25.9 at.% Mg with constant 65 at.% Ni. Ternary solubility of the binary compounds in the Mg-Cu-Y, Mg-Ni-Y and Cu-Ni-Y systems has been determined. A complete mutual solubility between CuY-NiY and $\text{Cu}_4\text{Y-Ni}_4\text{Y}$ in the Cu-Ni-Y system has been identified. Differential scanning calorimetry (DSC) experiments have been conducted for selected key samples of the Mg-

Cu-Y, Mg-Ni-Y and Cu-Ni-Y systems to determine the liquidus and other phase transformation temperatures. These results have been compared with the thermodynamic modeling which showed good agreement. Thermodynamic calculations of the Mg-Cu-Ni system also show consistency with the literature data.

Liquidus projections of the four ternary systems have been calculated based on the present thermodynamic modeling considering the current experimental results and data from the literature. All four ternary systems have been combined in one database for the Mg-Cu-Ni-Y quaternary.

ACKNOWLEDGEMENTS

First of all, I would like to express my profound gratitude to my thesis supervisor Dr. Mamoun Medraj for his constant guidance, suggestions and cooperation in helping me finish this work. Without his support it wouldn't be possible to complete this thesis.

I would also like to thank the members of Dr. Medraj's research group for their support and for creating a perfect research environment. Especially, I would like to thank Dr. Dmytro Kevorkov and Ahmad Omar Mostafa for their help during my research.

I like to thank Dr. Elhachmi Essadiqi of CANMET-MTL for his support in sample preparation. In addition, I would also like to acknowledge the financial assistance provided by the Natural Science and Engineering Research Council (NSERC) to keep the research work going.

No word could express my gratitude to my parents who have been consistently supporting me with their endless love, prayers, and encouragements. Also, I would like to appreciate the support of my brothers and sister in laws.

Finally, I would like to express my love and thanks to my wife, Sharila, who not only was very supportive and patient, but also helped me a great deal in organizing and finishing this work.

TABLE OF CONTENTS

LIST OF FIGURES	XI
LIST OF TABLES.....	XIX
LIST OF ABBREVIATIONS	XXI
CHAPTER 1	1
INTRODUCTION	1
1.1 Introduction	1
1.2 CALPHAD approach.....	4
1.1 Thesis Layout	6
CHAPTER 2	8
LITERATURE REVIEW	8
2.1 Mg-Ni binary system	8
2.2 Cu-Ni binary system.....	10
2.3 Ni-Y binary system.....	12
2.4 Mg-Y binary system	14
2.5 Mg-Cu and Cu-Y binary systems	16
2.6 Mg-Cu-Ni ternary system.....	16
2.7 Mg-Cu-Y ternary system	19
2.8 Mg-Ni-Y ternary system.....	20
2.9 Cu-Ni-Y ternary system.....	22
2.10 Objectives	24

CHAPTER 3	26
THERMODYNAMIC MODELING	26
3.1 Analytical Description of the Employed Thermodynamic Models	27
3.1.1 <i>Unary phases</i>	27
3.1.2 <i>Stoichiometric phases</i>	27
3.1.3 <i>Disordered solution phases</i>	28
3.1.3.1 Random solution phases	28
3.1.3.2 Liquid phases	30
3.1.4 <i>Ordered solution phases</i>	33
3.2 Extrapolation of Ternary Systems	34
CHAPTER 4	37
THERMODYNAMIC MODELING OF THE MG-CU-NI-Y SYSTEM	37
4.1 Thermodynamic Modeling of the Binary Sub-Systems	37
4.1.1 <i>Mg-Ni system</i>	37
4.1.2 <i>Cu-Ni system</i>	40
4.1.3 <i>Ni-Y system</i>	43
4.1.4 <i>Mg-Y system</i>	47
4.2 Thermodynamic Modeling of the Ternary Systems	50
4.2.1 <i>Mg-Cu-Ni phase diagram</i>	50
4.2.2 <i>Mg-Cu-Y phase diagram</i>	58
4.2.3 <i>Mg-Ni-Y Phase diagram</i>	66
4.2.4 <i>Cu-Ni-Y Phase diagram</i>	72
4.3 Mg-Cu-Ni-Y quaternary system	76

CHAPTER 5	78
EXPERIMENTAL PROCEDURE.....	78
5.1 Experimental Methods.....	78
5.2 Alloy preparation.....	83
5.3 Diffusion couple approach.....	84
5.4 X-Ray Diffraction.....	85
5.5 SEM and WDS analysis	85
5.6 Differential Scanning Calorimetry (DSC).....	86
 CHAPTER 6	 87
EXPERIMENTAL INVESTIGATION OF THE MG-CU-Y SYSTEM	87
6.1 Isothermal section at 673 K.....	87
6.2 Comparison between experimental results and thermodynamic modeling	93
6.3 Analysis of some important glass forming alloys	110
 CHAPTER 7	 112
EXPERIMENTAL INVESTIGATION OF THE MG-NI-Y SYSTEM	112
7.1 Diffusion couple analysis	112
7.2 Isothermal section based on diffusion couples and key sample analysis	125
7.3 Ternary intermetallic compounds in the Mg-Ni-Y system.....	126
7.4 Comparison between experimental results and thermodynamic modeling ..	140
 CHAPTER 8	 152
EXPERIMENTAL INVESTIGATION OF THE CU-NI-Y SYSTEM	152
8.1 Diffusion couples.....	152

8.2	Isothermal section based on diffusion couples and key alloys analysis	158
8.3	Complete mutual solubility between CuY and NiY	161
8.4	Complete mutual solubility between Cu ₄ Y and Ni ₄ Y	165
8.5	Partial solubility of Ni ₅ Y phase	166
8.6	Comparison between experimental results and thermodynamic modeling ..	168
CHAPTER 9		183
CONCLUDING REMARKS, CONTRIBUTIONS AND SUGGESTIONS FOR FUTURE WORK.....		183
9.1	Concluding remarks.....	183
9.2	Contributions	186
9.3	Suggestions for future work	189
REFERENCES		191
APPENDIX.....		204
Figure A-1: Calculated Mg-Cu phase diagram [87].....		204
Figure A-2: Calculated Cu-Y phase diagram [87]		204
Table A-3: Optimized model parameters for the Mg-Cu system.....		205
Table A-4: Optimized model parameters for the Cu-Y system.....		205
Table A-5: Crystallographic data on the ternary compounds of the Mg-Cu-Y system		206
Table A-6: Binary phases of the Cu-Ni, Cu-Y and Ni-Y systems and their structure data [138].....		207
Tale A-7: Ternary invariant points of the Mg-Cu-Ni system.....		208

Table A-8: Ternary invariant points of the Mg-Cu-Y system	209
Table A-9: Ternary invariant points of the Mg-Ni-Y system.....	211
Table A-10: Ternary invariant points of the Cu-Ni-Y system	214

LIST OF FIGURES

<i>Figure 1-1: Metallic glass of Mg₈₀Cu₁₀Y₁₀ alloy in a cylindrical form [3, 4]</i>	2
<i>Figure 1-2: Flowchart of the CALPHAD method [19]</i>	5
<i>Figure 2-1: Isothermal sections at (a) 1123 K; (b) 1081 K; (c) 1073 K; (d) 1003 K [114]</i>	18
<i>Figure 2-2: Composition of the published glass forming alloys: (O) amorphous alloys [3]; (♦) crystalline alloys [3]; (+) amorphous alloys [8]; (∇) crystalline alloys [8]; (∅) amorphous alloys [124]; (b) Isothermal section of the Mg-Cu-Y system at 673 K from 0 to 66.7 at.% Cu</i>	20
<i>Figure 2-3: Isothermal section of the Mg-Ni-Y system at 673 K (Ni-rich part) [125]; (b) calculated isothermal section of the Mg-Ni-Y system at 673 K [126]</i>	21
<i>Figure 2-4: A partial isothermal section of Cu-Ni-Y system (for Y ≤ 16.7 at.% Y) at 293 K [138]</i>	23
<i>Figure 3-1: Different “geometric” models for ternary extrapolation: (a) Kohler (b) Muggianu and (c) Kohler/Toop [157]</i>	35
<i>Figure 4-1: Calculated Mg-Ni phase diagram</i>	38
<i>Figure 4-2: Calculated enthalpy of mixing of liquid Mg-Ni at 1008 K</i>	38
<i>Figure 4-3: Calculated activity of liquid Mg and Ni at 1100 K</i>	39
<i>Figure 4-4: (a) Calculated heat capacity for the MgNi₂; (b) Enthalpy of formation of Mg₂Ni and MgNi₂</i>	40
<i>Figure 4-5: Calculated Cu-Ni phase diagram</i>	41
<i>Figure 4-6: Calculated (a) enthalpy of mixing of the liquid Cu-Ni at 1750 K; (b) activities of the liquid Cu and Ni at 1750 K</i>	42
<i>Figure 4-7: Calculated (a) enthalpy of mixing at of the Cu-Ni solid solution phase at 800 K; (b) activities of Cu and Ni in the fcc phase at 1000 and 1273 K</i>	43
<i>Figure 4-8: Calculated Ni-Y phase diagram</i>	44
<i>Figure 4-9: Calculated (a) enthalpy of mixing of liquid Ni-Y at 1973 K. V-shaped line shows the trend of the exp. data; (b) entropy of mixing of liquid Ni-Y at 1800 K</i>	45

<i>Figure 4-10: Calculated enthalpy of formation of the intermetallic compounds at 973 K in the Ni-Y system.....</i>	<i>46</i>
<i>Figure 4-11: Calculated Mg-Y phase diagram.....</i>	<i>47</i>
<i>Figure 4-12: Calculated (a) enthalpy of mixing of the Mg-Y liquid at 984 K; (b) activity of Mg in the Mg-Y liquid at 1173 K</i>	<i>48</i>
<i>Figure 4-13: Enthalpy of formation for the stoichiometric compounds in the Mg-Y system</i>	<i>49</i>
<i>Figure 4-14: Calculated isothermal section of the Mg-Cu-Ni system at 673 K with the experimental data of Karonik et al. [113]</i>	<i>52</i>
<i>Figure 4-15: Calculated isothermal section of the Mg-Cu-Ni system at 1073 K with the experimental data of Fehrenbach et al. [114]</i>	<i>53</i>
<i>Figure 4-16: Calculated vertical sections at (a) $x_{Cu} / x_{Ni} = 0.5$; (b) $x_{Cu} / x_{Ni} = 1.0$; (c) $x_{Cu} / x_{Ni} = 2.0$; (d) 71 at.% Mg.....</i>	<i>55</i>
<i>Figure 4-17: Calculated vertical section along $Cu_{0.78}Mg_{0.22} - Ni_{0.88}Mg_{0.12}$.....</i>	<i>56</i>
<i>Figure 4-18: Calculated liquidus projection of the Mg-Cu-Ni system.....</i>	<i>57</i>
<i>Figure 4-19: (a) Calculated enthalpy of mixing of the liquid at 1008 K for the component ratio of $X_{Cu} / X_{Ni} = 2.0, 1.0$ and 0.5; (b) Mg activity at 1173 K of the liquid for the component ratio of $X_{Cu} / X_{Ni} = 2.0$.....</i>	<i>58</i>
<i>Figure 4-20: Calculated isothermal section of the Mg-Cu-Y system at 673 K.....</i>	<i>64</i>
<i>Figure 4-21: Liquidus projection of the Mg-Cu-Y system</i>	<i>65</i>
<i>Figure 4-22: Liquidus projection of the Mg rich side of the Mg-Cu-Y system.....</i>	<i>66</i>
<i>Figure 4-23: Calculated liquidus projection of the Mg-Ni-Y system</i>	<i>67</i>
<i>Figure 4-24: Liquidus projection of the Mg rich side of the Mg-Ni-Y system.....</i>	<i>68</i>
<i>Figure 4-25: Calculated isothermal section of the Mg-Ni-Y system at 673 K.....</i>	<i>69</i>
<i>Figure 4-26: Calculated liquidus projection of the Cu-Ni-Y system</i>	<i>74</i>
<i>Figure 4-27: Calculated isothermal section of the Cu-Ni-Y system at 973 K.....</i>	<i>75</i>
<i>Figure 4-28: Liquidus projection of the Mg-Cu-Ni-Y quaternary system. τ^* represents. ..</i>	<i>77</i>
<i>Figure 5-1: Mg-Cu-Y isothermal section at 673 K, based on this work, showing the investigated compositions</i>	<i>81</i>

<i>Figure 5-2: Mg-Ni-Y isothermal section at 673 K, based on this work, showing the investigated compositions and diffusion couples.....</i>	<i>81</i>
<i>Figure 5-3: Cu-Ni-Y isothermal section at 973 K, based on this work, showing the investigated compositions and diffusion couples.....</i>	<i>82</i>
<i>Figure 6-1: BSE image of (a) sample 15 (7.6/57.4/35.0 Mg/Cu/Y at.%); (b) sample 17 (6.7/78.2/15.1 Mg/Cu/Y at.%).....</i>	<i>90</i>
<i>Figure 6-2: XRD pattern of sample sample 15 (7.6/57.4/35.0 Mg/Cu/Y at.%)</i>	<i>90</i>
<i>Figure 6-3: BSE image of sample 19 (1.1/93.7/5.2 Mg/Cu/Y at.%).....</i>	<i>90</i>
<i>Figure 6-4: BSE image of (a) sample 6 (62.6/12.4/25.0 Mg/Cu/Y at.%); (b) sample 7 (53.2/16.6/30.2 Mg/Cu/Y at.%).....</i>	<i>92</i>
<i>Figure 6-5: (a) DSC spectra; (b) the calculated vertical section at constant 7.2 at.% Y with DSC signals of sample 1 (84.9/7.9/7.2 Mg/Cu/Y at.%)</i>	<i>93</i>
<i>Figure 6-6: BSE image of sample 1 (84.9/7.9/7.2 Mg/Cu/Y at.%).....</i>	<i>94</i>
<i>Figure 6-7: (a) BSE image; (b) DSC spectra of sample 2 (80.4/12.8/6.8 Mg/Cu/Y at.%) 95</i>	
<i>Figure 6-8: (a) vertical section at 6.8 at.% Y with DSC signals; (b) phase assemblage diagram of sample 2 (80.4/12.8/6.8 Mg/Cu/Y at.%).....</i>	<i>96</i>
<i>Figure 6-9: (a) BSE image; (b) DSC spectra of sample 3 (70.5/15.3/14.2 Mg/Cu/Y at.%)</i>	<i>98</i>
<i>Figure 6-10: (a) vertical section at 70.5 at.% Mg; (b) phase assemblage diagram of sample 3 (70.5/15.3/14.2 Mg/Cu/Y at.%)</i>	<i>99</i>
<i>Figure 6-11: BSE image of (a) sample 4 (67.5/16.4/16.1 Mg/Cu/Y at.%); (b) BSE image of sample 5 (66.7/17.3/16.0 Mg/Cu/Y at.%)</i>	<i>100</i>
<i>Figure 6-12: (a) DSC spectra of sample 4; (b) DSC spectra of sample 5; (c) vertical section at 66.7 at.% Mg; (d) vertical section at constant 67.5 at.% Mg</i>	<i>101</i>
<i>Figure 6-13: (a) BSE image; (b) XRD pattern of sample 8 (55.6/36.9/7.5 Mg/Cu/Y at.%)</i>	<i>102</i>
<i>Figure 6-14: (a) DSC spectra; (b) the calculated vertical section at constant 7.52 at.% Y with DSC signals of sample 8 (55.6/36.9/7.5 Mg/Cu/Y at.%)</i>	<i>103</i>
<i>Figure 6-15: (a) DSC spectra; (b) vertical section at 17.16 at.% Cu with DSC signals of sample 9 (37.84/17.16/45.00 Mg/Cu/Y at.%)</i>	<i>104</i>
<i>Figure 6-16: (a) BSE image; (b) XRD pattern of sample 9 (37.8/17.2/45.0 Mg/Cu/Y at.%)</i>	<i>104</i>

<i>Figure 6-17: (a) BSE image; (b) XRD pattern of sample 11 (28.0/63.3/8.7 Mg/Cu/Y at.%)</i>	105
<i>Figure 6-18: (a) phase assemblage diagram; (b) DSC spectra; (c) vertical section at 8.74 at.% Y with DSC signals of sample 11 (28.0/63.3/8.7 Mg/Cu/Y at.%)</i>	106
<i>Figure 6-19: (a) BSE image; (b) XRD pattern of sample 13 (16.9/77.3/5.8 Mg/Cu/Y at.%)</i>	107
<i>Figure 6-20: Phase assemblage diagram of sample 13 (16.9/77.3/5.8 Mg/Cu/Y at.%)</i>	108
<i>Figure 6-21: (a) phase assemblage diagram; (b) DSC spectra; (c) vertical section at constant 5.82 at.% Y with DSC signals of sample 13 (16.9/77.3/5.8 Mg/Cu/Y at.%)</i>	108
<i>Figure 6-22: (a) BSE image; (b) DSC spectra; (c) vertical section at 4.3 at.% Y with DSC signals of sample 18 (4.1/91.6/4.3 Mg/Cu/Y at.%)</i>	109
<i>Figure 6-23: Vertical section at constant 10% Y with DSC results from the literature [12, 166]</i>	111
<i>Figure 7-1: (a) Solid-solid diffusion couple of Mg - sample 20 (18.5/22.4/59.1 Mg/Ni/Y at.%) annealed at 673 K for 4 weeks (b)magnified area of interest of the diffusion zone</i>	113
<i>Figure 7-2: (a) Diffusion path projected on the Mg-Ni-Y Gibbs triangle; (b) Composition profile of the diffusion couple 1 along the line scan shown in Figure 7-1(a)</i>	115
<i>Figure 7-3: BSE images of the solid–solid diffusion couple 2 annealed at 673 K for 4 weeks</i>	117
<i>Figure 7-4: Composition profile of the diffusion couple 2 along the line scan shown in Figure 7-3; (b) Diffusion path of the solid-solid diffusion couple 2 projected on the Mg-Ni-Y Gibbs triangle</i>	117
<i>Figure 7-5: (a) BSE images of the solid-solid diffusion couple-3 annealed at 673 K for 4 weeks; (b) magnified area of interest</i>	118
<i>Figure 7-6: (a) Composition profile along the line scan shown in Figure 7-5 (b); (b) Diffusion path projected on the Mg-Ni-Y Gibbs triangle</i>	119
<i>Figure 7-7: (a) BSE images of the solid–liquid diffusion couple-1 (Mg-Ni₇₈Y₂₃) annealed at 673 K for 4 weeks; (b) magnified area of interest</i>	120
<i>Figure 7-8: (a) BSE images of the solid–liquid diffusion couple-2 (Mg-Ni₅₂Y₄₈) annealed at 673 K for 4 weeks; (b) magnified area of interest</i>	120
<i>Figure 7-9: Composition profile of the solid–liquid diffusion couple-1 along the line scan shown in Figure 7-7 (b); (b) Diffusion path projected on the Mg-Ni-Y Gibbs triangle</i>	121

<i>Figure 7-10: (a) Composition profile of the solid–liquid diffusion couple-2 along the line scan shown in Figure 7-8 (b); (b) Diffusion path projected on the Mg-Ni-Y Gibbs triangle</i>	122
<i>Figure 7-11: Isothermal section of the Mg-Ni-Y system at 673 K for the whole composition range</i>	126
<i>Figure 7-12: BSE image of (a) sample 21 (13.1/26.7/60.2 Mg/Ni/Y at.%); (b) sample 22 (4.8/28.3/ 66.9 Mg/Ni/Y at.%); (c) sample 24 (5.9/20.9/73.2 Mg/Ni/Y at.%); (d) sample 25 (8.6/16.5/74.9 Mg/Ni/Y at.)</i>	127
<i>Figure 7-13: Unit cell of MgNiY₄</i>	129
<i>Figure 7-14: XRD pattern for (a) sample 20 (18.5/22.4/59.1 Mg/Ni/Y at.%); (b) sample 26 (37.0/15.0/48.0 Mg/Ni/Y at.)</i>	129
<i>Figure 7-15: BSE image of (a) sample 9 (8.4/58.6/33.0 Mg/Ni/Y at.%); (b) sample 10 (28.0/36.8/35.2 Mg/Ni/Y at.%); (c) sample 11 (26.0/38.2/35.8 Mg/Ni/Y at.%); (d)sample 12 (20.0/50.8/29.2 Mg/Ni/Y at.)</i>	130
<i>Figure 7-16: Unit cell for MgNi₂Y₂ (τ_2)</i>	132
<i>Figure 7-17: XRD patterns for (a) sample 10 (28.0/36.8/35.2 Mg/Ni/Y at.%); (b) sample 11 (26.0/38.2/35.8 Mg/Ni/Y at.%); (c) sample 12 (20.0/50.8/29.2 Mg/Ni/Y at.)</i>	133
<i>Figure 7-18: Variation of lattice parameter of τ_3</i>	133
<i>Figure 7-19: BSE image of (a) Sample 6 (28.7/69.1/2.2 Mg/Ni/Y at.%); (b) sample 7 (11.0/78.9/10.1 Mg/Ni/Y at.)</i>	134
<i>Figure 7-20: (a) BSE image; (b) XRD pattern for of sample 18 (25.0/30.3/44.7 Mg/Ni/Y at.)</i>	135
<i>Figure 7-21: (a) sample 14 (37.2/36.3/26.5 Mg/Ni/Y at.%); (b) sample 29 (51.4/12.3/36.3 Mg/Ni/Y at.)</i>	136
<i>Figure 7-22: BSE image of (a) sample 13 (24.6/52.4/23.0 Mg/Ni/Y at.%); (b) sample 15 (54.1/24.0/21.9 Mg/Ni/Y at.)</i>	137
<i>Figure 7-23: BSE image of (a) sample 30 (54.0/15.9/30.1 Mg/Ni/Y at.%); (b) sample 31 (69.1/9.4/21.5 Mg/Ni/Y at.%); (c) sample 32 (72.0/6.3/21.7 Mg/Ni/Y at.)</i>	138
<i>Figure 7-24: (a) BSE image of sample 2 (78.2/15.5/6.3 Mg/Ni/Y at.%); (b) XRD pattern of sample 3 (55.5/36.6/7.9 Mg/Ni/Y at.)</i>	139
<i>Figure 7-25: Mg-Ni-Y isothermal section at 673 K, based on this work, showing the samples investigated by DSC</i>	140

Figure 7-26: (a) DSC spectra during heating and cooling; (b) Calculated vertical section at 6.3 at.% Y with DSC signals of sample 2 (78.2/15.5/6.3 Mg/Ni/Y at.%)..... 141

Figure 7-27: (a) DSC spectra during heating and cooling; (b) Calculated vertical section at 21.94 at.% Y with DSC signals; (c) DSC measurements and calculated transformation temperature of sample 15 (54.1/24.0/21.9 Mg/Ni/Y at.%)..... 142

Figure 7-28: (a) DSC spectra during heating and cooling; (b) Calculated vertical section at 26.5 at.% Y with DSC signals of sample 14 (37.2/36.3/26.5 Mg/Ni/Y at.%)..... 143

Figure 7-29: DSC spectra of (a) sample 11 (26.0/38.2/35.8 Mg/Ni/Y at.); (b) sample 12 (28.0/36.8/35.2 Mg/Ni/Y at.); (c) Calculated vertical section at 35.2 at.% Y; (d) DSC measurements and calculated transformation temperature of samples 11 and 12 144

Figure 7-30: (a) DSC spectra during heating and cooling; (b) Calculated vertical section at 42.1 at.% Y with DSC signals of sample 28 (49.9/8.0/42.1 Mg/Ni/Y at.) ... 145

Figure 7-31: DSC spectra during heating and cooling; (b) Calculated vertical section at 46.8 at.% Y with DSC signals; (c) BSE image; (d) calculated phase assemblage diagram of sample 27 (38.2/15.0/46.8 Mg/Ni/Y at.) 146

Figure 7-32: (a) DSC spectra during heating and cooling; (b) Calculated vertical section at 48.0 at.% Y with DSC signals of sample 26 (37.0/15.0/48.0 Mg/Ni/Y at.)..... 147

Figure 7-33: DSC spectra of (a) sample 19 (19.5/29.5/51.0); (b) sample 20 (18.5/22.4/59.1 Mg/Ni/Y at.) during heating and cooling; Calculated vertical section at (c) 51.0 at.% Y; (d) 59.1 at.% Y with DSC signals of sample 20..... 148

Figure 7-34: (a) BSE image; (b) phase assemblage diagram of sample 19..... 150

Figure 7-35: Vertical section along $Mg_{56}Ni_{44}$ - MgY 150

Figure 7-36: Vertical section along $Mg_{84.2}Ni_{15.8}$ - $Ni_{15.8}Y_{84.2}$ 151

Figure 8-1: (a-c) BSE images of the solid–solid diffusion couple-1 annealed at 973 K for 6 weeks, showing the formation of four intermetallic compounds; (d) diffusion path projected on the Cu-Ni-Y Gibbs triangle. 154

Figure 8-2: Composition profile of the diffusion couple 1 along the line scan shown in figure 1(a). Different phases have been represented by different line type for clear understanding. 155

Figure 8-3: (a, b) BSE images of the solid–solid diffusion couple 2 annealed at 973 K for 6 weeks, showing the formation of six intermetallic compounds; (c) diffusion path in the Cu-Ni-Y Gibbs triangle. 157

<i>Figure 8-4: Composition profile of the diffusion couple 2 along the line scan shown in figure 3(b). Different phases have been represented by different line types for clear understanding.</i>	158
<i>Figure 8-5: Isothermal section of the Cu-Ni-Y system at 973 K. The arrow heads point to the location of the phase composition.</i>	159
<i>Figure 8-6: Variation of lattice parameters of (CuY) as a function of x for the $Cu_xNi_{1-x}Y$ ($0 \leq x \leq 1$) alloys (a) lattice parameter a; (b) lattice parameter b; (c) lattice parameter c; (d) cell volume.</i>	163
<i>Figure 8-7: The coordination spheres of a Ni atom of the (CuY) compound. The substitution sites of Ni by Cu have been denoted by M1.</i>	164
<i>Figure 8-8: XRD patterns of samples (a) 18 (Cu/Ni/Y 6.5/73.9/19.6 at.%); (b) 17 (Cu/Ni/Y 5.0/74.9/20.1 at.%); (c) 15 (Cu/Ni/Y 78.0/3.5/18.5 at.%) showing the effect of Cu_4Y-Ni_4Y extended solubility.</i>	166
<i>Figure 8-9: BSE image of sample 20 (Cu/Ni/Y 81.8/8.5/9.7 at.%).</i>	167
<i>Figure 8-10: (a) BSE image; (b) XRD pattern of sample 1 (20.8/9.1/70.1 Cu/Ni/Y at.%)</i>	168
<i>Figure 8-11: (a) DSC spectra; (b) Calculated vertical section at 9.1 at.% Ni with DSC signals; (c) phase assemblage diagram of sample 1 (20.8/9.1/70.1 Cu/Ni/Y at.%)</i>	169
<i>Figure 8-12: (a) BSE image; (b) XRD pattern of sample 4 (34.9/18.7/46.4 Cu/Ni/Y at.%)</i>	170
<i>Figure 8-13: DSC spectra of (a) sample 4 (34.9/18.7/46.4 Cu/Ni/Y at.%); (b) sample 5 (50.8/8.7/40.5 Cu/Ni/Y at.%) during heating and cooling; (c) calculated vertical section along $Cu_2Y-Ni_2Y_3$ with DSC signals</i>	171
<i>Figure 8-14: (a) BSE image; (b) XRD pattern of sample 6 (18.1/42.0/39.9 Cu/Ni/Y at.%)</i>	172
<i>Figure 8-15: Variation of lattice parameters of Cu_2Y as a function of x for the $Cu_{2-x}Ni_xY$ ($0 \leq x \leq 1.1$) alloys (a) lattice parameter a; (b) lattice parameter b; (c) lattice parameter c; (d) variation of cell volume.</i>	173
<i>Figure 8-16: BSE image of sample 7 (6.2/58.2/35.6 Cu/Ni/Y at.%)</i>	174
<i>Figure 8-17: DSC spectra of (a) sample 6 (18.2/42.7/39.1 Cu/Ni/Y at.%); (b) sample 7 (6.2/58.2/35.6 Cu/Ni/Y at.%) during heating and cooling; (c) calculated vertical section along Ni_2Y-CuY with DSC signals</i>	175

Figure 8-18: (a) XRD pattern of sample 9 (52.13/20.75/27.12 Cu/Ni/Y at.%); (b) DSC spectra of sample 10 (46.5/24.4/29.1 Cu/Ni/Y at.%) during heating and cooling; (c) Calculated vertical section at 24.38 at.% Ni with DSC signals of sample 10..... 176

Figure 8-19: BSE image of sample 12 (25.1/44.2/30.7 Cu/Ni/Y at.%)..... 177

Figure 8-20: XRD pattern of (a) sample 13 (15.9/54.4/29.7 Cu/Ni/Y at.%); (b) sample 18 (6.5/73.9/19.6 Cu/Ni/Y at.%) 178

Figure 8-21: (a) DSC spectra; (b) Calculated vertical section at 20.1 at.% Y with DSC signals of sample 17 (5.0/74.9/20.1 Cu/Ni/Y at.%)..... 179

Figure 8-22: (a) BSE image; (b) XRD pattern of sample 23 (80.9/14.1/5.0 Cu/Ni/Y at.%) 180

Figure 8-23: (a) BSE image (b) XRD pattern of sample 25 (53.4/37.9/8.7 Cu/Ni/Y at.%) 180

Figure 8-24: BSE image of (a) sample 27 (30.3/61.6/8.1 Cu/Ni/Y at.%); (b) sample 28 (14.0/79.6/6.4 Cu/Ni/Y at.%) 181

Figure 8-25: (a) DSC spectra of sample 28 (14.0/79.6/6.4 Cu/Ni/Y at.%) during heating and cooling; (b) Calculated vertical section at 79.6 at.% Ni with DSC signals 182

LIST OF TABLES

<i>Table 3-1: Atom-Atom “coordination numbers” of the liquid</i>	<i>33</i>
<i>Table 4-1: Optimized model parameters of the Mg-Ni system</i>	<i>37</i>
<i>Table 4-2: Optimized model parameters of the Cu-Ni system</i>	<i>41</i>
<i>Table 4-3: Optimized model parameters of the Ni-Y system</i>	<i>46</i>
<i>Table 4-4: Optimized model parameters of the Mg-Y system.....</i>	<i>49</i>
<i>Table 4-5: Parameters for the Mg-Cu-Ni ternary system.....</i>	<i>51</i>
<i>Table 4-6: Optimized thermodynamic parameters of the ternary Mg-Cu-Y system.....</i>	<i>61</i>
<i>Table 4-7: Optimized thermodynamic parameters of the ternary Mg-Ni-Y system.....</i>	<i>70</i>
<i>Table 4-8: Optimized thermodynamic parameters of the ternary Cu-Ni-Y system</i>	<i>73</i>
<i>Table 4-9: Ternary solubility of the Cu-Y and Ni-Y compounds in the Cu-Ni-Y ternary system.....</i>	<i>76</i>
<i>Table 5-1: Chemical composition of the Mg-Cu-Y alloys in at.%.....</i>	<i>79</i>
<i>Table 5-2: Chemical composition of the Mg-Ni-Y alloys in at.%.....</i>	<i>79</i>
<i>Table 5-3: Chemical composition of the Cu-Ni-Y alloys in at.%</i>	<i>80</i>
<i>Table 6-1: SEM–WDS data on selected Mg-Cu-Y alloys annealed at 673K.....</i>	<i>88</i>
<i>Table 6-2: Phase constituents by XRD/ WDS and DSC measurements and calculated transformation temperature of the investigated samples (h & c denotes heating & cooling)</i>	<i>97</i>
<i>Table 7-1: WDS data on the Mg-Ni-Y alloys annealed at 673 K.....</i>	<i>123</i>
<i>Table 7-2: The crystal structure data for MgNiY₄.....</i>	<i>128</i>
<i>Table 7-3: Atoms position in the unit cell for MgNiY₄</i>	<i>128</i>
<i>Table 7-4: The crystal structure data for MgNi₂Y₂.....</i>	<i>131</i>
<i>Table 7-5: Atoms position in the unit cell for MgNi₂Y₂.....</i>	<i>131</i>
<i>Table 8-1: WDS data on the Cu-Ni-Y alloys annealed at 973 K.....</i>	<i>160</i>

Table 8-2: The chemical compositions and unit cell parameters of (CuY) determined by WDS and Rietveld analysis 162

Table 8-3: Atomic bond lengths of the (CuY) compound in sample 1 and 7 165

LIST OF ABBREVIATIONS

DSC	Differential Scanning Calorimetry
DTA	Differential Thermal Analysis
XRD	X-ray Diffraction
OM	Optical Microscopy
SEM	Scanning Electron Microscopy
WDS	Wave Dispersive X-ray Spectrometer
MQCM	Modified Quasichemical model
BMG	Bulk Metallic Glass

Chapter 1

Introduction

1.1 Introduction

In the last decade, a new class of wonder materials called ‘metallic glass’ have begun to emerge from materials labs around the world. They exhibit properties of incredible strength and elasticity and are promoted as a true wonder material [1].

Unlike conventional metals, which are usually cooled slowly until they fully solidify, metallic glasses must be cooled very rapidly and very uniformly to freeze their random atomic pattern in place before crystallization occurs due to the nucleation and growth of crystal grains [1]. Until the middle of last decade, only thin films of metallic glass could be produced at high cooling rates. However, the high cost involved in this process made it unfeasible for any commercial application [2].

Scientists have been trying to find a way to prepare metallic glass in bulk form. The only way to achieve this is by reducing the critical cooling rate. Recently, it was possible to produce metallic glasses in bulk form on mixes of zirconium, magnesium, aluminum, and iron. The cooling rate was reduced to 1 K/sec or even less [2, 3]. These slower cooling rates mean that large parts can be fabricated. Furthermore, many of these metallic glasses remain stable against crystallization even when heated to temperatures slightly higher than their glass-transition temperatures [2, 3].

The availability of metallic glasses in relatively large samples allows the measurement of some relevant physical properties, particularly mechanical properties.

They are very promising for industrial applications because of their high strength to weight ratios, high hardness, rebound characteristics, corrosion resistance, good forming and shaping qualities and good magnetic properties. They are being considered for a range of applications including golf-club heads, high performance diaphragms for pressure sensors, precision micro-gears, surgical prosthetics, etc. [2, 3].

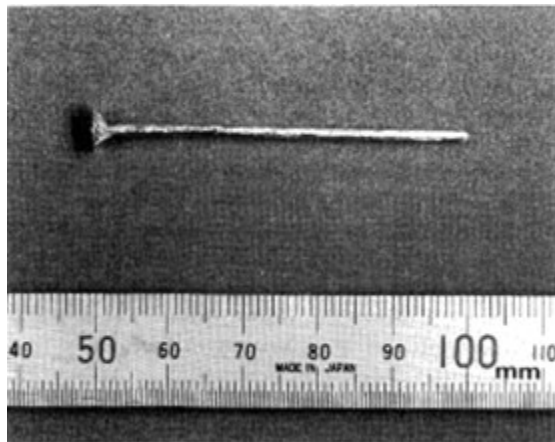


Figure 1-1: Metallic glass of Mg₈₀Cu₁₀Y₁₀ alloy in a cylindrical form [3, 4]

Mg-based alloys are very attractive as BMG (Bulk Metallic Glass) formers because of their high strength-to-weight ratio. Among the Mg alloys, Mg-Cu-Y has the largest super cooled liquid region [3, 4]. Hence, many research works on the formation of amorphous alloys on the Mg-Cu-Y system has been performed [2-13]. Inoue et al. [4] produced Mg-Cu-Y metallic glass by mold casting method into a copper mold. They obtained glasses of the Mg₈₀Cu₁₀Y₁₀ alloy as cylindrical specimens with diameters 1 mm and 1.5 mm as shown in Figure 1-1. Ma et al. [12] obtained even better results for the Mg₅₈Cu_{30.5}Y_{11.5} composition with a diameter of about 9 mm. Another recent work by Li et al. [9] on the Mg_{58.5}Cu_{27.5}Y₆ alloy showed that partial substitution of Cu and Y atoms

by Ni and Nd respectively, improves the glass forming ability. They were able to produce a fully amorphous rod of 13 mm in diameter.

Also, it is worth mentioning the importance of the Mg-based alloys for other industrial applications. Extensive attention has been paid to the utilization of Mg-based alloys as hydrogen storage materials owing to their high storage capacity [14]. The Mg-Ni-Y system is considered one of the promising candidates for nickel-metal hydride battery (MH) [15]. This kind of battery is expected to replace the nickel/cadmium rechargeable batteries in near future due to environment concern [15, 16].

Mg₂Ni has been used commercially as hydrogen storage material. Hara et al. [15] found that addition of Y to Mg₂Ni significantly improves the rate and amount of hydrogen absorption. They also reported a compound with an approximate composition MgNiY₃ plays a role as catalyst for the adsorption of hydrogen. However, they could not identify the crystal structure or phase relations of this compound.

The composition dependency of these applications suggests that a comprehensive thermodynamic analysis of the Mg-Cu-Ni-Y system can be very useful to identify some more suitable alloys. It is worth mentioning that phase relations and phase stability under given conditions can be better understood through computational thermodynamic modeling. Precise description of the ternary subsystems in the Mg-Cu-Ni-Y quaternary will provide an opportunity to approach the phase equilibria aspects of alloy development.

To date, very few studies have been reported on the phase relationships in the Mg-Ni-Y and Cu-Ni-Y systems. Only partial isothermal section of the Mg-Cu-Y system has been

reported in the literature. Hence a thorough investigation of these systems is required. Also, the Mg-Cu-Ni system will be thermodynamically modeled and combined with the other ternary systems into one database for the Mg-Cu-Ni-Y quaternary using CALPHAD approach.

1.2 CALPHAD approach

Experimental determination of phase diagram is a time consuming and expensive task. This effort can be reduced significantly through the use of thermodynamic optimization.

One of the most convenient and scientific approaches of optimization is CALPHAD (calculation of phase diagram). It was first introduced by Kaufman and Bernstein [17, 18]. Later Komar and Wollants [19] illustrated the CALPHAD method in a befitting way. It is based on minimization of the Gibbs free energy of the system and is thus, not only completely general and extensible, but also theoretically meaningful [18]. A preliminary phase diagram can be obtained by calculation of the thermodynamic functions of constituent subsystems. This preliminary diagram can then be used as a guide for the experimental work. In this way, maximum information can be obtained with minimum experimental effort focused on critical regions. Figure 1-2 shows a flowchart of this method.

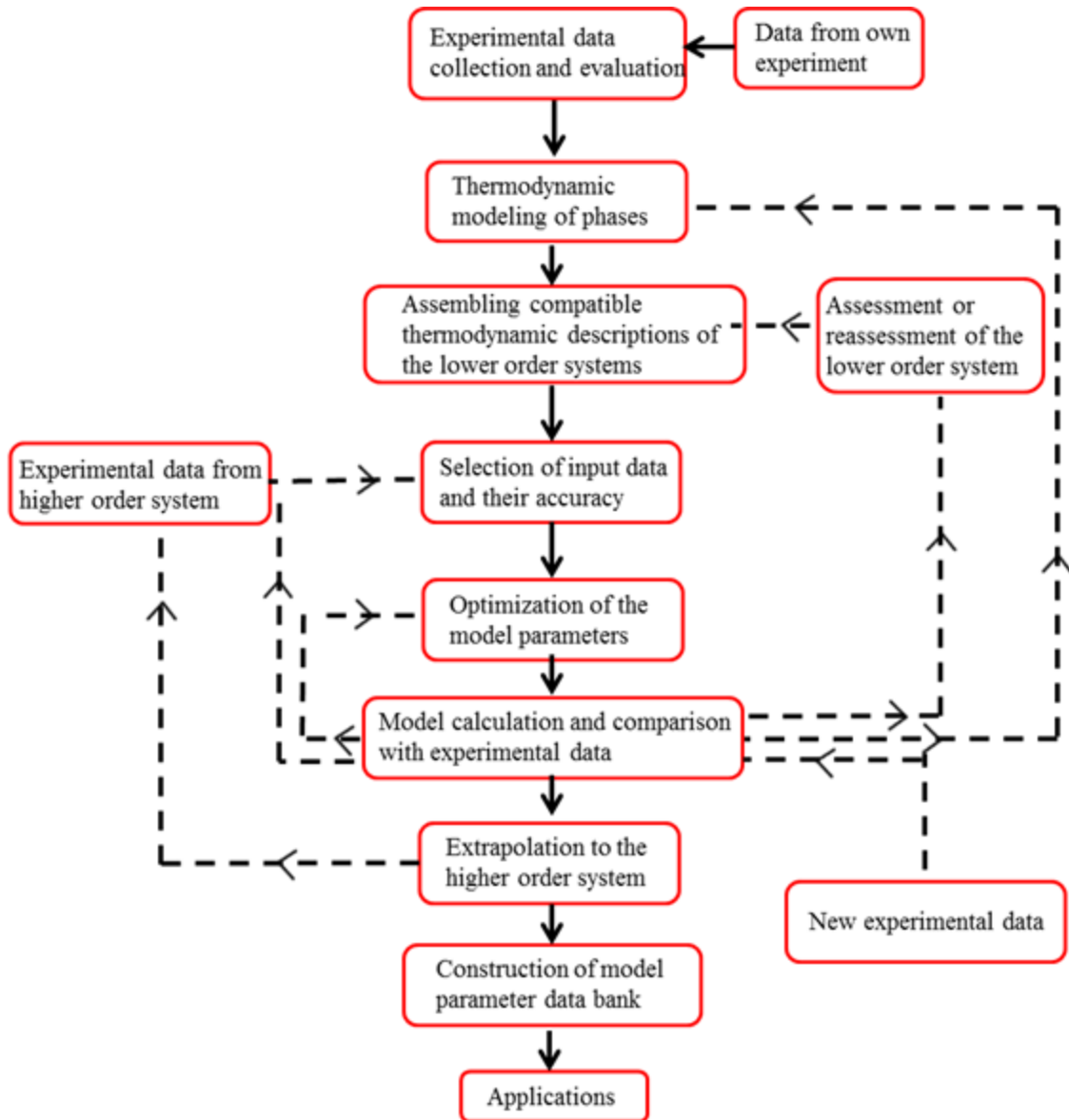


Figure 1-2: Flowchart of the CALPHAD method [19]

The first step of the thermodynamic optimization according to the CALPHAD method is to collect the experimental data from the relevant literature or from own experiments. Critical evaluation of these data is the second step. Elaborate discussion on the literature data are given in Chapter 2. The next step is to select a suitable

thermodynamic model for each phase. The selected model should be physically sound and it should be able to represent the P - T - x domain in which the phase is stable. Also, the model should have reasonable extrapolation characteristics in the higher order systems [19]. Before starting the optimization, it is essential to select the appropriate input data set for the calculation and assign a weighing factor based on the accuracy of the measurement. The subsequent steps are: the determination of the model parameters using the experimental data, and reproducing the phase diagram and the thermodynamic data, to verify the agreement between the calculations and the experimental data. The last two steps are iterative until a good agreement with the experimental data is achieved. After satisfactory optimization of the binaries the excess Gibbs energy parameters are used for the extrapolation of the higher order system. In this step, selection of a suitable geometric model is very important for reliable calculation. Several software packages are available. FactSage 6.3.1TM [20] program has been used in this work.

1.1 Thesis Layout

The entire thesis is divided into eight chapters; the following describes the contents of the remaining chapters. Chapter 2 presents a review of all the experimental phase equilibria and thermodynamic descriptions of the constituent binary and ternary systems of the Mg-Cu-Ni-Y quaternary. Chapter 3 describes the principles behind the phase diagram calculations. Also, different types of thermodynamic models used in the present work are explained. Chapter 4 presents results of the thermodynamic modeling of the binary and ternary subsystems in Mg-Cu-Ni-Y quaternary. A brief description of the experimental

methods used to construct the isothermal sections of the Mg-Cu-Y, Mg-Ni-Y and Cu-Ni-Y systems and to measure the phase transformation temperatures is presented in Chapter 5. Next, Chapters 6, 7 and 8 provide experimental results of the Mg-Cu-Y, Mg-Ni-Y and Cu-Ni-Y systems. Finally, Chapter 9 summarizes the contents of this thesis and suggests some possible directions for future research.

Chapter 2

Literature Review

A brief description of the previous works on the Mg-Cu-Ni, Mg-Ni-Y, Cu-Ni-Y and Mg-Cu-Y ternary systems and the sub-binaries Mg-Ni, Cu-Ni, Ni-Y and Mg-Y are given here. Enhanced assessment of the Mg-Cu-Y ternary and those of its binaries; Mg-Cu, Mg-Y and Cu-Y, have been done during the authors' M.A.Sc work. These binaries will not be discussed here. Since then, new experimental data have been published on the Mg-Y binary and Mg-Cu-Y ternary systems. They will be discussed in this chapter as well.

2.1 Mg-Ni binary system

Voss [21] was the first researcher who investigated the Mg-Ni system by thermal analysis in the composition range $0.04 < X_{Ni} < 0.98$. But in his work, the purity of Mg was not specified and the purity of Ni was low (97.7 wt%). Later, Haughton and Payne [22] determined the liquidus temperature more accurately in the Mg-rich end ($0 \leq X_{Ni} \leq 0.34$) by thermal analysis using high purity elements. Bagnoud and Feschotte [23] investigated the system using XRD, metallography, EPMA and DTA. Micke and Ipsier [24] determined the activity of magnesium over the Mg-Ni liquid in the $X_{Mg} > 0.65$ composition range by the isopiestic method. They also obtained the liquidus between $0.30 < X_{Ni} < 0.40$. According to these investigations, there are two eutectic and one peritectic reactions in the Mg-Ni system. Bagnoud and Feschotte [23] investigated the homogeneity range of $MgNi_2$ and mentioned that it extends from 66.2 at.% Ni at the peritectic three phase equilibrium of liquid, Mg_2Ni and $MgNi_2$ to 67.3 at.% Ni at the

eutectic three phase equilibrium of liquid, Ni-fcc and MgNi₂. All these data are used in the optimization except few data points of Voss [21] due to lack of consistency with more recent works.

Haughton and Payne [22] mentioned that the solid solubility of Ni in Mg is less than 0.04 at.% Ni at 773 K, whereas Merica and Waltenberg [25] reported that the solid solubility of Mg in Ni is less than 0.2 at.% Mg at 1373 K. These values have been used in the present work. Wollam and Wallace [26] and Buschow [27] disputed the ferromagnetic behavior of this system. They investigated the system by heat capacity and magnetic susceptibility measurements and did not find any anomaly in the behavior of MgNi₂ at any temperature. Hence the ferromagnetic behavior of Ni is not included in the current assessment.

Laves and Witte [28] determined the crystal structure of MgNi₂ to be hexagonal *hP*24-type with 8 molecules per unit cell, and the lattice parameters as $a = 0.48147$ nm and $c = 1.58019$ nm which are in good agreement with the reported values of Bagnoud and Feschotte [23] and Lieser and Witte [29]. The crystal structure of Mg₂Ni was determined by Schubert and Anderko [30] who reported a hexagonal, *C*16-type structure with 6 molecules per unit cell and lattice parameters of $a = 0.514$ nm and $c = 1.322$ nm which agree with the values reported by Buschow [27].

Feufel and Sommer [31] measured the integral enthalpy of mixing by calorimetric method at 1002 K and 1008 K. Sryvalin et al. [32] measured the activity of Mg and these results are in reasonable agreement with those of Micke and Ipser [24] in the composition range $X_{\text{Ni}} \leq 0.30$. Sieben et al. [33], also, measured the activity of Mg. Experimental data

on the heat capacity of MgNi_2 is also available. Feufel and Sommer [31] measured the heat capacity from 343 until 803 K with 20 K steps; whereas, Schubel [34] measured the same at about 100 K step from 474 to 867 K. These results will be compared with the present calculation. Enthalpy of formation of the MgNi_2 and Mg_2Ni compounds were measured by [33, 35-37]. All these data are in reasonable agreement among one another and will be compared with the current work.

Thermodynamic calculations of this system were carried out by Nayeb-Hashemi and Clark [38], Jacobs and Spencer [39] and most recently by Islam and Medraj [40]. But since the modified quasichemical model (MQCM) has been used for the liquid phase of the other binaries, Mg-Ni system needs to be re-optimized using this model.

2.2 Cu-Ni binary system

The equilibrium phases in the Cu-Ni system are the liquid phase and the fcc (Cu, Ni) phase. The liquid phase is miscible in all proportions. The solid solution is also miscible down to the critical (T_c) temperature where it shows immiscibility for a wide range. The fcc phase also shows magnetic property at lower temperature. A complete assessment of this system was done by Hansen and Anderko [41] and later by Chakrabarti and Laughlin [42]. Recent studies on the phase equilibria of the Cu-Ni system were done by [43-45] using XRD and microstructural analysis. All these results are in good agreement with each other and will be used for the present optimization.

The presence of the immiscibility in the fcc (Cu,Ni) phase is an important issue in this system. Several studies [46-49] on the electric, magnetic and structural properties of the alloys and their low temperature heat capacity confirmed the existence of the

immiscibility. Mozer et al. [46] used neutron diffraction method and suggested that the critical temperature should be between 506-536 K. They [46] used a sample of 47.5 at.% Ni and examined it over a range between 298 and 1298 K. While Ebel [47] employed X-ray analysis at 523 K and determined that the miscibility gap should exist between 10 to 90 at.% Ni at this temperature. Another neutron diffraction study by Vrijen and Radelaar [48] on compositions between 20 to 80 at.% Ni showed that the critical temperature is between 613-623K at 65 at.% Ni. Most of these analyses were summarized by Chakrabarti et al. [42] who concluded that the critical temperature should be below 627.5 K and may be shifted toward the nickel-rich region of this system. This conclusion along with other experimental data will be used as a guide line in the present work.

The enthalpy of mixing of the liquid Cu-Ni using calorimetric methods was carried out by several investigators [45, 50-54]. All these data except those of Predel [45, 50-54] are consistent with each other and will be used in the present calculation. Activities of the components in the liquid state was measured by [55-57] using different techniques. These data are also fairly reliable and will be used in this work.

Experimental results for the enthalpy of mixing of the solid fcc (Cu-Ni) phase was reported by [58-60]. The data of Leach and Bever [58] tend to be much higher than those of Oriani and Murphy [59] and Elford et al. [60]. Hence, for the present calculation the data of [59] and [60] will be used since these independent measurements are consistent with each other. Activity data for solid Cu-Ni alloys were reported by several investigators [61-65]. All the data show large positive deviation from ideality and are in reasonable agreement within the limits of experimental uncertainty. The present calculation will be compared with these data.

More recent works on this system was done by Mey [66] and Turchanin et al. [67]. They modeled the system thermodynamically quite well using the regular Bragg-Williams model which is suitable for random mixing solutions and Cu-Ni system does not show any indications of short range ordering in the liquid. However, all the other binaries in the Mg-Cu-Ni-Y quaternary system are modeled using the modified quasichemical model in the current work. Hence, Cu-Ni system is also re-optimized using MQCM for compatibility.

2.3 Ni-Y binary system

The phase diagram of the Ni-Y system was first investigated by Beaudry and Daane [68] and later by Domagala et al. [69]. Beaudry and Daane [68] used metallographic, thermal analysis and X-ray diffraction (XRD) methods in their investigation and reported the existence of nine intermetallic compounds; NiY_3 , Ni_2Y_3 , Ni_2Y , Ni_3Y , Ni_7Y_2 , Ni_4Y , Ni_{17}Y_2 , NiY and Ni_5Y . Except the last two, all other compounds undergo peritectic decomposition. Domagala et al. [69], however, reported eight compounds and missed Ni_7Y_2 . However, another investigation by Buschow [70] on several phases of the Ni-RE (RE = rare earth) showed that an Ni_7RE_2 phase occurs in all the heavier Ni-RE systems. Hence, the presence of Ni_7Y_2 compound in the Ni-Y system is consistent with the general trend and is included in this work. Domagala et al. [69], also, disagreed with Beaudry and Daane [68] regarding the stoichiometry of the most Ni-rich compound reporting the composition to be Ni_9Y not Ni_{17}Y_2 . Studying the crystal structure data reported by Buschow [71] reveals that the stoichiometry should be Ni_{17}Y_2 . This composition was also accepted by several other assessments [72-75] and hence it is used in the current analysis. The temperature and composition of the three eutectic reactions reported by [68] and [69]

are consistent with each other and are used in the current assessment with more weight for the data of [68] since the error associated with the data of [69] is higher.

Beaudry and Daane [68] reported the solubility of yttrium in nickel to be 0.1 at.% at 1523 K, while the solubility of nickel in yttrium to be 0.2 at.% at 1173 K. On the other hand, Domagala et al. [69] reported it to be about 1 wt.% in either terminal solutions. The value reported by Domagala et al. [69] seems to be very high considering the mutual solubility between Ni and other rare earth metals [76-80]. Hence, it is decided to be consistent with the solubilities reported by Beaudry and Daane [68].

The magnetic properties of the intermetallic compounds in the Ni-Y system were summarized by Buschow [70] and also by Gignoux et al. [81, 82]. None of the Ni-Y compounds has a magnetic ordering temperature above the room temperature. The highest value is found in the Ni_{17}Y_2 compound and is close to 160 K [70]. Also, Beaudry and Daane [68] did not find any of the intermetallic compounds to show ferromagnetic behavior at room temperature. Hence magnetic contribution is not considered in the optimization of this system.

Not many works on the experimental thermodynamic properties of the Ni-Y system could be found in the literature. Subramanian and Smith [73] determined the enthalpy of formation of the nine intermediate phases using electromotive force (emf) measurements. Enthalpy of formation of these compounds was estimated by [83-85]. However, only the experimentally measured values by Subramanian and Smith [73] will be used in the current optimization. Batalin et al. [86] measured the enthalpy of mixing of

the liquid Ni-Y at 1973 K using differential thermal analysis (DTA). The present calculation will be compared with their results.

Thermodynamic assessments were performed on the Ni-Y system by Nash [72], Du and Zhang [74] and Mattern et al. [75]. In spite of the high negative v-shaped experimental enthalpy of mixing data [86], none of these assessments considered the presence of short range ordering in the liquid. Therefore, it is decided to re-optimize the Ni-Y system using MQCM which accounts for the short range ordering.

2.4 Mg-Y binary system

The Mg-Y binary system has been modeled based on the available information by Mezbahul-Islam et al. [87]. Recently, in 2011, Zhao et al. [88] published new information on this system based on diffusion couple and key sample analysis. The homogeneity ranges of $\text{Mg}_{24}\text{Y}_5(\epsilon)$ and $\text{Mg}_2\text{Y}(\delta)$ has been re-established. Also, solubility of Y in the Mg-hcp has been adjusted. Hence, the Mg-Y system will be remodeled in this work to comply with these new findings.

Gibson et al. [89] were the first to report the Mg-Y phase diagram. They determined the maximum primary solid solubility of Y in Mg as 2.63 at.% Y at the eutectic temperature (840 K). This agrees well with the results of Sviderskaya and Padezhnova [90] who used thermal analysis to study the Mg-rich region of the Mg-Y system. Another investigation by Mizer and Clark [91] on this system using thermal analysis and metallography showed that the maximum solubility of Y in solid Mg was approximately 3.79 at.% Y at 838.5 K. This is, also, in good accord with the results of [89, 90].

Smith et al. [92] investigated the crystallography of $\text{MgY}(\gamma)$, $\text{Mg}_2\text{Y}(\delta)$ and $\text{Mg}_{24}\text{Y}_5(\epsilon)$ intermediate phases. The tangible homogeneity ranges of $\text{Mg}_{24}\text{Y}_5(\epsilon)$ and $\text{MgY}(\gamma)$ determined by them will be compared with the current analysis. The $\text{Mg}_2\text{Y}(\delta)$ compound was predicted as stoichiometric by [89, 92]. Their results do not agree with Flandorfer et al. [93], who employed XRD, optical microscopy, and microprobe analyses to study the Ce-Mg-Y isothermal section at 773 K. However, the homogeneity range for $\text{Mg}_{24}\text{Y}_5(\epsilon)$ and $\text{Mg}_2\text{Y}(\delta)$ reported by Zhao et al. [88] will be used during optimization since they diffusion couple analysis which is generally more accurate in determining solid solubility.

Agarwal et al. [94] measured calorimetrically the enthalpy of mixing of the Mg-Y liquid near the Mg-rich region (up to 21.8 at.% Y) at different temperatures. Activity of Mg was measured by Gansen et al. [95] using the vapour pressure technique. Their results are in agreement with those of Gansen and Ispert [96] who used the same method for the measurement. The enthalpy of formation of the three compounds was determined calorimetrically by Pyagai et al. [97]. Their results are in reasonable agreement with the calorimetric data of Smith et al. [92] except $\text{MgY}(\gamma)$, for which the value of Pyagai et al. [97] is twice more negative than that obtained by Smith et al. [92]. This is due to the difficulties in measuring the enthalpy of formation when the yttrium content increases resulting in more exothermic reactions. Also, Y has a high melting point compared to Mg and this leads to the sublimation of Mg during fusion of the metals [94]. The experimental results for enthalpy of formation of the compounds will be compared with the current modelling.

2.5 Mg-Cu and Cu-Y binary systems

The Mg-Cu and Cu-Y systems were optimized and published [87] based on the author's M.A.Sc thesis. No further work is needed on these systems. The calculated Mg-Cu and Cu-Y phase diagrams with the experimental data [98-102] [69, 103-106] from the literature are shown in Appendixes A-1 and A-2, respectively. The optimized parameters are listed in Appendixes A-3 and A-4. These parameters will be used for the ternary extrapolation.

2.6 Mg-Cu-Ni ternary system

Mg-Cu-Ni system has been studied by several investigators [107-109] and phase equilibria have been established through the determination of several isopleths, isothermal sections and liquidus projection. Experimental data on the thermodynamic properties of the liquid are also available. Comprehensive evaluation of these data was carried out by Gupta [110] and Lukas and Rokhlin [111]. A brief and critical assessment of the main literature data has been provided below.

Lieser and Witte [107] constructed a vertical section along 33.3 at.% Mg using thermal analysis, metallography and X-ray diffraction (XRD) methods. Mikheeva and Babayan [112] later confirmed the liquidus temperatures of Lieser and Witte [107]. Karonik et al. [113] investigated the Mg-rich side of the Mg-Cu-Ni system using metallography and XRD methods and reported an isothermal section at 673 K. Their [113] reported data will be used to determine the solubility of Cu in Mg₂Ni in the present work.

The compounds present in the Mg-Cu and Mg-Ni binary systems dissolve the third element. Mikheeva and Babayan [112] suggested that a complete mutual solubility exists between MgCu₂-MgNi₂. But later Lieser and Witte [107] showed by X-ray analysis that the crystal structures of Cu₂Mg and Ni₂Mg are not the same, indicating that the formation of complete mutual solid solubility is not possible. MgCu₂ has fcc crystal structure of the *C16* type while MgNi₂ is hcp with *C36* type. Lieser and Witte [107] estimated that the solubility of Cu in MgNi₂ is about 25 at.% in the 1193 K to 1423 K range. Whereas, Ipsier et al. [108] and Fehrenbach et al. [114] confirmed that the solubility should be less than 5 at.% between 931 K and 1203 K which is used in the current work. The solubility of Ni in MgCu₂ was estimated to be 26 at.% by Lieser and Witte [107] which is closer to Fehrenbach et al.'s [114] value of 20 at.%. Besides, the results of Ipsier et al. [108] suggested that the solubility should be higher than 22 at.%. In the present work the solubility reported by Ipsier et al. [108] has been used as it is the most accurate work.

Fehrenbach et al. [114], proposed four isothermal sections at 1003, 1073, 1081 and 1123 K based on their experimental data while taking into account previous analysis of Lieser and Witte [107], as can be seen in Figure 2-1. There is no accurate measurement for the positioning of the phase boundaries. Since these results were not supported by experiments, they will only be used as a guide line.

Ganasenkaran and Ipsier in a series of articles [115-117] constructed three vertical sections at constant ratio of, $X_{Cu} / X_{Ni} = 2.0, 1.0$ and 0.5 and one vertical section at 71 at.% Mg using DTA analysis. They also identified two quasi-peritectic and one ternary eutectic reaction. These data will be used for the thermodynamic optimization.

They [115-117] also measured Mg activities along the three vertical sections at constant $X_{\text{Cu}} / X_{\text{Ni}}$ ratio at 1173 K. Feufel and Sommer [31] measured the integral enthalpy of mixing of the ternary liquid for different compositions at a temperature of 1008 K using calorimetric method. The present calculation will be compared with these thermodynamic properties.

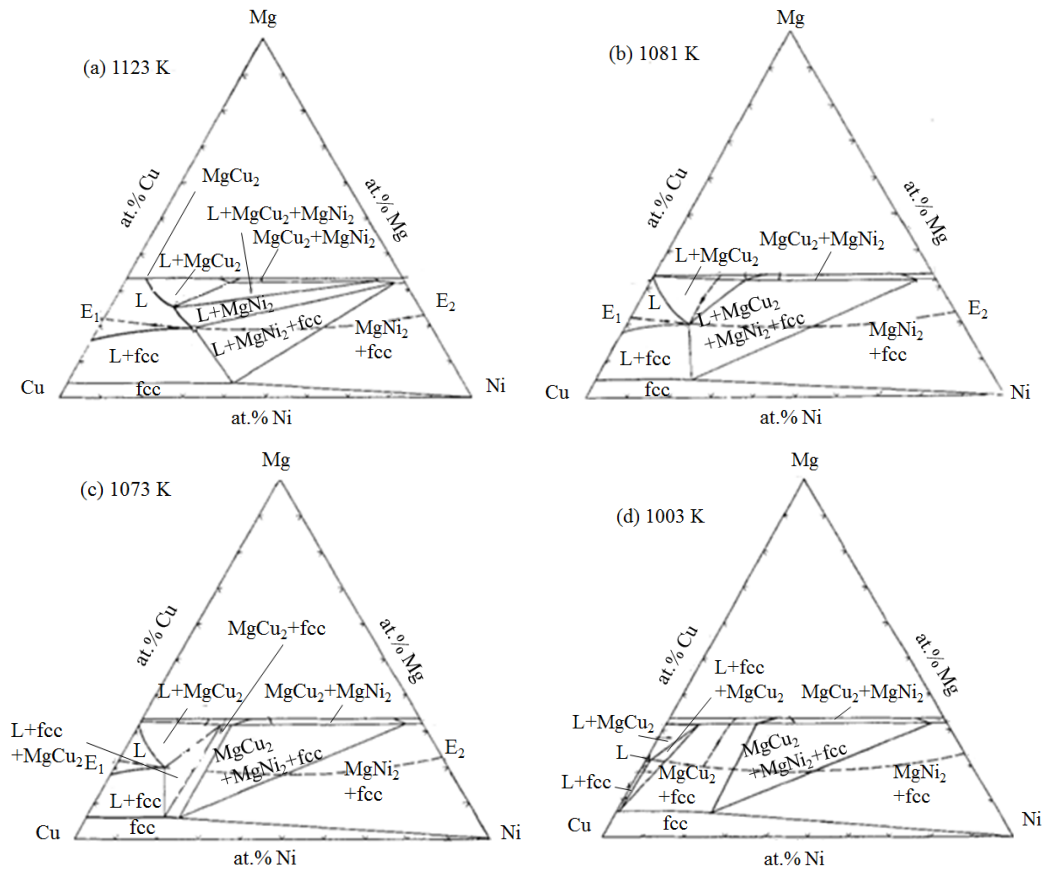


Figure 2-1: Isothermal sections at (a) 1123 K; (b) 1081 K; (c) 1073 K; (d) 1003 K [114]

Thermodynamic assessment of this system was done by Gorsse and Shiflet [118]. Unfortunately their calculations could not be reproduced apparently due to errors in some of the parameters. In 2008, two thermodynamic assessments of the Mg-Cu-Ni system were published by Miettinen [119] and Xiong et al. [109]. Both of them are consistent with most of the experimental data.

The phase equilibria of the Mg-Cu-Ni are well established and require no further experimental work. However due to the use of the modified quasichemical model for the liquid phase and to reduce the number of ternary parameters; this system was re-optimized in this work.

2.7 Mg-Cu-Y ternary system

Mg-Cu-Y is an important metallic glass system. Hence, a lot of work has been done on this system to identify and characterization of the best glass forming compositions [3, 6, 8, 13, 120]. Figure 2-2 (a) shows some of these compositions. But little work has been done to establish the equilibrium phase relations. Palumbo and Battezzati [121] used CALPHAD approach to describe thermodynamically short range order in the liquid, glass transition behavior and the rapid solidification behavior. However, because of lack of broader understanding of the phase equilibria their work was not conclusive. Considering the importance of this system and the need for the equilibrium phase relations, thermodynamic modeling of this system was published by Mezbahul-Islam and Medraj [87] using all the available information from the literature at that time. However, two recent publications by De Negri et al. [122] and Solokha et al. [123] reported the presence of nine additional ternary compounds in the Mg-Cu-Y system. De Negri et al. [122] also reported an isothermal section at 673 K in the 0-66.7 at.% Cu as shown in Figure 2-2 (b). The available crystal structure information of the ternary compounds is listed in Appendix A-5. Later, Mezbahul-Islam et al. [122] reported three vertical sections of Mg-Cu-Y system based on the DSC measurements of three key samples. But the complete assesment of the liquidus surface could not be done due to lack of experimental data.

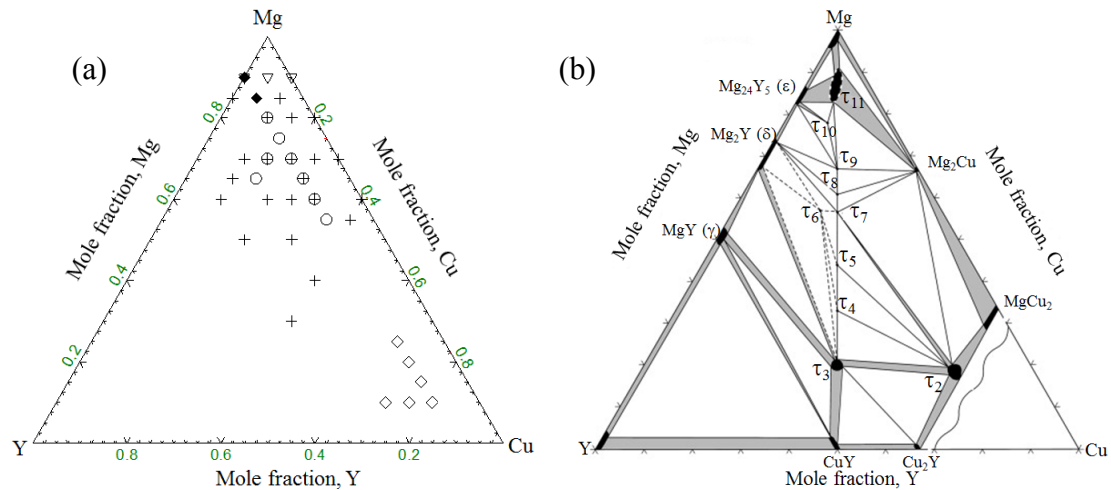


Figure 2-2: Composition of the published glass forming alloys: (O) amorphous alloys [3]; (◆) crystalline alloys [3]; (+) amorphous alloys [8]; (▽) crystalline alloys [8]; (◇) amorphous alloys [124]; (b) Isothermal section of the Mg-Cu-Y system at 673 K from 0 to 66.7 at.% Cu

Therefore a complete understanding of this system is still unknown. The isothermal section of the Mg-Cu-Y system at 673 K with more than 66 at.% Cu is not confirmed. Some of the amorphous alloys have been reported in the Cu-rich region [124] as can be seen in Figure 2-2 (a). Hence, experimental study is required on this portion (more than 66 at.% Cu) of the phase diagram. Also, very little information about the liquidus surface is available. It is important to understand the solidification behavior and phase transformations temperatures especially for alloys important for metallic glass. This can be obtained through DSC measurements on selected key samples. Furthermore, thermodynamic modeling with the newly discovered ternary compounds with their solubility has not been done. This will be attempted in the present work.

2.8 Mg-Ni-Y ternary system

The Mg-Ni-Y system is considered to be one of the promising candidates [15] for nickel-metal hydride battery (MH). Besides, this ternary is one of the promising Mg-

based metallic glass systems [8, 9]. Therefore, it is important to obtain a clear understanding of the phase equilibria of this system.

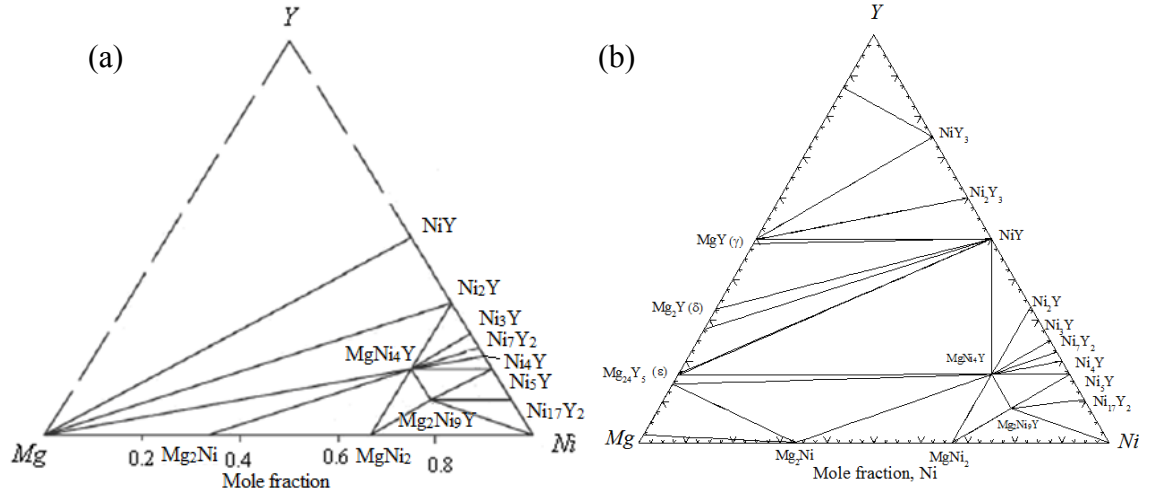


Figure 2-3: Isothermal section of the Mg-Ni-Y system at 673 K (Ni-rich part) [125]; (b) calculated isothermal section of the Mg-Ni-Y system at 673 K [126]

Yao et al. [125] investigated the 673 K isothermal section of the Ni-rich region using XRD, SEM and DTA and reported the partial section shown in Figure 2-3 (a). They [125] confirmed the existence of two ternary compounds Mg_2Ni_9Y and $MgNi_4Y$. The compositions of these ternary compounds were reported earlier by Kadir et al. [127-129] and Aona et al. [130]. However, the melting temperature and enthalpy of formation of these compounds have not been determined. Mezbahul-Islam and Medraj [126] optimized the Mg-Ni-Y system based on the available experimental data until 2009 as shown in Figure 2-3 (b). The melting temperatures of the ternary compounds were not known. Hence to predict these, they [126] made some assumption based on the annealing temperature of the alloys reported in the literature [15, 130].

It can be seen that only Ni-rich side of the Mg-Ni-Y system has been experimentally investigated. It is possible to have more ternary compounds in this

system. The chemistry of the phases and their microstructural details should be further studied. Therefore, it is decided to investigate the system experimentally in order to have better understanding of the phase equilibria for the whole composition range. The new experimental findings are incorporated in the current thermodynamic model of this system.

2.9 Cu-Ni-Y ternary system

Rare earth (RE)-Ni based alloys are promising candidates for the hydrogen storage and magnetic materials [131, 132]. $\text{Ni}_{2.5}\text{Cu}_{0.5}\text{Y}$ has been found to be a good hydrogen storage material [131]. Ni_{17}Y_2 has shown some magnetic characteristics with the addition of small amount of Cu [132]. Also, the Cu-Ni-Y is a constituent ternary of the Mg-Cu-Ni-Y which is an important metallic glass forming system [9, 133]. Therefore, one of the main aims of this work is to provide a clear idea about the phase relations in the Cu-Ni-Y system for the whole composition range.

Only limited amount of work has been done on this system. Zheng and Nong [134] reported a partial isothermal section ($\text{Y} \leq 16.7$ wt.%) at room temperature using XRD of key alloys. They reported two three-phase equilibrium regions among Cu_6Y , Ni_5Y and $\text{fcc}(\text{Cu},\text{Ni})$ phases and Ni_5Y , Ni_{17}Y_2 and $\text{fcc}(\text{Cu},\text{Ni})$ phases. Although, Cu_5Y does not exist in the accepted Cu-Y binary phase diagram, they proposed complete solubility between Ni_5Y and Cu_5Y . They also reported the solubility of Ni_{17}Y_2 to be about 35 at% Cu and the maximum solubility of Y in the $\text{fcc}(\text{Cu},\text{Ni})$ phase to be less than 1.5 at.% Y. Kadomatsu and Kurisu [135] studied the structural phase transitions in $\text{Cu}_{1-x}\text{Ni}_x\text{Y}$ ($0 \leq x \leq 0.06$) alloys using electrical resistivity measurements, thermal expansion

and X-ray analysis. They reported that the CsCl type CuY phase changes to FeB type structure at low temperature. This phase transition takes place with a very large thermal hysteresis. While heating, it was found that the low temperature phase (FeB type) is stable up to 783 K while during cooling, it was stable down to 120 K. Burnasheva and Tarasov [131] studied the hydrogen storage capacity of Ni₃Y by partially replacing Ni with other transition elements. They found Ni₃Y to be stable until 16.67 at.% Cu at 770 K. Paul-Boncour et al. [136] studied the (Ni,Cu)₂Y pseudobinary compounds for the structural change of the cubic Ni₂Y phase to the orthorhombic Cu₂Y phase using XRD, neutron diffraction, density measurement and EPMA. They reported that about 20% of Ni can be substituted by Cu while preserving the cubic superstructure of Ni₂Y_{0.95}; whereas 50% of Cu can be replaced by Ni in the orthorhombic Cu₂Y structure both at 1023 K. Dwight [137] studied the crystal structures of several Cu_xNi_{5-x}Y (0 ≤ x ≤ 5) alloys by XRD to understand the solubility of the Ni₅Y compound. They concluded that Ni₅Y has a solubility of about 66.67 at.% Cu at 1073 K. All these results will be compared with the present investigation. A summary of the previous work on this system up to 1994 has been published by Gupta [138], who proposed a partial isothermal section as shown in Figure 2-4. The crystal structure of the binary phases of the Cu-Ni-Y system has been documented in the Pearson database [139] and listed in Appendix A-6.

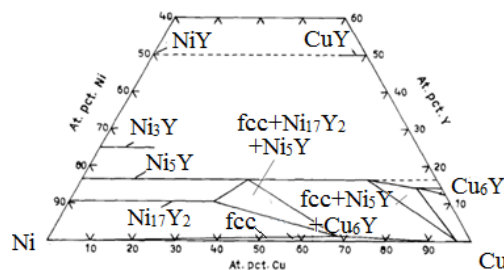


Figure 2-4: A partial isothermal section of Cu-Ni-Y system (for Y ≤ 16.7 at.% Y) at 293 K [138]

A few binary compounds in this system were reported to dissolve the third element. This needs to be confirmed. Also, the solubility of other binary compounds will be investigated in this work. Gupta [138] proposed a complete mutual solubility between CuY and NiY. This also needs to be confirmed. Finally, the equilibrium phase relationships need to be understood. In-order to clarify all these issues it is decided to experimentally investigate the Cu-Ni-Y system and construct the 973 K isothermal section for the whole composition range. Also, it is worth emphasizing that in the current work a combination of many experimental techniques have been used to obtain as accurate results as possible; whereas in the literature one experimental technique was used at a time to study this system.

2.10 Objectives

The main objective of this research is to construct a reliable thermodynamic database for the Mg-Cu-Ni-Y quaternary system using CALPHAD approach combined with experimental investigations. A systematic investigation of microstructural characterization and thermal analysis is carried out using X-ray Diffraction (XRD), Optical Microscopy (OM), Scanning Electron Microscopy (SEM), Wave Dispersive X-ray Spectrometer (WDS) and Differential Scanning Calorimetry (DSC) of the three ternary systems: Mg-Cu-Y, Mg-Ni-Y and Cu-Ni-Y. Specific objectives include:

- To thermodynamically model four of the binary systems: Mg-Ni, Ni-Y, Cu-Ni and Mg-Y. The model parameters for the other two binary systems: Mg-Cu and Cu-Y are already available from the author's M.A.Sc thesis [140] on the Mg-Cu-Y ternary system.

- To thermodynamically model the Mg-Cu-Ni ternary system taking into consideration the short range ordering in the liquid phase.
- To construct the isothermal sections of the Mg-Cu-Y, Mg-Ni-Y systems at 673 K and Cu-Ni-Y system at 973 K by means of experiments coupled with thermodynamic modeling.
- To measure phase transformation temperatures using DSC of the selected key alloys on the Mg-Cu-Y, Mg-Ni-Y and Cu-Ni-Y systems. This will provide valuable information during thermodynamic modeling.
- To provide liquidus projection of the ternary systems with the composition and temperature of all the invariant reactions using thermodynamic calculations.
- To build a self-consistent thermodynamic database for the Mg-Cu-Ni-Y quaternary.

Chapter 3

Thermodynamic Modeling

Thermodynamic modeling for any alloy system is nothing but a process of finding appropriate Gibbs energy equations for different phases in terms of temperature and composition of the constituent elements. By minimizing the total Gibbs energy, of all the phases present in equilibrium, phase diagrams can be calculated for a multicomponent system [18]. This is usually done by a computer-assisted statistical procedure using experimental thermochemical and phase equilibrium data as input within the framework of CALPHAD.

The Gibbs energy for any phase ‘ ϕ ’ can be defined as equation 3.1

$$G_i^\phi = {}^o G^\phi + {}^{ideal} G^\phi + {}^{Ex} G^\phi \quad \dots\dots\dots (3.1)$$

Where, G^o is the contribution from the mechanical mixing of pure components, ${}^{ideal}G^\phi$ is the ideal mixing contribution, and ${}^{ex}G^\phi$ is the excess Gibbs free energy contribution due to the interactions between the components. To expand the individual terms in equation 3.1, a hypothetical binary system with components A and B is considered. Thus mechanical mixing and ideal mixing of this system can be expressed by equations 3.2 and 3.3, respectively.

$${}^o G^\phi = x_A {}^o G_A + x_B {}^o G_B \quad \dots\dots\dots(3.2)$$

$$\begin{aligned} {}^{ideal} G^\phi &= H_{mix}^{ideal} + TS_{mix}^{ideal} \\ &= 0 - RT(x_A \ln x_A + x_B \ln x_B) \\ &= -RT(x_A \ln x_A + x_B \ln x_B) \quad \dots\dots\dots(3.3) \end{aligned}$$

Where, x_A and x_B are the compositions of the components A and B respectively; ${}^{\circ}G_A$ and ${}^{\circ}G_B$ are the Gibbs free energy of the pure components A and B at standard state (298.15 K and 1 bar); R is the universal gas constant. The contribution of ideal enthalpy of mixing, H_{mix}^{ideal} is zero since there is no change in bond energy upon mixing. The excess Gibbs energy, ${}^{ex}G^{\phi}$, can be described by different models and will be discussed in this chapter.

3.1 Analytical Description of the Employed Thermodynamic Models

Different thermodynamic models were used in the present work. A brief description of them is presented here.

3.1.1 Unary phases

The Gibbs energy function used for the pure elements i ($i = Mg, Cu, Ni$ and Y) in a phase ϕ is described by the following equation:

$${}^{\circ}G_i^{\phi}(T) = a + bT + cT \ln T + dT^2 + eT^3 + fT^{-1} + gT^7 + hT^{-9} \quad \dots\dots\dots (3.4)$$

Where, $G_i^{\phi}(T)$ is the Gibbs energy of the pure element at a standard state, T is the absolute temperature. The values of the coefficients a through h are assigned from the Scientific Group Thermodata Europe (SGTE) database [141].

3.1.2 Stoichiometric phases

The Gibbs energy of a binary stoichiometric phase is given by

$$G^{\phi} = x_i {}^{\circ}G_i^{\phi} + x_j {}^{\circ}G_j^{\phi} + \Delta G_f \quad \dots\dots\dots (3.5)$$

Where, x_i and x_j are mole fractions of elements i and j and are given by the stoichiometry of the compound. ${}^{\circ}G_i^{\phi}$ and ${}^{\circ}G_j^{\phi}$ denote the Gibbs energy of elements i and j in their standard state. ΔG_f is the Gibbs energy of formation per mole of atoms of the stoichiometric compound, which is expressed by the following equation:

$$\Delta G_f = a + bT \quad \dots\dots\dots (3.6)$$

The parameters a and b are obtained by optimization using experimental results of phase equilibria and thermodynamic data.

3.1.3 Disordered solution phases

To model the disordered solution phases, two different types of solution models were used in this work. To describe the terminal solid solution phases, the Bragg-Williams model [142, 143] with Redlich-Kister polynomial [144] was used. The Modified Quasichemical model was used to describe the liquid phase in order to account for the presence of short range ordering.

3.1.3.1 Random solution phases

The Gibbs energy for the Random solid solution phases is described by the following equation:

$$G = x_i {}^{\circ}G_i^{\phi} + x_j {}^{\circ}G_j^{\phi} + RT[x_i \ln x_i + x_j \ln x_j] + {}^{ex}G^{\phi} + {}^{ex}G_{mag}^{\phi} \quad \dots\dots\dots (3.7)$$

Where, ϕ denotes the phase of interest and x_i , x_j denote the mole fraction of components i and j , respectively. The first two terms of equation (3.7) represent the Gibbs energy of the mechanical mixture of the components, the third term is the ideal

Gibbs energy of mixing, and the fourth term is the excess Gibbs energy, which is described by the Redlich-Kister polynomial [144] in this work and can be represented as:

$${}^{ex} G^\phi = x_i x_j \sum_{n=0}^{m} {}^n L_{i,j}^\phi (x_i - x_j)^n \dots\dots\dots(3.8)$$

Here, ${}^n L_{i,j}^\phi = a_n + b_n T$ ($n = 0, 1, \dots, m$) where ${}^n L_{i,j}^\phi$ are the interaction parameters, $m+1$ is the number of terms, and a_n and b_n are the parameters of the model. The fifth term in equation (3.7) represents the magnetic contribution to the Gibbs energy of the ϕ phase and can be represented according to Hillert and Jarl [145] as:

$${}^{ex} G = RT(\ln \beta^\phi + 1)f(\tau) \dots\dots\dots (3.9)$$

where β^ϕ is a quantity related to the total magnetic entropy, which is set equal to the Bohr magnetic moment per mole of atoms; τ is defined as T/T_c , where T_c is the critical temperature for magnetic ordering, i.e. the Curie temperature of the alloy. $f(\tau)$ represents the polynomials obtained by Hillert and Jarl [145] based on the magnetic specific heat of iron. For a solution phase ϕ , T_c^ϕ and β^ϕ are described by the following expressions

$$T_c^\phi = x_i {}^o T_i^\phi + x_j {}^o T_j^\phi + x_i x_j \sum_{k=0}^n {}^k T_{i,j}^\phi (x_i - x_j)^k \dots\dots\dots (3.10)$$

$$\beta_c^\phi = x_i {}^o \beta_i^\phi + x_j {}^o \beta_j^\phi + x_i x_j \sum_{k=0}^n {}^k \beta_{i,j}^\phi (x_i - x_j)^k \dots\dots\dots (3.11)$$

Where ${}^o T_*^\phi$ and ${}^o \beta_*^\phi$ ($* = i$ or j) are the corresponding magnetic parameters of pure elements; ${}^k T_{i,j}^\phi$ and ${}^k \beta_{i,j}^\phi$ are adjustable binary magnetic interaction parameters.

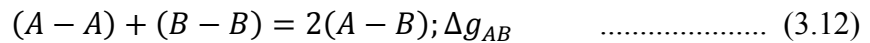
In this study, five terminal solid solutions: Mg-hcp, Y-hcp, Y-bcc, Cu-fcc, and Ni-fcc in different binary systems have been modeled using the random solution model. Only the fcc(Cu,Ni) phase shows some magnetic property at lower temperature.

Therefore, magnetic contribution has been used during modeling of this phase according to equation 3.7.

3.1.3.2 Liquid phases

The modified quasichemical model (MQCM) [146-149] was chosen to describe the liquid phases of the six constituent binaries of the Mg-Cu-Ni-Y quaternary system. Mg-Ni, Ni-Y, Mg-Y and Cu-Y binary systems have very high negative enthalpy of mixing. Also, the calculated entropy of mixing curves of Cu-Y and Mg-Y system assume the m-shape. These are indications of the presence of short range ordering [146] in the liquid. Also, it is observed that systems showing glass forming ability may have short range ordering in the liquid [150, 151]. Mg-Cu-Y and Mg-Ni-Y are promising glass forming systems. Therefore, it is decided to consider the presence of short range ordering in the liquid. MQCM is the most suitable model to describe this phenomenon. According to Pelton *et al.* [146-149] this model has three distinct characteristics: It permits choosing the composition of maximum short range ordering in a binary system. It expresses the energy of pair formation as a function of composition which can be expanded as a polynomial in the pair fraction. The model can be extended to multicomponent system.

To elaborate on this model, the following pair exchange reaction is discussed



In equation 3.12, (A-B) represents a first-nearest-neighbor pair and Δg_{AB} is the non-configurational Gibbs energy change for the formation of 2 moles of (A-B) pair [146-149]. The Gibbs energy of the binary A-B solution can be written as:

$$G = (n_A g_A^o + n_B g_B^o) - T \Delta S^{config} + \left(\frac{n_{AB}}{2}\right) \Delta g_{AB} \quad \dots\dots\dots (3.13)$$

Here, g_A^o and g_B^o are the molar Gibbs energies of the pure liquid, n_A and n_B are the number of moles of the components A and B , n_{AB} is the number of $(A-B)$ pairs, ΔS^{config} is the configurational entropy of mixing given by random distribution of $(A-A)$, $(B-B)$ and $(A-B)$ pairs which can be expressed as equation 3.14.

$$\Delta S^{config} = -R(n_A \ln x_A + n_B \ln x_B) - R[n_{AA} \ln \left(\frac{X_{AA}}{Y_A^2} \right) + n_{BB} \ln \left(\frac{X_{BB}}{Y_B^2} \right) + n_{AB} \ln \left(\frac{X_{AB}}{2Y_A Y_B} \right)] \dots\dots\dots(3.14)$$

Where, x_A and x_B are the overall mole fractions of A and B . X_{AA} , X_{BB} and X_{AB} are the pair fractions and can be expressed as in equation 3.15

$$X_{AA} = \frac{n_{AA}}{n_{AA}+n_{BB}+n_{AB}}; X_{BB} = \frac{n_{BB}}{n_{AA}+n_{BB}+n_{AB}}; X_{AB} = \frac{n_{AB}}{n_{AA}+n_{BB}+n_{AB}} \dots\dots\dots (3.15)$$

Y_A and Y_B in equation 3.14 are the coordination equivalent fraction and can be expressed as in equation 3.16.

$$Y_A = \frac{Z_A n_A}{Z_A n_A + Z_B n_B} = \frac{Z_A X_A}{Z_A X_A + Z_B X_B} = 1 - Y_B \dots\dots\dots (3.16)$$

Where, Z_A and Z_B are the coordination numbers of A and B which can be represented by equations 3.17 and 3.18.

$$\frac{1}{Z_A} = \frac{1}{Z_{AA}^A} \left(\frac{2n_{AA}}{2n_{AA}+n_{AB}} \right) + \frac{1}{Z_{AB}^A} \left(\frac{n_{AB}}{2n_{AA}+n_{AB}} \right) \dots\dots\dots(3.17)$$

$$\frac{1}{Z_B} = \frac{1}{Z_{BB}^B} \left(\frac{2n_{BB}}{2n_{BB}+n_{AB}} \right) + \frac{1}{Z_{BA}^B} \left(\frac{n_{AB}}{2n_{BB}+n_{AB}} \right) \dots\dots\dots (3.18)$$

Z_{AA}^A and Z_{AB}^A are the values of Z_A when all nearest neighbors of an A atom are A 's, and when all nearest neighbors of A atom are B 's, respectively. Similarly for Z_{BB}^B and Z_{BA}^B .

The composition of maximum short range ordering is determined by the ratio $\frac{Z_{BA}^B}{Z_{AB}^A}$ [146-149]. Values of Z_{AB}^A and Z_{BA}^B are unique to the A - B binary system and should be carefully determined to fit the thermodynamic experimental data (enthalpy of mixing, activity etc.). The selected values in the present work are given in Table 3-1. The tendency to maximum short range ordering near the composition 45 at.% Y in the Ni-Y system was obtained by setting $Z_{NiY}^{Ni} = 5$ and $Z_{NiY}^Y = 6$. For Mg-Ni system, experimental enthalpy of mixing data is available only near the Mg-rich region. Following the trend of these data and studying previous optimization works on this system [45-47], it is assumed that the maximum short range ordering should be near 35 at.% Ni which was obtained by setting $Z_{MgNi}^{Mg} = 2$ and $Z_{MgNi}^{Ni} = 4$. The Cu-Ni system does not show any tendency of short range ordering. The enthalpy of mixing of the Cu-Ni liquid is symmetric. Therefore coordination no of 6 has been used for both Z_{CuNi}^{Cu} and Z_{CuNi}^{Ni} . The values of Z_{AA}^A is common for all systems containing A as a component. The same is true for all components. For this work 6 was chosen for Z_{MgMg}^{Mg} , Z_{CuCu}^{Cu} , Z_{NiNi}^{Ni} and Z_{YY}^Y . The value 6 was chosen because it gave the best possible fit for many binary systems and is recommended by Dr. Pelton's group [146-149].

The energy of pair formation in equation 3.13 can be expressed as a polynomial in terms of the pair fraction as shown in equation 3.19 [146-149]:

$$\Delta g_{AB} = \Delta g_{AB}^o + \sum_{i \geq 1} g_{AB}^{io} X_{AA}^i + \sum_{j \geq 1} g_{AB}^{oj} X_{BB}^j \dots \dots \dots (3.19)$$

Where, Δg_{AB}^o , g_{AB}^{io} and g_{AB}^{oj} are model parameters and can be expressed as functions of temperature ($\Delta g_{AB}^o = a + bT$).

Table 3-1: Atom-Atom “coordination numbers” of the liquid

A	B	Z_{AB}^A	Z_{AB}^B
Mg	Mg	6	6
Cu	Cu	6	6
Ni	Ni	6	6
Y	Y	6	6
Mg	Cu	4	2
Cu	Y	3	6
Mg	Y	2	4
Mg	Ni	2	4
Cu	Ni	6	6
Y	Ni	6	5

3.1.4 Ordered solution phases

The Gibbs energy of an ordered solution phase is described by the compound energy formalism [152] as shown in the following equations:

$$G = G^{ref} + G^{ideal} + G^{excess} \quad \dots\dots\dots (3.20)$$

$$G^{ref} = \sum y_i^l y_j^m \dots y_k^q \quad \dots\dots\dots (3.21)$$

$$G^{ideal} = R(T/K) \sum_l f_l \sum_i y_i^l \ln y_i^l \quad \dots\dots\dots (3.22)$$

$$G^{excess} = \sum y_i^l y_j^l y_k^m \sum_{\gamma=0} \gamma L_{(i,j):k} \times (y_i^l - y_j^l)^\gamma \quad \dots\dots\dots (3.23)$$

where, $i, j, \dots k$ represent components or vacancy in l, m and q sublattices. y_i^l represents the site fraction of component i on sublattice l ; f_l is the fraction of sublattice l relative to the total lattice sites, ${}^oG_{(i,j,\dots,k)}$ represents the compound energy of a real or a hypothetical end member in the sublattice model. ${}^\gamma L_{(i,j):k}$ represents the interaction parameters which describe the interaction between the constituents within the sublattice.

Based on the experimental findings in this work as well as from the literature the binary and ternary solubility of the binary and ternary compounds have been modeled using the compound energy formalism. The details of the selection of the number of the sublattices and their constituents will be discussed in the results section.

3.2 Extrapolation of Ternary Systems

The thermodynamic properties of a ternary solution can be calculated from the optimized data of its binary subsystems. To obtain a precise ternary system, different ‘geometric’ extrapolation techniques have been proposed. Some of these are symmetric and some are asymmetric as shown in Figure 3-1. The Kohler [153] and Muggianu [154] are well known symmetric models while Toop [155] is an asymmetric model. In the asymmetric model, one component is singled out. The choice of the asymmetric component is a matter of experience. For systems with strong interactions, different models (or extrapolation techniques) can give quite different results. In particular, asymmetric models can give better results for some systems, while symmetric models can be better for other systems [156]. Different opinions, on the choice of the asymmetric component for the asymmetric models, can also be found in the literature [153].

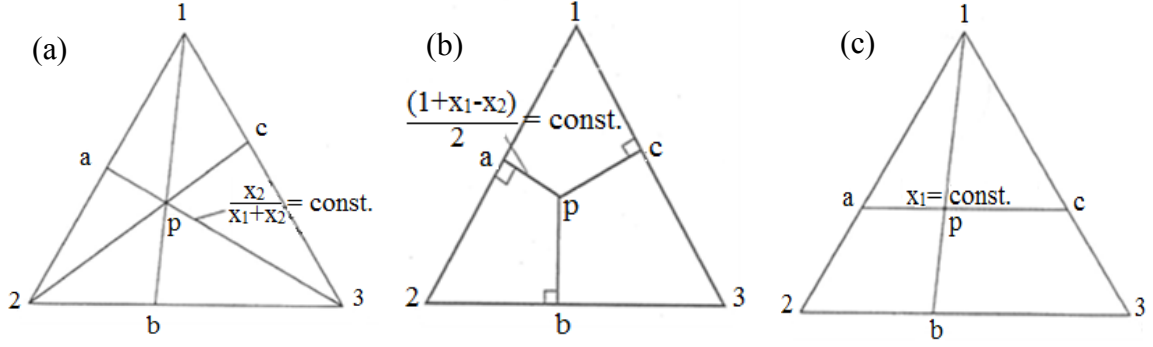


Figure 3-1: Different “geometric” models for ternary extrapolation: (a) Kohler (b) Muggianu and (c) Kohler/Toop [157]

The analytical interpretations of Kohler model [75], can be expressed as:

$$\Delta G^E = (x_1 + x_2)^2 \Delta G_{12}^E \left(\frac{x_1}{x_1 + x_2}; \frac{x_2}{x_1 + x_3} \right) + (x_2 + x_3)^2 \Delta G_{23}^E \left(\frac{x_2}{x_2 + x_3}; \frac{x_3}{x_2 + x_3} \right) + (x_3 + x_1)^2 \Delta G_{31}^E \left(\frac{x_3}{x_1 + x_3}; \frac{x_1}{x_1 + x_3} \right)$$

Muggianu model [75] uses the following expression:

$$\Delta G^E = \frac{4x_1x_2}{(1+x_1-x_2)(1+x_2-x_1)} \Delta G_{12}^E \left(\frac{1+x_1-x_2}{2}; \frac{1+x_2-x_1}{2} \right) + \frac{4x_2x_3}{(1+x_2-x_3)(1+x_3-x_2)} \Delta G_{23}^E \left(\frac{1+x_2-x_3}{2}; \frac{1+x_3-x_2}{2} \right) + \frac{4x_3x_1}{(1+x_3-x_1)(1+x_1-x_3)} \Delta G_{31}^E \left(\frac{1+x_3-x_1}{2}; \frac{1+x_1-x_3}{2} \right)$$

While Kohler/Toop model [77] uses the following expression:

$$\Delta G^E = \frac{x_2}{1-x_1} \Delta G_{12}^E(x_1; 1-x_1) + \frac{x_3}{1-x_1} \Delta G_{13}^E(x_1; 1-x_1) + (x_2 + x_3)^2 \Delta G_{23}^E \left(\frac{x_2}{x_2 + x_3}; \frac{x_3}{x_2 + x_3} \right)$$

In these equations, ΔG^E and ΔG_{ij}^E correspond to the integral molar excess Gibbs energy for ternary and binary systems, respectively, and x_1 , x_2 and x_3 are the mole fraction of components.

A polynomial ternary term (sometimes referred to as ternary interaction parameter) can be added to any of the above equations to fit the experimental data. However, with no ternary terms the extrapolation should provide a reasonable first estimation of the ternary molar excess Gibbs energy [19].

Chapter 4

Thermodynamic Modeling of the Mg-Cu-Ni-Y System

4.1 Thermodynamic Modeling of the Binary Sub-Systems

4.1.1 Mg-Ni system

The calculated Mg-Ni phase diagram in comparison with the available experimental data from the literature is shown in Figure 4-1. Hauhton and Payne [22] reported iron contamination from the crucible with higher Ni containing alloys (30-40 at.% Ni) which may have resulted in overestimation of the liquidus temperature. Hence the data of Micke and Ipsier [24] has been favoured over Hauhton and Payne [22] during optimization as can be seen in Figure 4-1. There is a lack of experimental data for the liquidus curve in the region between Mg₂Ni and MgNi₂. Nevertheless, the rest of the phase diagram shows very good agreement with the experimental data. The optimized parameters of the liquid, Mg-hcp, Ni-fcc and the intermetallic compounds are given in Table 4-1. A two sublattice model for the MgNi₂ as reported by Islam and Medraj [40] has been used to reproduce the homogeneity range of this phase.

Table 4-1: Optimized model parameters of the Mg-Ni system

Phase	Parameters
Liquid	$\Delta g_{\text{MgNi}}^0 = -16\,829.4 + 5.02T$; $\Delta g_{\text{MgNi}}^{10} = -15\,068.9 + 10.49T$; $\Delta g_{\text{MgNi}}^{01} = -16\,345.6 + 1.26T$ (J/mole)
Mg-hcp	${}^{\circ}L^{\text{Mg-hcp}} = 3\,767.2$ (J/mole)
Ni-fcc	${}^{\circ}L^{\text{Ni-fcc}} = 30\,012.90$ (J/mole)
Mg ₂ Ni	$\Delta G_f = -16\,075.7 + 4.66T$ (J/mole. atom)
MgNi ₂ (Mg%, Ni) ₁ (Mg, Ni%) ₂	${}^{\circ}G_{\text{Mg:Mg}}^{\text{MgNi}_2} = 8\,332.6 + 12.65T$; ${}^{\circ}G_{\text{Mg:Ni}}^{\text{MgNi}_2} = -21\,431.0 + 25.24T - 9.39$ $T \ln T + 22.17 \times 10^{-4} T^2 + 6.66 \times 10^4 T^{-1}$; ${}^{\circ}G_{\text{Ni:Mg}}^{\text{MgNi}_2} = 23\,343.37 + 4.66T$; ${}^{\circ}G_{\text{Ni:Ni}}^{\text{MgNi}_2} = 4\,908.55 + 7.0T$ (J/mole. atom)

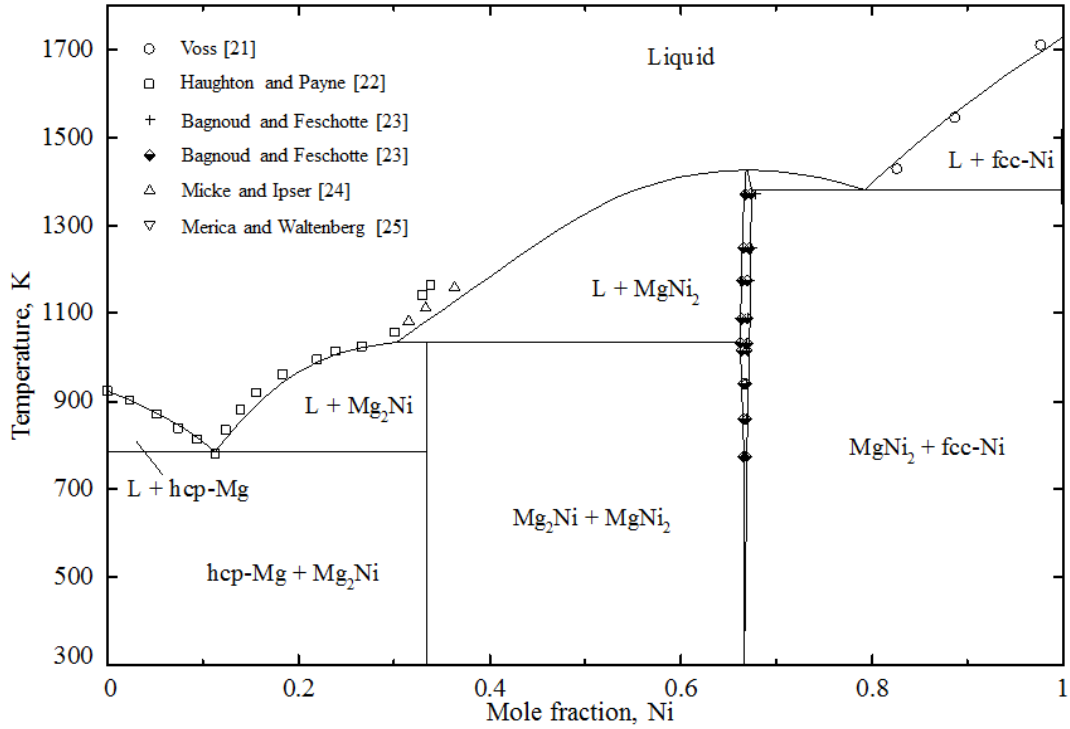


Figure 4-1: Calculated Mg-Ni phase diagram

The calculated integral enthalpy of mixing of the liquid at 1008 K is given in Figure 4-2 which shows very good agreement with the experimental data of Feufel and Sommer [31].

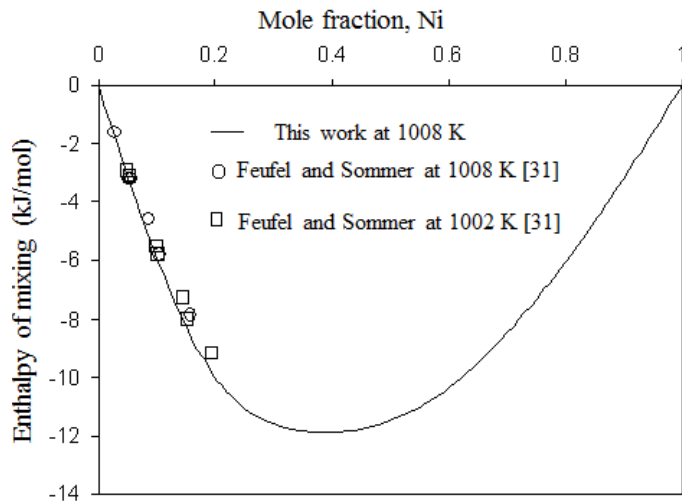


Figure 4-2: Calculated enthalpy of mixing of liquid Mg-Ni at 1008 K

The activity of liquid Mg and Ni calculated at 1100 K is shown in Figure 4-3. The calculated activity of Mg shows good agreement with the experimental data of Sryvalin et al. [32] and Micke and Ipser [24]. For the activity of Ni, however, not many experimental results are reported in the literature. The calculated activity of Ni shows good agreement with the experimental data of Sryvalin et al. [32] who used emf method. Also, a good agreement can be seen with the data of Sieben and Schmahl [33] who measured the vapor pressure of Mg and calculated the activity of Ni using the Gibbs-Duhem equation.

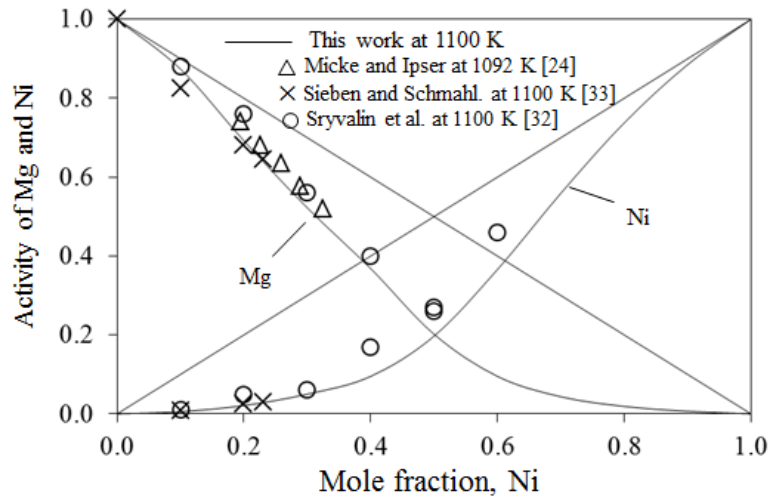


Figure 4-3: Calculated activity of liquid Mg and Ni at 1100 K

The heat capacity of MgNi_2 has been calculated and compared with the experimental data of Feufel and Sommer [31] and Schubel [34] as shown in Figure 4-4 (a). In order to be consistent with the experimental data, temperature dependant higher order terms are added during optimization of MgNi_2 as can be seen in Table 4-1. Also, the calculated enthalpy of formation of Mg_2Ni and MgNi_2 compared with the available experimental data is shown in Figure 4-4 (b). The current results are within the range of variation of the experimental data.

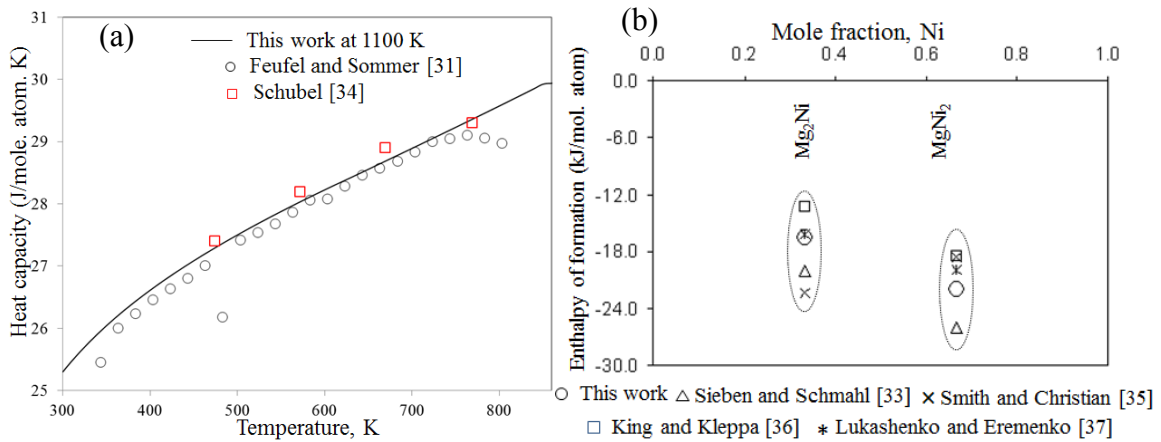


Figure 4-4: (a) Calculated heat capacity for the MgNi₂; (b) Enthalpy of formation of Mg₂Ni and MgNi₂

4.1.2 Cu-Ni system

The calculated Cu-Ni phase diagram is shown in Figure 4-5 in comparison with the available experimental data from the literature. The liquid phase has been modeled using the modified quasichemical model while the fcc(Cu,Ni) phase has been modeled using the Bragg-Williams model. All the parameters have been included in Table 4-2. The liquid phase shows very good agreement with all the available experimental data. The miscibility gap in the fcc(Cu,Ni) phase has been determined using the available experimental data as a guideline. It is worth noting that it is very difficult to obtain accurate experimental results at such low temperature due to the difficulty in obtaining equilibrium conditions. Hence lower weight is given to these data during optimization. The shape of the miscibility gap deviates from that of Vrijen and Radelaar [48] in the Cu-rich side. It was impossible to be consistent with the data of [48] as well as the thermodynamic properties of the solid which were more reliable. Some of the earlier thermodynamic modeling [66, 67, 158] on this system also showed wider miscibility gap like the current one. Moreover, according to Ebel [47] the miscibility gap should exist

between 10 to 90 at.% Ni at 523 K. Considering the above issues, it is decided to accept the present calculation. The critical temperature of the miscibility gap is determined to be 621 K near 65 at.% Ni which is consistent with the data of Vrijen and Radelaar [48].

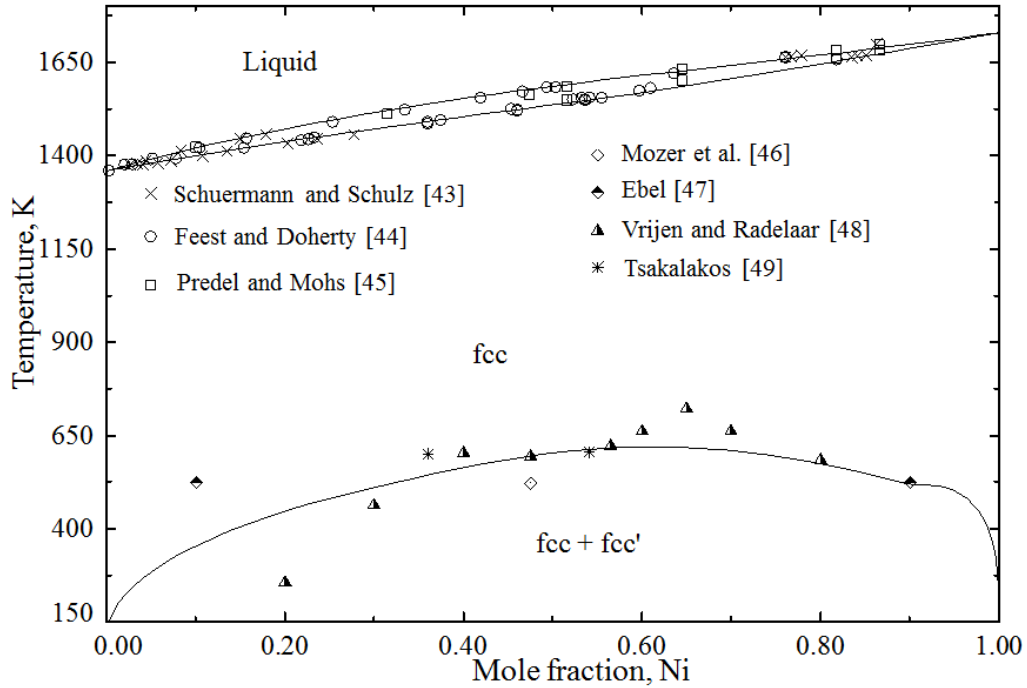


Figure 4-5: Calculated Cu-Ni phase diagram

Table 4-2: Optimized model parameters of the Cu-Ni system

Phase	Parameters
Liquid	$\Delta g_{\text{CuNi}}^0 = 5797.3 - 0.21T$; $\Delta g_{\text{CuNi}}^{10} = -1172.02$; (J/mole)
fcc (Cu, Ni)	${}^0L^{\text{fcc}} = 6790.5 + 4.64T$; ${}^1L^{\text{fcc}} = 1655$; (J/mole)
	${}^0T_c^{\text{fcc}} = -467.5$; ${}^1T_c^{\text{fcc}} = -297.5$; ${}^0\beta_{\text{CuNi}}^{\text{fcc}} = -0.7316$; ${}^0\beta_{\text{CuNi}}^{\text{fcc}} = -0.317$

The calculated enthalpy of mixing of the liquid phase at 1750 K in Figure 4-6 (a) shows reasonable agreement with the available experimental data. The data of Predel and Mohs [45] show less endothermic values than other experimental data. Hence, it is decided not to consider their data. The activities of Cu and Ni in the liquid are presented

in Figure 4-6 (b) and show good agreement with the experimental data. The activity of Cu shows deviation from the experimental data of Berezutskii and Lukashenko [57] but since the two other data sets of Schultz et al. [55] and Kulkarni and Johnson [56] are consistent with each other, it is decided to follow the latter two.

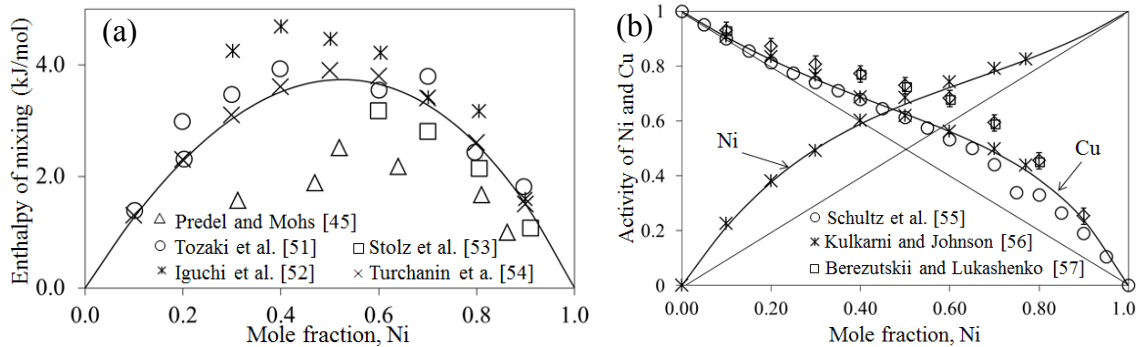


Figure 4-6: Calculated (a) enthalpy of mixing of the liquid Cu-Ni at 1750 K; (b) activities of the liquid Cu and Ni at 1750 K

The calculated enthalpy of mixing of the fcc phase at 800 K is shown in Figure 4-7 (a) in relation to the experimental data of Oriani and Murphy [59] at 973 K and Elford et al. [60] at 773 K. Both sets of data show an unusual break in the curve near 65 at.% Ni. According to [60] this is due to a non-equilibrium effect. Accepting this argument, it can be said that the present optimized parameters can reproduce the experimental results satisfactorily.

Activities for Cu and Ni in the fcc solution have been calculated using the present optimized parameters as shown in Figure 4-7 (b). The dotted line in this figure shows the activity of Ni at 1273 K which is compared with the data of Katayama et al. [63] and Kontopoulos [64]. The activity of Ni at 1000 K as represented by the solid line is also in good agreement with the data of Rapp and Maak [62] at 973 K, Kontopoulos [64] at 1073 K and Srikanth and Jacob [65] at 1000 K. The calculated activity of Cu at 1000 K shows

good consistency with the data of Vecher and Gerasimov [61] except for one point at 90 at.% Ni. This kind of flat activity can be expected in the solution due to the presence of immiscibility. But no other experimental evidence could be found in the literature which suggests that the miscibility gap exists at such a high temperature. Hence it is decided not to consider this point for the present calculation.

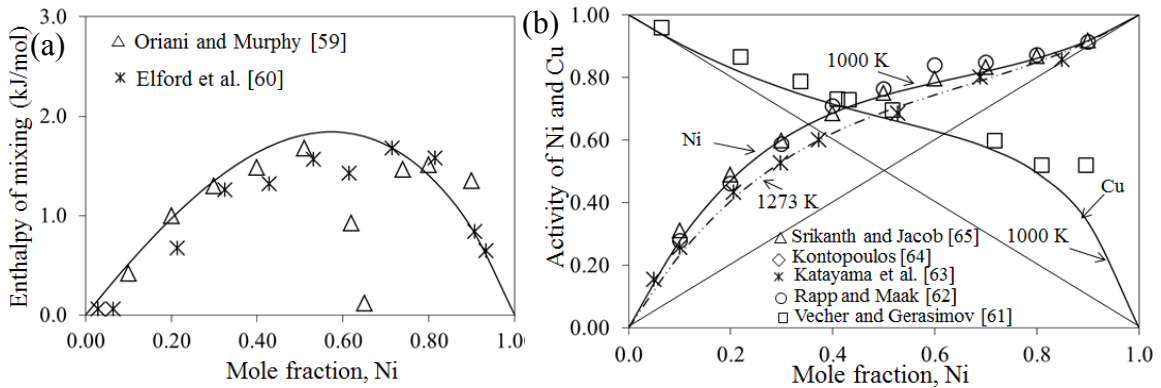


Figure 4-7: Calculated (a) enthalpy of mixing at of the Cu-Ni solid solution phase at 800 K; (b) activities of Cu and Ni in the fcc phase at 1000 and 1273 K

4.1.3 Ni-Y system

The calculated Ni-Y phase diagram along with the experimental data from Beaudry and Daane [68, 69] and Domagala et al. [68, 69] is shown in Figure 4-8, demonstrating good agreement with the experimental data of Beaudry and Daane [68]. Some melting temperature data of the compounds especially near the Ni-rich region (0.7 to 0.9 at.% Ni) disagreed with the data of Domagala et al. [69]. However it is decided to be consistent with the data of Beaudry and Daane [68] because Domagala et al. [69] determined the melting point of the compounds by visual analysis of the samples and reported relatively high error ± 25 K in these measurements. Whereas Beaudry and Daane [68] used thermal and metallographic methods and reported smaller error of ± 5 K. In the current

assessment, the mutual solubility between Y and Ni is considered very low based on the work of [68]. The optimized parameters of the liquid and intermetallic compounds are given in Table 4-3.

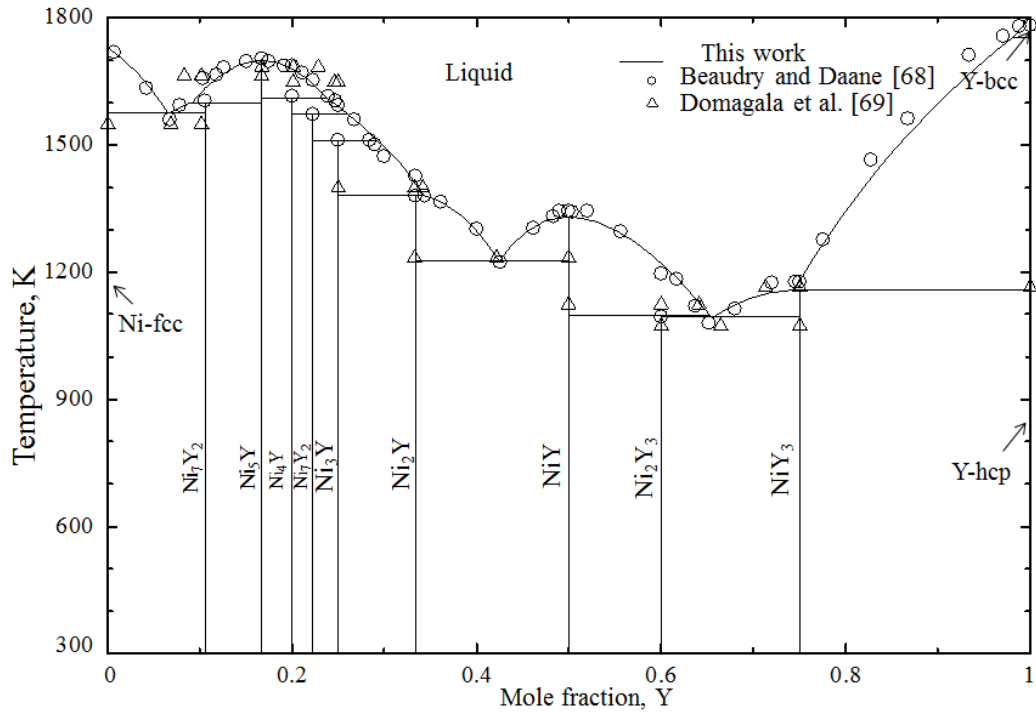


Figure 4-8: Calculated Ni-Y phase diagram

There is not enough experimental data on the thermodynamic properties of the liquid Ni-Y. The only available data is from Batalin et al. [86] who measured the enthalpy of mixing of the liquid at 1973 K. The calculated enthalpy of mixing curve at 1973 K with the experimental data of [86] is shown in Figure 4-9 (a). Even though the experimental enthalpy of mixing data reported by Batalin et al. [86] suggests that the maximum short range ordering should be around 20 at.% Y, this was impossible to obtain while maintaining the consistency with the other thermodynamic and phase diagram information of the system. The current thermodynamic calculation showed that the maximum short range ordering should be around 40 at.% Y. Near this composition, Ni₂Y

compound which has the most negative enthalpy of formation (-37.4 kJ/mole atom) occurs. Usually short range ordering is expected around the composition of the most stable compound. Besides, this calculation shows an improvement over the SGTE database [158] when the Bragg-Williams random mixing approximation was used as shown in Figure 4-9 (a). Also, the entropy of mixing curve of the SGTE database [158] shows negative value which is unusual. This is corrected in the current work which shows more realistic ‘*m-shaped*’ entropy of mixing in Figure 4-9 (b). The minimum of this curve is around 40 at.% Y which indicates that the maximum short range ordering should be near this composition.

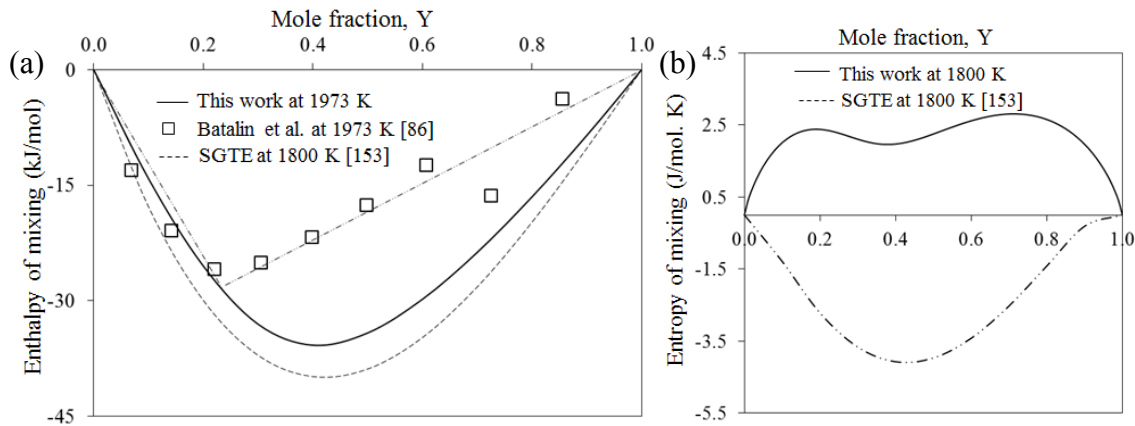


Figure 4-9: Calculated (a) enthalpy of mixing of liquid Ni-Y at 1973 K. V-shaped line shows the trend of the exp. data; (b) entropy of mixing of liquid Ni-Y at 1800 K

The calculated enthalpy of formation of the intermetallic compounds at 973 K with the experimental data of Subramanian and Smith [73] is shown in Figure 4-10. Also, this calculation is compared with the predicted enthalpy of formation by Mal et al. [83]. The calculated enthalpy of formation of most of the compounds show higher negative values than those of Subramanian and Smith [73]. Optimization of this system with a less negative enthalpy of formation of the compounds contradicted with the experimental

phase diagram information. Hence, higher negative values for the enthalpy of formation are used. The predicted values by Mal et al. [83] also show similar results as the present calculation.

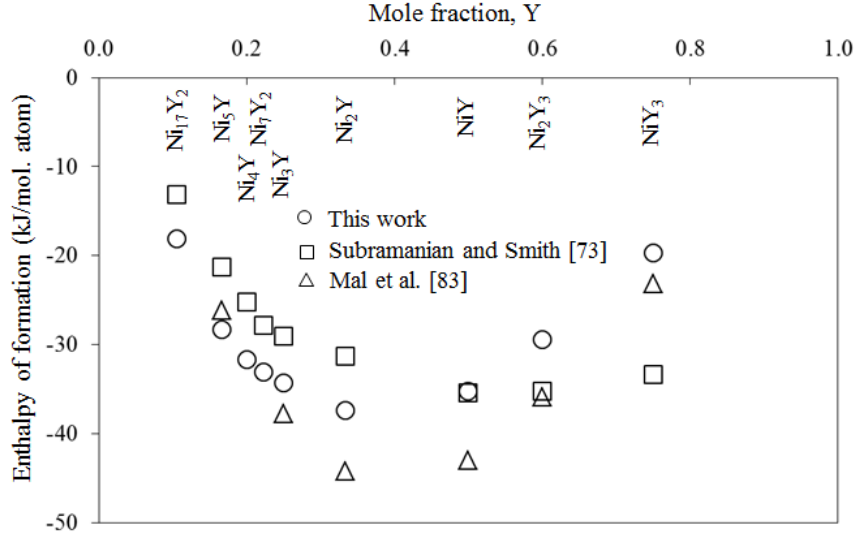


Figure 4-10: Calculated enthalpy of formation of the intermetallic compounds at 973 K in the Ni-Y system

Table 4-3: Optimized model parameters of the Ni-Y system

Phase	Parameters
Liquid	$\Delta g_{\text{NiY}}^0 = -33\,653.83 + 1.61T$; $\Delta g_{\text{NiY}}^{01} = -1\,339.46 + 1.26T$; $\Delta g_{\text{NiY}}^{10} = -17\,538.50$ (J/mole)
Ni-fcc	${}^0L^{\text{Ni-fcc}} = 3\,675.18$ (J/mole)
Y-bcc	${}^0L^{\text{Y-bcc}} = 62\,787.00$ (J/mole)
Ni ₁₇ Y ₂	$\Delta G_f = -19\,712.99 + 1.78T$ (J/mole. atom)
Ni ₅ Y	$\Delta G_f = -28\,350.16 + 1.49T$ (J/mole. atom)
Ni ₄ Y	$\Delta G_f = -31\,252.10T + 1.65T$ (J/mole. atom)
Ni ₇ Y ₂	$\Delta G_f = -32\,256.61 + 1.31T$ (J/mole. atom)
Ni ₃ Y	$\Delta G_f = -33\,597.01 + 1.19T$ (J/mole. atom)
Ni ₂ Y	$\Delta G_f = -37\,389.36 + 2.04T$ (J/mole. atom)
NiY	$\Delta G_f = -35\,284.53 + 0.83T$ (J/mole. atom)
Ni ₂ Y ₃	$\Delta G_f = -28\,752.36 + 0.08T$ (J/mole. atom)
NiY ₃	$\Delta G_f = -19\,219.52 + 0.44T$ (J/mole. atom)

4.1.4 Mg-Y system

The Mg-Y system has been re-optimized in order to be consistent with the recent publication by Zhao et al. [88] who repositioned the homogeneity ranges of $Mg_{24}Y_5(\epsilon)$ and $Mg_2Y(\delta)$ using diffusion couple experiments. The calculated phase diagram in Figure 4-11 shows good agreement with the reported values of Zhao et al. [88] as well as other experimental results from the literature [89-93].

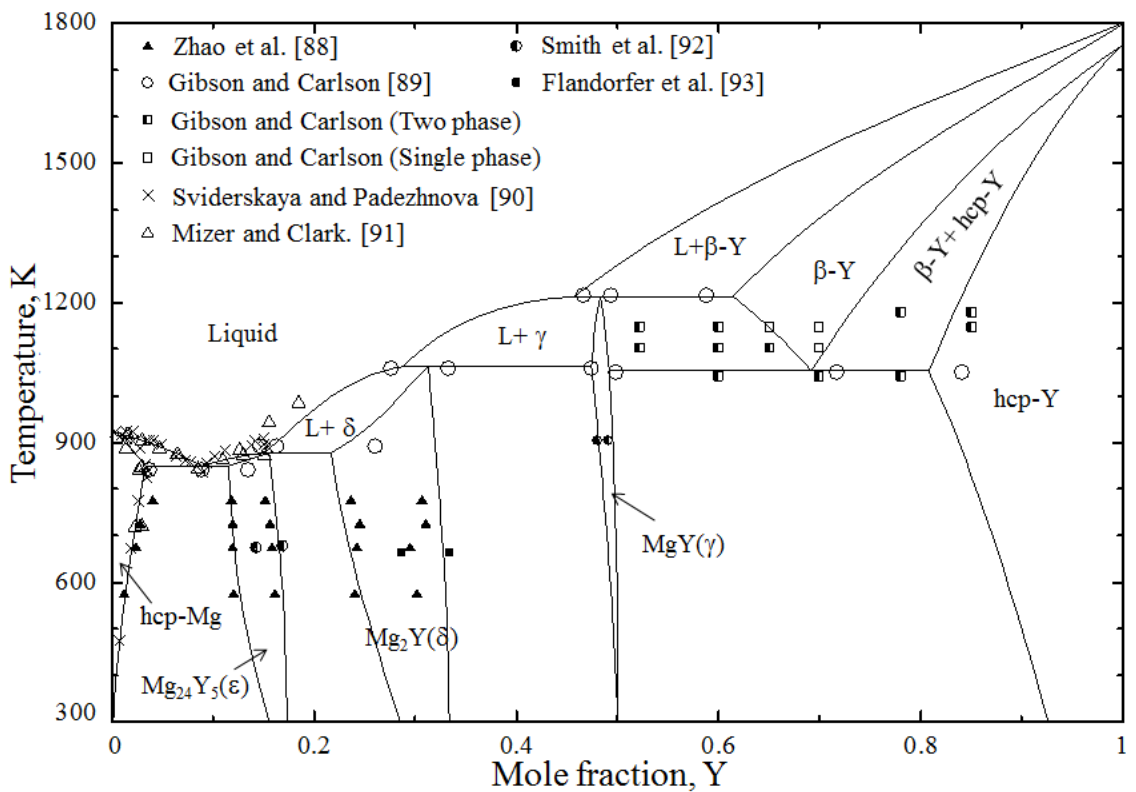


Figure 4-11: Calculated Mg-Y phase diagram

The optimized model parameters for the Mg-Y system are listed in Table 4-4. It has been tried to keep the liquid parameters same as the previous work [87] during the optimization processes. This has been done in order to be consistent with the thermodynamic properties of the liquid as those are in very good agreement with the literature experimental data.

The calculated enthalpy of mixing at 984 K is shown in Figure 4-12 (a). Reasonable agreement between the experimental results of Agarwal et al. [94] and the present calculation can be seen. The activity of Mg in liquid Mg-Y at 1173 K is presented in Figure 4-12 (b) which shows very good agreement with the experimental data [95, 96].

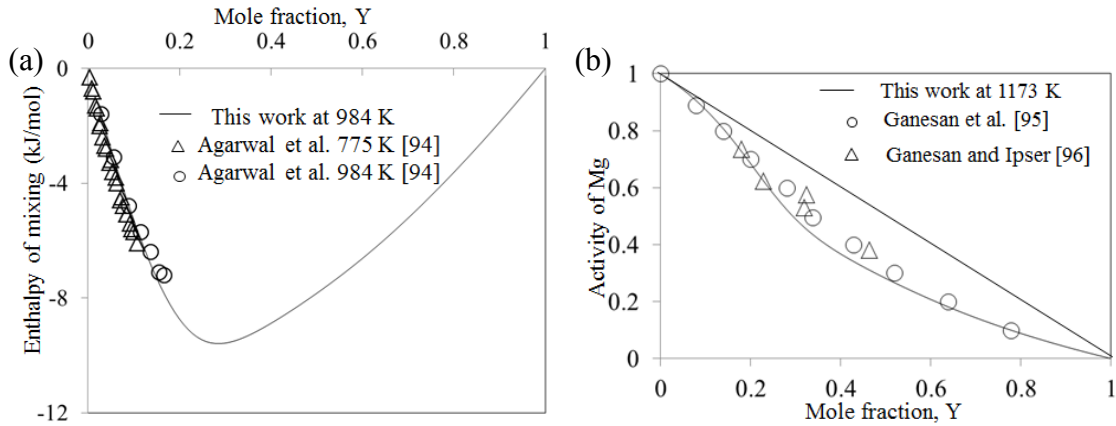


Figure 4-12: Calculated (a) enthalpy of mixing of the Mg-Y liquid at 984 K; (b) activity of Mg in the Mg-Y liquid at 1173 K

Figure 4-13 shows the calculated enthalpy of formation of the intermediate compounds in the Mg-Y system in relation to the experimental results from the literature. A good agreement between the present calculation and the experimental data of Smith et al. [92] and Pyagai et al. [97] can be seen. However, the enthalpy of formation for MgY (γ) measured by Pyagai et al. [97] is not consistent with the experimental value of Smith et al. [92] and the calculated value in this work. However, the results of Smith et al. [92] are more reliable since they used both the calorimetric and vapour pressure techniques.

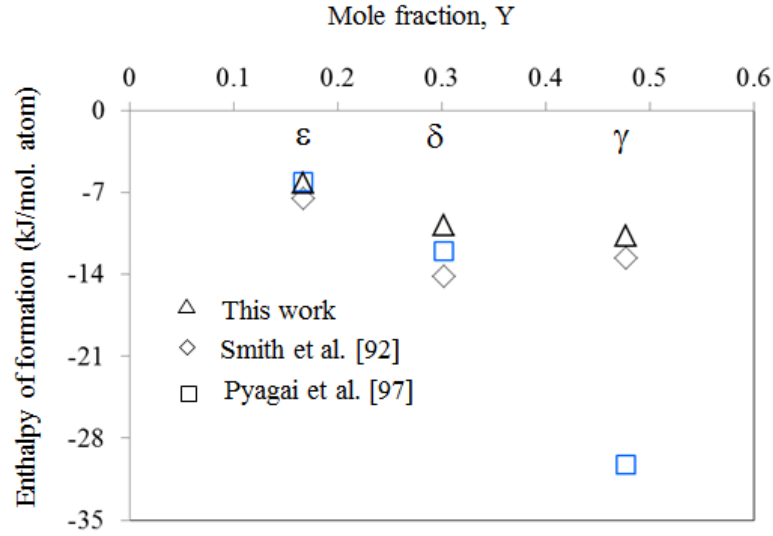


Figure 4-13: Enthalpy of formation for the stoichiometric compounds in the Mg-Y system

Table 4-4: Optimized model parameters of the Mg-Y system

Phase	Parameters
Liquid	$\Delta g_{MgY}^0 = -13\,980.6 + 6.45T$; $\Delta g_{MgY}^{10} = -15\,445.6 + 8.87T$; $\Delta g_{MgY}^{01} = -5\,274.1 + 2.09T$; (J/mole)
Mg-hcp	${}^0L^{Mg-hcp} = -12\,476.8 + 7.49T$; ${}^1L^{Mg-hcp} = -2\,724.6 + 2.4T$; ${}^2L^{Mg-hcp} = -2\,788.2 + 2.0T$; (J/mole)
Y-bcc (β)	${}^0L^{Y-bcc} = -28\,713.7 + 13.07T$; ${}^1L^{Y-bcc} = -2\,005.9 + 1.5T$; (J/mole)
Mg ₂₄ Y ₅ (ϵ) (Mg%, Y) ₂₉ (Y%, Mg) ₁₀ (Mg) ₁₉	${}^0G_{Mg:Y:Mg}^\epsilon = -6\,179.0$; ${}^0G_{Mg:Mg:Mg}^\epsilon = 935.5 + 0.14T$; ${}^0G_{Y:Y:Mg}^\epsilon = 8\,038.3$; ${}^0G_{Y:Mg:Mg}^\epsilon = 721.7$ (J/mole atom)
Mg ₂ Y (δ) (Mg%, Y) ₆ (Y%, Mg) ₄ (Mg) ₂	${}^0G_{Mg:Y:Mg}^\delta = -9\,767.5 + 0.66T$; ${}^0G_{Mg:Mg:Mg}^\delta = 3\,544.1 + 1.39T$; ${}^0G_{Y:Y:Mg}^\delta = {}^0G_{Y:Mg:Mg}^\delta = 6\,976.3$; ${}^0L_{Mg:Y:Y:Mg}^\delta = 641.8 + 11.86T$; ${}^0L_{Mg:Y:Mg:Mg}^\delta = {}^0L_{Y:Y:Mg:Mg}^\delta = 9\,006.5 + 88.60T$; ${}^0L_{Mg:Y:Mg:Mg}^\delta = -2\,096.2 + 0.05T$ (J/mole atom)
MgY (γ) (Mg%, Y) (Y%, Va)	${}^0G_{Mg:Y}^\gamma = -10\,727.3 + 1.26T$; ${}^0G_{Mg:Va}^\gamma = -10\,464.5$; ${}^0G_{Y:Y}^\gamma = {}^0G_{Y:Va}^\gamma = 13\,483.6$; ${}^0L_{Mg:Y:Y}^\gamma = 15\,006.5 + 16T$; ${}^0L_{Mg:Y:Va}^\gamma = 15\,006.5 + 15T$; ${}^0L_{Mg:Y:Va}^\gamma = {}^0L_{Y:Y:Va}^\gamma = -5\,000.0 + 7T$ (J/mole atom)

4.2 Thermodynamic Modeling of the Ternary Systems

4.2.1 Mg-Cu-Ni phase diagram

The thermodynamic descriptions of the binaries Mg-Cu, Cu-Ni and Mg-Ni are extrapolated to the ternary Mg-Cu-Ni system using Toop [155] geometric model. According to Qiao et al. [156] if the excess thermodynamic properties in two of the three binary systems show similarity and significantly differ from the third one, the ternary system should be considered as an asymmetric system and the common component in the two similar binary systems should be chosen as the asymmetric component. Mg has been singled out as the asymmetric component during the extrapolation because Cu-Ni system shows completely different thermodynamic characteristics than Mg-Cu and Mg-Ni binary systems. A self-consistent set of parameters has been obtained for the Mg-Cu-Ni system as shown in Table 4-5. Three ternary excess Gibbs energy terms for the liquid phase have been used in order to be consistent with the experimental data.

Sublattice model within the compound energy formalism was used to describe the ternary solubility of Mg_2Cu and Mg_2Ni in the Mg-Cu-Ni ternary. Mg_2Cu was modeled using two sublattices: $(Cu\%, Ni) (Mg\%)_2$, where '%' represents the major species in the sublattice. Similar sublattice model, $(Cu, Ni\%) (Mg\%)_2$ was applied to describe Mg_2Ni . The interaction parameters responsible for the solubility of Mg_2Cu and Mg_2Ni are: ${}^oL_{Mg:Ni,Cu}^{Mg_2Cu}$ and ${}^oL_{Mg:Ni,Cu}^{Mg_2Ni}$, respectively.

The solubility of $MgCu_2$ and $MgNi_2$ has been modeled using two sublattice model as follows: $(Mg, Cu\%, Ni)_2 (Cu, Mg\%, Ni)$ and $(Mg, Cu, Ni\%)_2 (Cu, Mg\%, Ni)$. Each one of these models has nine end members and eighteen interaction parameters. The Gibbs

energy of them has been reported in Table 4-5. The excess energy term ${}^{\circ}L_{Cu,Ni:Mg}^{MgCu_2}$ for $MgCu_2$ and ${}^{\circ}L_{Cu,Ni:Mg}^{MgNi_2}$ for $MgNi_2$ are dominating and have been determined carefully to be consistent with the experimental solubility.

Table 4-5: Parameters for the Mg-Cu-Ni ternary system

Phase	Parameters (J/mole)
Liquid	$\Delta g_{CuMg(Ni)}^{001} = -9\ 236.8; \Delta g_{CuMg(Ni)}^{011} = 7\ 842.1; \Delta g_{CuMg(Ni)}^{111} = 2\ 023.7$
Mg_2Cu (Mg) ₂ (Ni, Cu%)	${}^{\circ}G_{Mg:Ni}^{Mg_2Cu} = -29\ 012.5+12.14\ T; {}^{\circ}L_{Mg:Ni,Cu}^{Mg_2Cu} = 6\ 266.7$
Mg_2Ni (Mg) ₂ (Ni%, Cu)	${}^{\circ}G_{Mg:Cu}^{Mg_2Ni} = -26\ 011.2+1.0\ T;$ ${}^{\circ}L_{Mg:Ni,Cu}^{Mg_2Ni} = 70\ 274.2+55.96\ T; {}^1L_{Mg:Ni,Cu}^{Mg_2Ni} = -14\ 256.1$
$MgCu_2$ (Cu%,Mg,Ni) ₂ (Cu,Mg%,Ni)	${}^{\circ}G_{Cu:Ni}^{MgCu_2} = {}^{\circ}G_{Ni:Cu}^{MgCu_2} = {}^{\circ}G_{Ni:Ni}^{MgCu_2} = 15\ 000;$ ${}^{\circ}G_{Mg:Ni}^{MgCu_2} = 14\ 865-13.86\ T;$ ${}^{\circ}G_{Ni:Mg}^{MgCu_2} = -43\ 000+71.39\ T+66.49*10^{-4}T^2+20*10^4\ T^{-1}-9.39\ T\ \ln T;$ ${}^{\circ}L_{Cu,Mg:Ni}^{MgCu_2} = 13\ 005.8; {}^{\circ}L_{Ni:Cu,Mg}^{MgCu_2} = 6\ 596.6;$ ${}^{\circ}L_{Mg,Ni:Cu}^{MgCu_2} = {}^{\circ}L_{Mg,Ni:Mg}^{MgCu_2} = {}^{\circ}L_{Mg,Ni:Ni}^{MgCu_2} = 10\ 000+90\ T;$ ${}^{\circ}L_{Cu:Mg,Ni}^{MgCu_2} = {}^{\circ}L_{Mg:Mg,Ni}^{MgCu_2} = {}^{\circ}L_{Mg:Mg,Ni}^{MgCu_2} = {}^{\circ}L_{Ni:Mg,Ni}^{MgCu_2} = 30\ 000;$ ${}^{\circ}L_{Cu,Ni:Mg}^{MgCu_2} = -23\ 750+21\ T; {}^{\circ}L_{Cu,Ni:Mg}^{MgCu_2} = -51\ 000;$ ${}^{\circ}L_{Cu,Ni:Cu}^{MgCu_2} = {}^{\circ}L_{Cu,Ni:Ni}^{MgCu_2} = 10\ 000+21\ T$
$MgNi_2$ (Cu,Mg,Ni%) ₂ (Cu,Mg%,Ni)	${}^{\circ}G_{Cu:Cu}^{MgNi_2} = {}^{\circ}G_{Cu:Ni}^{MgNi_2} = {}^{\circ}G_{Ni:Cu}^{MgNi_2} = 15\ 000; {}^{\circ}G_{Cu:Mg}^{MgNi_2} = -4\ 000+49.4T;$ ${}^{\circ}G_{Mg:Cu}^{MgNi_2} = 90\ 970-16.46\ T; {}^{\circ}G_{Mg:Mg}^{MgNi_2} = 140\ 000;$ ${}^{\circ}L_{Cu,Mg:Cu}^{MgNi_2} = {}^{\circ}L_{Cu,Mg:Mg}^{MgNi_2} = 20\ 000; {}^{\circ}L_{Cu,Mg:Ni}^{MgNi_2} = 5\ 000;$ ${}^{\circ}L_{Cu:Cu,Mg}^{MgNi_2} = -24\ 050; {}^{\circ}L_{Mg:Cu,Mg}^{MgNi_2} = 6\ 596.6; {}^{\circ}L_{Ni:Cu,Mg}^{MgNi_2} = 14\ 000;$ ${}^{\circ}L_{Mg,Ni:Cu}^{MgNi_2} = 10\ 000+60\ T; {}^{\circ}L_{Cu:Mg,Ni}^{MgNi_2} = 20\ 000;$ ${}^{\circ}L_{Cu,Ni:Cu}^{MgNi_2} = {}^{\circ}L_{Cu,Ni:Ni}^{MgNi_2} = 35\ 000+30\ T; {}^{\circ}L_{Cu,Ni:Mg}^{MgNi_2} = -50\ 000$

Figure 4-14 and 4-15, shows good consistency of the isothermal sections at 673 K and 1073, between the present calculation and experimental work by Karonik et al. [113] and Fehrenbach et al. [114]. Both the Isothermal sections have been visually compared with the proposed diagrams by Fehrenbach et al. [114] shown in Figure 2-1. The phase relationships of these isothermal sections and those of [114] are exactly the same. However, the phase boundaries deviate a little. But since there is no experimental evidence for the accurate positions of the proposed phase boundaries by Fehrenbach et al. [114], it is difficult to judge which one is more accurate. The solubility of Ni in Mg_2Cu shows good agreement with those reported by Karonik et al. [113].

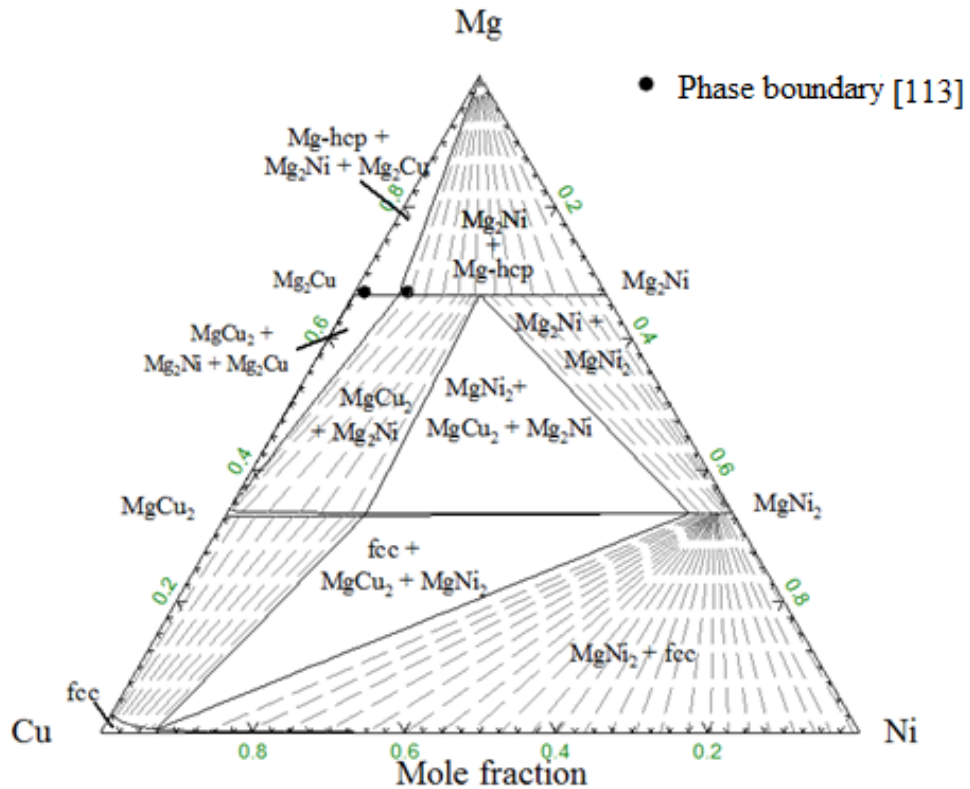


Figure 4-14: Calculated isothermal section of the Mg-Cu-Ni system at 673 K with the experimental data of Karonik et al. [113]

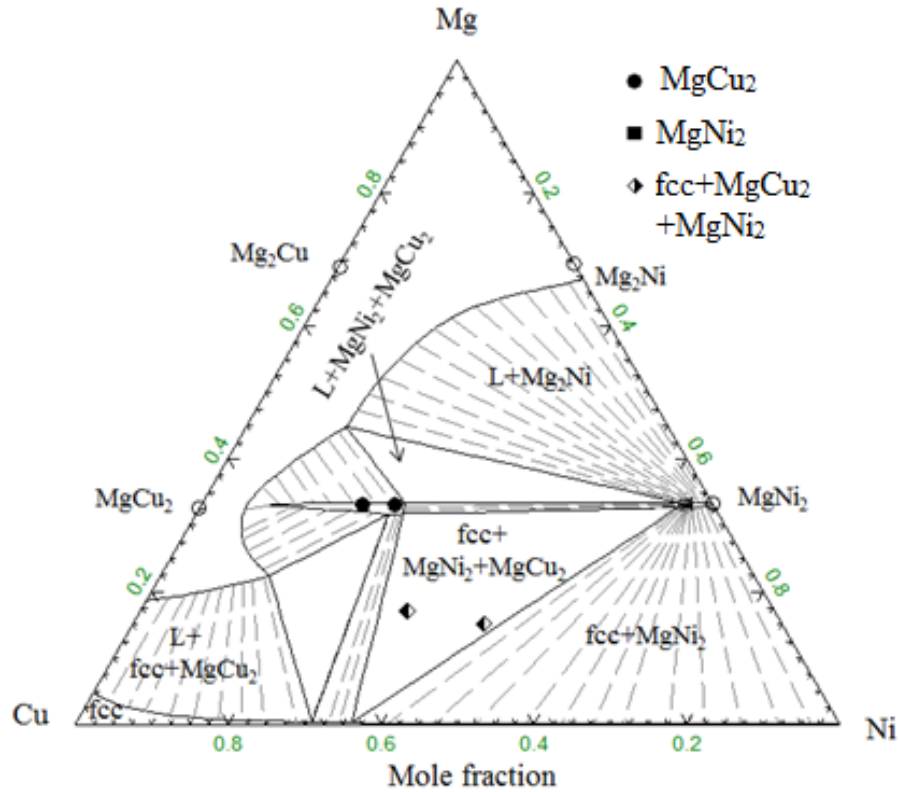
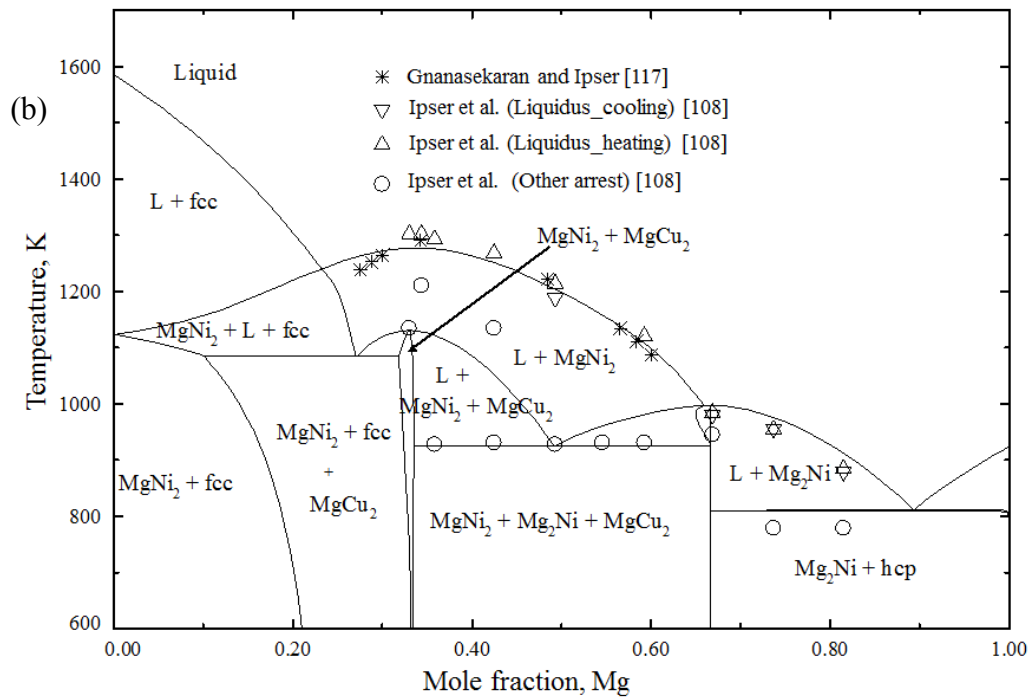
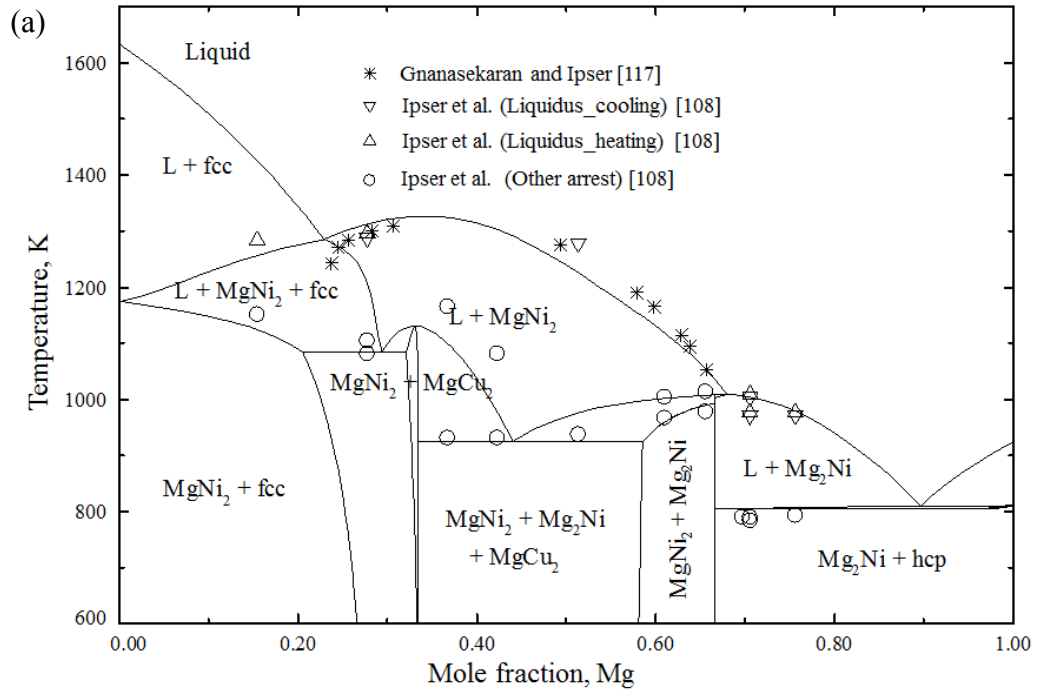


Figure 4-15: Calculated isothermal section of the Mg-Cu-Ni system at 1073 K with the experimental data of Fehrenbach et al. [114]

Figure 4-16 (a to c), shows the calculated vertical sections for $X_{Cu} / X_{Ni} = 0.5, 1.0$ and 2.0 ratio. Good agreement can be seen between the calculated liquidus temperatures and experimental data of Ipser et al. [108] and Ganasenkaran and Ipser [115-117]. Besides most of the experimental points, such as phase field limits and invariant reactions are reasonably reproduced. Also, the calculated vertical section at 71 at.% Mg in Figure 4-16 (d), shows good agreement with the experimental data of Ipser et al. [108].



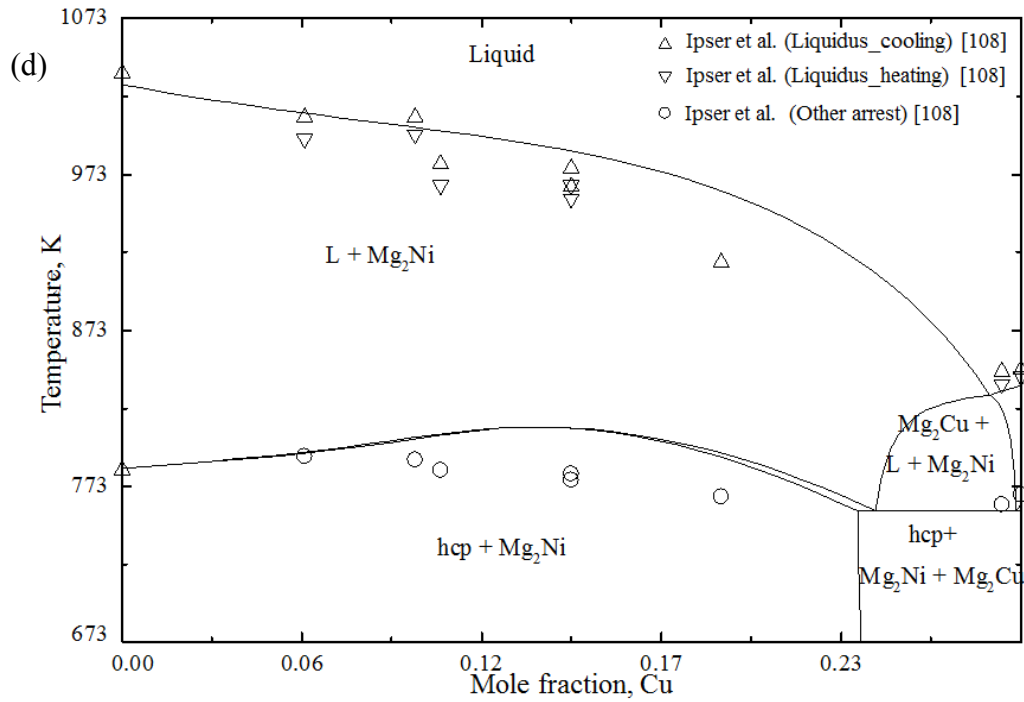
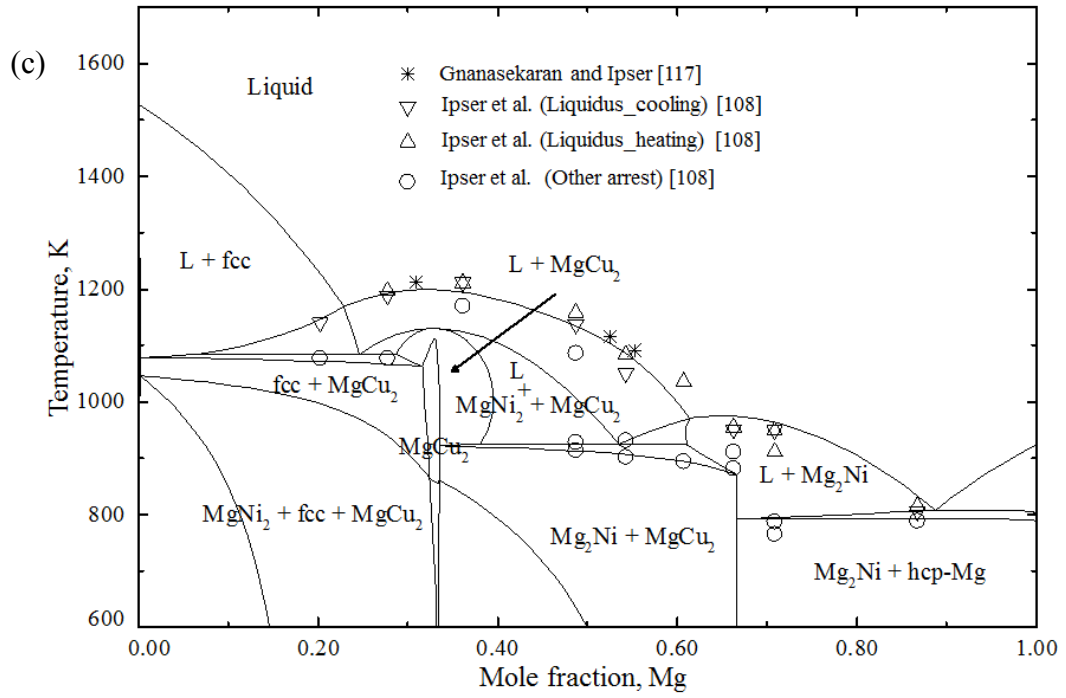


Figure 4-16: Calculated vertical sections at (a) $x_{Cu} / x_{Ni} = 0.5$; (b) $x_{Cu} / x_{Ni} = 1.0$; (c) $x_{Cu} / x_{Ni} = 2.0$; (d) 71 at.% Mg

Figure 4-17, shows a vertical section along the eutectic valley with the available experimental data from Fehrenbach et al. [114]. Deviation can be seen from the experimental data for samples with higher Ni concentration. But these data especially those with compositions more than 17 at.% Ni have a higher error of about ± 8 K. Fehrenbach et al. [114] used atomic absorption spectroscopy to measure only Ni concentration in the alloys which did not show much deviation (± 0.5 at.%) from the nominal composition. Based on this they assumed that the actual global composition of the alloys are same as the nominal composition. Since these alloys contain about 20 at.% Mg which is easy to oxidize it is likely that the compositions mentioned by Fehrenbach et al. [114] are not very accurate. Also, attempts to be consistent with the experimental results end up with large deviations from other experimental data. Considering these facts, it is decided not to use additional parameters to fix this.

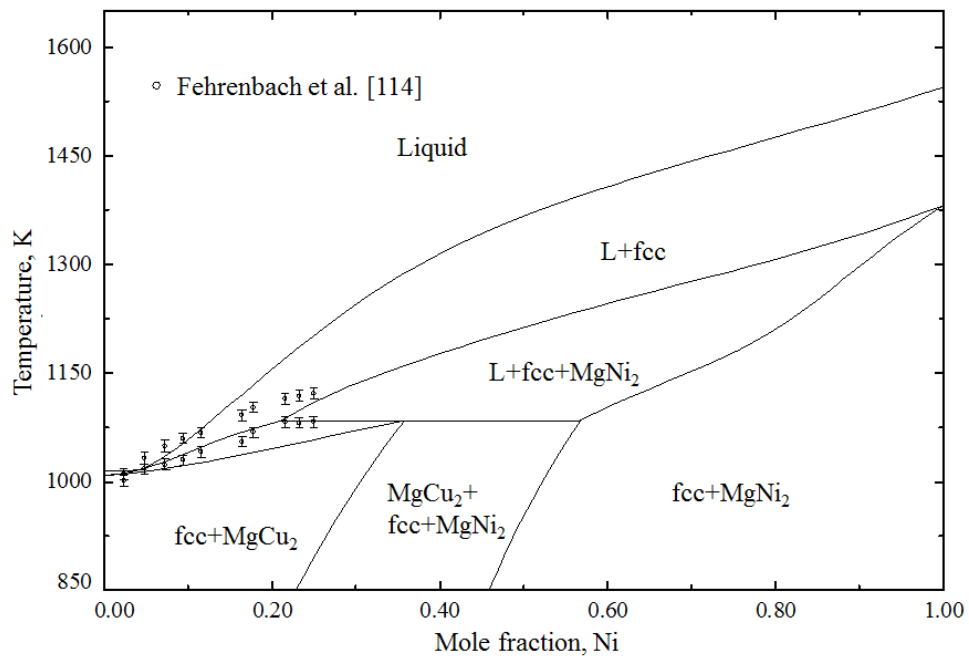


Figure 4-17: Calculated vertical section along $\text{Cu}_{0.78}\text{Mg}_{0.22} - \text{Ni}_{0.88}\text{Mg}_{0.12}$

A liquidus projection of the Mg-Cu-Ni system is shown in Figure 4-18 with the experimental data of Fehrenbach et al. [114]. Good consistency can be observed between the experimental data and the present assessment. The liquidus projection is divided into six primary crystallization fields: hcp-Mg, Mg₂Cu, Mg₂Ni, MgCu₂, MgNi₂ and fcc. The model predicted three quasiperitectic and one ternary eutectic point. The temperature and composition of these invariant reactions are listed in Appendix A-7.

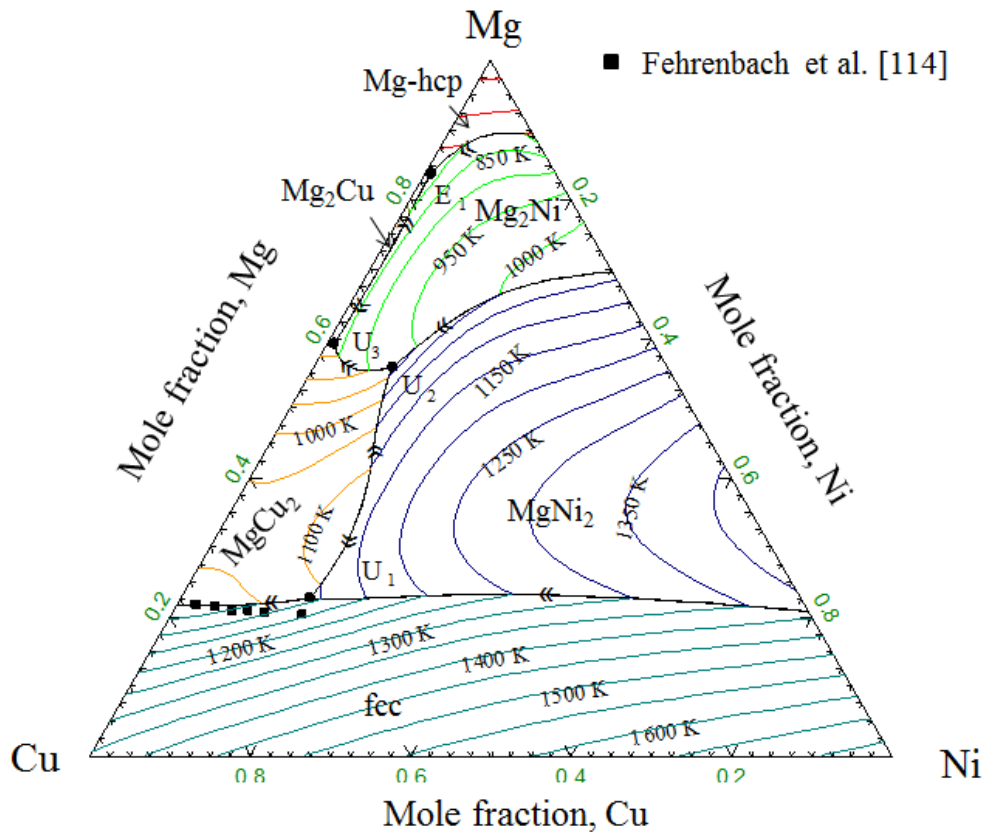


Figure 4-18: Calculated liquidus projection of the Mg-Cu-Ni system

The enthalpy of mixing of the ternary liquid calculated at 1008 K for the component ratio of $X_{Cu} / X_{Ni} = 2.0, 1.0$ and 0.5 with the experimental data from Feufel and Sommer [31] is shown in Figure 4-19 (a). It can be seen that the present calculation can represent the thermodynamic property within the claimed uncertainty limits of ± 0.3 - 0.8 kJ/mol with higher error for the higher concentrations. The same error range shown

for the data of $X_{\text{Cu}} / X_{\text{Ni}} = 1.0$ ratio applies to the other sets of data points. Also, the activity of Mg calculated at 1100 K shown in Figure 4-19 (b) agrees well with the available experimental data from Gnanasekaran and Ipser [115-117].

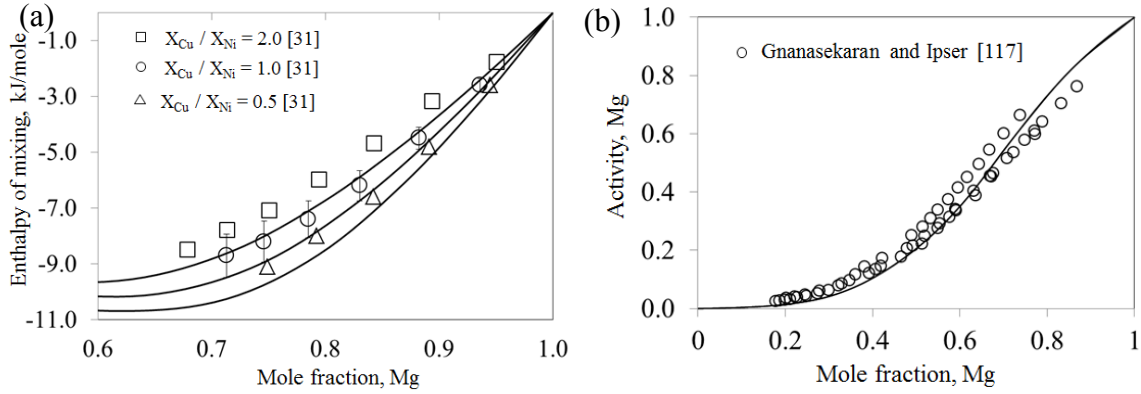
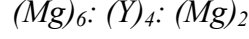


Figure 4-19: (a) Calculated enthalpy of mixing of the liquid at 1008 K for the component ratio of $X_{\text{Cu}} / X_{\text{Ni}} = 2.0, 1.0$ and 0.5 ; (b) Mg activity at 1173 K of the liquid for the component ratio of $X_{\text{Cu}} / X_{\text{Ni}} = 2.0$

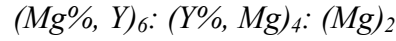
4.2.2 Mg-Cu-Y phase diagram

The thermodynamic descriptions of the binaries Mg-Cu, Cu-Y and Mg-Y are extrapolated to the ternary Mg-Cu-Y system using Toop [147] geometric model. Mg has been singled out as the asymmetric component since Cu-Y system shows significantly different thermodynamic characteristics than both Mg-Cu and Mg-Y. A self-consistent set of parameters has been determined for the Mg-Cu-Y system and is shown in Table 4-6. A discussion on the thermodynamic modeling of the different intermetallic compounds in the Mg-Cu-Y system is given below. During this discussion a term ${}^0G_y^x$ will be used frequently. It refers to the Gibbs energy of formation of the end member. The superscript 'x' refers to the phase of interest and 'y' refers to the species of different sublattices.

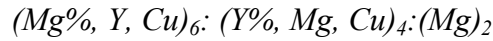
The sublattice model for the $Mg_2Y(\delta)$ phase based on the crystallographic data [139] is shown below:



This model represents the stoichiometry of the δ -phase which is the Mg_2Y . To obtain deviation from this stoichiometry, mixing of constituents is needed. The homogeneity range of δ -phase is achieved by mixing Y atom in the second sublattice and Mg in the third:



Here, ‘%’ represents the main constituent in the Sublattice. This model covers the composition range of $0 \leq X_Y \leq 0.833$. This range includes the homogeneity range of $0.24 \leq X_Y \leq 0.30$ which was reported by Zhao et al. [88]. However, ternary solubility of about 1 at.% Cu for $Mg_2Y(\delta)$ in the Mg-Cu-Y system has been found in the present work as well as in the literature [122]. The required solubility can be obtained by mixing Cu in the last two sublattices as following:



Based on this model, the Gibbs energy per mole of formula unit of $Mg_2Y(\delta)$ can be written as:

$$\begin{aligned} G_M^\delta = & y_{Mg}^I y_Y^{II 0} G_{Mg:Y:Mg}^\delta + y_{Mg}^I y_{Mg}^{II 0} G_{Mg:Mg:Mg}^\delta + y_{Mg}^I y_{Cu}^{II 0} G_{Mg:Cu:Mg}^\delta + y_Y^I y_Y^{II 0} G_{Y:Y:Mg}^\delta \\ & + y_Y^I y_{Mg}^{II 0} G_{Y:Mg:Mg}^\delta + y_Y^I y_{Cu}^{II 0} G_{Y:Cu:Mg}^\delta + y_{Cu}^I y_Y^{II 0} G_{Cu:Y:Mg}^\delta + y_{Cu}^I y_{Mg}^{II 0} G_{Cu:Mg:Mg}^\delta + y_{Cu}^I y_{Cu}^{II 0} G_{Cu:Cu:Mg}^\delta \\ & + 0.5RT(y_{Mg}^I \ln y_{Mg}^I + y_Y^I \ln y_Y^I + y_{Cu}^I \ln y_{Cu}^I) + 0.33RT(y_Y^{II} \ln y_Y^{II} + y_{Mg}^{II} \ln y_{Mg}^{II} + y_{Cu}^{II} \ln y_{Cu}^{II}) \end{aligned}$$

$$\begin{aligned}
& + y_{Mg}^I [y_Y^II y_{Mg}^II \sum^i L_{Mg:Y,Mg}^\delta (y_Y^II - y_{Mg}^II)^j + y_{Mg}^II y_{Cu}^II \sum^i L_{Mg:Mg,Cu}^\delta (y_{Mg}^II - y_{Cu}^II)^j \\
& + y_Y^II y_{Cu}^II \sum^i L_{Mg:Y,Cu}^\delta (y_Y^II - y_{Cu}^II)^j + y_Y^II y_{Mg}^II y_{Cu}^II L_{Mg:Y,Cu,Mg:Mg}^\delta] + y_Y^I [y_Y^II y_{Mg}^II \sum^i L_{Y:Y,Mg}^\delta (y_Y^II - y_{Mg}^II)^j \\
& + y_{Mg}^II y_{Cu}^II \sum^i L_{Y:Mg,Cu}^\delta (y_{Mg}^II - y_{Cu}^II)^j + y_Y^II y_{Cu}^II \sum^i L_{Y:Y,Cu}^\delta (y_Y^II - y_{Cu}^II)^j + y_Y^II y_{Mg}^II y_{Cu}^II L_{Mg:Y,Cu,Mg:Mg}^\delta] \\
& + y_{Cu}^I [y_Y^II y_{Mg}^II \sum^i L_{Cu:Y,Mg}^\delta (y_Y^II - y_{Mg}^II)^j + y_{Mg}^II y_{Cu}^II \sum^i L_{Cu:Mg,Cu}^\delta (y_{Mg}^II - y_{Cu}^II)^j + y_Y^II y_{Cu}^II \sum^i L_{Cu:Y,Cu}^\delta (y_Y^II - y_{Cu}^II)^j \\
& + y_Y^II y_{Mg}^II y_{Cu}^II L_{Mg:Y,Cu,Mg:Mg}^\delta] + y_Y^II [y_{Mg}^I y_Y^I \sum^i L_{Y:Mg,Y}^\delta (y_{Mg}^I - y_Y^I)^j + y_Y^I y_{Cu}^I \sum^i L_{Y:Y,Cu}^\delta (y_Y^I - y_{Cu}^I)^j \\
& + y_{Mg}^I y_{Cu}^I \sum^i L_{Y:Mg,Cu}^\delta (y_{Mg}^I - y_{Cu}^I)^j + y_{Mg}^I y_Y^I y_{Cu}^I L_{Y:Mg,Y,Cu::Mg}^\delta] + y_{Mg}^II [y_{Mg}^I y_Y^I \sum^i L_{Mg:Mg,Y}^\delta (y_{Mg}^I - y_Y^I)^j \\
& + y_Y^I y_{Cu}^I \sum^i L_{Mg:Y,Cu}^\delta (y_Y^I - y_{Cu}^I)^j + y_{Mg}^I y_{Cu}^I \sum^i L_{Mg:Mg,Cu}^\delta (y_{Mg}^I - y_{Cu}^I)^j + y_{Mg}^I y_Y^I y_{Cu}^I L_{Mg:Mg,Y,Cu::Mg}^\delta] \\
& + y_{Cu}^II [y_{Mg}^I y_Y^I \sum^i L_{Cu:Mg,Y}^\delta (y_{Mg}^I - y_Y^I)^j + y_Y^I y_{Cu}^I \sum^i L_{Cu:Y,Cu}^\delta (y_Y^I - y_{Cu}^I)^j + y_{Mg}^I y_{Cu}^I \sum^i L_{Cu:Mg,Cu}^\delta (y_{Mg}^I - y_{Cu}^I)^j \\
& + y_{Mg}^I y_Y^I y_{Cu}^I L_{Cu:Mg,Y,Cu::Mg}^\delta] \\
& + y_{Mg}^I y_Y^I y_{Cu}^I L_{Cu:Mg,Y,Cu::Mg}^\delta]
\end{aligned}$$

This model has nine hypothetical end members and eighteen interaction parameters. The Gibbs energy of the end members: ${}^0G_{Mg:Y:Mg}^\delta (Mg_4Y_2)$, ${}^0G_{Mg:Mg:Mg}^\delta (Mg_6)$, ${}^0G_{Y:Y:Mg}^\delta (MgY_5)$ and ${}^0G_{Y:Mg:Mg}^\delta (Mg_3Y_3)$ is taken from the thermodynamic descriptions of the binary system as listed in Table 4-4. The Gibbs energy of two of the end members: ${}^0G_{Mg:Cu:Mg}^\delta (Mg_4Cu_2)$ and ${}^0G_{Cu:Y:Mg}^\delta (MgCu_3Y_2)$ has been used to produce the required ternary solubility as listed in Table 4-6. Sufficiently high positive values have been used for the rest of the end members to avoid any unwanted formation of the hypothetical compounds. No ternary interaction parameter has been used for this phase.

Similar approach has been followed for $MgY(\gamma)$ and $Mg_{24}Y_{10}(\epsilon)$. The models and their parameters have been listed in Table 4-6. The parameters ${}^0G_{Mg:Cu}^\gamma$, ${}^0G_{Y:Cu}^\gamma$ and ${}^0G_{Cu:Y}^\gamma$

for $\text{MgY}(\gamma)$ and ${}^0G_{\text{Mg:Cu:Mg}}^\varepsilon$, ${}^0G_{\text{Cu:Y:Mg}}^\varepsilon$ and ${}^0G_{\text{Cu:Mg:Mg}}^\varepsilon$ for $\text{Mg}_{24}\text{Y}_{10}(\varepsilon)$ have been used to generate the ternary solubility.

Table 4-6: Optimized thermodynamic parameters of the ternary Mg-Cu-Y system

Phase	Parameters
Liquid	$\Delta g_{\text{CuMg(Y)}}^{001} = -6\,697.3$; $\Delta g_{\text{CuY(Mg)}}^{001} = 4\,185.8$; $\Delta g_{\text{MgY(Cu)}}^{001} = -3\,348.6$ (J/mole)
$\text{Mg}_{24}\text{Y}_5(\varepsilon)$ (Mg%, Y, Cu) ₂₉ (Y%, Mg, Cu) ₁₀ (Mg) ₁₉	${}^0G_{\text{Mg:Cu:Mg}}^\varepsilon = -3\,031.3+0.07T$; ${}^0G_{\text{Cu:Y:Mg}}^\varepsilon = -6\,495.2+0.35T$; ${}^0G_{\text{Cu:Mg:Mg}}^\varepsilon = -3\,031.1+0.03T$; ${}^0G_{\text{Cu:Cu:Mg}}^\varepsilon = {}^0G_{\text{Y:Cu:Mg}}^\varepsilon = 721.7$; (J/mole atom)
$\text{Mg}_2\text{Y}(\delta)$ (Mg%, Y, Cu) ₃ (Y%, Mg, Cu) ₂ (Mg)	${}^0G_{\text{Mg:Cu:Mg}}^\delta = -1\,813.9$; ${}^0G_{\text{Cu:Y:Mg}}^\delta = -14\,371.3+3.14T$; ${}^0G_{\text{Y:Cu:Mg}}^\delta = {}^0G_{\text{Cu:Mg:Mg}}^\delta = {}^0G_{\text{Cu:Cu:Mg}}^\delta = 698.0$ (J/mole atom)
$\text{MgY}(\gamma)$ (Mg%, Y, Cu) (Y%, Cu Va)	${}^0G_{\text{Mg:Cu}}^\gamma = -6\,278.7+2.09T$; ${}^0G_{\text{Y:Cu}}^\gamma = {}^0G_{\text{Cu:Y}}^\gamma = -12\,557.4+1.47T$; ${}^0G_{\text{Cu:Cu}}^\gamma = {}^0G_{\text{Cu:Va}}^\gamma = 6\,278.7$ (J/mole atom)
CuY (Y%) (Cu%, Mg)	${}^0G_{\text{Y:Mg}}^{\text{CuY}} = 2\,092.9$; ${}^0L_{\text{Y:Cu,Mg}}^{\text{CuY}} = -3\,892.8+0.42T$ (J/mole atom)
Cu_2Y (Y%) (Cu%, Mg) ₂	${}^0G_{\text{Y:Mg}}^{\text{Cu}_2\text{Y}} = 1\,395.3$; ${}^0L_{\text{Y:Cu,Mg}}^{\text{Cu}_2\text{Y}} = -6\,976.3+1.39T$ (J/mole atom)
Cu_7Y_2 (Y%) ₂ (Cu%, Mg) ₇	${}^0G_{\text{Y:Mg}}^{\text{Cu}_7\text{Y}_2} = -3\,255.6+0.93T$; ${}^0L_{\text{Y:Cu,Mg}}^{\text{Cu}_7\text{Y}_2} = -9\,655.2+2.79T$ (J/mole atom)
Cu_4Y (Y%) (Cu%, Mg) ₄	${}^0G_{\text{Y:Mg}}^{\text{Cu}_4\text{Y}} = -4\,185.8+1.67T$; ${}^0L_{\text{Y:Cu,Mg}}^{\text{Cu}_4\text{Y}} = -10\,045.9+2.51T$ (J/mole atom)
Mg_2Cu (Mg%) ₂ (Cu%, Y)	${}^0G_{\text{Mg:Y}}^{\text{Mg}_2\text{Cu}} = -2\,790.5+0.69T$; ${}^0G_{\text{Mg:Cu,Y}}^{\text{Mg}_2\text{Cu}} = -3\,209+3.07T$ (J/mole atom)
MgCu_2 (Cu%, Mg) ₂ (Cu, Mg%, Y)	${}^0G_{\text{Mg:Y}}^{\text{MgCu}_2} = {}^0G_{\text{Y:Cu}}^{\text{MgCu}_2} = 1\,395$; ${}^0G_{\text{Y:Mg}}^{\text{MgCu}_2} = 6\,976$; ${}^0G_{\text{Y:Y}}^{\text{MgCu}_2} = 1\,395$; ${}^0G_{\text{Cu:Y}}^{\text{MgCu}_2} = -21\,068.5+2T$; ${}^0L_{\text{Cu,Mg,Y:Y}}^{\text{MgCu}_2} = -4\,185.8+1.39T$ (J/mole atom)
Cu_6Y (Cu%) ₅ (Y%, Cu ₂ , Mg)	${}^0G_{\text{Y:Mg}}^{\text{Cu}_6\text{Y}} = -2\,391.9+0.42T$; ${}^0L_{\text{Y:Cu,Mg}}^{\text{Cu}_6\text{Y}} = -4\,185.8+0.42T$ (J/mole atom)

Table 4.6 (continued)

Phase	Parameters
MgCu_4Y (τ_2) $(\text{Cu}\%, \text{Mg}, \text{Y})_4$ $(\text{Mg}\%, \text{Y})$ $(\text{Y}\%, \text{Mg})$	${}^0G_{\text{Cu:Mg:Y}}^{\tau_2} = {}^0G_{\text{Cu:Y:Mg}}^{\tau_2} = -19\,030.7 + 0.05T;$ ${}^0G_{\text{Mg:Mg:Y}}^{\tau_2} = {}^0G_{\text{Mg:Y:Mg}}^{\tau_2} = -3\,486.7 + 0.21T;$ ${}^0G_{\text{Y:Mg:Y}}^{\tau_2} = {}^0G_{\text{Y:Y:Mg}}^{\tau_2} = 836.8; {}^0G_{\text{Cu:Mg:Mg}}^{\tau_2} = -9\,623.2$ ${}^0G_{\text{Cu:Y:Y}}^{\tau_2} = {}^0G_{\text{Mg:Mg:Mg}}^{\tau_2} = {}^0G_{\text{Mg:Y:Y}}^{\tau_2} = {}^0G_{\text{Y:Mg:Mg}}^{\tau_2} = {}^0G_{\text{Y:Y:Y}}^{\tau_2} = 1\,394.7$ (J/mole atom)
MgCu_2Y_2 (τ_3) $(\text{Cu}, \text{Mg}, \text{Y})_2$ $(\text{Y}, \text{Cu}, \text{Mg})_2$ $(\text{Mg}, \text{Cu}, \text{Y})$	${}^0G_{\text{Cu:Y:Mg}}^{\tau_3} = {}^0G_{\text{Y:Cu:Mg}}^{\tau_3} = -20\,083.2 + 1.08T;$ ${}^0G_{\text{Cu:Y:Cu}}^{\tau_3} = {}^0G_{\text{Y:Cu:Cu}}^{\tau_3} = -10\,041.6 + 2.51T;$ ${}^0G_{\text{Cu:Cu:Mg}}^{\tau_3} = -4\,184 + 1.67T;$ ${}^0G_{\text{Cu:Mg:Mg}}^{\tau_3} = {}^0G_{\text{Mg:Cu:Mg}}^{\tau_3} = -7\,573 + 4.18T;$ ${}^0G_{\text{Cu:Mg:Cu}}^{\tau_3} = {}^0G_{\text{Mg:Cu:Cu}}^{\tau_3} = -3\,347.2 + 1.67T;$ ${}^0G_{\text{Mg:Y:Mg}}^{\tau_3} = {}^0G_{\text{Y:Mg:Mg}}^{\tau_3} = -5\,857.6 + 3.77T;$ ${}^0G_{\text{Cu:Cu:Cu}}^{\tau_3} = {}^0G_{\text{Y:Cu:Y}}^{\tau_3} = {}^0G_{\text{Cu:Mg:Y}}^{\tau_3} = {}^0G_{\text{Mg:Y:Cu}}^{\tau_3} = {}^0G_{\text{Mg:Y:Y}}^{\tau_3} =$ ${}^0G_{\text{Mg:Cu:Y}}^{\tau_3} = {}^0G_{\text{Mg:Mg:Mg}}^{\tau_3} = {}^0G_{\text{Mg:Mg:Cu}}^{\tau_3} = {}^0G_{\text{Mg:Mg:Y}}^{\tau_3} = {}^0G_{\text{Y:Y:Mg}}^{\tau_3} =$ ${}^0G_{\text{Y:Y:Cu}}^{\tau_3} = {}^0G_{\text{Y:Y:Y}}^{\tau_3} = {}^0G_{\text{Y:Mg:Cu}}^{\tau_3} = {}^0G_{\text{Y:Mg:Y}}^{\tau_3} = 2\,510$ (J/mole atom)
$\text{Mg}_{9-18}\text{CuY}$ (τ_{11}) $(\text{Mg}\%, \text{Cu}, \text{Y})_7$ $(\text{Mg}\%, \text{Va})_{12}$ $(\text{Cu}) (\text{Y})$	${}^0G_{\text{Mg:Mg:Cu:Y}}^{\tau_{11}} = -4\,303.5 + 1.99T; {}^0G_{\text{Mg:Va:Cu:Y}}^{\tau_{11}} = -4\,018.6 + 2.19T;$ ${}^0G_{\text{Cu:Mg:Cu:Y}}^{\tau_{11}} = {}^0G_{\text{Cu:Va:Cu:Y}}^{\tau_{11}} = {}^0G_{\text{Y:Mg:Cu:Y}}^{\tau_{11}} = {}^0G_{\text{Y:Va:Cu:Y}}^{\tau_{11}} = 4185.8$ ${}^0L_{\text{Mg:Mg:Va:Cu:Y}}^{\tau_{11}} = {}^0L_{\text{Mg,Cu,Y:Va:Cu:Y}}^{\tau_{11}} = 1195.4 + 6.57T$
$\text{Mg}_2\text{Cu}_9\text{Y} (\tau_1)$	${}^0G^{\tau_1} = -16\,522.7 + 2.77T$ (J/mole atom)
$\text{MgCuY} (\tau_4)$	${}^0G^{\tau_4} = -17\,529.3 + 0.33T$ (J/mole atom)
$\text{Mg}_8\text{Cu}_5\text{Y}_5 (\tau_5)$	${}^0G^{\tau_5} = -15\,603.8 + 0.54T$ (J/mole atom)
$\text{Mg}_{57}\text{Cu}_{18}\text{Y}_{25} (\tau_6)$	${}^0G^{\tau_6} = -12\,932.4 + 0.47T$ (J/mole atom)
$\text{Mg}_{13}\text{Cu}_5\text{Y}_5 (\tau_7)$	${}^0G^{\tau_7} = -13\,521.8 + 0.89T$ (J/mole atom)
$\text{Mg}_{16}\text{Cu}_5\text{Y}_5 (\tau_8)$	${}^0G^{\tau_8} = -12\,569.6 + 1.15T$ (J/mole atom)
$\text{Mg}_4\text{CuY} (\tau_9)$	${}^0G^{\tau_9} = -11\,573.0 + 1.50T$ (J/mole atom)
$\text{Mg}_{78}\text{Cu}_9\text{Y}_{13} (\tau_{10})$	${}^0G^{\tau_{10}} = -8\,274.0 + 1.13T$ (J/mole atom)

It has been found in the present work that all the Cu-Y binary compounds dissolve small amount of Mg. The solubility of Mg in these compounds has been modeled with a two sublattice model where Y occupies the first lattice. Cu and Mg replace each other and their mixing is allowed on the second sublattice, such as: $(\text{Y}\%) (\text{Cu}\%, \text{Mg})$, $(\text{Y}\%) (\text{Cu}\%$,

$Mg)_2, (Y\%)_2 (Cu\%, Mg)_7$ and $(Y\%) (Cu\%, Mg)_4$. The Cu_6Y phase has been modeled using $(Cu\%)_5 (Y\%, Cu_2, Mg)$ model since it has homogeneity range in the binary Cu-Y system.

The sublattice model and the optimized parameters for $MgCu_2$ and Mg_2Cu have been listed in Table 4-6. The parameters $G_{Y:Mg}^{MgCu_2}$; $G_{Y:Y}^{MgCu_2}$; $G_{Cu:Y}^{MgCu_2}$ and ${}^0L_{Cu,Mg,Y:Y}^{MgCu_2}$ have been used to reproduce Y solubility in $MgCu_2$.

According to the experimental result in the present work as well as reported in the literature [122, 123], the Mg-Cu-Y system has eleven ternary compounds. All of them except τ_2 , τ_3 and τ_{11} have been found as stoichiometric compounds. These have been reproduced using stoichiometric model. The other three phases have been found to have homogeneity ranges which have been obtained through sublattice modeling as listed in Table 4-6.

The model used to reproduce the homogeneity range of $MgCu_4Y(\tau_2)$ has twelve end members. However, Gibbs energy of only few end members: $MgCu_4Y$, Mg_5Y and Mg_2Cu_4 have impact on the solubility range. The values of these terms have been determined carefully to fit the experimental data.

As reported by De Negri et al. [122], $MgCu_2Y_2(\tau_3)$ has solubility extending towards both Y and Cu-rich regions from the stoichiometric composition. Therefore, mixing of all the species in all three sublattices has been allowed. This is a very complex model and care was taken during optimization. However, few end members of the model have been selected observing their influence on the homogeneity range of the compound. These are: Mg_2Cu_2Y , $MgCu_2Y_2$, Cu_4Y , Mg_3Cu_2 , Mg_2Cu_3 , Mg_3Y_2 , $MgCu_2Y_2$, Cu_3Y_2 , Careful determination of the Gibbs energy values of these end members could generate

the required solubility. The other end members were assigned sufficiently large positive Gibbs energy values to avoid formation. The crystal structure of $\text{Mg}_{9-18}\text{CuY}(\tau_{11})$ is not known. Therefore, it has been modeled using an arbitrary model as shown in Table 4-6.

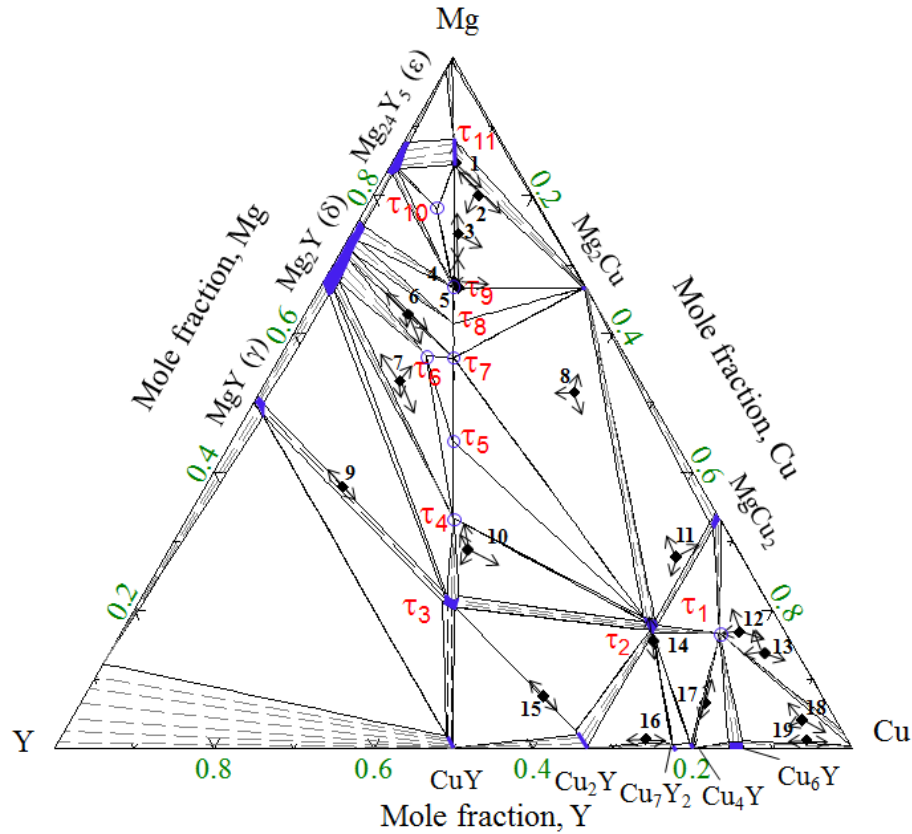


Figure 4-20: Calculated isothermal section of the Mg-Cu-Y system at 673 K

The calculated isothermal section of the Mg-Cu-Y system at 673 K is shown in Figure 4-20. According to De Negri et al. [122], $\text{Mg}_{24}\text{Y}_5(\epsilon)$, $\text{Mg}_2\text{Y}(\delta)$ and $\text{MgY}(\gamma)$ dissolve about 1 at.% Cu. This is in agreement with the present thermodynamic modeling. The solubility of Mg in CuY and Cu_2Y have been found as 1.8 at.% and 2 at.% respectively which are in reasonable agreement with the reported values of 3 at.% and 1 at.% in [122]. The ternary solubility of Cu_4Y , Cu_7Y_2 and Cu_6Y have been determined about 1 at.% Mg in the present experimental work which was reproduced

thermodynamically within the experimental error of ± 0.8 at.%. The maximum solubility of MgCu_2 that could be achieved by thermodynamic modeling was 1.7 at.% Y which was measured as 4 at.% Y in the current experimental work. The lower solubility is due to the presence of the very stable ternary compound $\text{MgCu}_4\text{Y}(\tau_2)$ which has a large homogeneity range. Mg_2Cu has been found to have negligible solubility of Y (~ 0.45 at.%).

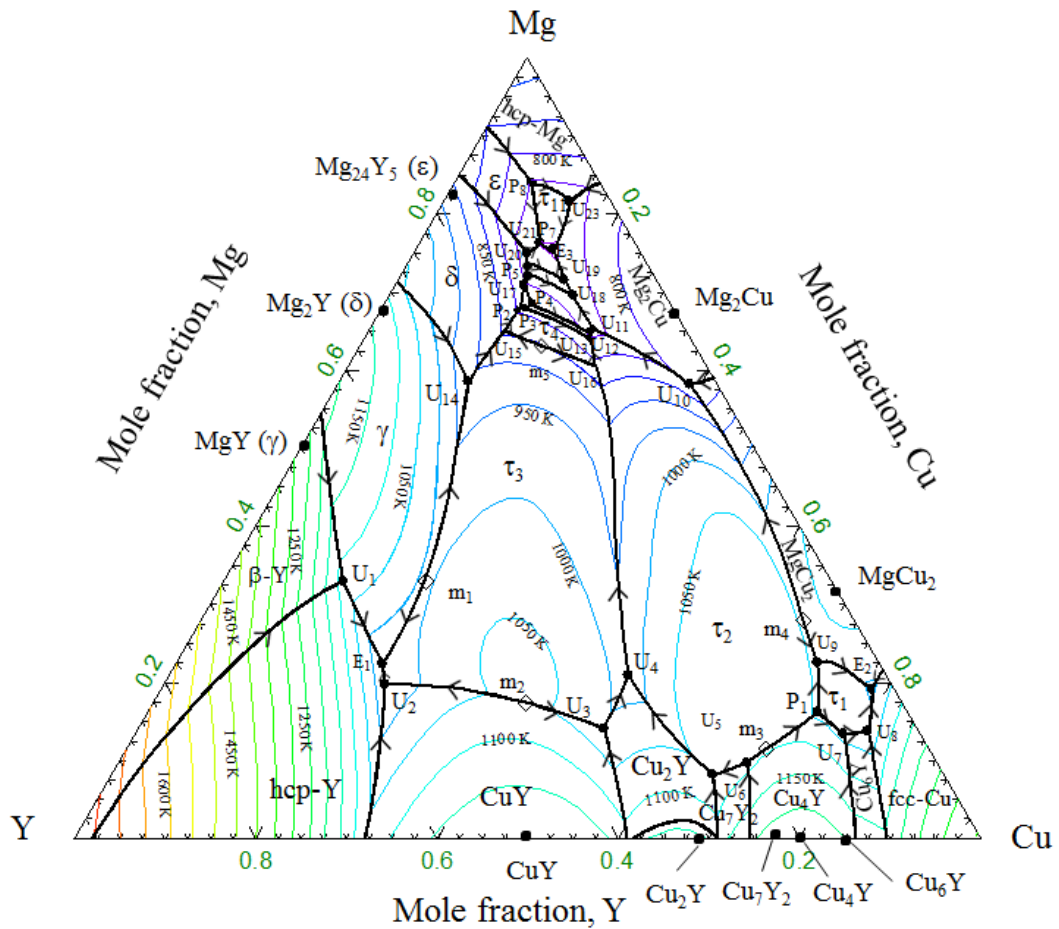


Figure 4-21: Liquidus projection of the Mg-Cu-Y system

The liquidus projection of the Mg-Cu-Y system has been calculated as shown in Figure 4-21. Also, Figure 4-22 shows the magnified Mg-rich corner of the liquidus projection. According to this calculation the system has five saddle (m), twenty three

quasi-peritectic (U), eight peritectic (P) and three ternary eutectic (E) points. The composition and temperature of the invariant reactions are listed in Appendix A-8. Three ternary excess Gibbs energy terms have been used during modeling of the liquid phase. These parameters have been used to adjust phase transformation temperature in order to be consistent with the current DSC results.

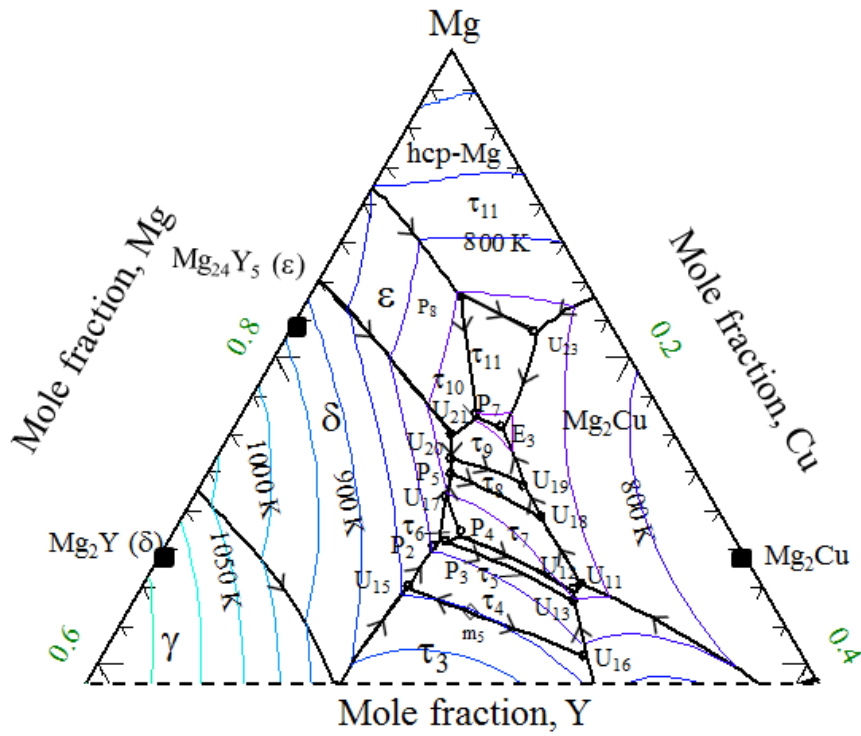


Figure 4-22: Liquidus projection of the Mg rich side of the Mg-Cu-Y system

4.2.3 Mg-Ni-Y Phase diagram

A self-consistent thermodynamic database for the Mg-Ni-Y system has been constructed by combining the thermodynamic descriptions of the three constituent binaries Mg-Ni, Ni-Y and Mg-Y using Toop geometric model [155] with Mg as the asymmetric component. Ternary adjustable terms were added based on the current experimental results on the Mg-Ni-Y system as listed in Table 4-7. The database was used to calculate

polythermic projections of the liquidus surface shown in Figure 4-23. Figure 4-24 shows the magnified Mg-rich corner. The liquidus projection of the Mg-Ni-Y system is divided into 27 primary crystallization fields. The model predicted seventeen saddle points, twenty nine quasi-peritectic, two ternary peritectic and eight ternary eutectic points. The respective reactions of these points are listed in Appendix A-9.

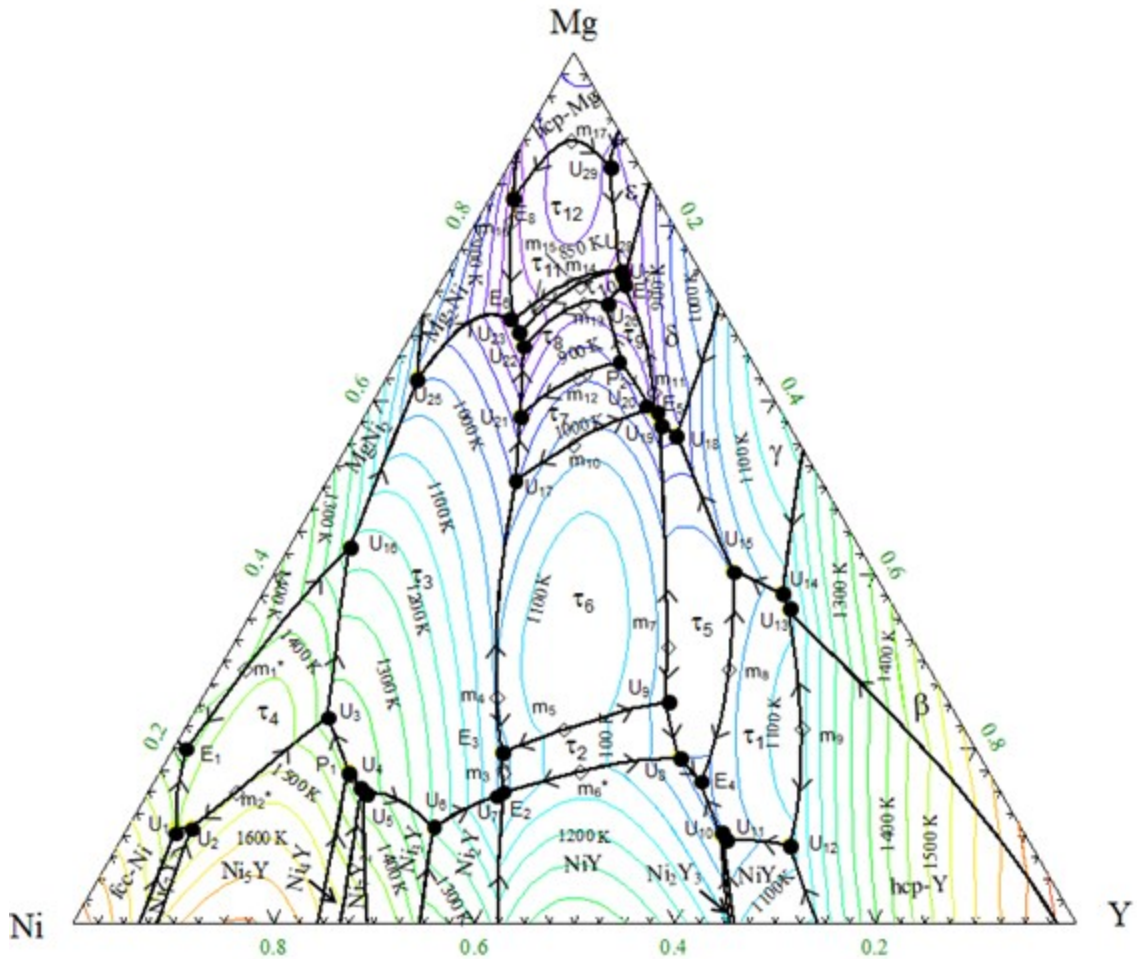


Figure 4-23: Calculated liquidus projection of the Mg-Ni-Y system

Based on the current experimental data, the location of the pertinent solid phases of the Mg-Ni-Y system at 673K is presented in the calculated isothermal section in Figure 4-25. However, the present understanding of the isothermal section is quite

different than that of Yao et al. [159] as shown in Figure 2-3 (a). The presence of several ternary compounds as identified in this work changed the understandings of the phase relationships.

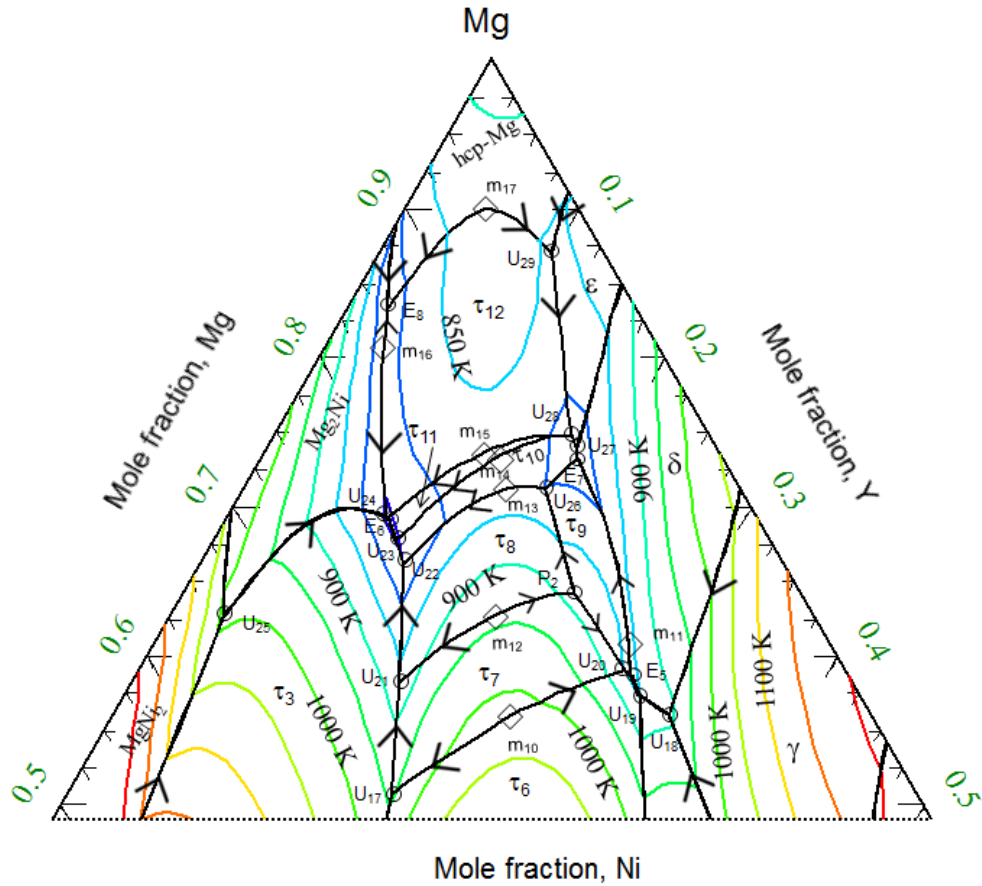


Figure 4-24: Liquidus projection of the Mg rich side of the Mg-Ni-Y system

Thermodynamic modeling of the different ternary intermetallic compounds of the Mg-Ni-Y system is discussed below.

The homogeneity range of $\text{MgNiY}_4(\tau_1)$ as obtained in the present experimental work has been reproduced thermodynamically using a three sublattice model: $(Y\%, \text{Ni})_4(\text{Ni}\%, \text{Mg})(\text{Mg}\%, \text{Y})$. The model has eight end members where $G_{Y:\text{Ni}:\text{Mg}}^{\tau_1}$ represents the stoichiometric composition of MgNiY_4 . The Gibbs energy of this compound has

significant influence on the melting temperature of τ_1 . Hence it has been determined with care to be consistent with the current DSC measurements. The parameters $G_{Y:NeY}^{\tau_1}$, $G_{Y:Mg:Mg}^{\tau_1}$ and $G_{Y:Mg:Y}^{\tau_1}$ represent the hypothetical compounds: NiY_5 , Mg_2Y_4 and MgY_5 , respectively. These have major impact on the solubility range of τ_1 and have been determined to be consistent with the experimental data. The Gibbs energy of the other end members does not have any influence and are given a fixed positive value (+1395 J/mole.atom) to avoid any unwanted formation. Two adjustable parameters have also been used to generate the proper solubility.

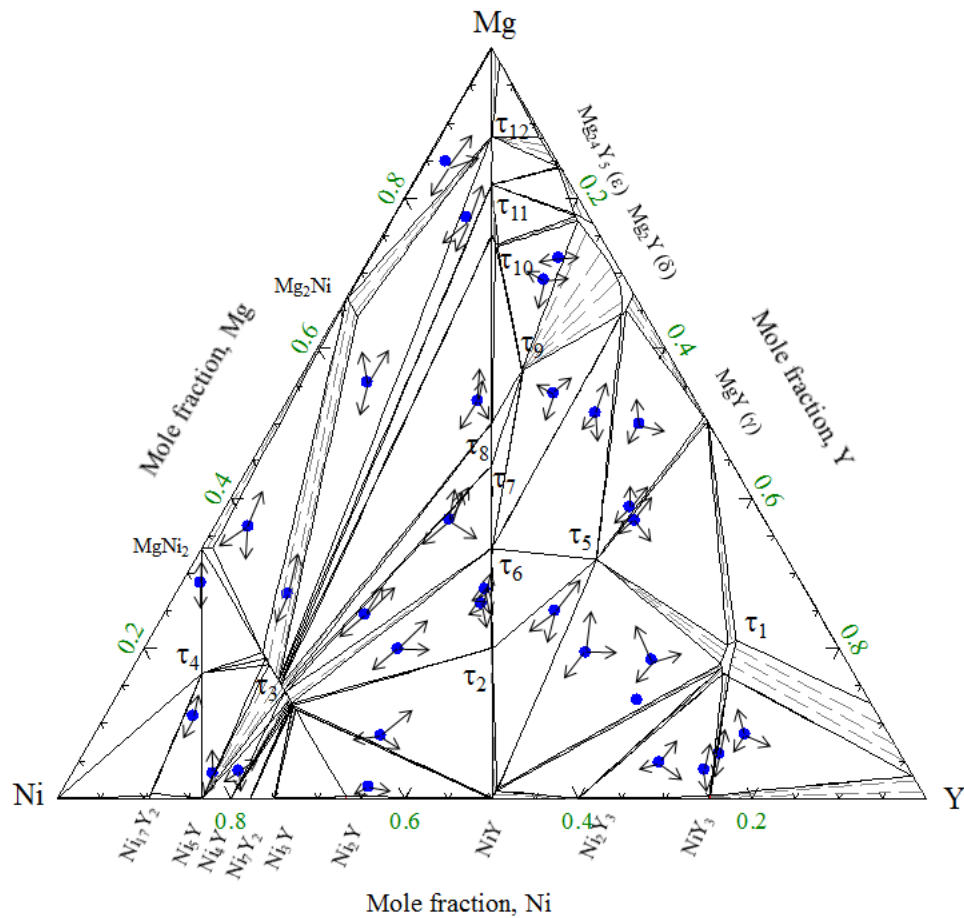


Figure 4-25: Calculated isothermal section of the Mg-Ni-Y system at 673 K

Table 4-7: Optimized thermodynamic parameters of the ternary Mg-Ni-Y system

Phase	Parameters
Liquid	$\Delta g_{MgY(Ni)}^{001} = 11720.24; \Delta g_{MgNi(Y)}^{001} = 10045.92;$ $\Delta g_{NiY(Mg)}^{001} = -30933.06 + 2.51T$ (J/mole)
Bcc-Y	+15000 (J/mole)
Mg ₂ Ni (Mg%, Y) ₂ (Ni%)	${}^oG_{Y:Ni}^{Mg_2Ni} = -15347.9; {}^oL_{Mg,Y:Ni}^{Mg_2Ni} = -27207.7$ (J/mole. atom)
MgNi ₂ (Ni%, Mg, Y) ₂ (Mg%, Ni, Y)	${}^oG_{Ni:Y}^{MgNi_2} = {}^oG_{Mg:Y}^{MgNi_2} = {}^oG_{Y:Mg}^{MgNi_2} = {}^oG_{Y:Y}^{MgNi_2} = 1395.3$ ${}^oG_{Y:Ni}^{MgNi_2} = -5581; {}^oL_{Ni:Mg,Y}^{MgNi_2} = -83716 + 20.93T$ (J/mole. atom)
Ni ₁₇ Y ₂ (Ni%, Mg) ₁₂ (Ni%, Mg) ₃ (Ni%, Mg) ₂ (Y%) ₂	${}^oG_{Ni:Ni:Mg:Y}^{Ni_{17}Y_2} = {}^oG_{Ni:Mg:Ni:Y}^{Ni_{17}Y_2} = {}^oG_{Ni:Mg:Mg:Y}^{Ni_{17}Y_2} = {}^oG_{Mg:Ni:Ni:Y}^{Ni_{17}Y_2} =$ ${}^oG_{Mg:Ni:Mg:Y}^{Ni_{17}Y_2} = {}^oG_{Mg:Mg:Ni:Y}^{Ni_{17}Y_2} = 881.22;$ ${}^oG_{Mg:Mg:Mg:Y}^{Ni_{17}Y_2} = -4053.62 + 0.88T;$ ${}^oL_{Ni,Mg:Ni:Ni:Y}^{Ni_{17}Y_2} = -35248.84 + 0.88T;$ (J/mole. atom)
Ni ₃ Y (Ni%, Mg) ₃ (Y%)	${}^oG_{Mg:Y}^{Ni_3Y} = 1046.5; {}^oL_{Ni,Mg:Y}^{Ni_3Y} = 17789.7$ (J/mole. atom)
Ni ₂ Y (Ni%) ₂ (Y%, Mg)	${}^oG_{Ni:Mg}^{Ni_2Y} = -1395.3 + 19.53T; {}^oL_{Ni:Y,Mg}^{Ni_2Y} = -33486.4 + 8.65T$ (J/mole. atom)
NiY (Ni%, Mg) (Y%)	${}^oG_{Mg:Y}^{NiY} = -8371.6 + 12.55T; {}^oL_{Ni,Mg:Y}^{NiY} = -8371.6 + 6.28T$ (J/mole. atom)
NiY ₃ (Ni%, Mg) (Y%) ₃	${}^oG_{Y:Mg}^{NiY_3} = -2616$ (J/mole. atom)
Mg ₄₈ Y ₁₀ (ε) (Y%, Mg, Ni) ₄ (Mg%, Y, Ni) ₂₉ (Mg%) ₁₉	${}^oG_{Y:Ni:Mg}^{\epsilon} = -10825 + 1.01T; {}^oG_{Ni:Mg:Mg}^{\epsilon} = -5917.9 + 0.29T;$ ${}^oG_{Mg:Ni:Mg}^{\epsilon} = {}^oG_{Ni:Y:Mg}^{\epsilon} = {}^oG_{Ni:Ni:Mg}^{\epsilon} = 72.2;$ ${}^oL_{Y,Mg,Ni:Mg:Mg}^{\epsilon} = -3608.5; {}^oL_{Y,Mg,Ni:Ni:Mg}^{\epsilon} = -14433.8$ (J/mole. atom)
Mg ₂ Y (δ) (Y%, Mg, Ni) ₂ (Mg%, Y, Ni) ₃ (Mg%)	${}^oG_{Y:Ni:Mg}^{\delta} = -66275.2 + 2.79T; {}^oG_{Mg:Ni:Mg}^{\delta} = -13952.7 + 1.12T;$ ${}^oG_{Ni:Mg:Mg}^{\delta} = -1534.8 + 1.12T; {}^oG_{Ni:Ni:Mg}^{\delta} = {}^oG_{Y:Ni:Mg}^{\delta} = 1395.3;$ ${}^oL_{Y,Mg,Ni:Mg:Mg}^{\delta} = -362769.3 + 72.55T$ (J/mole. atom)
MgY (γ) (Mg%, Y, Ni) (Y%, Va, Ni)	${}^oG_{Mg:Ni}^{\gamma} = -14650.3 + 2.09T; {}^oG_{Y:Ni}^{\gamma} = {}^oG_{Ni:Y}^{\gamma} = -29300.6 + 8.37T$ ${}^oG_{Ni:Va}^{\gamma} = {}^oG_{Ni:Ni}^{\gamma} = 6278.7$ ${}^oL_{Y,Ni:Mg}^{\gamma} = 10464.5 + 2.09T$ (J/mole. atom)

Table 4-7 (continued)

Phase	Parameters
MgNiY ₄ (τ_1) (Y%, Ni) ₄ (Ni%, Mg) (Mg%, Y)	${}^{\circ}G_{Y:Ni:Mg}^{\tau_1} = -18557+1.39T$; ${}^{\circ}G_{Y:Ni:Y}^{\tau_1} = -5622.9+0.35T$; ${}^{\circ}G_{Y:Mg:Mg}^{\tau_1} = -1395.3+0.35T$; ${}^{\circ}G_{Y:Mg:Y}^{\tau_1} = -3488.2+0.35T$ ${}^{\circ}G_{Ni:Ni:Mg}^{\tau_1} = {}^{\circ}G_{Ni:Ni:Y}^{\tau_1} = {}^{\circ}G_{Ni:Mg:Mg}^{\tau_1} = {}^{\circ}G_{Ni:Mg:Y}^{\tau_1} = 1395.3$; ${}^{\circ}L_{Y:Ni:Mg:Mg}^{\tau_1} = -11859.8+2.79T$; ${}^{\circ}L_{Y:Ni:Mg:Y}^{\tau_1} = -9069.2+2.79T$ (J/mole. atom)
MgNi ₄ Y (τ_3) (Ni) ₂ (Mg, Y)	${}^{\circ}G_{Ni:Mg}^{\tau_3} = -15068.8+6.98T$; ${}^{\circ}G_{Ni:Y}^{\tau_3} = -24138.1+6.14T$ ${}^{\circ}L_{Ni:Mg,Y}^{\tau_3} = -78762.8+8.69T$; ${}^{\circ}L_{Ni:Mg,Y}^{\tau_3} = -34881.7+7.67T$ (J/mole. atom)
Mg ₆ NiY (τ_{10}) (Mg%, Y) ₄ (Ni%) (Y%, Mg)	${}^{\circ}G_{Mg:Ni:Y}^{\tau_{10}} = -15369.7+3.37T$; ${}^{\circ}G_{Y:Ni:Y}^{\tau_{10}} = -10098+1.88T$ ${}^{\circ}G_{Mg:Ni:Mg}^{\tau_{10}} = {}^{\circ}G_{Y:Ni:Mg}^{\tau_{10}} = -523.22$; ${}^{\circ}L_{Mg,Y:Ni:Y}^{\tau_{10}} = -7377.5$ (J/mole. atom)
MgNi ₂ Y ₂ (τ_2)	${}^{\circ}G^{\tau_2} = -32216.8-0.07T$ (J/mole. atom)
Mg ₂ Ni ₉ Y (τ_4)	${}^{\circ}G^{\tau_4} = -23376.9-0.67T$ (J/mole. atom)
Mg ₂₉ Ni ₂₀ Y ₄₂ (τ_5)	${}^{\circ}G^{\tau_5} = -23603.4+0.11T$ (J/mole. atom)
MgNiY (τ_6)	${}^{\circ}G^{\tau_6} = -30100+0.23T$ (J/mole. atom)
Mg ₈ Ni ₅ Y ₅ (τ_7)	${}^{\circ}G^{\tau_7} = -26208.5+0.16T$ (J/mole. atom)
Mg ₂ NiY (τ_8)	${}^{\circ}G^{\tau_8} = -24246.8+0.38T$ (J/mole. atom)
Mg ₅₇ Ni ₁₈ Y ₂₅ (τ_9)	${}^{\circ}G^{\tau_9} = -20066+0.11T$ (J/mole. atom)
Mg ₉ NiY (τ_{11})	${}^{\circ}G^{\tau_{11}} = -12249.9+3.27T$ (J/mole. atom)
Mg ₁₅ NiY (τ_{12})	${}^{\circ}G^{\tau_{12}} = -9021+2.98T$ (J/mole. atom)

According to the present experimental analysis, MgNi₄Y(τ_3) has solubility from 10.5 to 23.5 at.% Mg with constant 66.67 at.% Ni. Based on the crystallographic data [136] a two sublattice model: (Ni%)₂ (Mg%, Y)₂; has been used to describe this solubility. With this model the compound energy formalism has two end members: $G_{Ni:Mg}^{\tau_3}$ representing MgNi₂ and $G_{Ni:Y}^{\tau_3}$ representing Ni₂Y. Adjustment of the Gibbs energy of

formation of these two members as well as two ternary interaction parameters: ${}^0L_{Ni:Mg,Y}^{\tau^3}$ and ${}^0L_{Ni:Mg,Y}^{\tau^3}$; generates the required solubility.

Another ternary compound, Mg_6NiY (τ_{10}) has been found to have solubility. The crystal structure of this compound is not known. Therefore an arbitrary sublattice model: $(Mg\%, Y)_4 (Ni\%) (Y\%, Mg)$, has been used to generate the solubility.

The ternary solubility of the binary compounds has been modeled in a similar manner as those of the Mg-Cu-Y system. The sublattices used for these compounds with the adjustable parameters are listed in Table 4-7.

4.2.4 Cu-Ni-Y Phase diagram

The thermodynamic properties of the liquid have been estimated from the optimized binary parameters using Toop extrapolation [147]. Y has been singled out as the asymmetric component since Cu-Ni system shows significantly different thermodynamic characteristics than Cu-Y and Ni-Y binary systems. In order to be consistent with the DSC experimental data two excess Gibbs energy terms, $\Delta g_{CuY(Ni)}^{001}$ and $\Delta g_{NiY(Cu)}^{001}$, have been used for the liquid phase. The $\Delta g_{CuY(Ni)}^{001}$ parameter is related to the influence of Ni on the Cu-Y bonding energy in ternary liquid, and $\Delta g_{NiY(Cu)}^{001}$ is the influence of Cu on the Ni-Y bonding energy in ternary liquid. A self-consistent set of parameters for all the phases in the Cu-Ni-Y system is listed in Table 4-8.

Table 4-8: Optimized thermodynamic parameters of the ternary Cu-Ni-Y system

Phase	Parameters (J/mole. atom)
Liquid	$\Delta g_{\text{CuY(Ni)}}^{011} = 1674.32; \Delta g_{\text{NiY(Cu)}}^{011} = -2092.90$ (J/mole)
fcc (Cu,Ni,Y) (Va)	${}^{\circ}L_{\text{Cu,Ni,Y:Va}}^{\text{fcc}} = -355793+9.63T$ (J/mole)
$\text{Cu}_x\text{Ni}_{1-x}\text{Y}$ ($0 \leq x \leq 1$) (Y%) (Cu, Ni)	${}^{\circ}L_{\text{Y:Cu,Ni}}^{\text{Cu}_x\text{Ni}_{1-x}\text{Y}} = -5232.25+5.86T$ (J/mole. atom)
$\text{Cu}_x\text{Ni}_{4-x}\text{Y}$ ($0 \leq x \leq 4$) (Y%) (Cu, Ni) ₄	${}^{\circ}L_{\text{Y:Cu,Ni}}^{\text{Cu}_x\text{Ni}_{4-x}\text{Y}} = -10422.64+13.23T$ (J/mole. atom)
Cu_2Y (Y%) (Cu%, Ni) ₂	${}^{\circ}G_{\text{Y:Ni}}^{\text{Cu}_2\text{Y}} = -27797.90+1.76T; {}^{\circ}L_{\text{Y:Cu,Ni}}^{\text{Cu}_2\text{Y}} = -34742.14+20.23T$ (J/mole. atom)
Cu_7Y_2 (Y%) ₂ (Cu%, Ni) ₇	${}^{\circ}G_{\text{Y:Ni}}^{\text{Cu}_7\text{Y}_2} = -32256.61+1.31T; {}^{\circ}L_{\text{Y:Cu,Ni}}^{\text{Cu}_7\text{Y}_2} = -195.34+7.67T$ (J/mole. atom)
Cu_6Y (Cu%) ₅ (Y%, Cu ₂ , Ni)	${}^{\circ}G_{\text{Cu:Ni}}^{\text{Cu}_6\text{Y}} = {}^{\circ}G_{\text{Ni:Cu}_2}^{\text{Cu}_6\text{Y}} = 2391.88; {}^{\circ}G_{\text{Ni:Y}}^{\text{Cu}_6\text{Y}} = 1195.94;$ ${}^{\circ}G_{\text{Ni:Ni}}^{\text{Cu}_6\text{Y}} = 4783.77; {}^{\circ}L_{\text{Ni:Y,Cu}_2}^{\text{Cu}_6\text{Y}} = -20929.0+16.74T;$ ${}^{\circ}L_{\text{Cu,Ni:Y}}^{\text{Cu}_6\text{Y}} = -32888.43+12.56T$ (J/mole. atom)
NiY_3 (Y%) (Ni%, Cu) ₃	${}^{\circ}G_{\text{Y:Cu}}^{\text{NiY}_3} = -9836.63+3.66T; {}^{\circ}L_{\text{Y:Cu,Ni}}^{\text{NiY}_3} = -8371.60+3.14T$ (J/mole. atom)
Ni_2Y (Y%) (Ni%, Cu) ₂	${}^{\circ}G_{\text{Y:Cu}}^{\text{Ni}_2\text{Y}} = -7912.56+2.47T; {}^{\circ}L_{\text{Y:Cu,Ni}}^{\text{Ni}_2\text{Y}} = -22184.74+10.18T$ (J/mole. atom)
Ni_3Y (Y%) (Ni%, Cu) ₃	${}^{\circ}G_{\text{Y:Cu}}^{\text{Ni}_3\text{Y}} = -3997.44+1.57T; {}^{\circ}L_{\text{Y:Cu,Ni}}^{\text{Ni}_3\text{Y}} = -29562.21+11.41T$ (J/mole. atom)
Ni_5Y (Y%) (Ni%, Cu) ₅	${}^{\circ}G_{\text{Y:Cu}}^{\text{Ni}_5\text{Y}} = -14638.0+1.14T; {}^{\circ}L_{\text{Y:Cu,Ni}}^{\text{Ni}_5\text{Y}} = -12836.45+14.99T$ (J/mole. atom)
Ni_{17}Y_2 (Y%) ₂ (Ni%, Cu) ₁₂ (Ni%, Cu) ₃ (Ni%, Cu) ₂	${}^{\circ}G_{\text{Ni:Ni:Cu:Y}}^{\text{Ni}_{17}\text{Y}_2} = {}^{\circ}G_{\text{Ni:Cu:Ni:Y}}^{\text{Ni}_{17}\text{Y}_2} = -19827.47+2.20T;$ ${}^{\circ}G_{\text{Ni:Cu:Cu:Y}}^{\text{Ni}_{17}\text{Y}_2} = {}^{\circ}G_{\text{Cu:Ni:Ni:Y}}^{\text{Ni}_{17}\text{Y}_2} = {}^{\circ}G_{\text{Cu:Ni:Cu:Y}}^{\text{Ni}_{17}\text{Y}_2} = 0;$ ${}^{\circ}G_{\text{Cu:Cu:Ni:Y}}^{\text{Ni}_{17}\text{Y}_2} = -12998.01+4.18T;$ ${}^{\circ}G_{\text{Cu:Cu:Cu:Y}}^{\text{Ni}_{17}\text{Y}_2} = -6609.16+5.29T;$ ${}^{\circ}L_{\text{Ni,Cu:Ni:Ni:Y}}^{\text{Ni}_{17}\text{Y}_2} = -14099.54+5.51T;$ ${}^{\circ}L_{\text{Ni,Cu:Ni:Cu:Ni}}^{\text{Ni}_{17}\text{Y}_2} = -7049.77+4.41T$ (J/mole. atom)

The calculated liquidus projection in Figure 4-26 is divided into thirteen primary crystallization fields: hcp-Y, NiY_3 , $\text{Cu}_x\text{Ni}_{1-x}\text{Y}$ ($0 \leq x \leq 1$), Cu_2Y , Ni_2Y , Cu_7Y_2 , Ni_3Y ,

Ni_7Y_2 , $\text{Cu}_x\text{Ni}_{4-x}\text{Y}$ ($0 \leq x \leq 1$), Cu_6Y , Ni_5Y , Ni_{17}Y_2 and fcc. The model predicted five quasi-peritectic, one peritectic and three ternary eutectics. The respective reactions of these points are listed in Appendix A-10. Relatively flat liquidus can be seen near CuY-NiY section of the projection in Figure 4-26. This can be explained by the close melting temperatures of CuY (1209 K) and NiY (1329 K) which generates flat liquidus surface when extrapolated to the ternary.

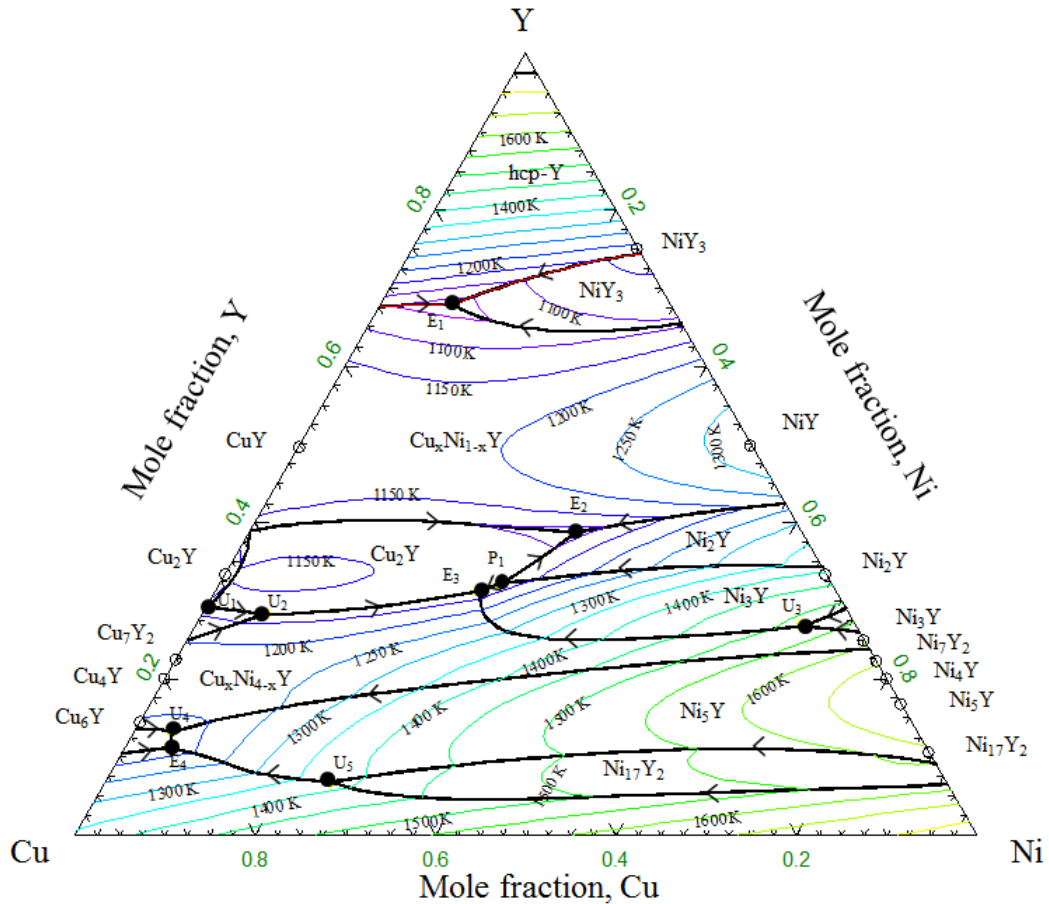


Figure 4-26: Calculated liquidus projection of the Cu-Ni-Y system

The phase equilibria of the Cu-Ni-Y system have been studied in this work at 973 K which will be discussed in the experimental results section. The ternary solubility of the binary compounds of the Cu-Ni-Y system has been modeled based on the findings of the experimental study. The calculated isothermal section at 973 K is shown in Figure

4-27. A comparison between the experimental and thermodynamic calculation of the ternary solubility of the binary compounds in the Cu-Y and Ni-Y systems is given in Table 4-9. It showed acceptable agreement except Ni_7Y_2 . The solubility limit of this compound has been obtained through five spot WDS measurements of sample 17 (5.0/74.9/20.1 Cu/Ni/Y at.%) which showed scattered data with standard deviation of 0.99 at.%. Hence, lower weight has been given to the maximum solubility limit of Ni_7Y_2 during optimization.

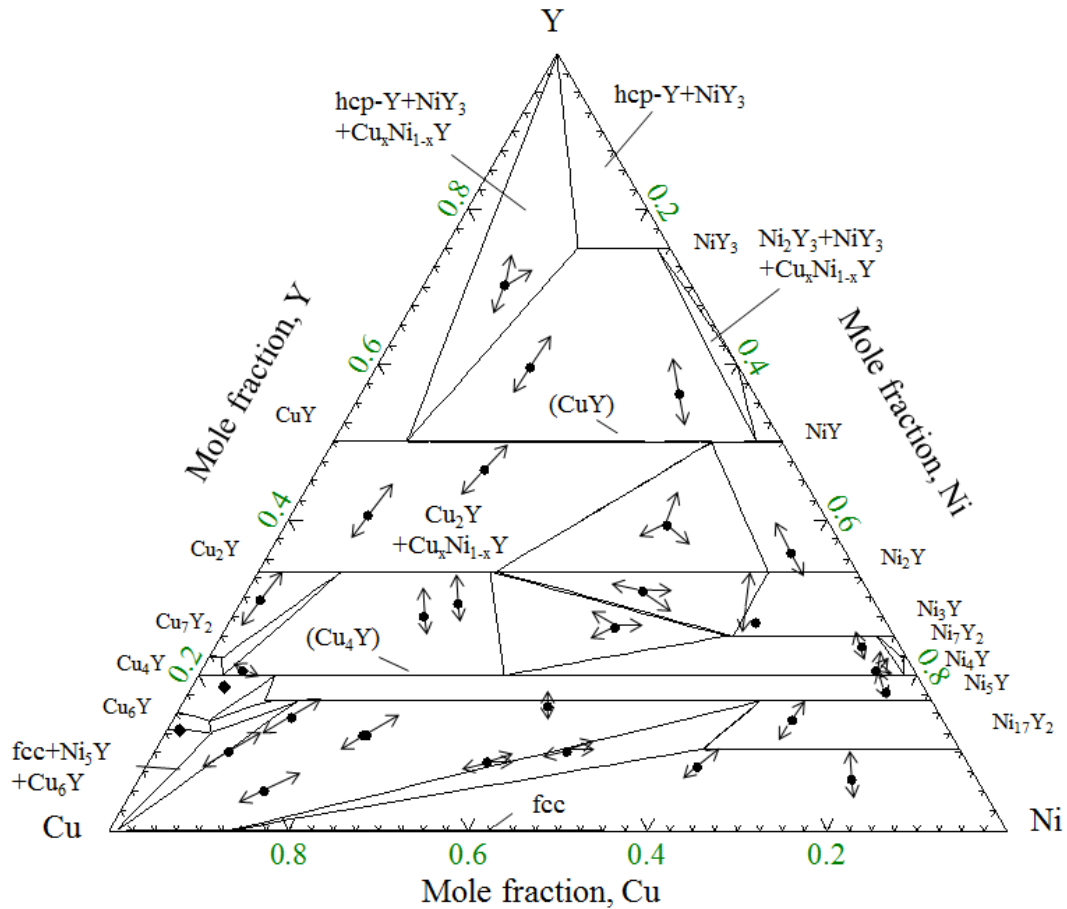


Figure 4-27: Calculated isothermal section of the Cu-Ni-Y system at 973 K

Several binary compounds in the Cu-Y and Ni-Y systems have been found to have significant ternary solubility. The solubility of Cu in the Ni-Y binary compounds have been modeled using two sublattices with Y occupying the first lattice. The atomic

size of Cu and Ni are very similar. These two elements replace each other and their mixing is allowed on the second sublattice, such as: $(Y\%)_3(Ni\%,Cu)$, $(Y\%)(Ni\%,Cu)_2$, $(Y\%)(Ni\%,Cu)_3$, $(Y\%)_2(Ni\%,Cu)_7$ and $(Y\%)(Ni\%,Cu)_5$. Similar approach has been adopted for the solubility of Ni in the Cu-Y binary compounds as $(Y\%)(Cu\%,Ni)_2$ and $(Y\%)_2(Cu\%,Ni)_7$. Complete mutual solubility between CuY-NiY ($Cu_xNi_{1-x}Y$, $0 \leq x \leq 1$) and Cu_4Y-Ni_4Y ($Cu_xNi_{4-x}Y$, $0 \leq x \leq 4$) have been modeled using $(Y\%)(Cu, Ni)$ and $(Y\%)(Cu, Ni)_4$ sublattices. $Ni_{17}Y_2$ has been modeled using a four sublattice model as $(Y\%)_2(Ni\%,Cu)_{12}(Ni\%,Cu)_3(Ni\%,Cu)_2$. The Cu_6Y compound has been modeled using $(Cu\%)_5(Y\%, Cu_2, Ni)$ model since it has homogeneity range in the binary Cu-Y system.

Table 4-9: Ternary solubility of the Cu-Y and Ni-Y compounds in the Cu-Ni-Y ternary system

Phase	Ternary solubility (Calculated)	Ternary solubility Measured (This work)	Ternary solubility Measured (literature)
Cu_2Y	26.5 at.% Ni	28.0 at.% Ni	30.5 at.% Ni [136]
Cu_7Y_2	1.7 at.% Ni	3.5 at.% Ni	
Cu_6Y	5.1 at.% Ni	-	~ 5.0 at.% Ni [138]
NiY_3	10.3 at.% Cu	12.0 at.% Cu	
Ni_2Y	9.9 at.% Cu	9.7 at.% Cu	10.4 at.% Cu [136]
Ni_3Y	18.7 at.% Cu	25.0 at.% Cu	> 16.67 at.% Cu [134]
Ni_7Y_2	0.5 at.% Cu	3.1 at.% Cu	
Ni_5Y	74.4 at.% Cu	75.0 at.% Cu	
$Ni_{17}Y_2$	28.5 at.% Cu	37.0 at.% Cu	35 at.% Cu [137]

4.3 Mg-Cu-Ni-Y quaternary system

The Mg-Cu-Ni, Mg-Cu-Y, Mg-Ni-Y and Cu-Ni-Y ternary systems are combined to represent the quaternary system. No quaternary interaction parameters were used because of the lack of experimental data. Figure 4-28 shows the liquidus projection of the quaternary system. The colors in the diagram indicate the primary solidification regions

of different phases shared by two different ternary systems. This kind of diagram gives a general understanding of the whole quaternary system. Detailed information regarding a specific alloy or region can be obtained through calculations using the current database. It can be seen that the ternary compounds; τ_2 and τ_3 in the Mg-Cu-Y system and τ_3 and τ_6 in the Mg-Ni-Y system are dominating phases. The Cu-Ni-Y system does not have any ternary compounds. However, the ternary solubility of the binary Ni-Y and Cu-Y compounds governs the solidification behavior in this system. The Mg-Cu-Ni system shows rather simple solidification compared to the other three ternary systems. Large primary crystallization field for fcc and $MgNi_2$ are of importance in this system. Experimental results on this quaternary could not be found in the literature.

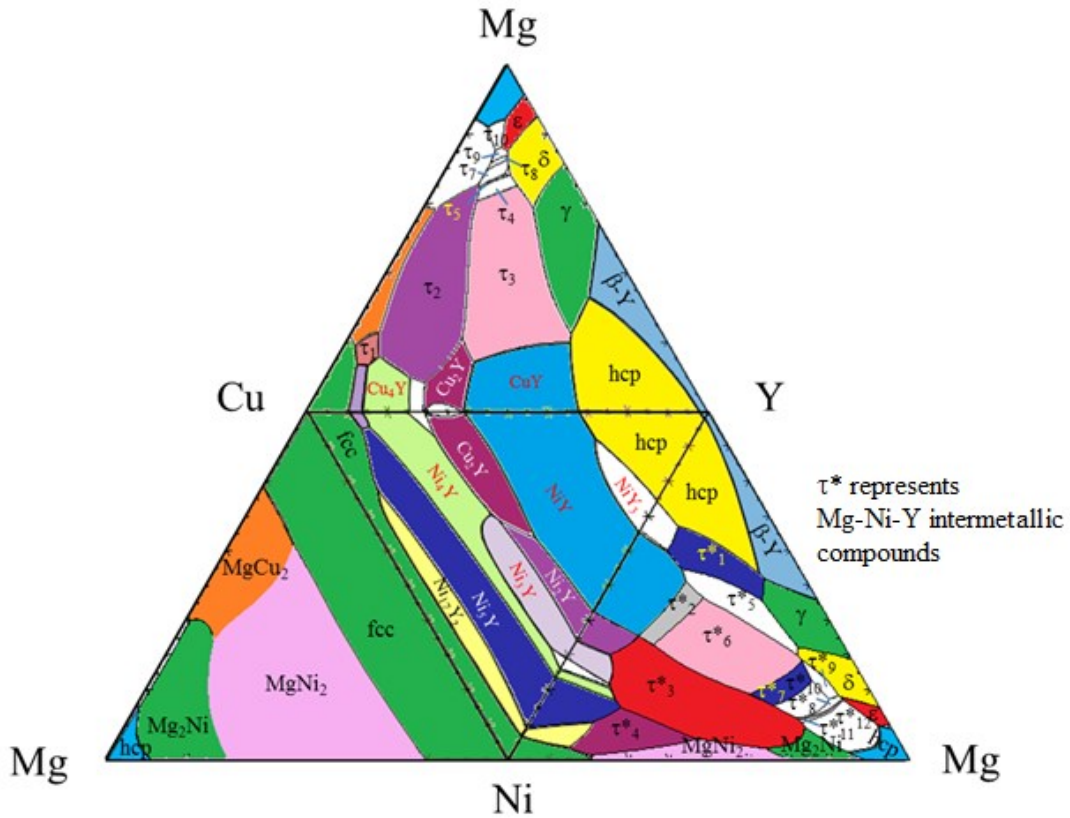


Figure 4-28: Liquidus projection of the Mg-Cu-Ni-Y quaternary system. τ^* represents Mg-Ni-Y intermetallic compounds.

Chapter 5

Experimental Procedure

5.1 Experimental Methods

Thermal investigations, phase identification and microstructural characterization were carried out using key alloys in the Mg-Cu-Y, Mg-Ni-Y and Cu-Ni-Y systems. These alloys were chosen by critical assessment of the experimental data from the literature as well as preliminary thermodynamic datasets obtain through extrapolation of the binary systems. The actual composition of the alloys is shown in Tables 5.1 to 5.3. Along with the key samples, the diffusion couple technique has been utilized to investigate the phase equilibria of the Mg-Ni-Y and Cu-Ni-Y systems. Three solid-solid and two solid-liquid diffusion couples in the Mg-Ni-Y system were investigated; whereas two solid-solid diffusion couples in the Cu-Ni-Y system have been studied.

Nine ternary compounds have been reported along the Mg-CuY section of the Mg-Cu-Y system. Therefore, several key samples have been prepared along this section. Some of the alloys with more than 66 at.% Cu have been prepared to establish the phase relationship in the Cu-rich side of the Mg-Cu-Y system. This region was not studied experimentally before. The composition of the studied alloys is shown in Figure 5-1.

Table 5-1: Chemical composition of the Mg-Cu-Y alloys in at.%

Sample No	Mg	Cu	Y	Sample No	Mg	Cu	Y
1	84.86	7.92	7.22	11	27.97	63.28	8.74
2	80.42	12.80	6.78	12	18.52	7.43	74.05
3	70.50	15.30	14.20	13	16.89	77.29	5.82
4	67.50	16.40	16.10	14	16.78	66.52	16.69
5	66.67	17.33	16.00	15	7.55	57.40	35.06
6	62.65	12.38	24.97	16	1.42	73.29	25.29
7	53.21	16.63	30.16	17	6.66	78.21	15.13
8	55.64	36.86	7.52	18	4.08	91.58	4.34
9	37.84	17.16	45.00	19	1.15	93.65	5.19
10	28.36	37.64	34.00				

Table 5-2: Chemical composition of the Mg-Ni-Y alloys in at.%

Sample No	Mg	Ni	Y	Sample No	Mg	Ni	Y
1	84.9	12.9	2.2	17	1.5	63.4	35.1
2	78.2	15.5	6.3	18	25.0	30.3	44.7
3	55.5	36.6	7.9	19	19.5	29.5	51.0
4	27.2	59.9	12.9	20	18.5	22.4	59.1
5	36.2	59.9	3.9	21	13.1	26.7	60.2
6	28.7	69.1	2.2	22	4.8	28.3	66.9
7	11.0	78.9	10.1	23	3.9	23.6	72.5
8	3.7	77.3	19.0	24	5.9	20.9	73.2
9	8.4	58.6	33.0	25	8.6	16.5	74.9
10	20.0	50.8	29.2	26	37.0	15.0	48.0
11	23.8	40.4	35.8	27	38.2	15.0	46.8
12	28.0	36.8	35.2	28	49.9	8.0	42.1
13	24.5	52.4	23.1	29	51.4	12.3	36.3
14	37.2	36.3	26.5	30	54.0	15.9	30.1
15	54.1	24.0	21.9	31	69.1	9.4	21.5
16	3.3	80.5	16.2	32	72.0	6.3	21.7

Table 5-3: Chemical composition of the Cu-Ni-Y alloys in at.%

Sample No	Cu	Ni	Y	Sample No	Cu	Ni	Y
1	20.80	9.07	70.13	16	4.68	71.81	23.51
2	23.26	17.23	59.51	17	5.0	74.9	20.10
3	8.38	35.51	56.12	18	6.48	73.92	19.60
4	34.92	18.71	46.37	19	85.64	1.37	12.99
5	50.81	8.75	40.44	20	81.78	8.46	9.74
6	18.15	42.70	39.15	21	72.38	13.14	14.48
7	6.15	58.25	35.60	22	65.57	22.34	12.09
8	68.17	2.17	29.66	23	80.90	14.13	4.97
9	52.13	20.75	27.12	24	44.96	36.30	18.74
10	41.57	26.80	31.62	25	53.44	37.91	8.65
11	30.34	43.78	25.88	26	43.94	45.99	10.07
12	25.10	44.23	30.67	27	30.34	61.57	8.08
13	15.92	54.38	29.70	28	13.99	79.60	6.41
14	72.74	6.03	21.23	29	16.71	69.17	14.12
15	77.99	3.48	18.53				

Almost no experimental study has been done on the Mg-Ni-Y system prior to this work. Therefore, a preliminary ternary phase diagram has been calculated by extrapolating the parameters of the constituent binary systems for experimental design. Based on this phase diagram, ten key alloys have been chosen. The analysis of these alloys showed the existence of many ternary compounds in the Mg-Ni-Y system. Diffusion couples and the rest of the key alloys have been selected depending on this initial data. The actual composition of the key alloys along with the terminal composition of the diffusion couples are shown in Figure 5-2.

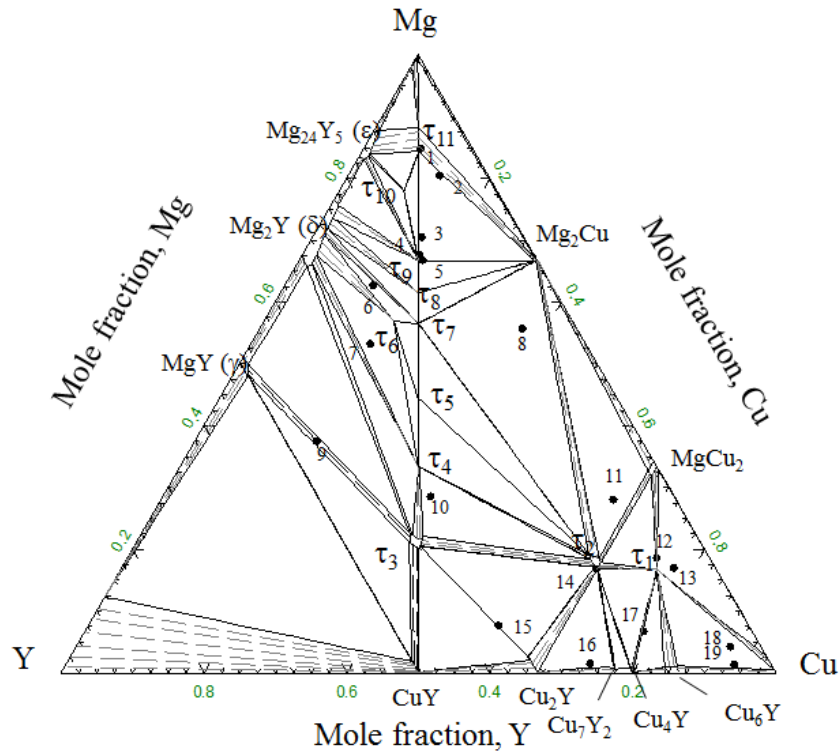


Figure 5-1: Mg-Cu-Y isothermal section at 673 K, based on this work, showing the investigated compositions

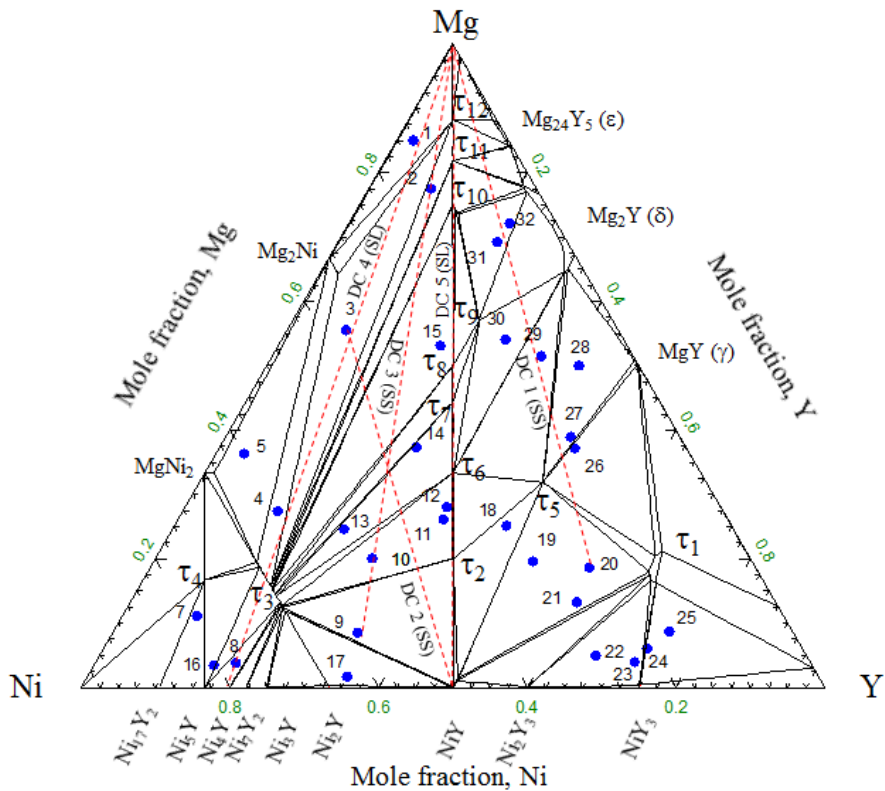


Figure 5-2: Mg-Ni-Y isothermal section at 673 K, based on this work, showing the investigated compositions and diffusion couples.

Very little information on the phase equilibria of the Cu-Ni-Y system could be found in the literature. However, the partial phase diagram reported by Gupta [138] in Figure 2-4 showed that some of the binary compounds in the Cu-Y and Ni-Y systems dissolve the third element significantly. Taking this into consideration, the key samples and diffusion couples of the Cu-Ni-Y system have been selected. Figure 5-3 shows the location of the key samples and diffusion couple end members.

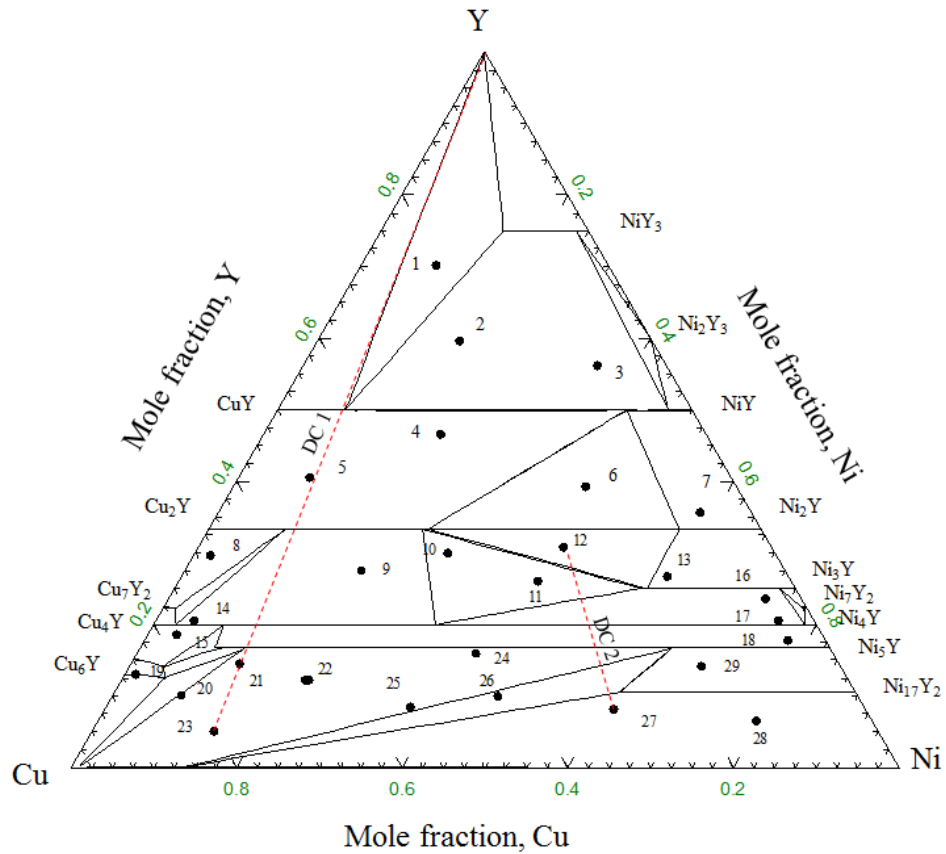


Figure 5-3: Cu-Ni-Y isothermal section at 973 K, based on this work, showing the investigated compositions and diffusion couples

5.2 Alloy preparation

The key samples as well as the end members of the diffusion couples were prepared in an arc melting furnace using a water-cooled copper crucible under flowing argon. The purity of the elements used is Mg 99.99%, Cu 99.99%, Ni 99.99%, and Y 99.9%, all supplied by Alfa Aesar. The furnace chamber was evacuated and purged by argon several times before melting. Each alloy was crushed and re-melted at least four times to ensure homogeneity. Mg has lower melting temperature compared to Y, Ni or Cu which makes it difficult to melt alloys in the Mg-Ni-Y and Mg-Cu-Y systems. Therefore, some of the Mg-rich alloys of these systems were re-melted in an induction furnace after pre-melting in the arc melting furnace to improve the homogeneity.

Some of the key alloys of the Mg-Cu-Y (10 samples) and Mg-Ni-Y (10 samples) system were prepared at CANMET-MTL. The proper amount of the pure elements were charged in a graphite crucible where melting occurs under flowing argon. In order to ensure the homogeneity of the samples the melt was stirred slowly with a graphite rod.

In order to verify the final alloy composition after melting, the chemical compositions of the as-cast alloys were analyzed using Inductively Coupled Plasma-Optical Emission Spectrometry (ICP-OES). Compositional variation of about 3 at.% has been observed for the Mg-rich (>60 at.% Mg) alloys in the Mg-Cu-Y and Mg-Ni-Y systems. The global composition of the alloys for the Cu-Ni-Y system did not show large variation (less than 1 at.%) from the starting composition. Nevertheless, the actual composition was used for the analysis in this work.

Each solid-solid diffusion couple was prepared from two end member blocks of ternary alloys or pure elements. Contacting surfaces of these blocks were pre-grounded down to 1200 grit using SiC paper and polished with 1 μm diamond paste and 99% ethanol as a lubricant. The blocks were pressed together using clamping rings to ensure good contact.

For annealing, the key alloys and diffusion couples were wrapped in tantalum foil and sealed in a quartz tube. Before sealing, the tube was evacuated and purged several times using flowing argon. These capsules were then placed in the furnace for annealing. Although higher annealing temperature is desirable for faster kinetics, it should be chosen below the lowest melting temperature of the system to avoid melting during annealing. In the present work, the annealing temperature has been chosen based on the lowest eutectic of the three pertinent binary systems. For instance, in the Cu-Ni-Y system, among the three binaries the lowest eutectic occurs in the Cu-Y system at around 1073 K. Therefore, it is decided to anneal the samples at 973 K to reach equilibrium faster without melting. These alloys were annealed six weeks at this temperature. Similarly, Mg-Cu-Y and Mg-Ni-Y alloys were annealed at 673K for four weeks.

5.3 Diffusion couple approach

In this work the diffusion couple technique has been utilized to establish the phase relationships and identify the ternary compounds and their solubility. Diffusion couple is a powerful and efficient technique for mapping the phase diagram of ternary systems [160-162]. It also eliminates the problems associated with alloy preparation especially for systems with high melting temperatures [163]. Within the diffusion layers the equilibrium

phases occur, whereas at the interface local equilibrium takes place [163]. However, one should always consider the possibility of missing phases [163, 164] while using diffusion couple for determining phase diagram. This may occur because of the slow nucleation of the phase which prevents formation of the diffusion layer. In order to obtain more reliable information, diffusion couples are combined with key sample analysis in the present work.

5.4 X-Ray Diffraction

X-ray diffraction (XRD) was used for the phase identification of the key alloys. The XRD patterns were obtained using PANanalytical Xpert Pro powder X-ray diffractometer with a $\text{CuK}\alpha$ radiation at 45kV and 40mA. The XRD spectrum is acquired from 20 to 120° 2 θ with a 0.02° step size. Analysis of the XRD spectrum was carried out using the X'Pert HighScore Plus Rietveld analysis software in combination with Pearson's crystal database [139]. All the samples were investigated in the powder form after annealing.

5.5 SEM and WDS analysis

SEM (Scanning Electron Microscopy) and WDS (Wave Dispersive X-ray Spectrometer) were used to examine the phase composition of the alloys. At least three measurements were carried out on three locations for each phase and the average was used in the present analysis. For the diffusion couple analysis, the phase composition measurements were performed perpendicular to the interfaces between every two adjacent layers. The equilibrium compositions of each phase were obtained by analyzing the composition-distance curves of each element. The error of the WDS measurements is estimated to be about ± 1 at.%.

5.6 Differential Scanning Calorimetry (DSC)

Thermal investigation was performed using a Setaram Setsys DSC-2400 instrument. Temperature calibration of the DSC equipment was done using standard samples of Al, Zn, Ni and Au. The samples were cut and mechanically polished to remove any possible contaminated surface layers. Afterwards, they were cleaned with 99% ethanol and placed in an alumina crucible with a lid cover. To avoid oxidation, evacuations followed by rinses with argon were done. The DSC measurements were carried out under flowing argon atmosphere with the same heating and cooling rate of 5 K/min. The weight of the sample is kept in the range 50~70 mg. The reproducibility of every measurement was confirmed by collecting the data during three heating and cooling cycles on two different replicas of each sample. The estimated error of measurements between the repetitive cycles is ± 7 K or less. Temperatures corresponding to various thermal events were obtained from the analysis of the DSC curves during heating and cooling runs. On heating, onset temperature was used for invariant reactions, while peak maximum was used for liquidus temperature. On cooling, onset temperature was used for both the invariant reactions and liquidus temperature. Details on the interpretation of the DSC experiments were discussed by Boettinger et al. [165] and have been utilized in this work. In this work, the onset of cooling peaks will be compared with the thermodynamic modeling except the last transformation to solid for which the onset of heating will be considered.

Chapter 6

Experimental Investigation of the Mg-Cu-Y System

In this chapter, the phase relations of the Mg-Cu-Y system are discussed using experimental analysis as well as thermodynamic calculations of the key alloys. In section 6.1, a discussion on the isothermal section based on key sample analysis will clarify some of the issues on this system not resolved by De Negri et al. [122]. Based on the recent understandings, thermodynamic modeling of the Mg-Cu-Y system has been performed. In section 6.2, the thermodynamic modeling will be compared with the experimental results using vertical sections and phase assemblage diagrams.

De Negri et al. [122] used 51 key alloys to construct a partial isothermal section of the Mg-Cu-Y system. Some of their alloys were not completely in equilibrium. Hence, some of the phase triangulations and solubility limits of the binary and ternary compounds need to be verified. Also, they focused their work on less than 66.7 at.% Cu. The phase relations in the Cu-rich region of this system need to be understood for better thermodynamic modeling. Nineteen key alloys have been examined in this work to establish the phase equilibria of the Mg-Cu-Y system. The WDS analysis of the alloys has been summarized in Table 6-1. Also, locations of the alloys are shown in Figure 5-1.

6.1 Isothermal section at 673 K

The ternary solubility of the binary compounds in the Cu-rich corner of the phase diagram has been determined using the key samples 15-19. The WDS analysis in Table 6-1 shows that Cu_2Y , Cu_7Y_2 , Cu_4Y and Cu_6Y compounds dissolve ~ 1 at.% Mg. But the

error of WDS measurement is about ± 1 at.%. Hence, the above mentioned solubility may not be accurate. However, it was found that for these Cu-rich (12-19) alloys the WDS measurement is more accurate with an error of about ± 0.8 at.%. Therefore, it is decided to consider small amount of Mg solubility (~ 1 at.%) in these Cu-Y binary compounds. No solubility of Y could be found in the Cu-fcc phase. The phase boundaries of two three-phase regions $\text{MgCu}_2+\text{Mg}_2\text{Cu}_9\text{Y}(\tau_1)+\text{Cu-fcc}$ and $\text{Mg}_2\text{Cu}_9\text{Y}(\tau_1)+\text{Cu}_6\text{Y}+\text{Cu-fcc}$ have been determined. Also, four two-phase regions: $\text{Cu}_2\text{Y}+\tau_3$, $\text{Cu}_2\text{Y}+\text{Cu}_7\text{Y}_2$, $\text{Cu}_4\text{Y}+\text{Mg}_2\text{Cu}_9\text{Y}(\tau_1)$ and $\text{Cu}_6\text{Y}+\text{Cu-fcc}$ have been identified. Discussion on the phase relations of the Cu-rich side of the phase diagram in light of the key sample analysis is given below.

Table 6-1: SEM–WDS data on selected Mg-Cu-Y alloys annealed at 673K

Actual Composition				Identified phases			
No	at.%			Name	Compositions by WDS		
	Mg	Cu	Y		Mg	Cu	Y
1	84.9	7.9	7.2	Mg_2Cu	68.9	30.8	0.3
				τ_{11}	84.4	7.3	8.3
2	80.4	12.8	6.8	Mg_2Cu	68.6	31.3	0.1
				τ_{11}	84.7	7.1	8.2
				τ_9	68.6	16.1	15.3
3	70.5	15.3	14.2	Mg_2Cu	69.5	30.3	0.2
				τ_{11}	85.0	7.0	8.0
				τ_9	68.9	15.9	15.2
4	67.5	16.4	16.1	Mg_2Cu	69.4	30.4	0.2
				τ_{11}	84.0	7.6	8.4
				τ_9	69.2	15.9	14.9
5	66.7	17.3	16.0	Mg_2Cu	69.6	30.0	0.3
				τ_{11}	84.1	7.6	8.2
				τ_9	68.8	16.0	15.1

Table 6-1 (continued)

Actual Composition				Identified phases			
No	at.%			Name	Compositions by WDS		
	Mg	Cu	Y		Mg	Cu	Y
6*	62.6	12.4	25.0	Mg ₂ Y	74.2	0.8	25.1
				τ_7	58.5	20.8	20.7
				τ_5	47.2	26.5	26.3
				τ_4	36.1	31.7	32.2
7*	53.2	16.6	30.2	Mg ₂ Y	66.3	0.7	33.0
				τ_{11}	53.9	19.8	26.3
				τ_4	33.1	33.0	33.8
				τ_3	18.4	40.6	41.0
8	55.6	36.9	7.5	Mg ₂ Cu	65.1	34.6	0.3
				τ_2	22.3	62.5	15.3
				τ_6	53.5	23.6	23.9
9	37.4	17.2	45.4	MgY	48.8	1.1	50.1
				τ_3	19.8	38.7	41.5
10*	28.4	37.6	34.0	τ_5	43.2	27.0	29.8
				τ_4	34.4	31.4	34.2
				τ_3	21.8	38.5	39.7
				τ_2	22.2	61.6	16.3
11	28.0	63.3	8.7	Mg ₂ Cu	67.1	32.8	0.1
				τ_2	17.3	69.4	13.4
				MgCu ₂	26.9	66.8	6.3
12	18.5	74.1	7.4	MgCu ₂	29.3	2.5	68.2
				τ_1	19.3	7.5	73.2
13	16.9	77.3	5.8	Cu	2.7	97.2	0.1
				τ_1	17.9	73.8	8.3
				MgCu ₂	33.0 to 25.0	65.5 to 69.8	1.5 to 5.2
14	16.8	66.5	16.7	τ_2	16.6	67.1	16.2
				Mg ₂ Cu	66.1	0.2	33.7
15	7.6	57.4	35.0	τ_3	21.9	39.9	38.2
				Cu ₂ Y	0.3	66.2	33.5
16	1.4	73.3	25.3	Cu ₇ Y ₂	2.0	77.4	20.6
				Cu ₂ Y	0.6	65.3	34.1
17	6.7	78.2	15.1	Cu ₄ Y	1.8	79.6	18.6
				τ_1	14.9	76.1	0.9
18	4.1	91.6	4.3	Cu	1.9	97.9	0.2
				Cu ₆ Y	1.1	86.6	12.3
				τ_1	14.7	76.9	8.3
19	1.1	93.7	5.2	Cu	1.4	98.5	0.1
				Cu ₆ Y	0.7 to 0.8	87.4 to 89.6	11.9 to 9.6

* Appearance of four phases due to peritectic reaction.

The two-phase equilibrium between τ_3 and Cu_2Y has been revealed in sample 15 (7.6/57.4/35.0 Mg/Cu/Y at.%) as shown in Figure 6-1 (a). The XRD pattern of this sample in Figure 6-2 also confirms these phases. The BSE image of sample 17 (6.7/78.2/15.1 Mg/Cu/Y at.%) in Figure 6-1 (b) shows another two-phase region between Cu_4Y and τ_1 .

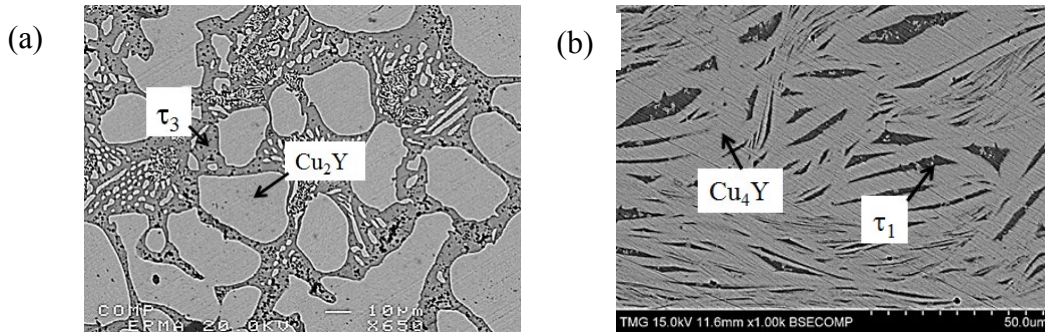


Figure 6-1: BSE image of (a) sample 15 (7.6/57.4/35.0 Mg/Cu/Y at.%; (b) sample 17 (6.7/78.2/15.1 Mg/Cu/Y at.%)

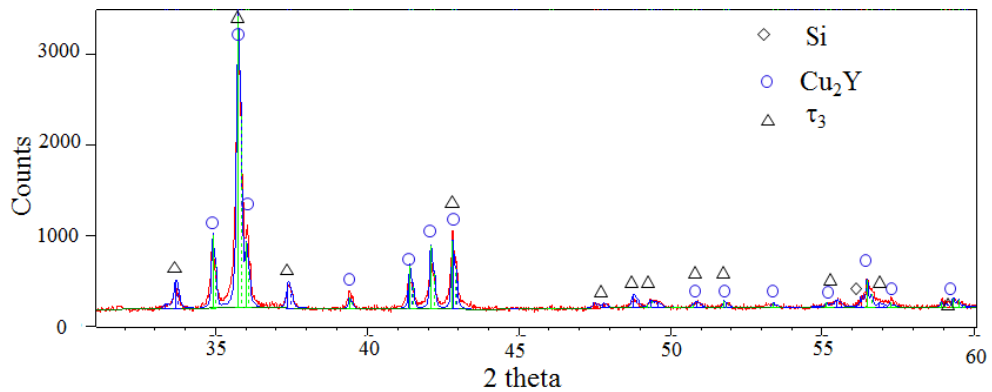


Figure 6-2: XRD pattern of sample sample 15 (7.6/57.4/35.0 Mg/Cu/Y at.%)

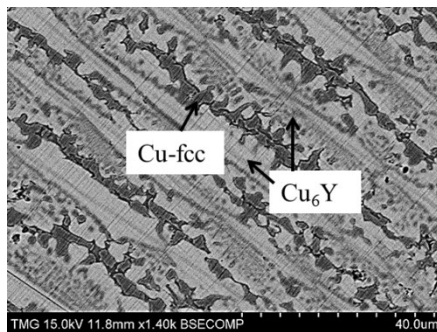


Figure 6-3: BSE image of sample 19 (1.1/93.7/5.2 Mg/Cu/Y at.%)

The micrograph of sample 19 (1.1/93.7/5.2 Mg/Cu/Y at.%) in Figure 6-3 shows the two phase region of Cu-fcc and Cu_6Y . The Cu_6Y phase has been found in white and grey shades due to the solid solubility. The homogeneity of this compound has been found to be about 87 to 89 at.% Cu which is slightly higher than the values (85 to 87 at.% Cu) reported by Fries et al. [105] for the binary Cu-Y system.

The phase relations in the central portion of the Mg-Cu-Y system were shown by dotted lines in the reported isothermal section by De Negri et al. [122] because the alloys were not in complete equilibrium even after annealing for four weeks. To resolve this, three alloys (6, 7 and 9) have been prepared in the current work and annealed for 40 days at 673 K. The BSE image of sample 6 (62.6/12.4/25.0 Mg/Cu/Y at.%) and sample 7 (53.2/16.7/30.2 Mg/Cu/Y at.%) are shown in Figure 6-4 (a and b). Still the samples are not in complete equilibrium and showing more than three phases. However, it was found in sample 6 that τ_4 and τ_5 always formed within τ_7 , whereas, τ_6 , τ_7 and Mg_2Y are in contact with each other. This is probably due to a peritectic type reaction. With longer annealing time τ_4 and τ_5 will dissolve more Mg to form τ_7 . Based on the analysis of this sample, it can be said that a three phase equilibrium: $\tau_6 + \tau_7 + \text{Mg}_2\text{Y}(\delta)$ should exist in the Mg-Cu-Y system.

Similarly, sample 7 (53.2/16.6/30.2 Mg/Cu/Y at.%) which has lower Mg content than the previous one, shows that τ_3 (white) always remain within the τ_4 (grey) and never in contact with τ_7 (dark grey). Again, this is a typical behavior of peritectic type decomposition and τ_3 should decompose to τ_4 and $\text{Mg}_2\text{Y}(\delta)$. The effect is more pronounced in this case because τ_3 has a higher melting temperature with a larger

solidification region than τ_4 . This reflects the high thermal stability of τ_3 and its sluggish decomposition kinetics. Therefore, it is decided that τ_7 has a phase triangulation with τ_4 and $\text{Mg}_2\text{Y}(\delta)$ and no equilibrium relation with τ_3 .

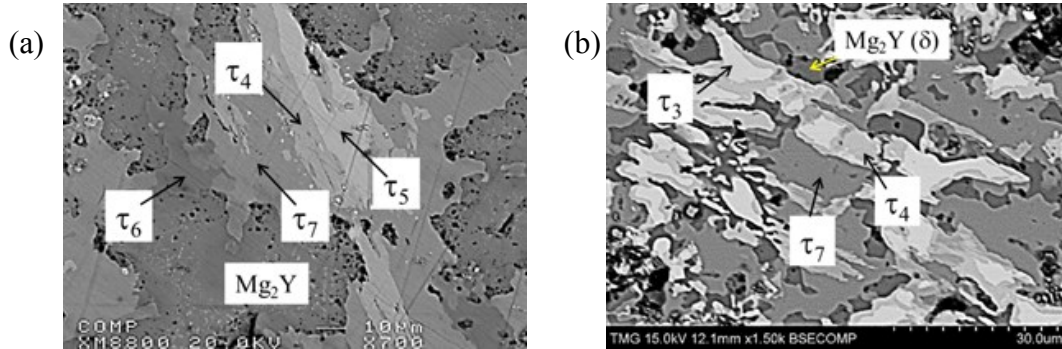


Figure 6-4: BSE image of (a) sample 6 (62.6/12.4/25.0 Mg/Cu/Y at.%); (b) sample 7 (53.2/16.6/30.2 Mg/Cu/Y at.%)

The solubility of Cu in $\text{MgY}(\gamma)$ and $\text{Mg}_2\text{Y}(\delta)$ has been found to be about 1 at.% which is within the error of WDS measurement. However, it is decided to accept this value since De Negri et al. [122], also reported the same amount of Cu solubility in $\text{MgY}(\gamma)$, $\text{Mg}_2\text{Y}(\delta)$ and $\text{Mg}_{24}\text{Y}_5(\epsilon)$. Also, the solubility of Y in MgCu_2 has been found to be about 6 at.%. Three of the ternary compounds τ_2 , τ_3 and τ_{11} have been found to have solubility ranges. $\tau_2(\text{MgCu}_4\text{Y})$ has been found with a homogeneity range $\sim 61.6\text{--}69.4$ at.% Cu, 16.6-22.3 at.% Mg and 13.4-16.3 at.% Y. For $\tau_3(\text{MgCu}_2\text{Y}_2)$, it has been found from ~ 38.4 to 40.7 at.% Cu and 38.2 to 41.5 at.% Y with respect to the stoichiometric formula. The solubility of τ_{11} has been found a little bit different than those of De Negri et al. [122]. Three key alloys (3-5) have been prepared in this region and all of them showed that the start of the solubility is from 84 at.% Mg which was reported as 82 at.% Mg earlier [122].

6.2 Comparison between experimental results and thermodynamic modeling

The phase equilibria of the Mg-Cu-Y system has been understood by combining the analysis of the key alloys in the present work with those reported by De Negri et al. [122]. Based on that, the thermodynamic modeling of the Mg-Cu-Y system has been modified. The isothermal section at 673 K calculated using the present model is shown in Figure 4-20. In-order to construct the liquidus surface, DSC experiments have been done on several key alloys. The present thermodynamic modeling will be compared with these results in this section.

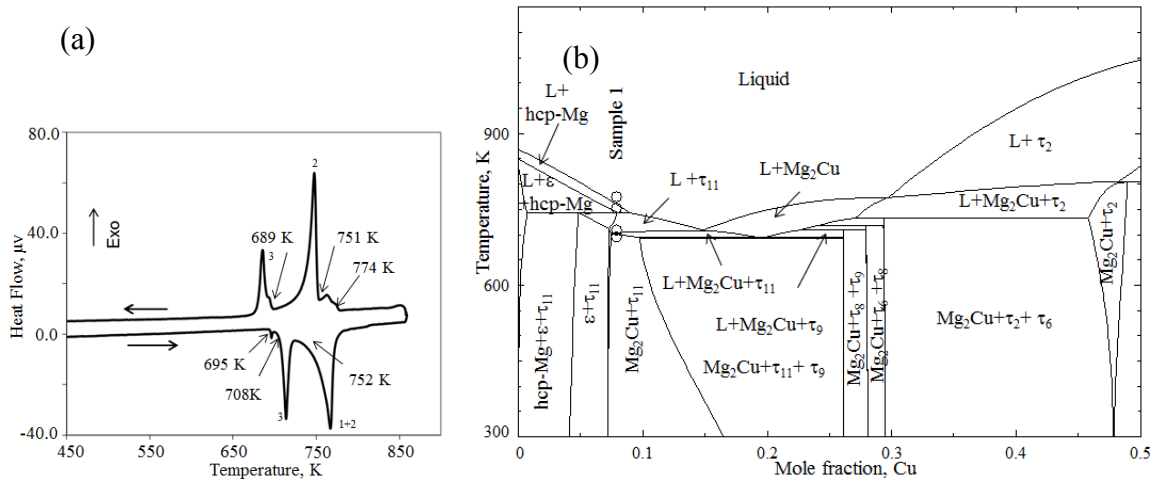


Figure 6-5: (a) DSC spectra; (b) the calculated vertical section at constant 7.2 at.% Y with DSC signals of sample 1 (84.9/7.9/7.2 Mg/Cu/Y at.%)

DSC spectra of sample 1 (84.9/7.9/7.2 Mg/Cu/Y at.%) with heating and cooling runs are shown in Figure 6-5 (a). This figure shows three peaks during heating and three peaks during cooling. However, during cooling the 1st and 3rd peaks have shoulders. Similar results were observed in all the three cooling cycles indicating that some of the peaks overlapped. The absence of a clean shoulder-free sharp peak during cooling indicates the sample did not melt congruently. The thermal arrest points observed during

cooling are at temperatures of 774 K, 751 K and 689 K. While during heating the peaks' temperatures are 752 K, 708 K and 695 K. The first two peaks during cooling were very close and they overlapped during heating cycle and were not distinguishable. The reason for this can be seen in the vertical section corresponding to the sample composition shown in Figure 6-5 (b). This figure shows that two phase transformations [L / L+hcp-Mg and L+hcp-Mg / L+ τ_{11}] occur within a narrow temperature range of less than 5 K (from 758 K to 755 K). Therefore, during heating these two peaks overlapped with the adjacent dominating peak. Also, areas under the curve between the first two cooling peaks (-144 J/g) and the first heating peak (154 J/g) are similar which confirms that the heating peak is in fact two overlapping peaks. Similar overlapping peaks have been observed for the 3rd peak in the cooling cycle. This is because of two very close phase transformations [L+ τ_{11} / L+ τ_{11} +Mg₂Cu and L+ τ_{11} +Mg₂Cu / τ_{11} +Mg₂Cu] in this region as can be seen in Figure 6-5 (b).

This sample is located in the two phase region of Mg₂Cu+ τ_{11} . The two phases can be clearly identified in the BSE image shown in Figure 6-6. The dark matrix is τ_{11} with plate like brighter Mg₂Cu phase. The phase constituents are summarized in Table 6-1. Negligible solubility of Y (0.31 at.%) has been found in Mg₂Cu.

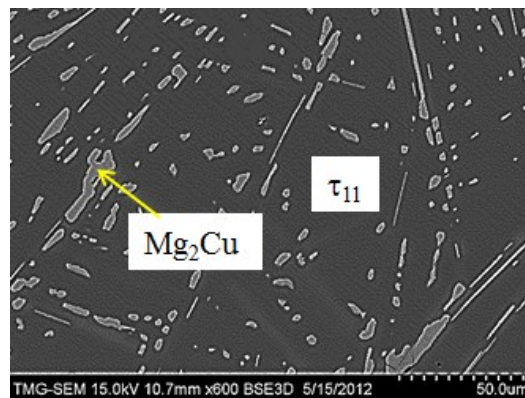


Figure 6-6: BSE image of sample 1 (84.9/7.9/7.2 Mg/Cu/Y at.%)

It has been observed from the literature survey that most of the promising glass forming alloys lie in the three-phase region of $\text{Mg}_2\text{Cu}+\text{Mg}_4\text{CuY}(\tau_9)+\text{Mg}_9\text{CuY}(\tau_{11})$. Therefore, 4 key samples (2-5) have been prepared in this 3-phase region in order to obtain better understanding of the solidification behavior as well as the phase relationships.

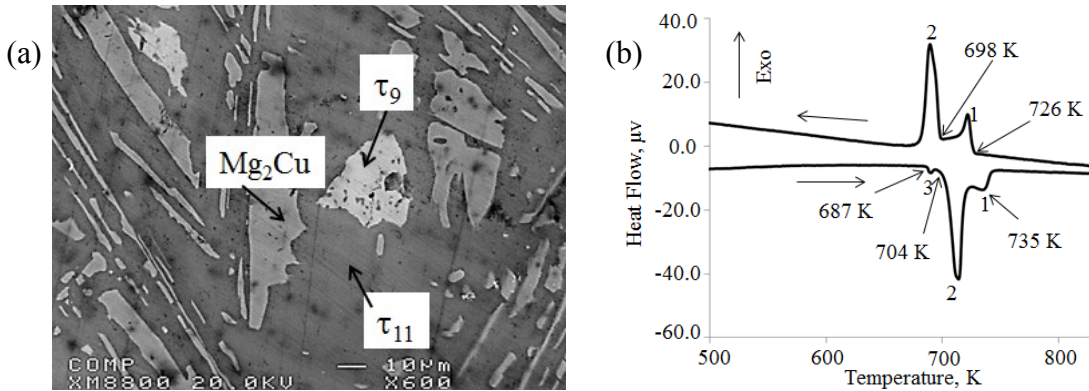


Figure 6-7: (a) BSE image; (b) DSC spectra of sample 2 (80.4/12.8/6.8 Mg/Cu/Y at.%)

The BSE image of sample 2 (80.4/12.8/6.8 Mg/Cu/Y at.%) in Figure 6-7 (a) shows the three-phase equilibrium between Mg_2Cu , τ_{11} and τ_9 . According to the WDS analysis listed in the Table 6-1, the matrix is τ_{11} which constitutes 84.7 at.% Mg, 7.1 at.% Cu and 8.2 at.% Y. The grey phase is the Mg_2Cu which dissolves negligible amount of Y (0.15 at%). Small amount of the white phase which is another ternary compound τ_9 , constitutes 68.6 at.% Mg, 16.1 at.% Cu and 15.3 at.% Y. The DSC heating and cooling curves of sample 2 are shown in Figure 6-7 (b). Two exotherms appear in the cooling curve at 726 and 698 K, which correspond to the endotherms that appear in the heating spectrum at 735 and 704 K. Another endothermic signal was revealed in the heating curve at 687K, but could not be identified in the cooling spectrum. The transformation

temperatures are very close to each other which lead to overlapping of two peaks during cooling. The liquidus temperature of this sample should be in between 726 and 735K.

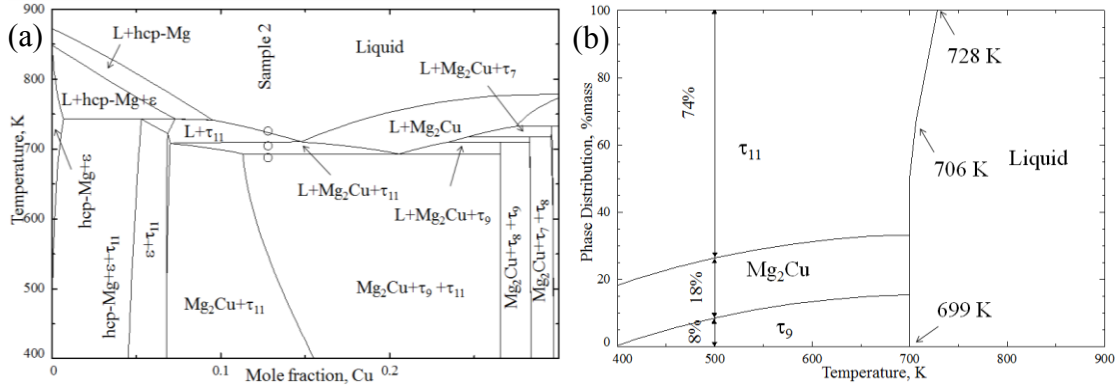


Figure 6-8: (a) vertical section at 6.8 at.% Y with DSC signals; (b) phase assemblage diagram of sample 2 (80.4/12.8/6.8 Mg/Cu/Y at.%)

Figure 6-8 (a) shows the calculated vertical section at constant 6.78 at.% Y with the DSC signals. The measured thermal arrests correspond to the following phase transformations in the vertical section: L / L+τ₁₁ / L+τ₁₁+Mg₂Cu / τ₁₁+Mg₂Cu+τ₉. The calculated liquidus temperature is found to be 728 K which agrees well with the DSC result as 735 K. Large amount of τ₁₁ forms as the sample is close to this compound. Figure 6-8 (b) shows the phase assemblage diagram of sample 2, where the relative mass versus temperature is calculated. The proportion of each phase at any temperature of interest can easily be interpreted from this diagram. For instance, at 500 K, 100 g of the overall material consists of 8 g of τ₉, 18 g of Mg₂Cu and 74 g of τ₁₁. Moreover, Figure 6-8 (b) shows that while cooling this sample from the melt, τ₁₁ solidifies first at 728 K, followed by Mg₂Cu at 706 K, and then τ₉ at 699 K. A comparison between the DSC thermal arrests and the thermodynamic calculations is presented in Table 6-2.

Table 6-2: Phase constituents by XRD/ WDS and DSC measurements and calculated transformation temperature of the investigated samples (h & c denotes heating & cooling)

Sample	Identified phases	DSC thermal signals, K	Thermodynamic calculation	
			Temp. K	Reaction or phase boundary
1	Mg ₂ Cu τ ₁₁	774c 751c/752h 689c/708h 695h	758 755 708 707	L / L+hcp-Mg L+hcp-Mg / L+τ ₁₁ L+τ ₁₁ / L+Mg ₂ Cu+τ ₁₁ L+Mg ₂ Cu+τ ₁₁ / Mg ₂ Cu+τ ₁₁
2	Mg ₂ Cu τ ₁₁ τ ₉	726c/735h 698c/704h 687h	728 706 699	L / L+τ ₁₁ L+τ ₁₁ / L+τ ₁₁ +Mg ₂ Cu L+τ ₁₁ +Mg ₂ Cu / τ ₁₁ +Mg ₂ Cu+τ ₉
3	Mg ₂ Cu τ ₁₁ τ ₉	769c/781h 736c/731h - 698c/702h 687c/694h	752 734 721 698 692	L / L+τ ₇ L+τ ₇ / L+τ ₈ L+τ ₈ / L+τ ₉ L+τ ₉ / L+τ ₉ +τ ₁₁ L+τ ₉ +τ ₁₁ / τ ₉ +τ ₁₁ +Mg ₂ Cu
4	Mg ₂ Cu τ ₁₁ τ ₉	796c/805h 779c/778h 761c - 717c/721h 695c/701h 692h	801 784 773 733 720 709 692	L / L+τ ₄ L+τ ₄ / L+τ ₅ L+τ ₅ / L+τ ₇ L+τ ₇ / L+τ ₈ L+τ ₈ / L+τ ₈ +τ ₉ L+τ ₈ +τ ₉ / L+τ ₉ +Mg ₂ Cu L+τ ₉ +Mg ₂ Cu / Mg ₂ Cu+τ ₉ +τ ₁₁
5	Mg ₂ Cu τ ₁₁ τ ₉	798c/798h 784c 781c 761c/772h - 714c 700c/707h 693h	789 784 777 765 734 721 696 692	L / L+τ ₄ L+τ ₄ / L+τ ₅ L+τ ₅ / L+τ ₆ +τ ₇ L+τ ₆ +τ ₇ / L+τ ₇ L+τ ₇ / L+τ ₈ L+τ ₈ / L+τ ₉ L+τ ₉ / L+τ ₉ +τ ₁₁ L+τ ₉ +τ ₁₁ / Mg ₂ Cu+τ ₉ +τ ₁₁
8	Mg ₂ Cu τ ₂ τ ₇	867c 793c/780h 720c/724h	915 785 732	L / L+τ ₂ L+τ ₂ / L+τ ₂ +Mg ₂ Cu L+τ ₂ +Mg ₂ Cu / τ ₂ +Mg ₂ Cu+τ ₇
11	Mg ₂ Cu τ ₂ MgCu ₂	1075c/1075h 1046c/1038h 733c/742h	1081 1025 802	L / L+τ ₂ L+τ ₂ / L+τ ₂ +MgCu ₂ L+τ ₂ +MgCu ₂ / τ ₂ +MgCu ₂ +Mg ₂ Cu
13	Cu-fcc τ ₁ MgCu ₂	1028c/1040h 1012c/1001h 989c/991h	1027 1010 985	L / L+τ ₁ L+τ ₁ / L+τ ₁ +Cu-fcc L+τ ₁ +Cu-fcc / τ ₁ +MgCu ₂ +Cu-fcc
15	τ ₂ Cu ₂ Y	1119c/1112h 1043c 996c/998h	1066 1040 992	L / L+Cu ₂ Y L+ Cu ₂ Y / L+ Cu ₂ Y+CuY L+ Cu ₂ Y+CuY / L+ Cu ₂ Y+ τ ₂
18	Cu-fcc Cu ₆ Y τ ₁	1263c/1256h 1126c/1101h 1015c/1022h	1239 1099 1009	L / L+Cu-fcc L+Cu-fcc / L+Cu-fcc+Cu ₆ Y L+Cu-fcc+Cu ₆ Y / Cu-fcc+Cu ₆ Y+ τ ₁

The next alloy in the $\text{Mg}_2\text{Cu}+\text{Mg}_4\text{CuY}(\tau_9)+\text{Mg}_{9-18}\text{CuY}(\tau_{11})$ three-phase region is sample 3 (70.5/15.3/14.2 Mg/Cu/Y at.%). The BSE image, in Figure 6-9 (a) clearly shows the existence of the two ternary compounds τ_9 and τ_{11} along with Mg_2Cu . The WDS analysis of these phases is listed in Table 6-1. The composition of τ_9 (68.9/15.9/15.2 Mg/Cu/Y at.%) and τ_{11} (85.0/7.0/8.0 Mg/Cu/Y at.%) in this alloy are very similar to those found in sample 2. This shows the repeatability and accuracy of the measurement.

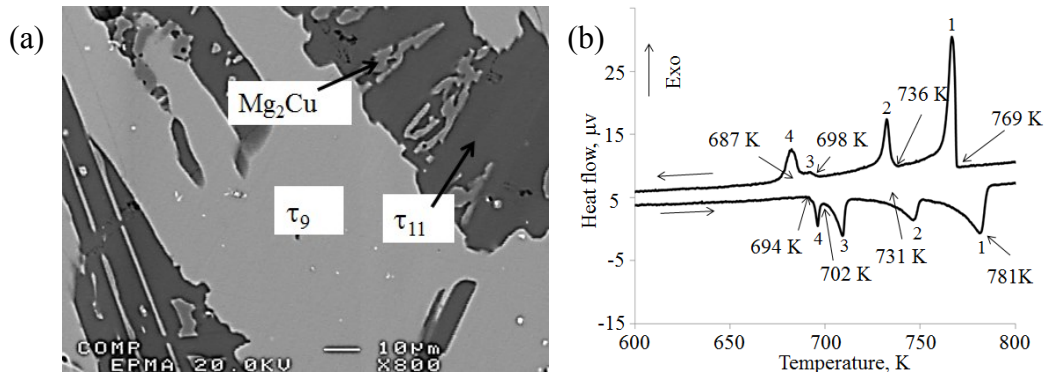


Figure 6-9: (a) BSE image; (b) DSC spectra of sample 3 (70.5/15.3/14.2 Mg/Cu/Y at.%)

The DSC spectra of sample 3 during heating and cooling are shown in Figure 6-9 (b). Four thermal events during heating as well as cooling could be identified. The liquidus temperature was identified as 781 K during heating and 769 K during cooling. The thermal arrests are projected on the vertical section drawn at 70.50 at.% Mg in Figure 6-10 (a) which shows reasonable agreement. According to the thermodynamic calculation, the liquidus temperature is 752 K where the precipitation of τ_7 starts. The next thermal arrest is due to the reaction: $L+\tau_7 / L+\tau_8$, which occurs at 734 K compared to the DSC signal at 736 K. Later τ_8 dissolves more Mg to obtain the stable τ_9 phase according to the transformation: $L+\tau_8 / L+\tau_9$. Thermodynamic calculation shows that this transformation takes place at 721 K. But a clear thermal peak for this reaction could not

be identified in the DSC spectra. However, the 2nd thermal event both in heating and cooling show a long tail which is probably due to the overlapping of two consecutive peaks and was not separable. Over time τ_9 , grows consuming about 78% of the liquid as can be seen in the phase assemblage diagram in Figure 6-10 (b). Different shades have been used to identify the different phase amounts clearly. It can be seen that at 721 K, τ_9 starts to precipitate forming 50% of the alloy. Then at 698 and 692 K the remaining liquid transformed to τ_{11} and Mg_2Cu , respectively. The growth of τ_9 continues until the precipitation of τ_{11} starts.

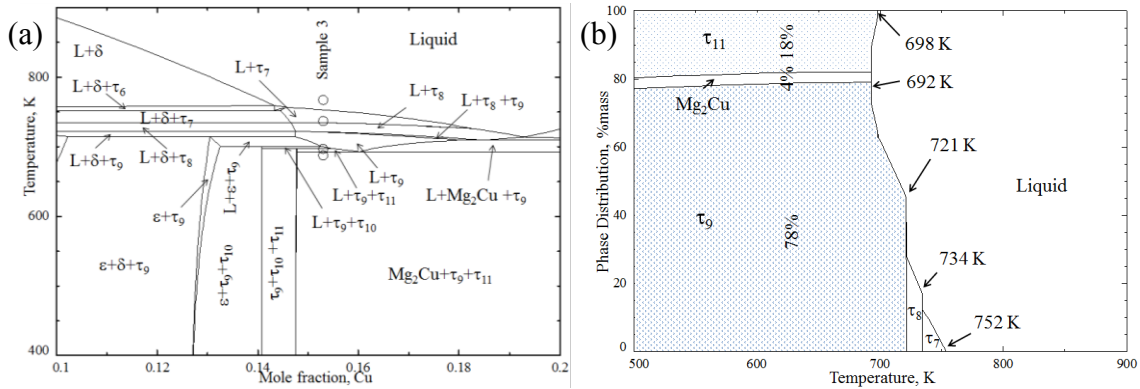


Figure 6-10: (a) vertical section at 70.5 at.% Mg; (b) phase assemblage diagram of sample 3 (70.5/15.3/14.2 Mg/Cu/Y at.%)

The last two samples (4 and 5) in the $Mg_2Cu+Mg_4CuY(\tau_9)+Mg_9CuY(\tau_{11})$ phase field are located very close to the ternary compound τ_9 . The BSE images of both samples in Figure 6-11 (a and b) clearly show the three phases with massive amount of τ_9 . The WDS analysis of these alloys is listed in Table 6-1. The growth of τ_9 with the decrease of Mg content from 70.5 at.% to about 66.7 at.% can be understood by comparing these two alloys in Figure 6-11 (a) and (b) with the previous alloy (sample 3) in Figure 6-9 (a). It can be seen that the amount of Mg_2Cu remains almost the same in both cases. The amount of τ_9 increased from $\sim 70\%$ to $\sim 95\%$ in samples 4 and 5 whereas the amount of τ_{11}

decreased significantly. The nature of phase growth of τ_9 and τ_{11} determines the solidification behavior of the alloys in this region. By comparing the four alloys (2-5), it can be said that for any alloy containing more than ~ 75 at.% Mg with approximately equal amount of Cu and Y, τ_{11} will be dominant. This also reflects the boundary of the primary precipitation field of τ_{11} .

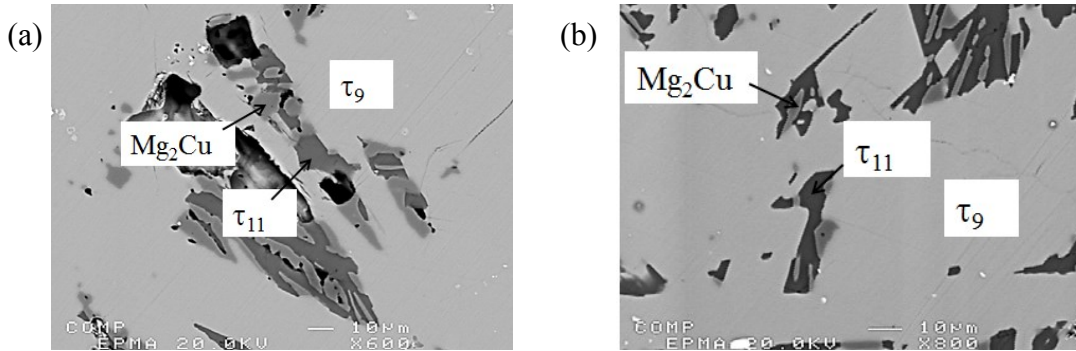


Figure 6-11: BSE image of (a) sample 4 (67.5/16.4/16.1 Mg/Cu/Y at.%); (b) BSE image of sample 5 (66.7/17.3/16.0 Mg/Cu/Y at.%)

The DSC spectra of these two alloys (4 and 5) are shown in Figure 6-12 (a) and (b). The presence of several thermal arrests suggests the occurrence of a rather complicated melting behavior. In order to identify the phase transformations more accurately, these two samples have been prepared close to each other. Two vertical sections at 66.7 at.% and 67.5 at.% Mg have been constructed as shown in Figure 6-12 (c and d) with the DSC arrests of samples 4 and 5, respectively. The complexity arises because of the presence of six ternary compounds (τ_4 to τ_9) in close proximity. All these compounds are incongruent and decompose in a narrow temperature range as can be seen in the corresponding vertical sections. However, an effort has been made to separate these thermal events according to the equilibrium phase transformation which is listed in Table 6-2. The experimental and thermodynamic calculation show reasonable agreement.

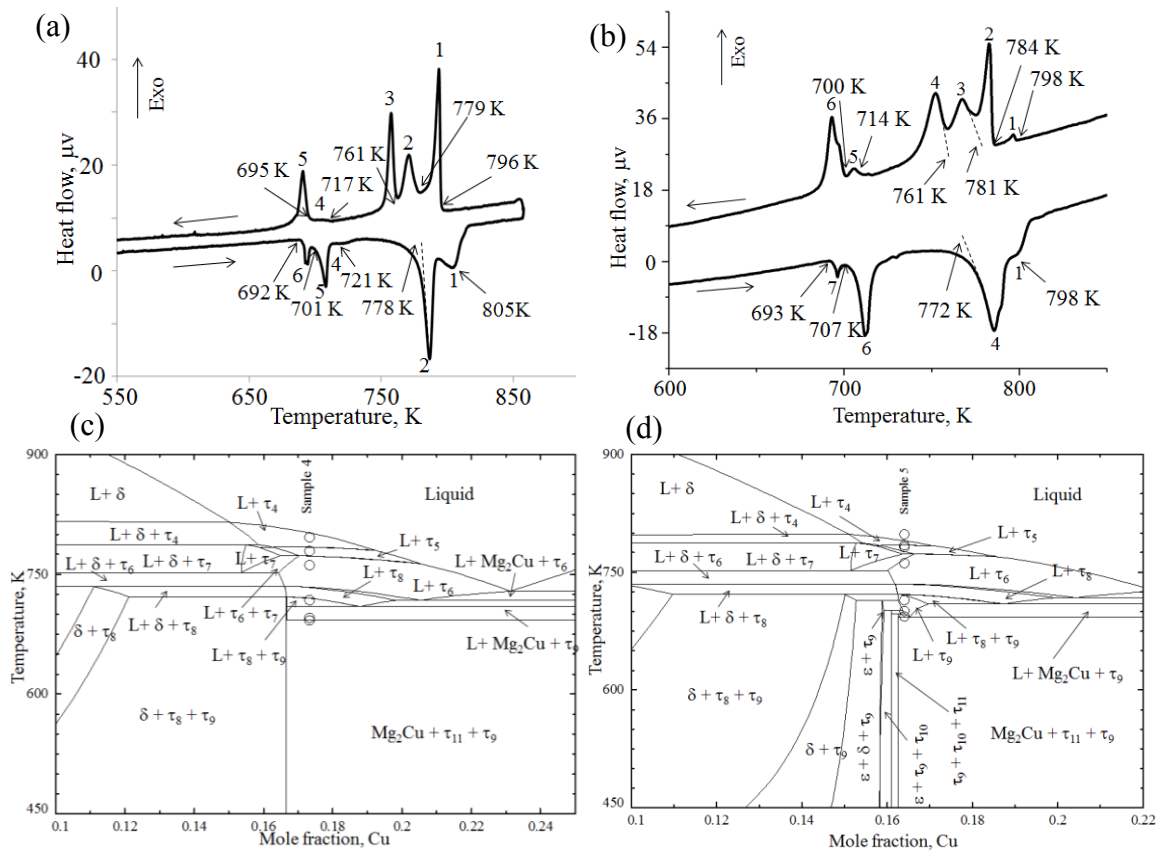


Figure 6-12: (a) DSC spectra of sample 4; (b) DSC spectra of sample 5; (c) vertical section at 66.7 at.% Mg; (d) vertical section at constant 67.5 at.% Mg

One of the criteria for BMG forming alloys is to create chaos where confusion is generated by adding several elements in the alloy to have a sluggish equilibrium [6, 166]. It can be seen in these vertical sections that several phase transformations occur in a relatively narrow temperature range which unsettle the alloys and prevent equilibrium. This slows the kinetics and produces a desirable condition for metallic glass.

Sample 8 (55.6/36.9/7.5 Mg/Cu/Y at.%) is located in the three-phase region of Mg_2Cu , τ_2 and τ_7 . The SEM image and XRD pattern in Figure 6-13 (a) and (b) clearly shows these three phases. The WDS analysis of these phases is listed in Table 6-1. The solubility of Mg in τ_2 has been found to be ~ 22.3 at.% which is close to that of De Negri et al. [122] who reported ~ 24.0 at.%. The present thermodynamic modeling shows this

solubility at 673 K to be 19.6 at.% Mg. The solubility of the compounds, MgCu_2 , τ_2 (MgCu_4Y) and Cu_2Y are related because they are located close to each other along the 66.7 at.% Cu line. A larger solubility for τ_2 will reduce the same for MgCu_2 and Cu_2Y . Hence, an optimum solubility for these three compounds has been obtained which deviates of about 2.7 at.% from the current experimental results. The Y solubility in Mg_2Cu is negligible. The third phase in this sample is τ_7 which can be seen as a network of the grey phase in the SEM image.

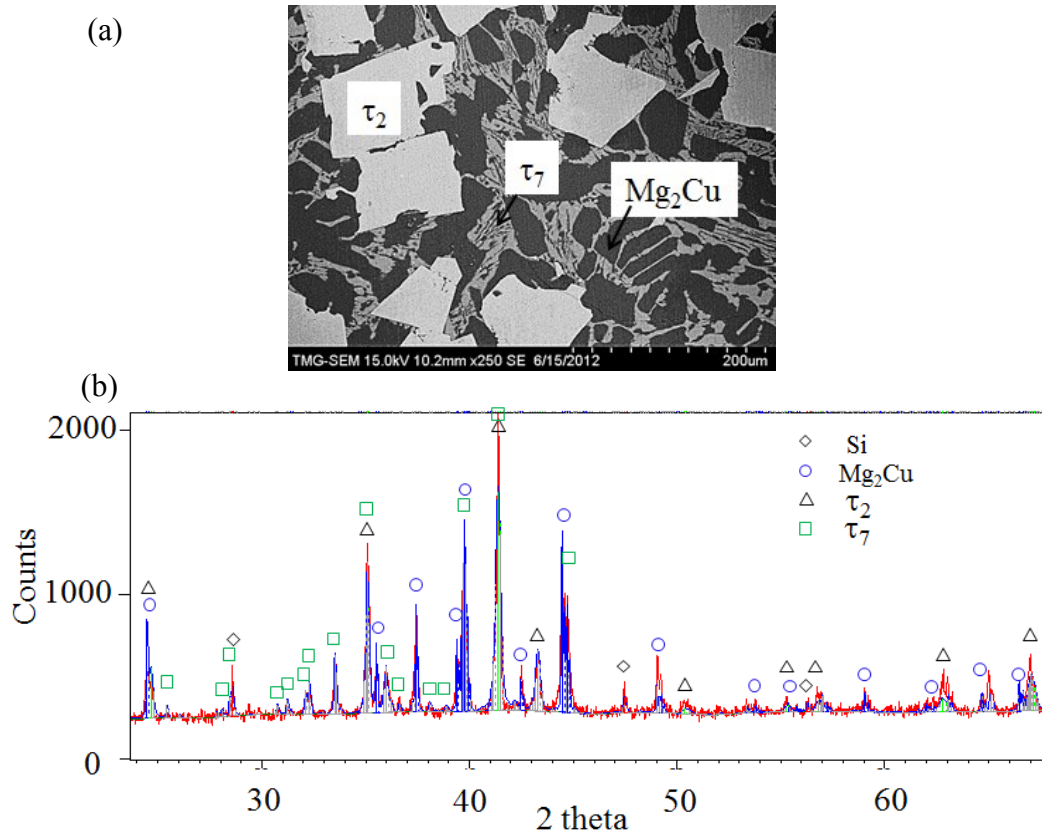


Figure 6-13: (a) BSE image; (b) XRD pattern of sample 8 (55.6/36.9/7.5 Mg/Cu/Y at.%)

The DSC spectra during cooling and heating for sample 8 are shown in Figure 6-14 (a). Three thermal events are observed and they have been projected on the vertical section calculated at 7.5 at.% Y in Figure 6-14 (b). The predicted phase transformation

temperatures are in accord with the DSC measurements. The liquidus temperature is clearly observed during cooling at 867 K compared to the prediction from thermodynamic calculations as 905 K. The other two thermal arrests are observed at 793 and 720 K during cooling and 780 and 724 K during heating. These two events occurred due to the phase transformation: $L+\tau_2 / L+\tau_2+\text{Mg}_2\text{Cu} / \tau_2+\text{Mg}_2\text{Cu} + \tau_7$. The experimental measurements agree well with the thermodynamic calculation which showed the transformation temperatures at 785 and 731 K, respectively.

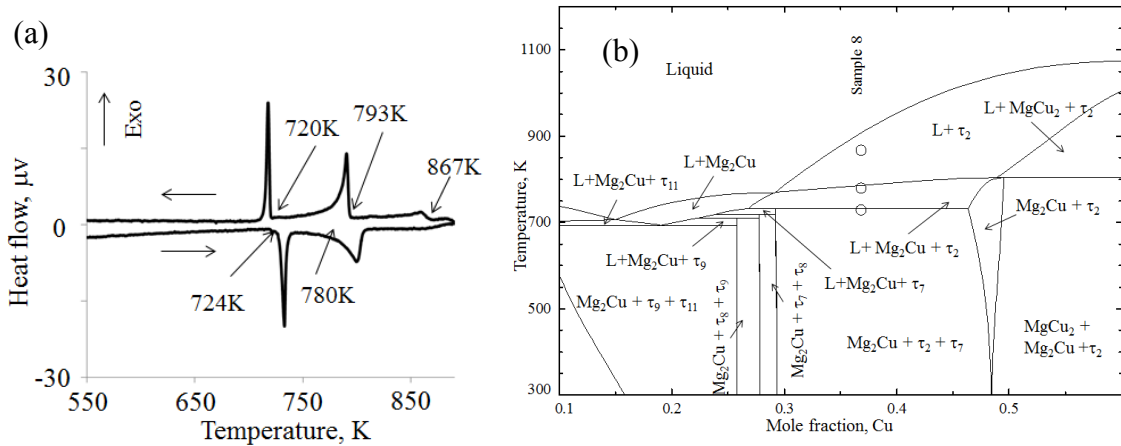


Figure 6-14: (a) DSC spectra; (b) the calculated vertical section at constant 7.52 at.% Y with DSC signals of sample 8 (55.6/36.9/7.5 Mg/Cu/Y at.%)

Sample 9 (37.8/17.2/45.0 Mg/Cu/Y at.%) is located in the $\text{MgY}(\gamma)+\tau_3$ two-phase region as shown in Figure 5-1. DSC spectra of this sample during heating and cooling runs are shown in Figure 6-15 (a). Three peaks occurred during heating at 1033, 991 and 976 K that were encountered at 1033, 980 and 976 K during cooling. It should be noted that the second peak both in heating and cooling overlapped with the third peak because of close transformation temperatures. These transformation temperatures are correlated to the calculated vertical section at 17.16 at.% Cu in Figure 6-15 (b). The predicted temperatures are in very good agreement with the measurement.

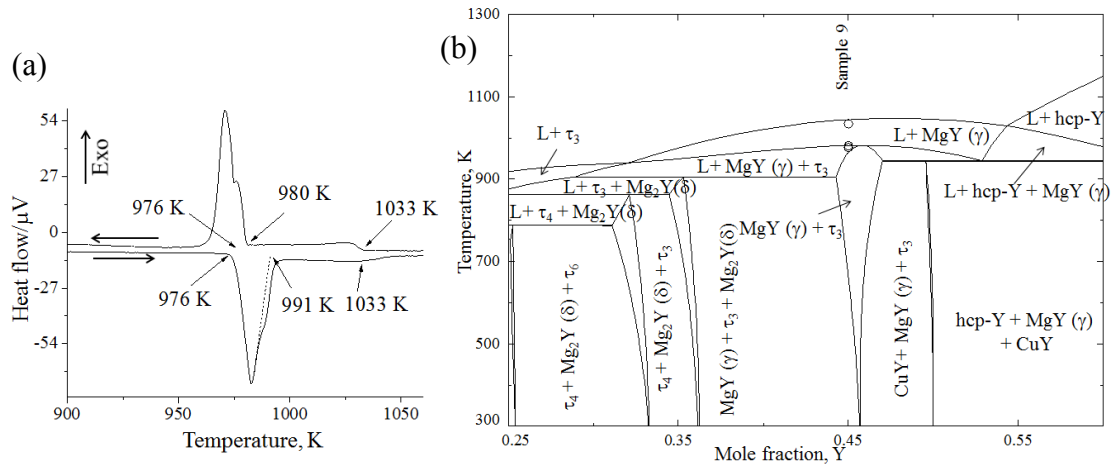


Figure 6-15: (a) DSC spectra; (b) vertical section at 17.16 at.% Cu with DSC signals of sample 9 (37.84/17.16/45.00 Mg/Cu/Y at.%)

Two phases, namely $\text{MgY}(\gamma)$ and τ_3 , are observed in the SEM image of sample 9 as can be seen in Figure 6-16 (a). The matrix, $\text{MgY}(\gamma)$, indicates that this alloy is located in the $\text{MgY}(\gamma)$ crystallization field. XRD pattern of this sample in Figure 6-16 (b) shows clearly the existence of $\text{MgY}(\gamma)$ and τ_3 which is in agreement with the WDS analysis.

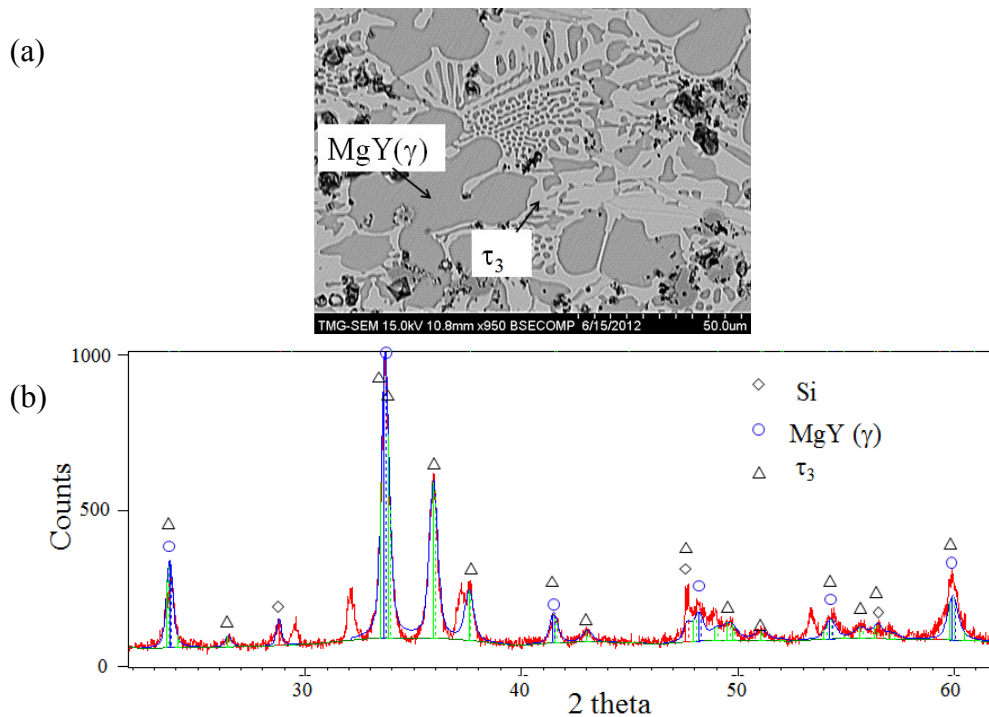


Figure 6-16: (a) BSE image; (b) XRD pattern of sample 9 (37.8/17.2/45.0 Mg/Cu/Y at.%)

Sample 11 (28.0/63.3/8.7 Mg/Cu/Y at.%) is located in the three-phase region of $\text{Mg}_2\text{Cu} + \text{MgCu}_4\text{Y}(\tau_2) + \text{MgCu}_2$ as can be seen in Figure 5-1. Several amorphous alloys have been reported [124] in this region as demonstrated in Figure 2-2 (a). The BSE image in Figure 6-17 (a) and WDS results in Table 6-1 show the 3-phase relationship among MgCu_2 , Mg_2Cu and τ_2 . The dominating phase is τ_2 as the sample composition is near it. The solubility of Y in the MgCu_2 phase has been found to be about 6.0 at.% which is in agreement with those of De Negri et al. [122] who reported about 5 at.%.

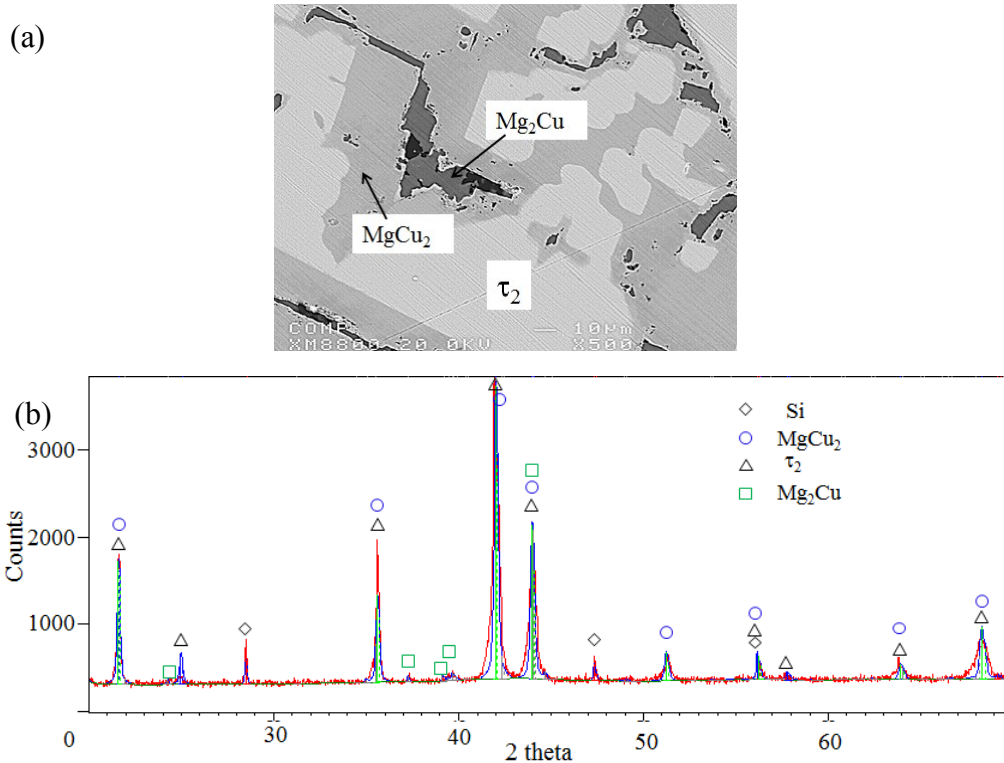


Figure 6-17: (a) BSE image; (b) XRD pattern of sample 11 (28.0/63.3/8.7 Mg/Cu/Y at.%)

The XRD pattern of sample 11 in Figure 6-17 (b) positively identified the three phases. The relative mass fractions of the phases, from Rietveld analysis, are 68% τ_2 , 26% MgCu_2 and 6% Mg_2Cu which is in agreement with the thermodynamic prediction as can be seen in the phase assemblage diagram in Figure 6-18 (a). The DSC spectra in

Figure 6-18 (b) show three thermal events during cooling as well as heating. According to the cooling signal the liquidus temperature is 1075 K which agrees well with the thermodynamic calculation of 1081 K where the precipitation of τ_2 starts. The next transformation occurs at 1046 K (cooling) according to the reaction $L+\tau_2 / L+\tau_2+\text{MgCu}_2$. The last thermal event is due to the precipitation of the Mg_2Cu . This signal is very weak because of the small amount of Mg_2Cu . According to the phase assemblage diagram, only 6 wt.% of the sample is Mg_2Cu . The DSC signals have been projected on the 8.7 at.% Y vertical section in Figure 6-18 (c) which shows good agreement.

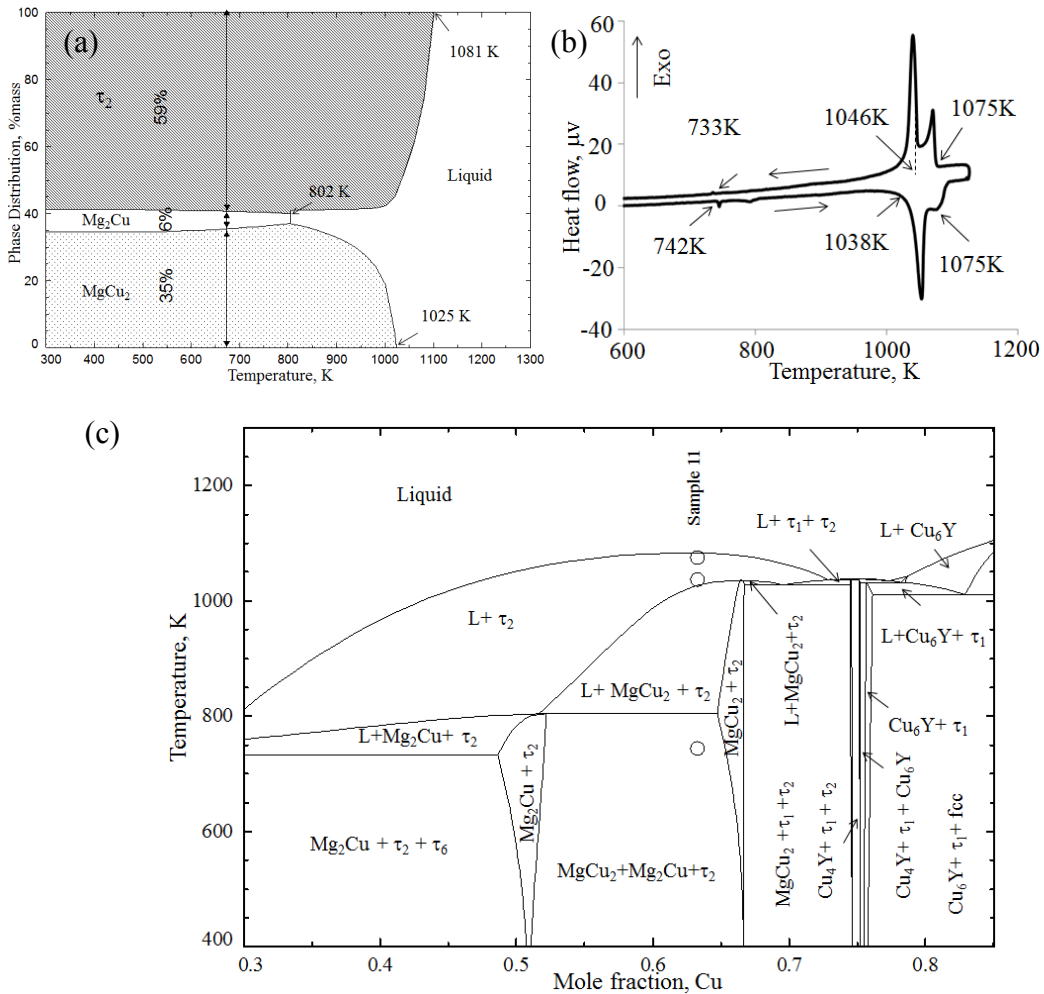


Figure 6-18: (a) phase assemblage diagram; (b) DSC spectra; (c) vertical section at 8.74 at.% Y with DSC signals of sample 11 (28.0/63.3/8.7 Mg/Cu/Y at.%)

Sample 12 (18.5/74.1/7.4 Mg/Cu/Y at.%) is located in the two phase region of $\text{MgCu}_2+\tau_1$. The WDS measurements for this alloy are listed in Table 6-1. No DSC experiment is done on this sample. Sample 13 (16.9/77.3/5.8 Mg/Cu/Y at.%) is located in the three phase region of $\text{MgCu}_2+\tau_1+\text{fcc}$. The BSE image and XRD pattern in Figure 6-19 (a) and (b) positively showed these phases. The MgCu_2 phase has been found in two different grey shades as can be seen in Figure 6-19 (a). This reflects the ternary solubility of Y in MgCu_2 . WDS analysis shows the compositions range of this compound as: 33.0/65.5/1.5 and 25.0/69.8/5.2 Mg/Cu/Y at.%. This is in agreement with De Negri et al. [122] who reported about 5 at.% Y solubility in MgCu_2 .

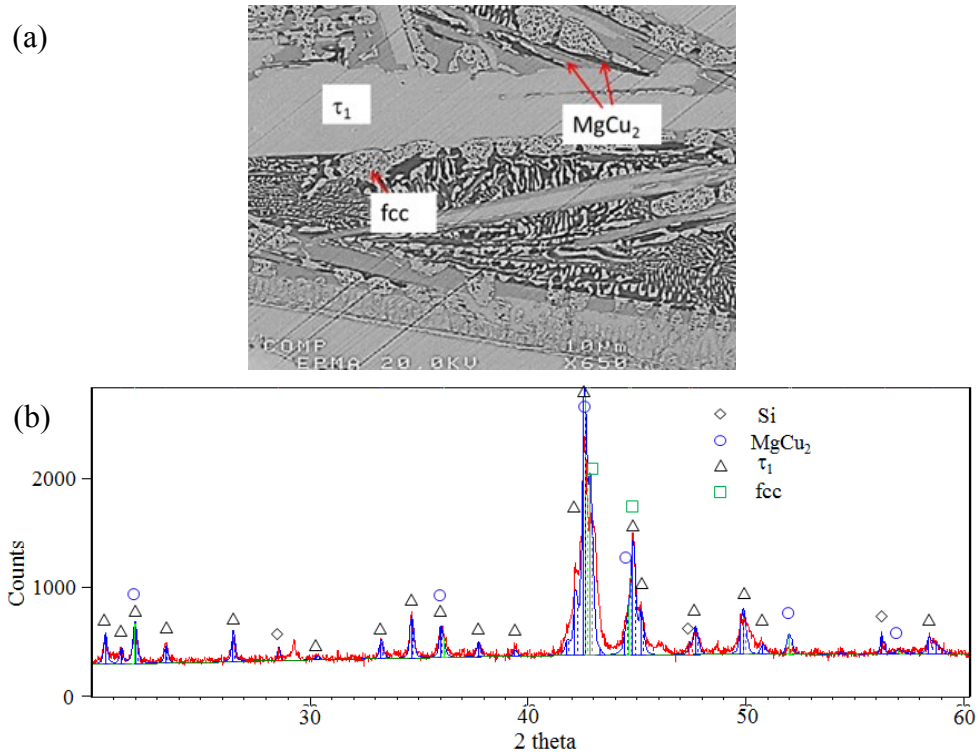


Figure 6-19: (a) BSE image; (b) XRD pattern of sample 13 (16.9/77.3/5.8 Mg/Cu/Y at.%)

The phase assemblage diagram of this alloy has been calculated using the present thermodynamic model as shown in Figure 6-20. According to the calculation the microstructure of this alloy should contain about 70% τ_1 , 13% MgCu_2 and 17% fcc

phase. This is in reasonable agreement with the relative mass fractions of the phases, resulting from Rietveld analysis; 63% τ_1 , 14% MgCu_2 and 23% fcc.

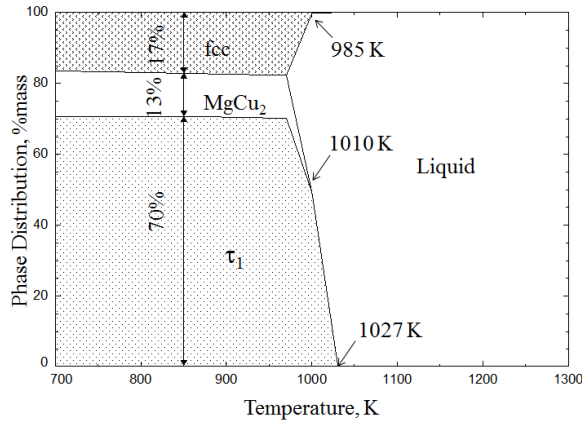


Figure 6-20: Phase assemblage diagram of sample 13 (16.9/77.3/5.8 Mg/Cu/Y at.%)

The DSC spectra of sample 13 during heating and cooling events are shown in Figure 6-21 (a). Three exothermic peaks appear in the cooling curve at 1028, 1012 and 989 K which correspond to the endothermic peaks measured from the heating spectrum as 1040, 1001 and 991 K. A vertical section has been constructed at 5.8 at.% Y as shown in Figure 6-21 (b). Good agreement with the DSC thermal events can be observed. Detailed comparison with the thermodynamic prediction has been given in Table 6-2

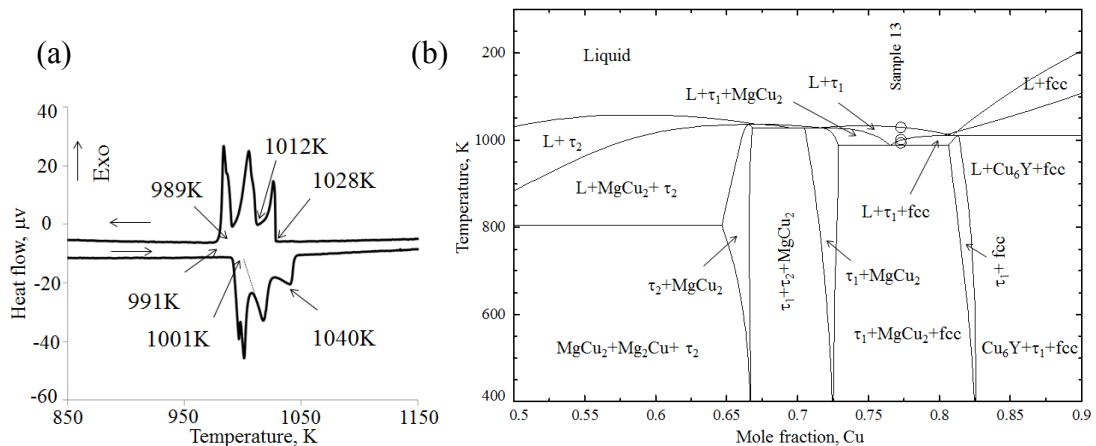


Figure 6-21: (a) phase assemblage diagram; (b) DSC spectra; (c) vertical section at constant 5.82 at.% Y with DSC signals of sample 13 (16.9/77.3/5.8 Mg/Cu/Y at.%)

Only two (15 and 18) out of the six Cu-rich (14-19) samples have been chosen for DSC measurements, as they provide sufficient information to verify the thermodynamic modeling of this part of the Mg-Cu-Y system. The DSC thermal arrests of Sample 15 (7.6/57.4/35.0 Mg/Cu/Y at.%) show reasonable agreement with the current calculations as demonstrated in Table 6-2.

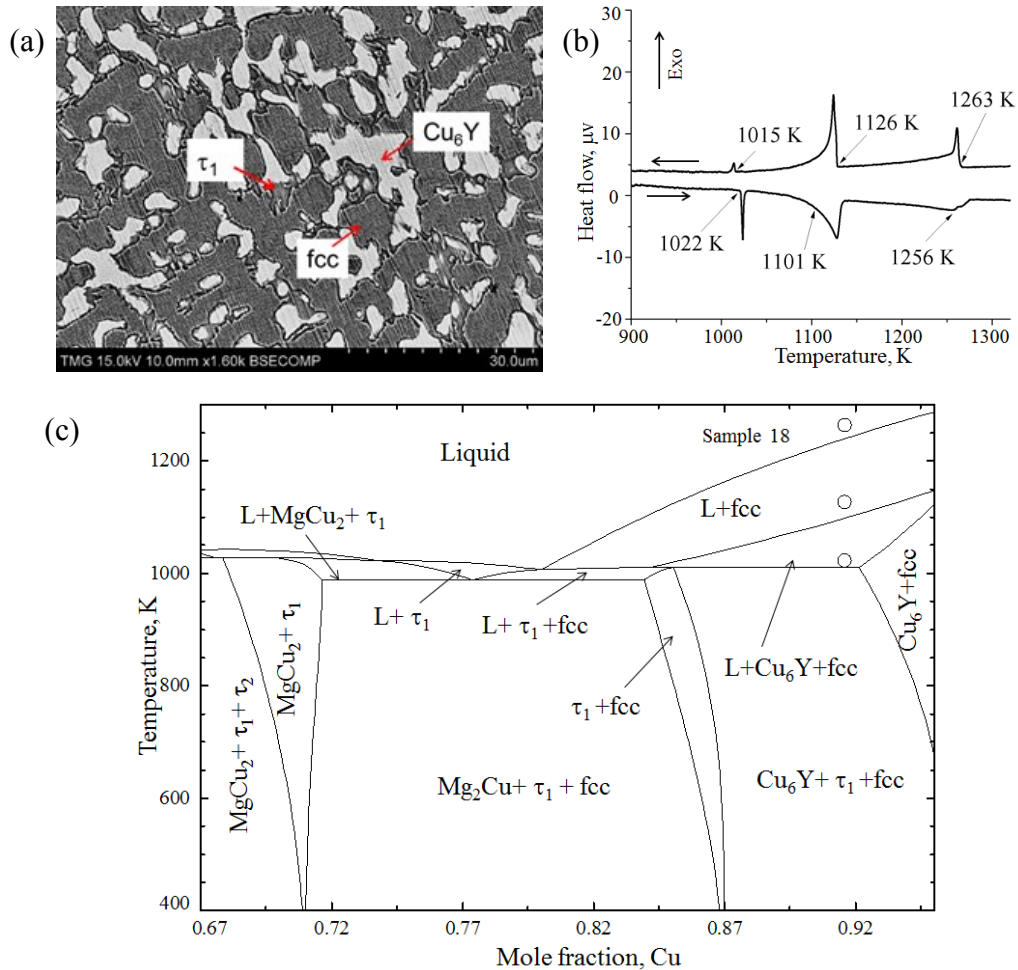


Figure 6-22: (a) BSE image; (b) DSC spectra; (c) vertical section at 4.3 at.% Y with DSC signals of sample 18 (4.1/91.6/4.3 Mg/Cu/Y at.%)

Sample 18 (4.1/91.6/4.3 Mg/Cu/Y at.%) is located in the fcc, Cu_6Y and τ_1 phase field as shown in Figure 5-1. The BSE image in Figure 6-22 (a) shows the three phases. The DSC spectra in Figure 6-22 (b), show three thermal arrests in heating as well as

cooling. The heating signals: 1256, 1101 and 1022 K correspond well with the cooling signals: 1263, 1126 and 1015 K, respectively. These are projected on the 4.3 at.% Y vertical section in Figure 6-22 (c) which shows reasonable agreement. The measured thermal arrests correspond to the following phase transformations in the vertical section: $L / L+\text{fcc} / L+\text{fcc}+\text{Cu}_6\text{Y} / \tau_1+\text{fcc}+\text{Cu}_6\text{Y}$.

The location of this alloy is on the slope of a steep liquidus surface as can be seen in Figure 6-22 (c). This liquidus is going towards a deep eutectic and generates a possible glass forming zone. This explains the availability of several fully amorphous alloys (Figure 2-2) near this region.

6.3 Analysis of some important glass forming alloys

Inoue et al. [3] reported $\text{Mg}_{65}\text{Cu}_{25}\text{Y}_{10}$ to be the most favorable composition for glass formation. They used conventional mold casting and could produce samples up to 4 mm in diameter. They also referred to this composition as eutectic. Latter Ma et al. [11, 12] reported that they found $\text{Mg}_{58}\text{Cu}_{30.5}\text{Y}_{11.5}$ and $\text{Mg}_{58.5}\text{Cu}_{30.5}\text{Y}_{11.0}$ compositions which show higher glass forming ability. They produced fully amorphous samples of upto 9 mm diameter. However, they found these compositions little bit away from the eutectic point. Therefore, they suggested that the optimum glass forming alloys should be found at off-eutectic locations. Satta et al. [166] investigated the $\text{Mg}_{65}\text{Cu}_{25}\text{Y}_{10}$ alloy and compared their results with preliminary thermodynamic understanding of the ternary system. To obtain equilibrium state they annealed the amorphous alloy at 713 K for two weeks. But during annealing the sample lost 4 at.% Mg and obtain a final composition of $\text{Mg}_{61}\text{Cu}_{29}\text{Y}_{10}$. They recognized three different phases in the sample but only could

identify Mg_2Cu in the XRD pattern. According to their EDS analysis these two phases have compositions of 60/23/17 and 65/20/15 Mg/Cu/Y at.%. Based on the current work, it can be said that these two phases are τ_7 and τ_8 , respectively. Both Ma et al. [12] and Satta et al. [166] used DSC experiments to identify the liquidus and solidus temperatures of the amorphous alloys. These measurements were done at relatively high heating rate of 20 K/min and mostly on non-equilibrium samples. Also, the reproducibility of these measurements was not confirmed. Therefore these results were not considered during the optimization but will be compared with the current calculation. A vertical section at 10 at.% Y is presented in Figure 6-23 with the DSC measurements of Ma et al. [12] and Satta et al. [166] which shows good agreement. According to Ma et al. [11, 12] the best glass forming alloys should be found at an off-eutectic composition which is not far from the deep eutectic point. Considering this and observing the vertical section in Figure 6-23 it can be said that alloys with 10 at.% Y and 10 to 20 at.% Cu are good candidate for metallic glass.

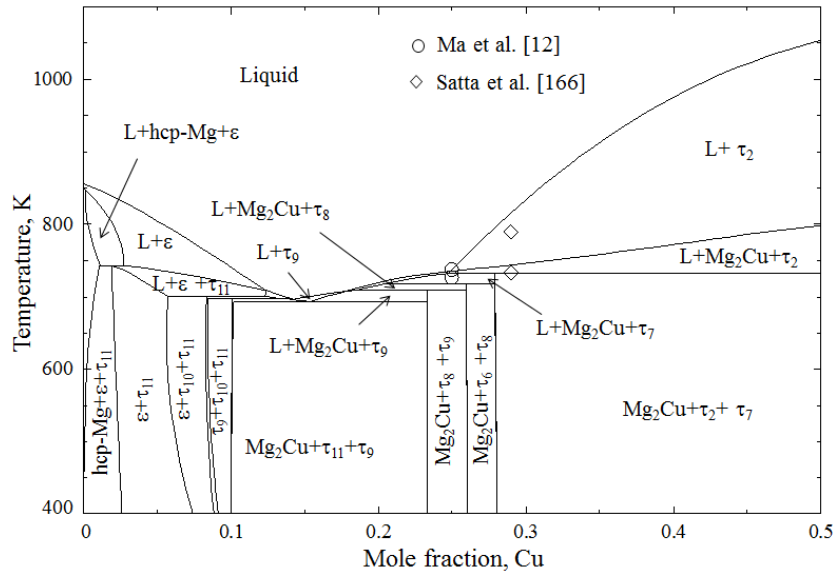


Figure 6-23: Vertical section at constant 10% Y with DSC results from the literature [12, 166]

Chapter 7

Experimental Investigation of the Mg-Ni-Y System

The Mg-Ni-Y system needed significant effort as little experimental work has been done to construct the phase relationships prior to this work. Three solid-solid and two solid-liquid diffusion couples have been used to discover new ternary intermetallic compounds and to understand the equilibrium phases. The analysis of the diffusion couples is done in section 7.1. Then 32 key alloys have been used to confirm these ternary compounds as well as to construct the phase diagram using WDS and XRD analysis. The phase relationships in the Mg-Ni-Y system are very complex due to the presence of 12 intermetallic compounds. Therefore, an extensive analysis of the key alloys has been done in section 7.2. DSC experiments have been conducted on some of the key alloys to calibrate the liquidus surface. The present thermodynamic modeling will be compared with the DSC measurements in section 7.3.

7.1 Diffusion couple analysis

7.1.1 Solid-Solid diffusion couple 1

Backscatter electron (BSE) images of the solid-solid diffusion couple 1 has been shown in Figure 7-1 (a) and (b) with gradual magnification. This diffusion couple has been performed between Mg and sample 20 (18.5/22.4/59.1 Mg/Ni/Y at.%) as shown in Figure 5-2. The ternary alloy consists of three phases: NiY, $\tau_1(\text{MgNiY}_4)$ and $\tau_5(\text{Mg}_{29}\text{Ni}_{20}\text{Y}_{42})$. These end members have been chosen in order to identify the intermetallic compounds located in the Mg-Y side of the Gibbs triangle.

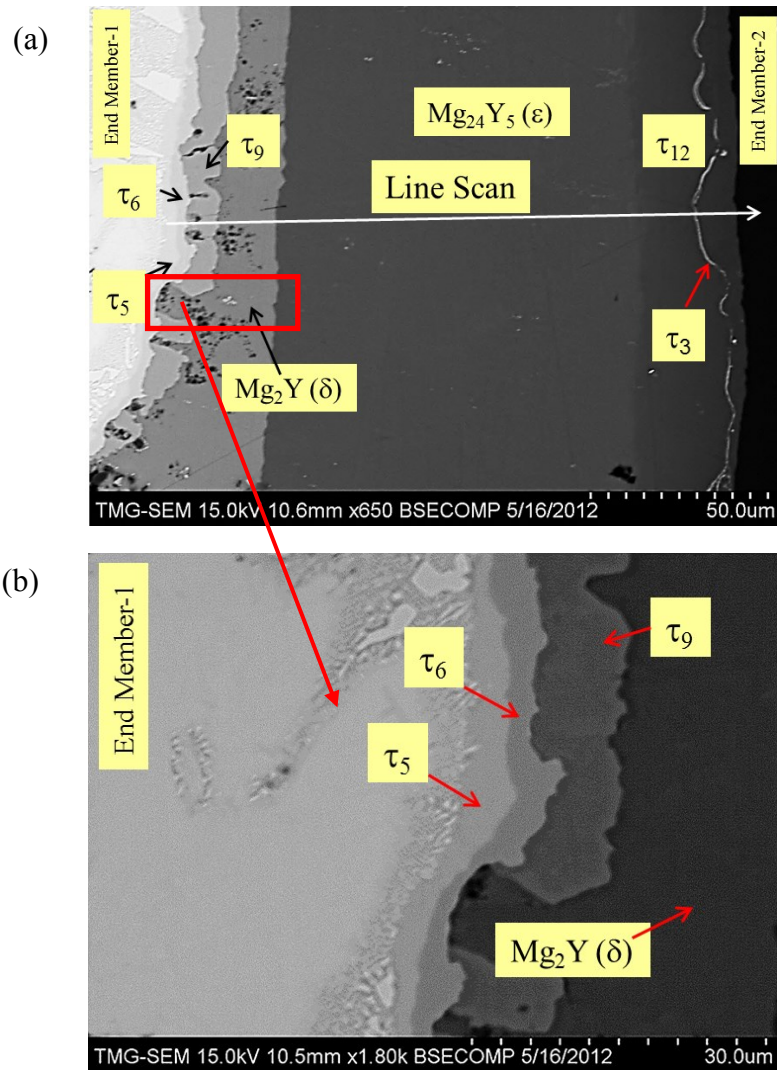


Figure 7-1: (a) Solid-solid diffusion couple of Mg - sample 20 (18.5/22.4/59.1 Mg/Ni/Y at.%) annealed at 673 K for 4 weeks (b)magnified area of interest of the diffusion zone

The diffusion couple has been annealed for 4 weeks at 673 K. During the heat treatment, extensive inter diffusion among Mg, Ni and Y took place allowing various equilibrium phases to form. Each layer represents a phase which is in equilibrium with its adjacent layers. The diffusion path through the entire system is shown in Figure 7-2 (a). The composition profile as shown in Figure 7-2 (b) explains the configuration of these layers and has been used to distinguish each layer. By taking advantage of the local

equilibrium at the interfaces formed between the layers, the sequence of phases along the diffusion path can be deduced as:

$\{\text{NiY}+\tau_1+\tau_5\}$ (end-member) $\rightarrow \tau_5 \rightarrow \tau_5+\tau_6 \rightarrow \tau_6 \rightarrow \tau_6+\tau_9 \rightarrow \tau_9 \rightarrow \tau_9+\text{Mg}_2\text{Y}(\delta) \rightarrow \text{Mg}_2\text{Y}(\delta) \rightarrow \text{Mg}_2\text{Y}(\delta)+\text{Mg}_{24}\text{Y}_5(\epsilon) \rightarrow \text{Mg}_{24}\text{Y}_5(\epsilon) \rightarrow \text{Mg}_{24}\text{Y}_5(\epsilon)+\tau_{12} \rightarrow \tau_{12} \rightarrow \{\text{hcp-Mg}\}$ (end-member).

The first diffusion layer has been found to have a composition of 32.9/22.5/44.6 Mg/Ni/Y at.%. The layer is very thin but can be seen clearly at higher magnification in Figure 7-1(b). According to the WDS analysis this layer is identified as a ternary compound, $\tau_5(\text{Mg}_{29}\text{Ni}_{20}\text{Y}_{42})$. After that the diffusion path reaches the second layer with a composition of 35.4/31.5/33.1 Mg/Ni/Y at.% which is considered a ternary compound, τ_6 . The layer is about 5 μm in width. The composition of this layer indicates a ternary compound of almost equal amount of each element suggesting the MgNiY formula. Next diffusion layer represents $\tau_9(\text{Mg}_{57}\text{Ni}_{18}\text{Y}_{25})$ which is another ternary compound with approximate composition of 59.1/16.5/24.4 Mg/Ni/Y at% as shown in Figure 7-1(a) and with higher magnification in Figure 7-1(b). Then, the diffusion path goes to a diffusion layer which represents $\text{Mg}_2\text{Y}(\delta)$. The width of this layer is about 30 μm . Then the diffusion path enters to a large layer of about 90 μm width which has been identified as $\text{Mg}_{24}\text{Y}_5(\epsilon)$. Ni solubility in both $\text{Mg}_2\text{Y}(\delta)$ and $\text{Mg}_{24}\text{Y}_5(\epsilon)$ is found negligible (0.5 at.% ± 1). The next diffusion layer represents $\tau_{12}(\text{Mg}_{15}\text{NiY})$ with a composition of 86.8/5.5/7.7 Mg/Ni/Y at.%. The composition profile of this layer in Figure 7-2 (b) shows variation of Mg content from 86.3 at.% to 89.0 at.% which demonstrates the homogeneity range of τ_{12} . A very thin white layer can be seen in Figure 7-1(a), within this diffusion layer. Spot

analysis of this thin layer revealed a composition that represents $\tau_3(\text{MgNi}_4\text{Y})$ which has been reported earlier [129]. This indicates equilibrium relationship between τ_{12} and τ_3 . However this layer could not be shown in Figure 7-2 (b) due to lack of sufficient spots along the line scan. The phase relation: $\tau_{12}+\tau_3$ will be confirmed latter by key samples.

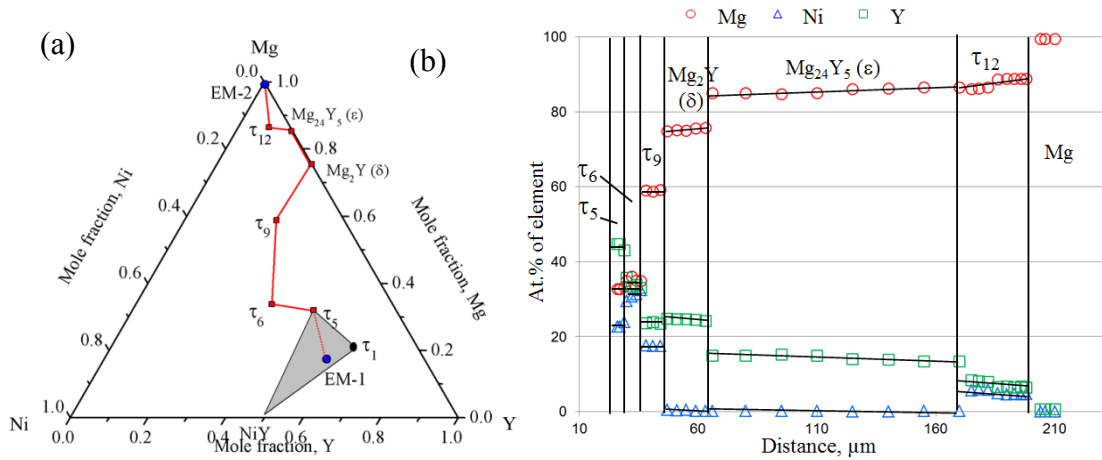


Figure 7-2: (a) Diffusion path projected on the Mg-Ni-Y Gibbs triangle; (b) Composition profile of the diffusion couple 1 along the line scan shown in Figure 7-1(a).

7.1.2 Solid-Solid diffusion couple 2

The second solid-solid diffusion couple has been used to identify and understand the ternary compounds in the Mg-Ni side of the Mg-Ni-Y system. The two end members have the compositions of 6.2/64.9/28.9 and 55.5/36.6/7.9 Mg/Ni/Y at.%. End member 1 is in a two phase region consisting NiY and $\tau_3(\text{MgNi}_4\text{Y})$ whereas end member 2 is located in a three phase region of $\tau_3(\text{MgNi}_4\text{Y})$, Mg_2Ni and $\tau_{12}(\text{Mg}_{15}\text{NiY})$. These end members have been selected to obtain maximum amount of information. They contain a common phase τ_3 which is dominating in this part of the phase diagram. In diffusion couple 1 shown in Figure 7-1 (a), a thin layer with a composition similar to τ_3 has been observed within the τ_{12} phase. It reflects that τ_3 is in equilibrium with τ_{12} . Hence it is

possible that τ_3 will have equilibrium relation with all the ternary compounds located on the Mg-NiY line. Therefore, a successful diffusion couple with these end members will not only provide information about the existence of any new compounds but also establish the phase relationship in this region.

The BSE image of the diffusion zone can be seen in Figure 7-3. Five diffusion layers have been identified and a line scan through these layers is shown in Figure 7-4 (a). Based on the WDS analysis, the diffusion path has been estimated as projected on the Gibbs triangle in Figure 7-4 (b). The diffusion starts with the formation of a white bush shape layer which has been identified as NiY. The next layer is about 15 μm thick and is identified as a ternary compound, $\tau_8(\text{Mg}_2\text{NiY})$ with composition of 51.0/24.7/24.2 Mg/Ni/Y at.%. The next layer is quite thin and is about 6 μm . According to the WDS analysis, its composition is 74.7/12.9/12.4 Mg/Ni/Y at.%. It represents another ternary compound, $\tau_{10}(\text{Mg}_6\text{NiY})$. The subsequent layer is $\tau_{11}(\text{Mg}_9\text{NiY})$. This layer is about 20 μm thick. The compositional profile in Figure 7-4 (a) shows a concentration gradient for this compound. The Mg concentration increased from 82 at.% to 85 at.%. This reflects solubility for τ_{11} where Mg has been replaced by Ni and Y. Then, the diffusion ends in the three-phase region ($\text{Mg}_2\text{Ni}+\tau_{12}+\tau_3$) of end member 2. The BSE image of the diffusion zone in Figure 7-3, shows the existence of τ_3 in contact with all the diffusion layers. This demonstrates that τ_3 has equilibrium phase relation with all the compounds on the Mg-NiY line. Some of the phase triangulations will be confirmed using key samples.

Continuous diffusion layers could not be obtained for this diffusion couple because of the uneven contact between the end members. Hence, it will not give accurate measurement for path dependant analysis like solid solubility, diffusion coefficient etc.

However, it can be used for identifying ternary compounds and their relations with other phases.

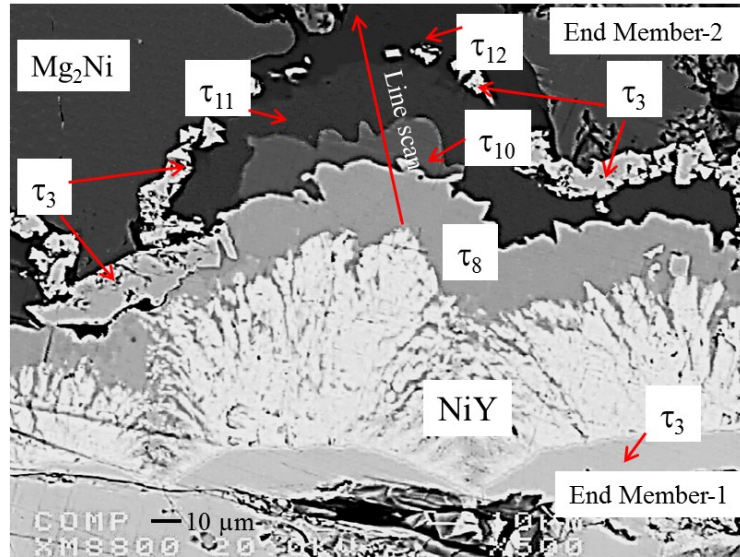


Figure 7-3: BSE images of the solid–solid diffusion couple 2 annealed at 673 K for 4 weeks

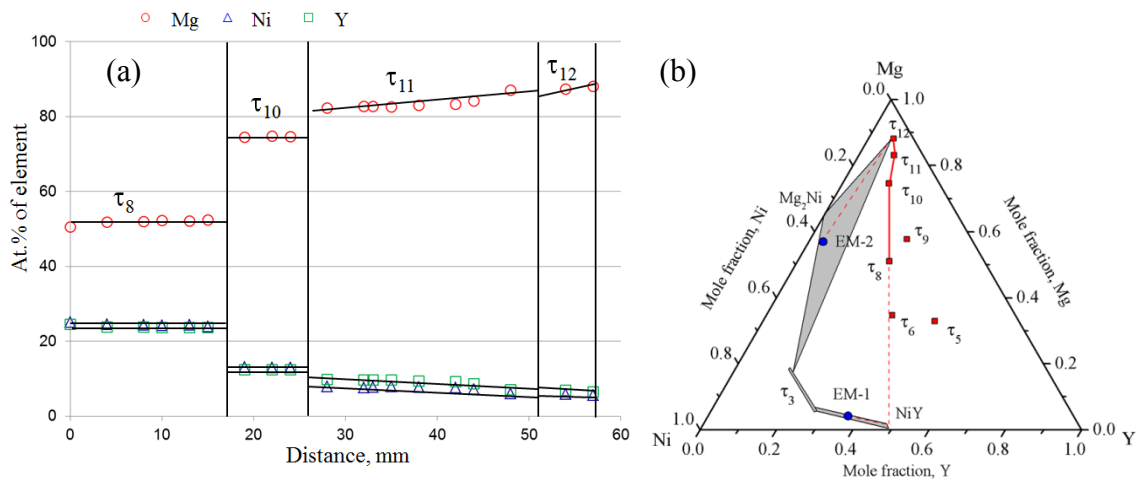


Figure 7-4: Composition profile of the diffusion couple 2 along the line scan shown in Figure 7-3; (b) Diffusion path of the solid-solid diffusion couple 2 projected on the Mg-Ni-Y Gibbs triangle

7.1.3 Solid-Solid diffusion couple 3

The third solid-solid diffusion couple has been prepared to confirm some of the ternary compounds already identified in the first two diffusion couples. End members of this

diffusion couple are Mg and a ternary alloy with the composition 6.2/64.9/28.9 Mg/Ni/Y at.%. This alloy is located in the two-phase region of NiY and τ_3 . The BSE image of the diffusion couple has been shown in Figure 7-5 (a) and (b) with increased magnification.

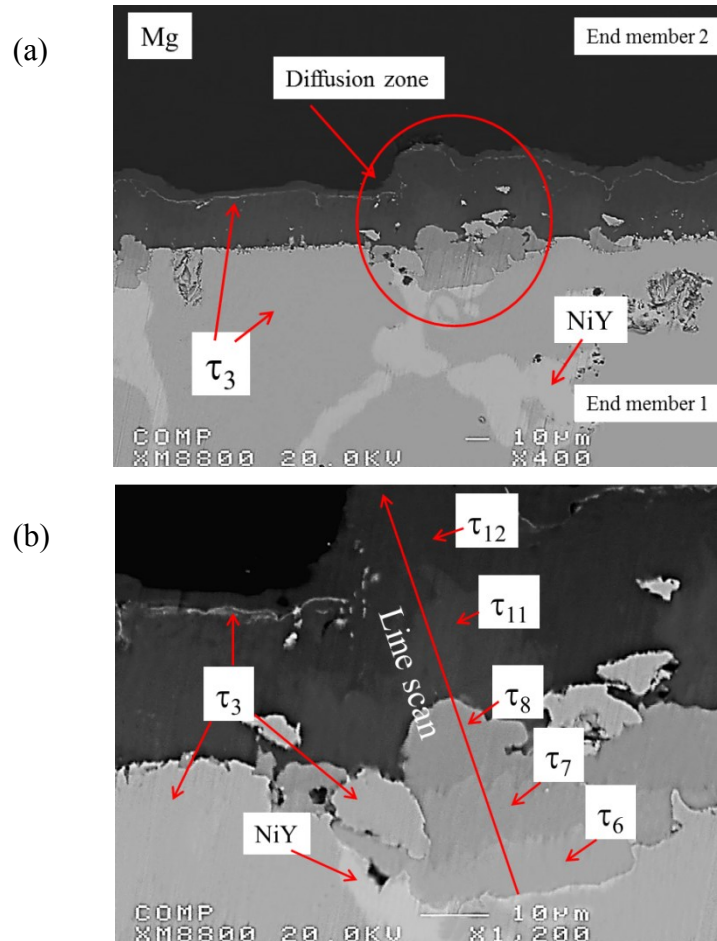


Figure 7-5: (a) BSE images of the solid-solid diffusion couple-3 annealed at 673 K for 4 weeks; (b) magnified area of interest.

The BSE image in Figure 7-5 (b) shows the formation of a small region with five diffusion layers. In order to identify them properly, a WDS line scan has been carried out. The composition profile as a result of the line-scan has been shown in Figure 7-6 (a). It reveals five ternary compounds. These compounds are $\tau_6(\text{MgNiY})$, $\tau_7(\text{Mg}_8\text{Ni}_5\text{Y}_5)$,

$\tau_8(\text{Mg}_2\text{NiY})$, $\tau_{11}(\text{Mg}_9\text{NiY})$ and $\tau_{12}(\text{Mg}_9\text{NiY})$. Except $\tau_7(\text{Mg}_8\text{Ni}_5\text{Y}_5)$, others have been identified in the previous two diffusion couples.

$\tau_{11}(\text{Mg}_9\text{NiY})$ and $\tau_{12}(\text{Mg}_9\text{NiY})$ show some solubility as can be seen in the composition profile in Figure 7-6 (a). Both these compounds show similar type of solubility where Mg has been replaced by equal amount of Ni and Y. The diffusion path of diffusion couple 3 can be seen in Figure 7-6 (b). The ternary compounds identified in all the three solid-solid diffusion couples have been shown with red squares. It can be observed that the diffusion failed to pass through all the compounds. However, the possibility of missing phase is a common phenomenon [163] in diffusion couple. Sometimes the nucleation of the phase is too slow to form a diffusion layer to be detected by WDS. In order to overcome this uncertainty a combined investigation with key sample analysis has been carried out and will be discussed in section 7.3.

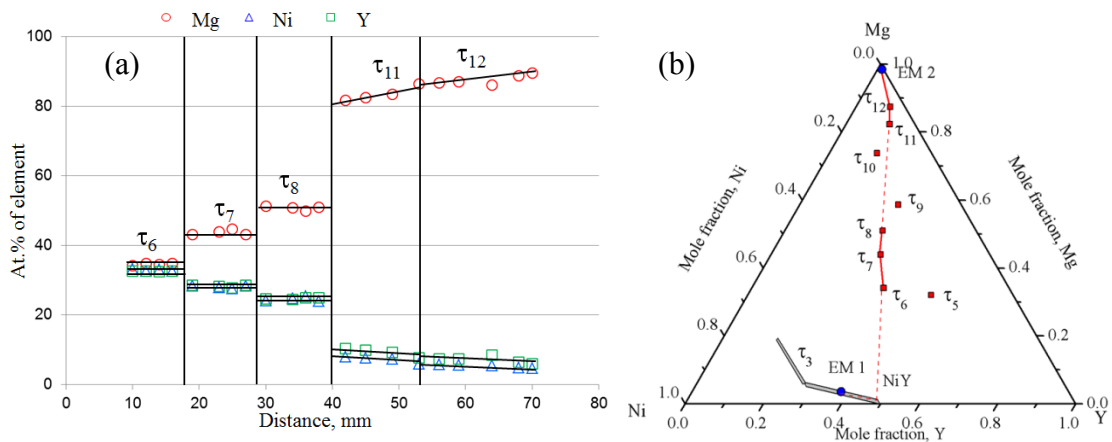


Figure 7-6: (a) Composition profile along the line scan shown in Figure 7-5 (b); (b) Diffusion path projected on the Mg-Ni-Y Gibbs triangle

7.1.4 Solid-liquid diffusion couple

Two solid-liquid diffusion couples have been used to verify the existence of the ternary compounds identified in the three prior solid-solid diffusion couples. The diffusion zone

in diffusion couples 2 and 3 is quite small because of non-uniform contact between the end members. To improve the contact and obtain continuous diffusion layers Mg block was partially melted on top of two different alloy blocks ($\text{Ni}_{78}\text{Y}_{22}$ and $\text{Ni}_{52}\text{Y}_{48}$) in an induction melting furnace to form two diffusion couples. This improved the contact and formed continuous diffusion layers as can be seen in Figure 7-7 and 7-8.

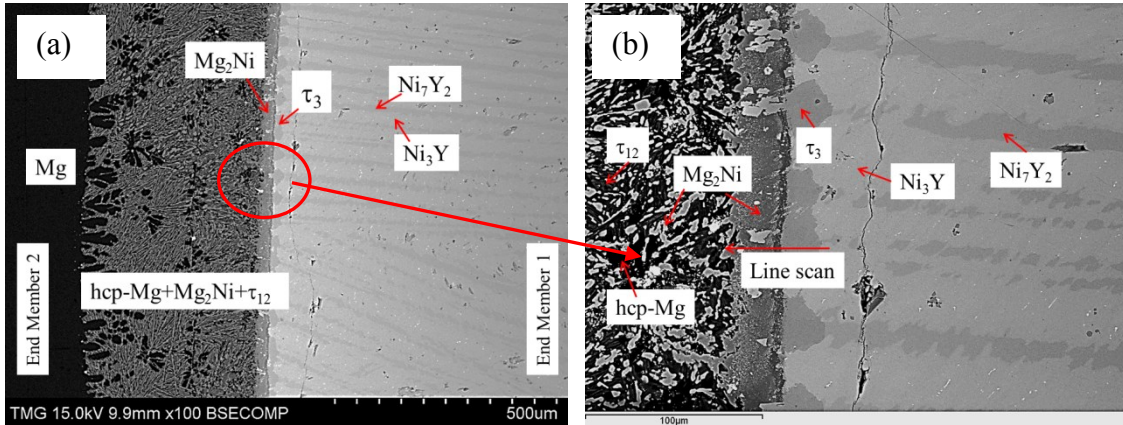


Figure 7-7: (a) BSE images of the solid–liquid diffusion couple-1 ($\text{Mg-Ni}_{78}\text{Y}_{23}$) annealed at 673 K for 4 weeks; (b) magnified area of interest

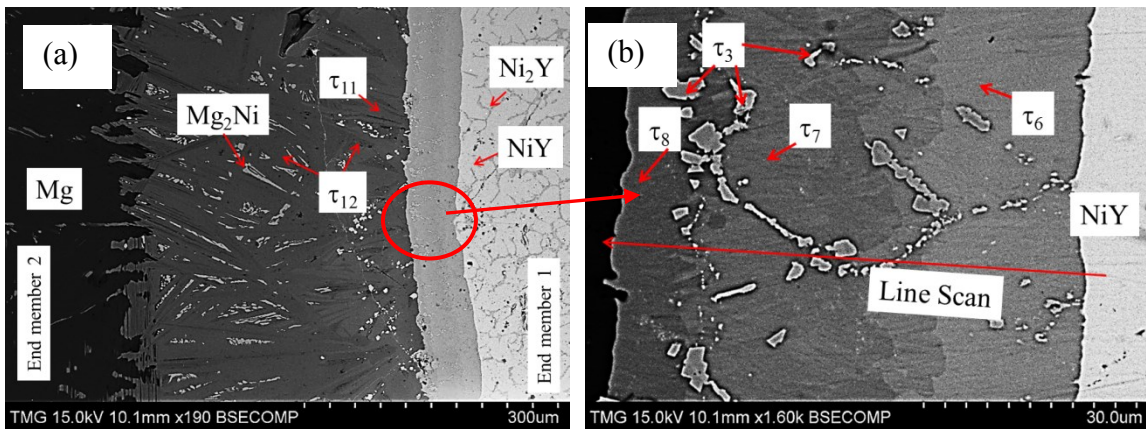


Figure 7-8: (a) BSE images of the solid–liquid diffusion couple-2 ($\text{Mg-Ni}_{52}\text{Y}_{48}$) annealed at 673 K for 4 weeks; (b) magnified area of interest

The BSE image of the solid-liquid diffusion couple 1 ($\text{Mg-Ni}_{78}\text{Y}_{22}$) in Figure 7-7 (a) shows a three-phase region among hcp-Mg , Mg_2Ni and τ_{12} in contact with pure Mg. Diffusion layers containing 3 phases are not possible in a ternary system. Most probably during melting Mg reacted with the other end member, $\text{Ni}_{78}\text{Y}_{22}$, and generated an alloy in

the three-phase region of hcp-Mg+Mg₂Ni+τ₁₂. According to the EDS area scan the average composition of this layer is 84.8/12.6/2.6 Mg/Ni/Y at.%. This 3-phase alloy has been considered as the end member of this diffusion couple. A line WDS analysis has been performed as can be seen in Figure 7-9 (a). It indicates the following sequence of phases along the diffusion path: {Ni₃Y+Ni₁₇Y₂} (End member) → τ₃ → τ₃+Mg₂Ni → Mg₂Ni → {hcp-Mg+Mg₂Ni+τ₁₂}. The diffusion path has been projected on Mg-Ni-Y Gibbs triangle as can be seen in Figure 7-9 (b). The first layer is τ₃ as can be seen in Figure 7-7 (b). The composition profile in Figure 7-9 (a) shows the homogeneity range of τ₃ from 14.5 to 19.3 at.% Mg with constant ~64 at.% Ni. The solubility limit of this compound will be confirmed using key samples. The next layer is a two-phase region of Mg₂Ni and τ₃. After this, a thin layer of Mg₂Ni can be seen. The maximum solubility of Y in Mg₂Ni has been found to be about 3.5 at.%. Then the three-phase region of hcp-Mg+Mg₂Ni+τ₁₂ can be seen. No solubility of Y or Ni could be found in the hcp-Mg phase.

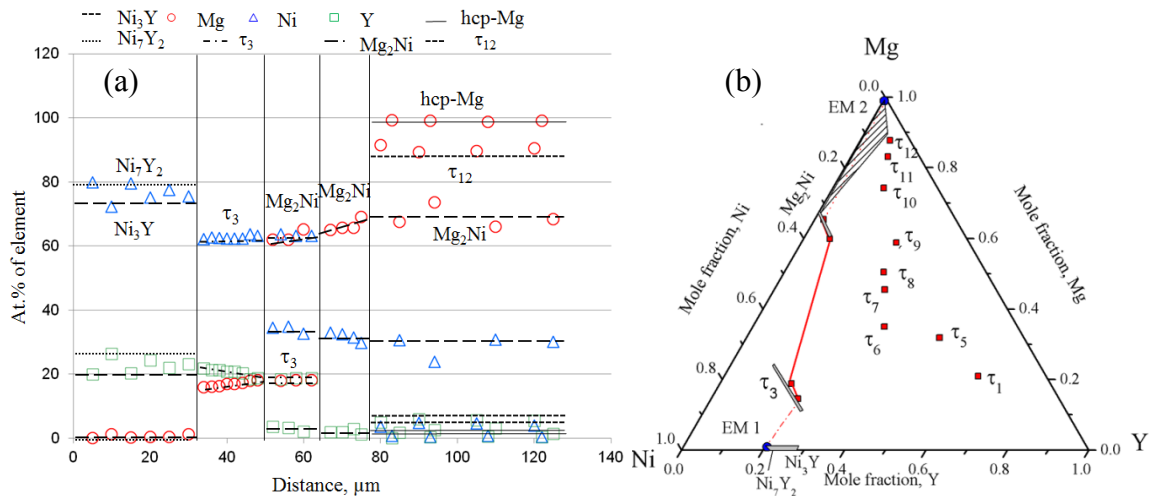


Figure 7-9: Composition profile of the solid–liquid diffusion couple-1 along the line scan shown in Figure 7-7 (b); (b) Diffusion path projected on the Mg-Ni-Y Gibbs triangle

The 2nd solid-liquid diffusion couple (Mg-Ni₅₂Y₄₈) in Figure 7-8 also indicates reaction between Mg and the end member Ni₅₂Y₄₈. It produced an alloy (78.4/15.5/6.1 Mg/Ni/Y at.%) containing a two-phase region between τ_{12} and Mg₂Ni. This alloy will be considered as the end member of this diffusion couple. Four diffusion layers formed during annealing and a line WDS scan has been carried out through them as can be seen in Figure 7-8 (b). The composition profile and diffusion path deduced from the line scan is shown in Figure 7-10 (a) and (b). Three intermetallic compounds τ_6 (~32.0/31.5/36.5 Mg/Ni/Y at.%), τ_7 (~42.1/26.2/31.7 Mg/Ni/Y at.%) and τ_8 (~48.3/23.5/28.1 Mg/Ni/Y at.%) are identified in the first three layers as can be seen in Figure 7-10 (a). In these layers small precipitates of another phase can be seen. Spot WDS analysis found this as τ_3 . This means that τ_3 is in equilibrium with all of the ternary compounds in this diffusion couple. This is in agreement with the previous diffusion couples. The fourth diffusion layer is a two-phase region between τ_{11} and τ_{12} . After this the diffusion ends in the two phase region of Mg₂Ni and τ_{12} .

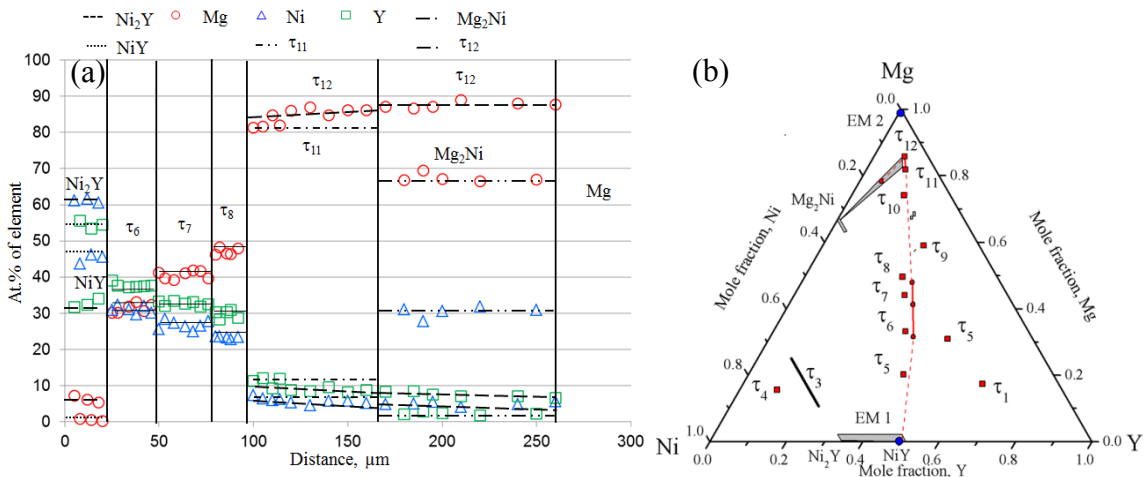


Figure 7-10: (a) Composition profile of the solid-liquid diffusion couple-2 along the line scan shown in Figure 7-8 (b); (b) Diffusion path projected on the Mg-Ni-Y Gibbs triangle

Table 7-1: WDS data on the Mg-Ni-Y alloys annealed at 673 K

No.	Actual composition			Identified phases			
	at.%			Name	Composition by WDS		
	Mg	Ni	Y		Mg	Ni	Y
1	84.9	12.9	2.2	hcp-Mg	99.4	0.5	0.1
				τ_{12}	92.0	4.1	3.9
				Mg ₂ Ni	67.9	30.2	1.9
2	78.2	15.5	6.3	τ_{12}	85.3	6.3	8.4
				Mg ₂ Ni	67.5	30.7	1.8
				τ_3	18.8	64.5	16.5
3	55.5	36.6	7.9	τ_{12}	85.1	6.7	8.2
				Mg ₂ Ni	65.3	33.8	0.9
				τ_3	17.4	66.8	15.8
4	27.2	59.9	12.9	Mg ₂ Ni	67.2	32.5	0.3
				τ_3	22.7	64.9	12.3
5	36.2	59.9	3.9	Mg ₂ Ni	67.2	32.5	0.3
				τ_3	25.9	64.9	9.2
				MgNi ₂	31.4	64.3	4.3
6	28.7	69.1	2.2	MgNi ₂	31.3	66.8	1.8
				τ_4	16.5	75.4	8.1
7	11.0	78.9	10.1	Ni ₁₇ Y ₂	3.5	84.9	11.6
				τ_4	17.6	75.6	6.8
8	3.7	77.3	19.0	Ni ₅ Y	0.4	82.9	16.7
				τ_3	9.8	66.9	23.3
				Ni ₄ Y	1.3	78.8	19.9
9	8.4	58.6	33.0	NiY	1.3	49.6	49.1
				τ_2	21.2	39.3	39.5
				τ_3	18.0	66.5	15.5
10	20.0	50.8	29.2	τ_2	19.7	40.5	39.8
				τ_3	11.8	66.5	21.7
				τ_6	32.2	34.3	33.5
11	26.0	38.2	35.8	τ_2	21.4	39.2	39.4
				τ_3	16.4	64.0	19.6
				τ_6	35.6	32.3	32.1
12	28.0	36.8	35.2	τ_2	22.4	39.3	38.3
				τ_3	16.3	64.2	19.5
				τ_6	35.9	32.7	31.4
13	24.5	52.4	23.1	τ_3	15.1	64.7	20.2
				τ_7	45.9	27.1	27.0
				τ_8	51.2	24.5	24.3
14	37.2	36.3	26.5	τ_3	15.6	65.1	19.3
				τ_6	34.6	31.7	33.7
				τ_8	51.2	24.4	24.4
				τ_{10}	74.1	13.0	12.9
				τ_{11}	82.5	8.6	8.9
15	54.1	24.0	21.9	τ_3	17.8	64.1	18.1
				τ_8	52.3	24.3	23.4
				τ_{10}	74.5	12.8	12.7
				τ_{11}	84.5	7.6	7.9

Table 7-1 (continued)

Actual composition				Identified phases			
No.	at.%			Name	Composition by WDS		
	Mg	Ni	Y		Mg	Ni	Y
16	3.3	80.5	16.2	Ni ₅ Y	0.7	82.9	16.4
				τ_4	15.5	74.7	9.8
17	1.5	63.4	35.1	Ni ₂ Y	0.7	63.1	36.2
				NiY	0.5	46.7	52.8
18	25.0	30.3	44.7	τ_2	20.9	37.9	41.2
				τ_5	35.0	21.5	43.5
				NiY	0.3	49.2	50.5
19	19.5	29.5	51.0	τ_1	20.9	16.6	62.5
				τ_5	33.6	21.9	44.5
				NiY	0.9	48.9	50.2
20	18.5	22.4	59.1	τ_1	20.1	17.3	62.6
				τ_5	31.7	21.6	46.7
				NiY	0.4	48.7	50.9
21	13.1	26.7	60.2	τ_1	16.4	20.3	63.3
				Eutectic	12.96	29.1	58.0
22	4.8	28.3	66.9	τ_1	16.4	21.3	62.3
				NiY ₃	0.9	24.9	74.2
				NiY	0.4	48.8	50.8
23	3.9	23.6	72.5	τ_1	14.7	22.1	63.2
				NiY ₃	0.7	25.5	73.8
24	5.9	20.9	73.2	τ_1	16.2	18.6	65.2
				NiY ₃	1.2	24.3	74.5
25	8.6	16.5	74.9	τ_1	17.2	16.5	66.2
				NiY ₃	0.9	24.4	74.7
				Y-hcp	0.7	0.8	98.5
26	37.0	15.0	48.0	MgY(γ)	51.5	1.6	46.9
				τ_1	26.3	15.6	58.1
				τ_5	32.8	21.4	45.8
27	38.5	14.7	46.8	MgY(γ)	49.6	1.1	49.3
				τ_5	34.1	21.5	44.4
				Mg ₂ Y(δ)	-	-	-
28	49.9	8.0	42.1	Mg ₂ Y(δ)	66.8	1.2	32.0
				MgY(γ)	53.4	0.8	45.8
				τ_5	34.1	21.1	44.8
29	51.4	12.3	36.3	τ_2	21.4	37.5	41.1
				τ_5	35.7	21.6	42.7
				τ_6	36.2	30.8	33.0
				Mg ₂ Y(δ)	71.7	0.8	27.5
30	54.0	15.9	30.1	τ_6	32.9	30.8	36.3
				τ_9	56.7	16.5	26.8
				Mg ₂ Y(δ)	64.9	0.9	34.1
31	69.1	9.4	21.5	τ_9	57.5	16.4	26.1
				τ_{10}	66.4	12.7	20.9
				Mg ₂ Y(δ)	70.7	1.1	28.2
32	72.0	6.3	21.7	τ_{10}	67.1	12.3	20.6
				Mg ₂ Y(δ)	69.4	1.0	29.6

7.2 Isothermal section based on diffusion couples and key sample analysis

29 key alloys have been prepared and investigated in order to construct the isothermal section at 673 K. The WDS analysis of the key samples listed in Table 7-1 shows the occurrence of twelve ternary compounds (τ_1 - τ_{12}) in the Mg-Ni-Y system. Only two of them τ_3 and τ_4 have been reported before and been confirmed in this work. Based on the current analysis, approximate composition of these compounds has been determined. The ternary solubility of the binary compounds has also been determined. $\text{Mg}_2\text{Y}(\delta)$ has been found to dissolve about 1.0 at.% Ni. Limited ternary solubility of about 0.5 at.% Ni for $\text{MgY}(\gamma)$ and $\text{Mg}_{24}\text{Y}_5(\epsilon)$ has been identified. These are very stable binary compounds with large homogeneity range and expected to have ternary solubility. Also, these compounds are found in the Mg-Cu-Y system with similar ternary solubility in the current work as well as in the literature [122]. Since both Mg-Ni-Y and Mg-Cu-Y systems show a lot of resemblance it is decided to consider small solubility of Ni in all the Mg-Y compounds. Among the Ni-Y compounds, Ni_{17}Y_2 and NiY dissolved about 3.5 and 1.3 at.% Mg. The solubility of Mg in Ni_3Y , Ni_4Y and NiY_3 is negligible ($\sim 0.5 \pm 1$ at.% Mg). Both, Mg_2Ni and MgNi_2 have been found to dissolve about 4.0 at.% Y. Based on the recent understanding an isothermal section of the Mg-Ni-Y system at 673 K has been constructed as shown in Figure 7-11. The dotted lines in the isothermal section show the tentative phase relations, as these could not be confirmed experimentally due to very sluggish equilibrium.

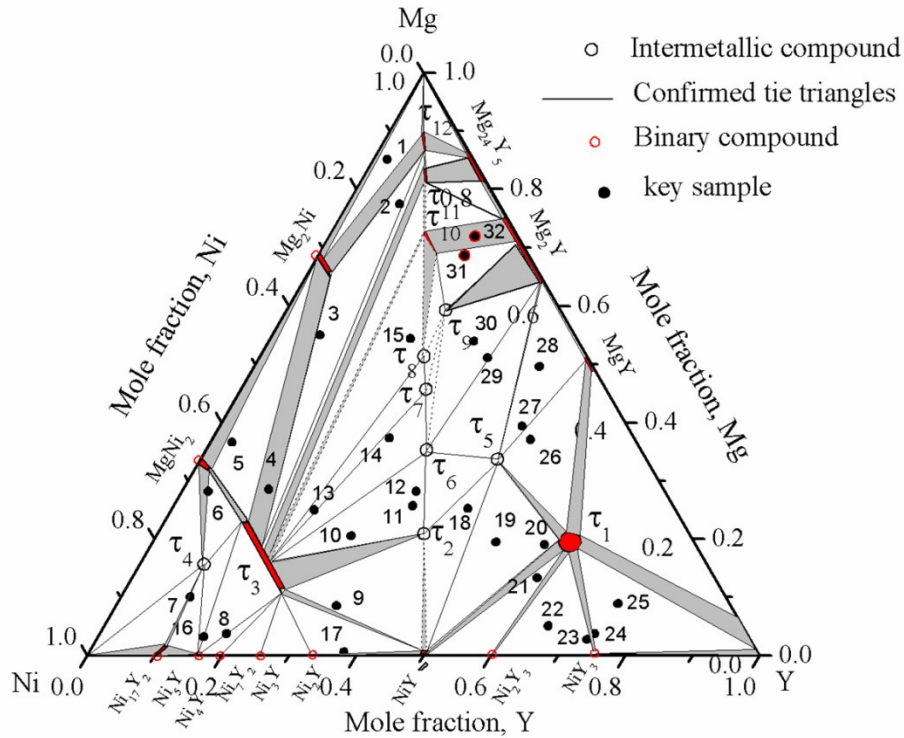


Figure 7-11: Isothermal section of the Mg-Ni-Y system at 673 K for the whole composition range

7.3 Ternary intermetallic compounds in the Mg-Ni-Y system

Twelve ternary intermetallic compounds have been found in the Mg-Ni-Y system as shown in Figure 7-11. The following discussion on the key samples using XRD and WDS analysis confirms the presence of these compounds.

In order to verify the existence of τ_1 and to establish the phase relationship in the Y-rich portion of the phase diagram, eight key samples 19, 20, 21-26 have been prepared. The locations of these alloys have been shown in Figure 7-11. The BSE images of sample 21 (13.1/26.7/60.2 Mg/Ni/Y at.%), sample 22 (4.8/28.3/ 66.9 Mg/Ni/Y at.%), sample 24 (5.9/20.9/73.2 Mg/Ni/Y at.%) and sample 25 (8.6/16.5/74.9 Mg/Ni/Y at.%) are shown in Figure 7-12. In all these alloys, τ_1 is positively identified. The WDS analysis listed in Table 7-1 shows large range of composition (~15-20 at.% Mg, ~16-20 at.% Ni) of τ_1

suggesting solid solubility. Variation in all the three elements indicates random substitution of atoms. Therefore, a round shape has been assigned to demonstrate the solubility range of τ_1 in Figure 7-11. According to the WDS analysis of τ_1 containing alloys (19, 20, 21-26), 5 three-phase regions has been established: τ_1 +NiY+Ni₂Y₃, τ_1 +NiY₃+Ni₂Y₃, τ_1 +NiY+ τ_5 , τ_1 +MgY+ τ_5 and τ_1 + NiY₃+ hcp-Y.

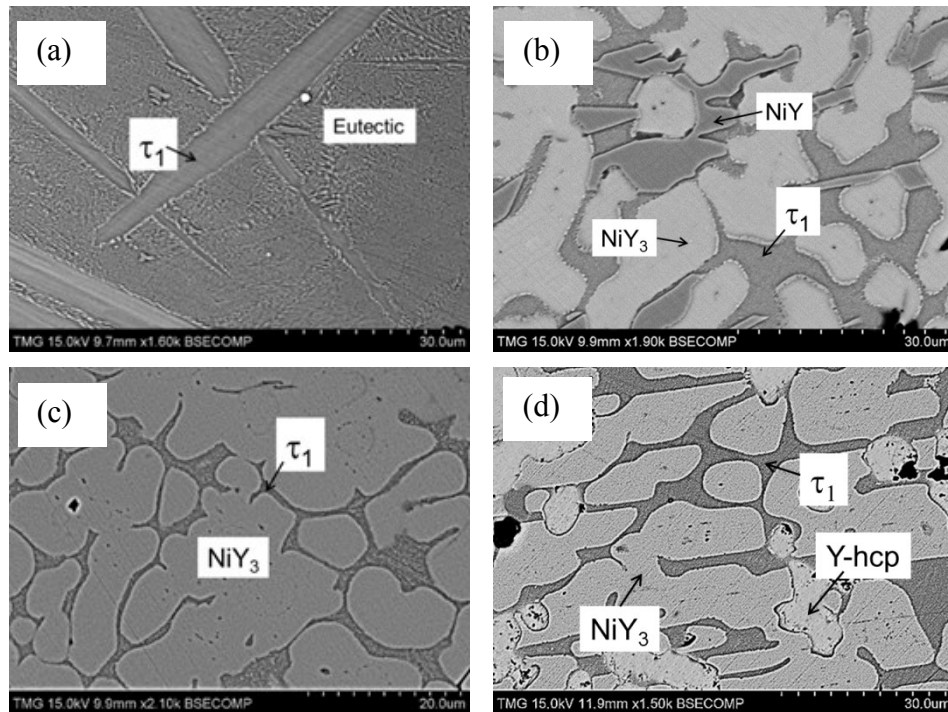


Figure 7-12: BSE image of (a) sample 21 (13.1/26.7/60.2 Mg/Ni/Y at.%); (b) sample 22 (4.8/28.3/ 66.9 Mg/Ni/Y at.%); (c) sample 24 (5.9/20.9/73.2 Mg/Ni/Y at.%); (d) sample 25 (8.6/16.5/74.9 Mg/Ni/Y at.%)

Hara et al. [15] in their hydrogen storage work on the Mg-Ni-Y system, reported an unknown phase of composition MgNiY₃. They reported that this compound plays a role as a catalyst for the adsorption of hydrogen. However, they could not identify the crystal structure of this compound. The composition of this compound (MgNiY₃) is very close the single phase region of τ_1 . Hence, it is likely that Hara et al. [15] were actually detecting τ_1 (MgNiY₄).

The crystallographic information of τ_1 has been determined in this work. This has been done by comparing XRD patterns of several τ_1 containing alloys with similar structure type compounds from Pearson crystal structure database [139]. It has been found that the XRD pattern of Gd_4RhIn is very similar to that of τ_1 . Tappe et al. [167] reported several rare earth containing compounds with this structure type. Refinement of the XRD patterns using Rietveld analysis determines the lattice parameters for τ_1 , $a = 13.666 \text{ \AA}$. The crystal structure data and atomic positions of τ_1 have been listed Table 7-2 and 7-3. Also, the unit cell is shown in Figure 7-13. The XRD patterns of sample 20 and 26 shown in Figure 7-14 (a) and (b) positively identify τ_1 . NiY in sample 20 and MgY(γ) in sample 26 are also identified. The unknown peaks in these alloys belong to τ_5 . Since the crystal structure of τ_5 is unknown all the peaks of the XRD patterns could not be indexed.

Table 7-2: The crystal structure data for MgNiY₄

Structure	Cubic		
Structure type	Gd_4RhIn		
Space group number	216		
Lattice parameter (\AA)	a	b	c
	13.666	13.666	13.666
Angles	α	β	γ
	90°	90°	90°
Atoms in unit cell	128		

Table 7-3: Atoms position in the unit cell for MgNiY₄

Atom	Wyckoff position	x	y	z
Mg	16e	0.080	0.080	0.080
Ni	16e	0.640	0.640	0.640
Y1	24g	0.560	0.250	0.250
Y2	24f	0.310	0	0
Y3	16e	0.153	0.153	0.153

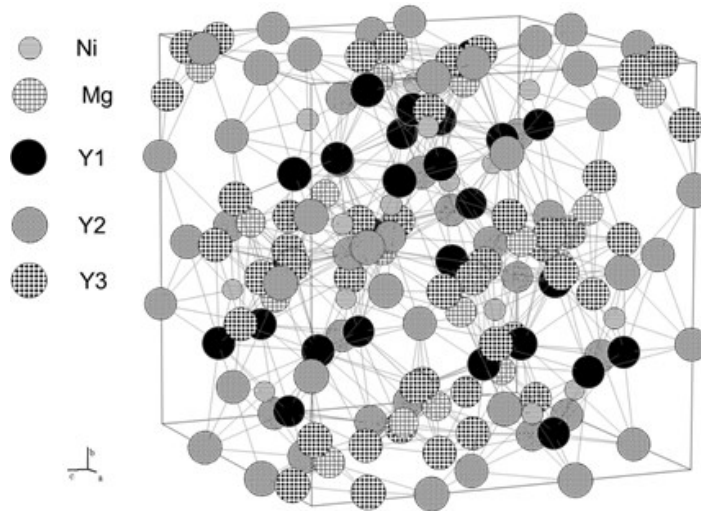


Figure 7-13: Unit cell of MgNiY_4

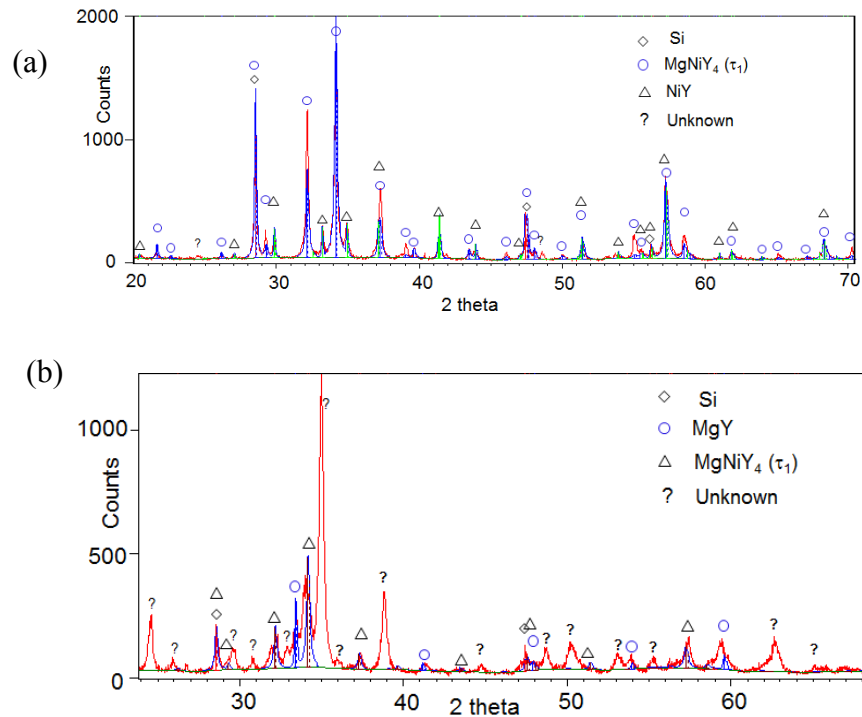


Figure 7-14: XRD pattern for (a) sample 20 (18.5/22.4/59.1 Mg/Ni/Y at.%); (b) sample 26 (37.0/15.0/48.0 Mg/Ni/Y at.%)

The ternary compound, τ_2 was not observed in any of the diffusion couples. Therefore more effort will be dedicated towards confirming its presence as discussed below. Five key alloys (9-12, 18) have been prepared near this compound as can be seen in Figure 7-11. τ_2 is found to exist in all of them. According to the WDS analysis listed in

Table 7-1, the composition of this compound is 20/40/40 Mg/Ni/Y at.%. Based on this, $MgNi_2Y_2$ formula has been assigned. The BSE images of sample 9 (8.4/58.6/33.0 Mg/Ni/Y at.%), sample 10 (28.0/36.8/35.2 Mg/Ni/Y at.%), sample 11 (26.0/38.2/35.8 Mg/Ni/Y at.%) and sample 12 (20.0/50.8/29.2 Mg/Ni/Y at.%) in Figure 7-15 clearly show τ_2 . Three 3-phase equilibria, $\tau_2+\tau_3+NiY$, $\tau_2+\tau_5+NiY$ and $\tau_2+\tau_3+\tau_6$ has been established based on the WDS analysis of these alloys (9-12, 18). The location of sample 9 is at the edge of the three phase region, $\tau_2+\tau_3+NiY$, as can be seen in Figure 7-11 (a). Therefore only small amount of τ_2 could be seen in the microstructure. However, the other three samples (10-12) clearly show τ_2 . Because of the distinct locations of the alloys, the relative amount of the phases varies.

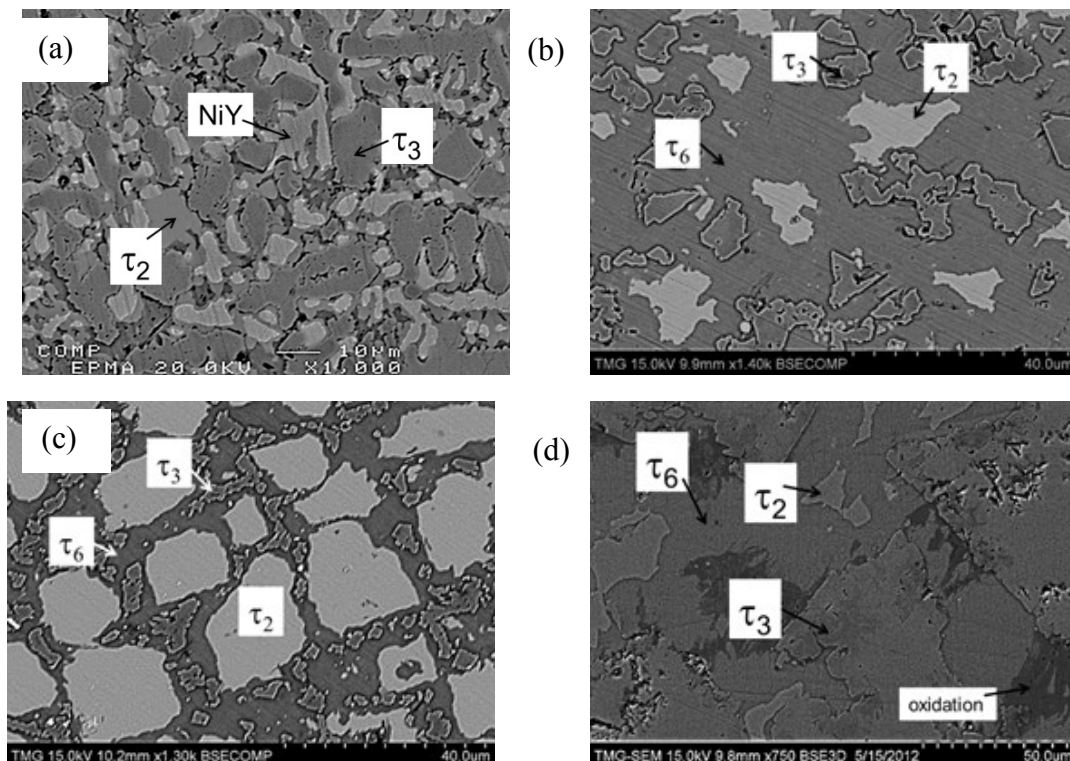


Figure 7-15: BSE image of (a) sample 9 (8.4/58.6/33.0 Mg/Ni/Y at.%); (b) sample 10 (28.0/36.8/35.2 Mg/Ni/Y at.%); (c) sample 11 (26.0/38.2/35.8 Mg/Ni/Y at.%); (d) sample 12 (20.0/50.8/29.2 Mg/Ni/Y at.%)

Crystal structure of τ_2 has been determined in this work. It has been found that τ_2 has Mo_2FeB_2 structure type. This has been done by comparing XRD patterns of five key alloys (9-12, 18) containing τ_2 with similar structure type compounds from Pearson crystal structure database [139]. Refinement of the XRD patterns using Rietveld analysis determines the lattice parameters for τ_2 to be $a = 7.395(9) \text{ \AA}$ and $c = 3.736(3) \text{ \AA}$. The crystal structure data and atoms position within the unit cell are listed in Table 7-4 and 7-5, respectively. Also, the unit cell of τ_2 is shown in Figure 7-16.

Table 7-4: The crystal structure data for $MgNi_2Y_2$

Structure	Tetragonal		
Structure type	Mo_2FeB_2		
Space group number	127		
Lattice parameter (\AA)	a	b	c
	7.395(9)	7.395(9)	3.736(3)
Angles	α	β	γ
	90°	90°	90°
Atoms in unit cell	22		

Table 7-5: Atoms position in the unit cell for $MgNi_2Y_2$

Atom	Wyckoff position	x	y	z
Mg	2a	0	0	0
Ni	4g	0.6216	0.1216	0
Y	4h	0.1716	0.6716	0.5000

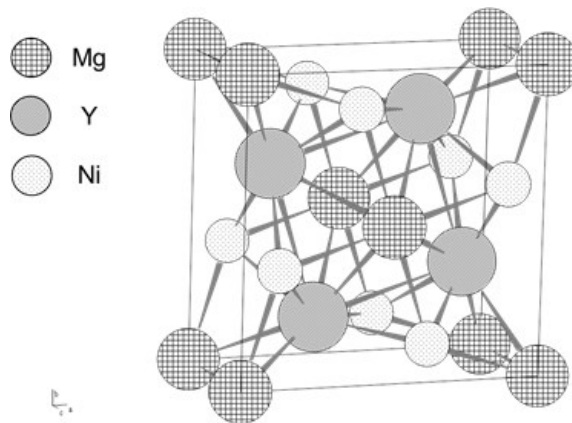


Figure 7-16: Unit cell for MgNi_2Y_2 (τ_2)

XRD patterns of the key alloys 10, 11 and 12 are shown in Figure 7-17 (a-c). τ_2 has been positively identified in all of them. The unknown phase in these XRD patterns belongs to τ_6 . Another ternary compound, τ_3 has also been positively identified in these XRD patterns. This compound was first reported by Kadir et al. [129]. They reported SnMgCu_4 type crystal structure with lattice parameter of 7.1853 \AA for τ_3 . This compound has been found in several alloys (2-5, 8-15) in the current work. According to the WDS analysis listed in Table 7-1, $\tau_3(\text{MgNi}_4\text{Y})$ has solubility from ~ 11 to 24 at.% Mg with constant 66.67 at.% Ni. The variation of lattice parameter of τ_3 has been observed in the Rietveld analysis that has been performed on the XRD patterns of four key alloys (5, 9, 10 and 11). The change of lattice parameter ' a ' can be seen in Figure 7-18. It can be seen that ' a ' decreases with the increase of Mg concentration. It reflects substitutional solid solution for τ_3 where Mg replaces Y atoms.

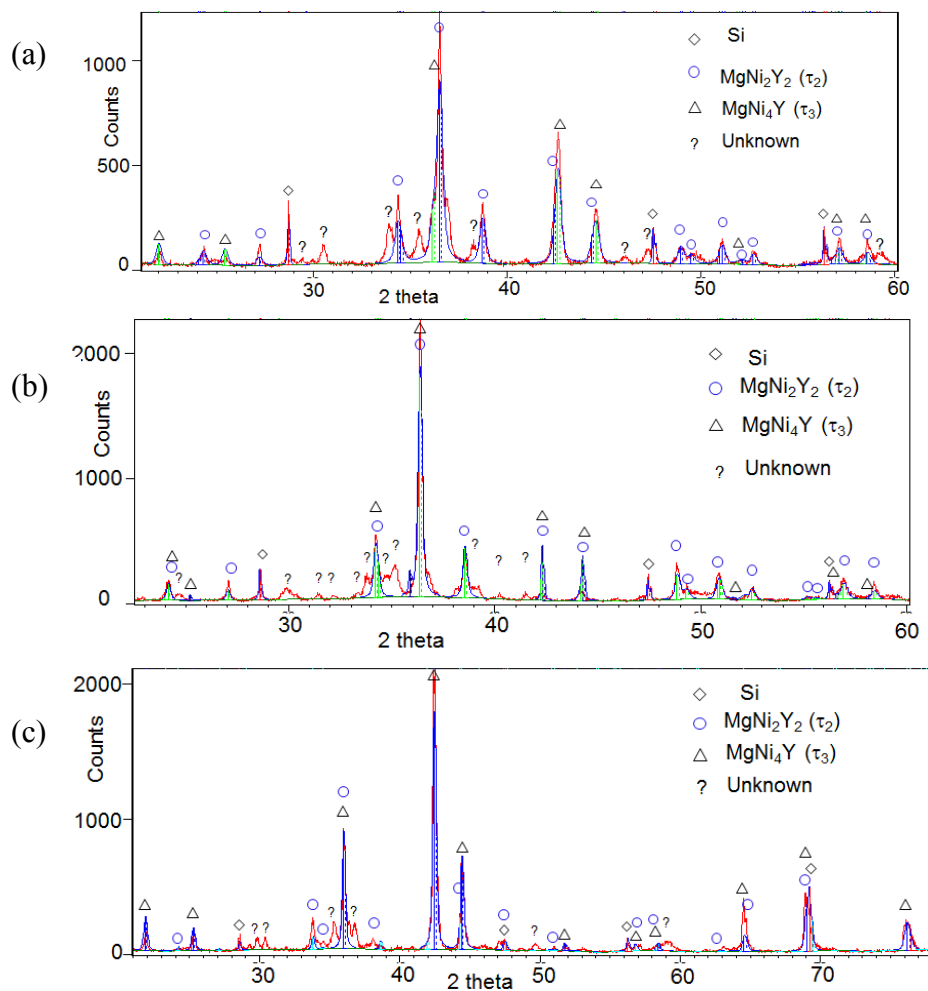


Figure 7-17: XRD patterns for (a) sample 10 (28.0/36.8/35.2 Mg/Ni/Y at.%); (b) sample 11 (26.0/38.2/35.8 Mg/Ni/Y at.%); (c) sample 12 (20.0/50.8/29.2 Mg/Ni/Y at.%)

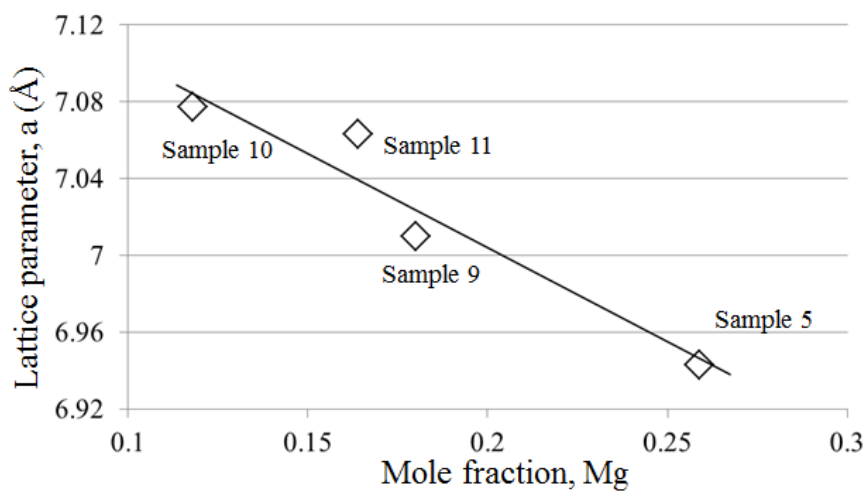


Figure 7-18: Variation of lattice parameter of τ_3

τ_4 has been identified in sample 6 (28.7/69.1/2.2 Mg/Ni/Y at.%) and sample 7 (11.0/78.9/10.1 Mg/Ni/Y at.%). The BSE image in Figure 7-19 (a) and (b) clearly shows this compound. According to the WDS analysis in Table 7-1, τ_4 has an average composition of 17.0/75.5/7.5 Mg/Ni/Y at.%, which can be represented by the formula Mg_2Ni_9Y . Two different plate-like structures can be seen in the BSE image of sample 6 in Figure 7-19 (a). These have been identified as $MgNi_2$ and τ_4 . Also, sample 7 shows equilibrium phases of $Ni_{17}Y_2$ and τ_4 . In these alloys, $MgNi_2$ dissolves about 1.8 at.% Y whereas $Ni_{17}Y_2$ dissolves about 0.9 at.% Mg.

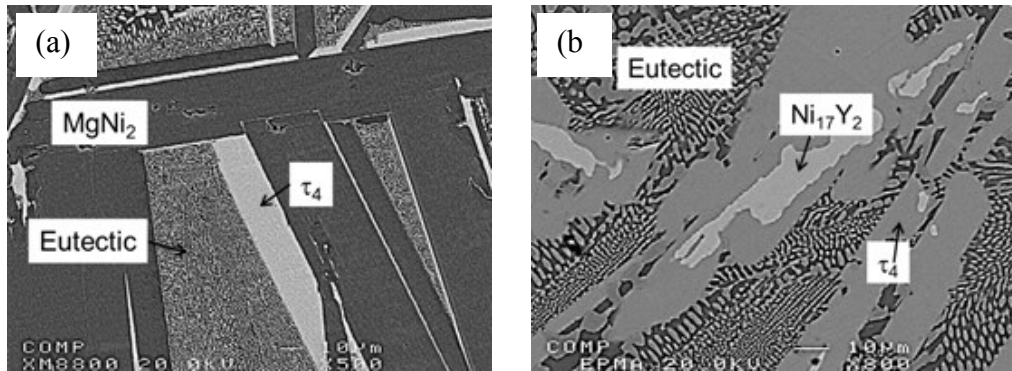


Figure 7-19: BSE image of (a) Sample 6 (28.7/69.1/2.2 Mg/Ni/Y at.%); (b) sample 7 (11.0/78.9/10.1 Mg/Ni/Y at.%)

The intermetallic compound, τ_5 has been found to exist in samples 18-20 and 26-29. Based on the WDS analysis of these alloys in Table 7-1, the approximate composition of τ_5 has been determined as 33.8/21.5/44.7 Mg/Ni/Y at.%. The BSE image of sample 18 (25.0/30.3/44.7 Mg/Ni/Y at.%) in Figure 7-20 (a) clearly shows τ_5 which is in equilibrium with τ_2 and NiY. The XRD pattern in Figure 7-20 (b) positively identifies τ_2 and NiY. The crystal structure of τ_5 is not known. Determining the crystal structure of τ_5 in the same approach as for τ_1 and τ_2 was not successful because a crystallographic

prototype could not be found. Therefore the peaks marked as unknown in this figure likely belong to τ_5 .

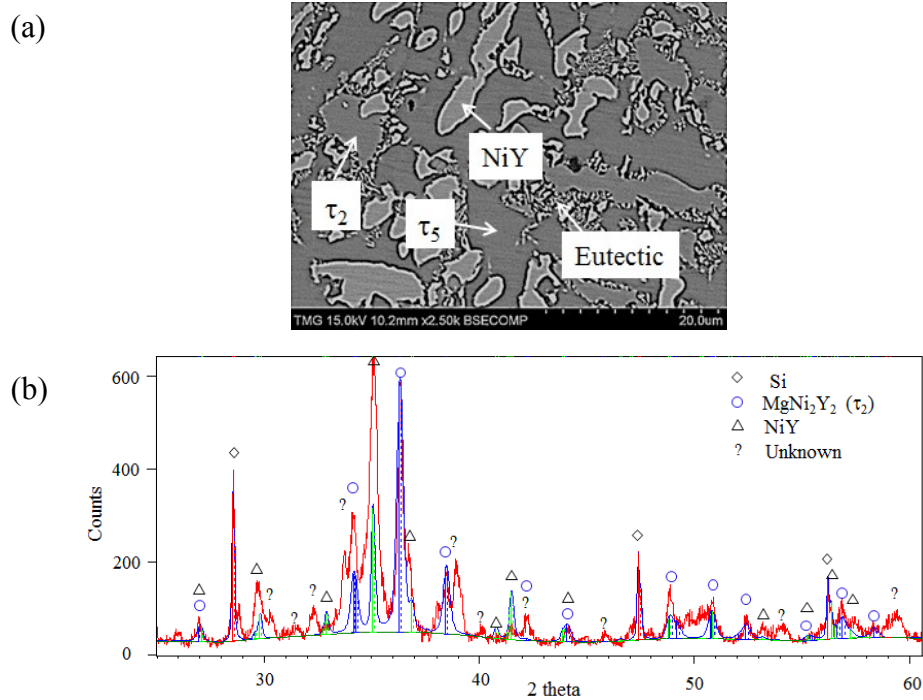


Figure 7-20: (a) BSE image; (b) XRD pattern for of sample 18 (25.0/30.3/44.7 Mg/Ni/Y at.%)

The BSE images of sample 14 (37.2/36.3/26.5 Mg/Ni/Y at.%) and sample 29 (51.4/12.3/36.3 Mg/Ni/Y at.%) in Figure 7-21 (a) and (b), show the existence of τ_6 . This compound has also been found in samples 10-12 and 29. In order to obtain equilibrium, these alloys have been annealed for six instead of 4 weeks. Still complete equilibrium could not be obtained. This is probably due to the peritectic decomposition of the compounds. The BSE image of sample 14 in Figure 7-21 (a) shows several phases; τ_3 , τ_6 , τ_8 , τ_{10} and τ_{11} . Sample 15 (54.1/24.0/21.9 Mg/Ni/Y at.%) in Figure 7-22 (b) also displays similar condition and shows four phases: τ_3 , τ_8 , τ_{10} and τ_{11} . Based on the analysis of samples 14 and 15 and the diffusion couples, it can be concluded that τ_3 is in equilibrium

with all the compounds in the Mg-Ni-Y line. The phase triangulation of this region has been shown in Figure 7-11.

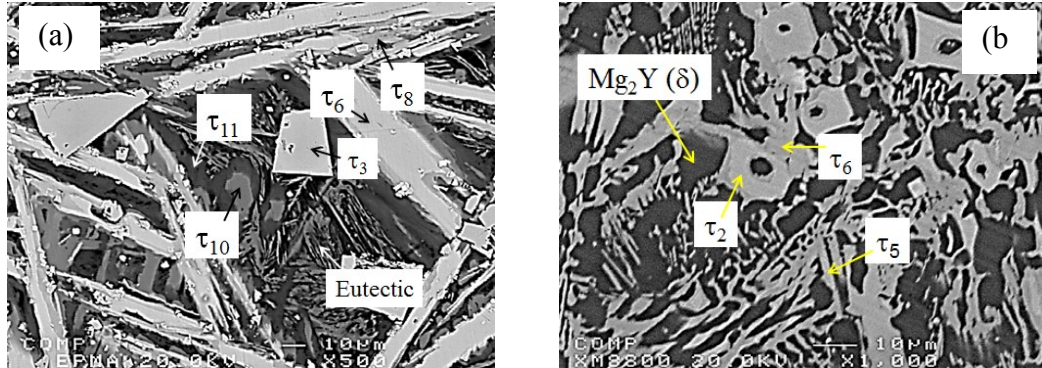


Figure 7-21: (a) sample 14 (37.2/36.3/26.5 Mg/Ni/Y at.%); (b) sample 29 (51.4/12.3/36.3 Mg/Ni/Y at.%)

Although not in complete equilibrium, a three-phase relation among $\text{Mg}_2\text{Y}(\delta)$, τ_5 and τ_6 can be identified in sample 29 (51.4/12.3/36.3 Mg/Ni/Y at.%) in Figure 7-21 (b). It is observed that τ_2 (white-square shape) always remains within τ_6 and will probably transfer to τ_6 with more annealing time. This indicates a three-phase region: $\text{Mg}_2\text{Y}(\delta)+\tau_5+\tau_6$. The contrast of τ_5 and τ_6 is very close because of their similar compositions. This makes it difficult to recognize these two phases in the BSE image. However, the WDS detector could measure the compositions as listed in Table 7-1.

The ternary compound τ_7 has been found in sample 13 (24.6/52.4/23.0 Mg/Ni/Y at.%) as shown in Figure 7-22 (a). Another compound, τ_8 can be seen in this sample. τ_8 is also identified in samples 14 and 15. The WDS analysis of these alloys is summarized in Table 7-1. Sample 13 is located at the boarder of two three-phase region of $\tau_3+\tau_6+\tau_7$ and $\tau_3+\tau_7+\tau_8$ as can be seen in Figure 7-11. Large amount of τ_3 is observed because the sample is very close to this compound. Small amount of τ_7 and τ_8 can be seen in this

alloy. Because of their similar compositions these two compounds τ_7 ($\text{Mg}_8\text{Ni}_5\text{Y}_5$) and τ_8 (Mg_2NiY) have close contrast in the micrograph. However, their existence has been confirmed in three diffusion couples ($\text{DC}_{\{\text{SS}\}}$ 2, 3 and $\text{DC}_{\{\text{SL}\}}$ 2) as shown earlier in Figure 7-3, 7-5 and 7-8. Sample 13 also confirms the phase relationship of τ_3 , τ_7 and τ_8 . Sample 15 (54.1/24.0/21.9 Mg/Ni/Y at.%) in Figure 7-22 (b) shows four phases: τ_3 , τ_8 , τ_{10} and τ_{11} because of peritectic decomposition. However, it can be seen that τ_{11} is never in contact with τ_8 which suggests a three-phase equilibrium between τ_3 , τ_8 and τ_{10} .

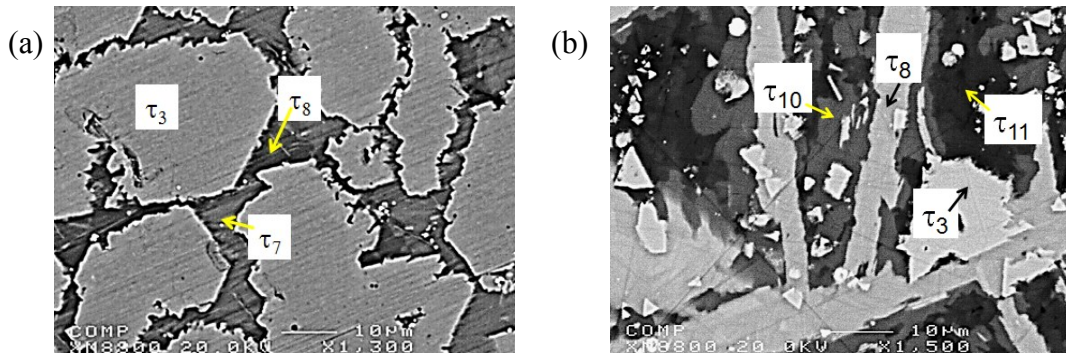


Figure 7-22: BSE image of (a) sample 13 (24.6/52.4/23.0 Mg/Ni/Y at.); (b) sample 15 (54.1/24.0/21.9 Mg/Ni/Y at.)

The BSE image of sample 30 (54.0/15.9/30.1 Mg/Ni/Y at.%) in Figure 7-23 (a) shows a three-phase equilibrium among $\text{Mg}_2\text{Y}(\delta)$, τ_6 and τ_9 . The white flakes and the grey matrix in the microstructure have been identified as τ_6 and τ_9 , respectively. $\text{Mg}_2\text{Y}(\delta)$ has been found as small precipitates in the grey matrix. According to the WDS analysis of sample 30 in Table 7-1, the composition of the ternary compound τ_9 is 56.7/16.5/26.8 Mg/Ni/Y at.%. This compound has also been observed in the solid-solid diffusion couple 1 in Figure 7-1 with slightly different composition 59.1/16.5/24.3 Mg/Ni/Y at.%. The WDS analysis of sample 31 (69.1/9.4/21.5 Mg/Ni/Y at.%) in Table 7-1, identified this compound, τ_9 , as 57.5/16.4/26.1 Mg/Ni/Y at.% which is closer to the diffusion couple

analysis. Therefore, it is decided to use the composition found in the diffusion couple analysis since it is generally more reliable.

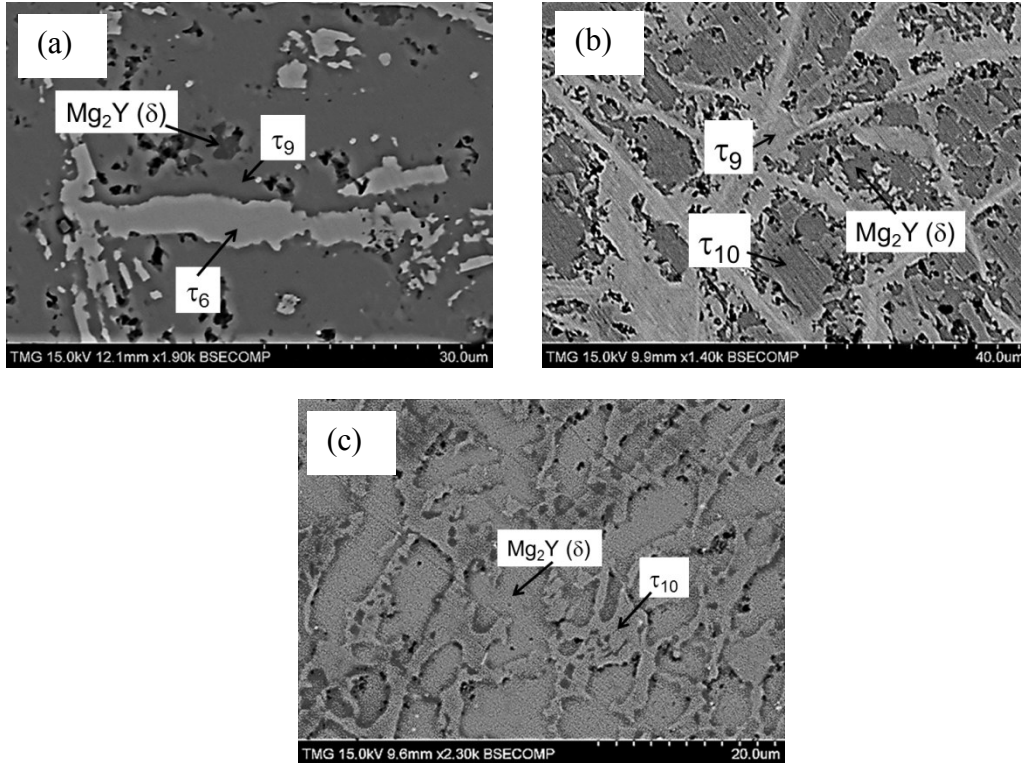


Figure 7-23: BSE image of (a) sample 30 (54.0/15.9/30.1 Mg/Ni/Y at.%); (b) sample 31 (69.1/9.4/21.5 Mg/Ni/Y at.%); (c) sample 32 (72.0/6.3/21.7 Mg/Ni/Y at.%)

The BSE image of sample 31 (69.1/9.4/21.5 Mg/Ni/Y at.%) and sample 32 (72.0/6.3/21.7 Mg/Ni/Y at.%) in Figure 7-23 (b) and (c) shows a three-phase, $Mg_2Y(\delta)+\tau_9+\tau_{10}$, and a two-phase, $Mg_2Y(\delta)+\tau_{10}$ equilibria. Both of these alloys showed the existence of the ternary compound τ_{10} with an average composition 66.4/12.7/20.9 Mg/Ni/Y at.%. But the solid-solid diffusion couple 2 in Figure 7-3 exhibited this compound at 74.7/12.9/12.4 Mg/Ni/Y at.%. It indicates a linear solubility of τ_{10} from ~ 66.4 to 74.7 at.% Mg at constant Ni of ~ 12.7 at.%.

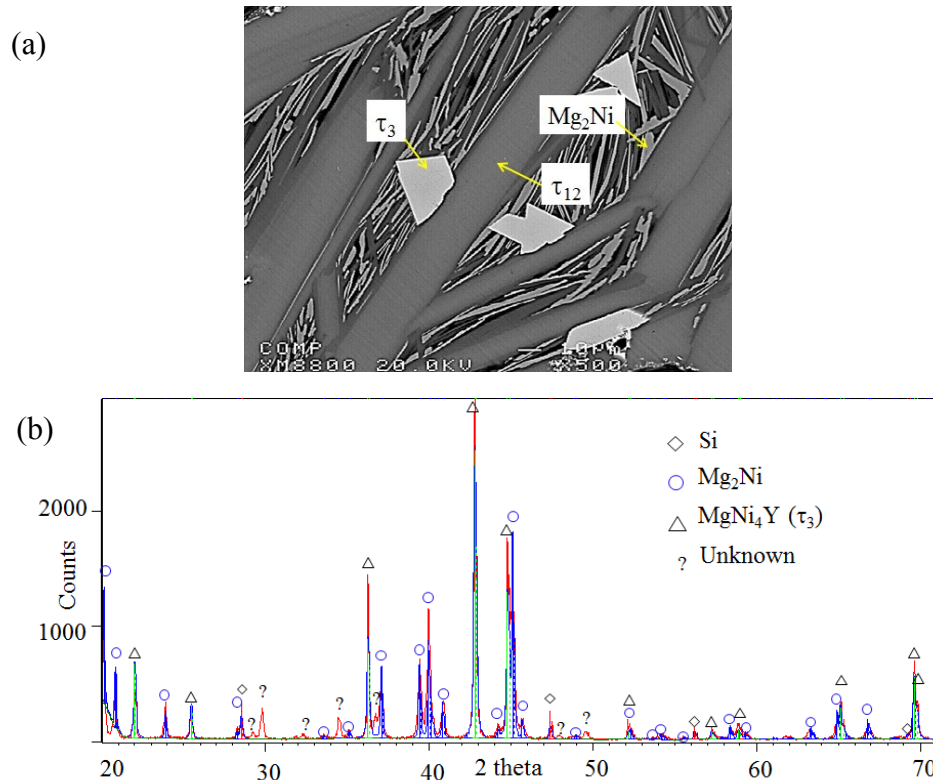


Figure 7-24: (a) BSE image of sample 2 (78.2/15.5/6.3 Mg/Ni/Y at.%); (b) XRD pattern of sample 3 (55.5/36.6/7.9 Mg/Ni/Y at.%)

Two ternary compounds τ_{11} and τ_{12} in the Mg-rich corner of the Mg-Ni-Y phase diagram have been identified in this work. τ_{11} has been found in key samples 14 (37.2/36.3/26.5 Mg/Ni/Y at.%) and 15 (53.0/25.1/21.9 Mg/Ni/Y at.%). The WDS analysis of these alloys is listed in Table 7-1. Also, solid-solid diffusion couples 2 and 3 in Figure 7-3 and 7-5, showed the existence of τ_{11} . It has been found that τ_{11} has a solid solubility which extends from ~83 to 84.5 at.% Mg.

τ_{12} has been found in all three solid-solid diffusion couples as shown earlier in Figure 7-1, 7-3 and 7-5. Also, the key samples 1 (84.9/12.9/2.2 Mg/Ni/Y at.%), 2 (78.2/15.5/6.3 Mg/Ni/Y at.%) and 3 (55.5/36.6/7.9 Mg/Ni/Y at.%) show this compound. The BSE image of sample 2, in Figure 7-24 (a) clearly shows τ_{12} . According to the WDS

analysis of the diffusion couples and key samples τ_{12} has a solubility range which extends from ~85 to 90 at.% Mg. The XRD pattern of sample 3 in Figure 7-24 (b) positively identifies Mg_2Ni and τ_3 . The crystallographic information of τ_{12} is unknown. Therefore, it was not possible to index the peaks of τ_{12} .

7.4 Comparison between experimental results and thermodynamic modeling

DSC experiments on thirteen key alloys of the Mg-Ni-Y system have been carried out in order to calibrate the liquidus surface. The locations of these alloys are shown in Figure 7-25. These results will be used to verify the current thermodynamic modeling. This combined approach will also help distinguish the thermal arrest points observed in the DSC spectra.

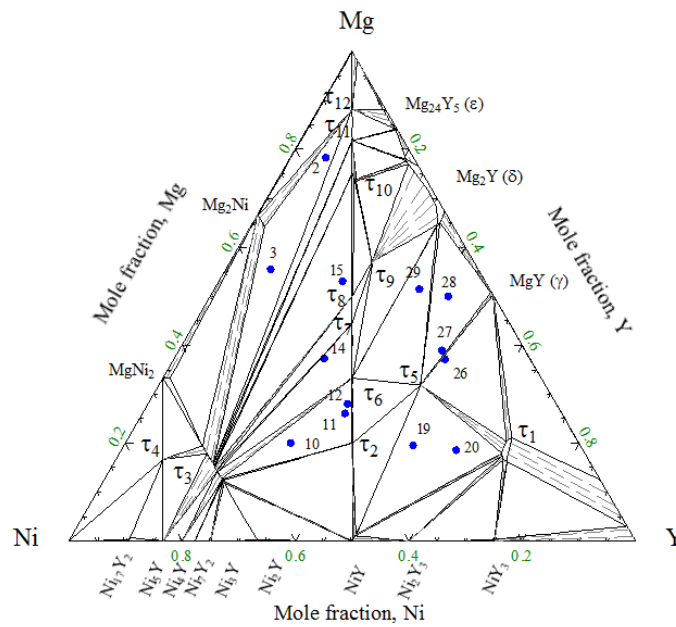


Figure 7-25: Mg-Ni-Y isothermal section at 673 K, based on this work, showing the samples investigated by DSC

The DSC spectra of sample 2 (78.2/15.5/6.3 Mg/Ni/Y at.%) during heating and cooling events are shown in Figure 7-26 (a). Two exothermic peaks appear in the cooling

curve at 782 and 767 K which correspond to the endothermic peaks at 803 and 770 K in the heating spectrum. Another small endothermic peak appeared in the heating curve at 727 K, but was not detected in the cooling spectrum due to overlapping with the peak at 767 K. The liquidus temperature for this alloy should be in between 782 and 803 K which is calculated at 814 K by thermodynamic modeling. The difference in the liquidus temperature during heating and cooling cycles indicates super-cooling effect which is not uncommon for metallic glass systems like Mg-Ni-Y. The calculated vertical section at 6.3 at.% Y with DSC signals of sample 2 is shown in Figure 7-26 (b). It can be seen in this figure that the measured transformation temperatures correspond to three phase boundaries in the vertical section: $L / L+\tau_{12} / L+\tau_{12}+\text{Mg}_2\text{Ni} / \tau_3+\tau_{12}+\text{Mg}_2\text{Ni}$, occurring at 814, 761 and 741 K, respectively.

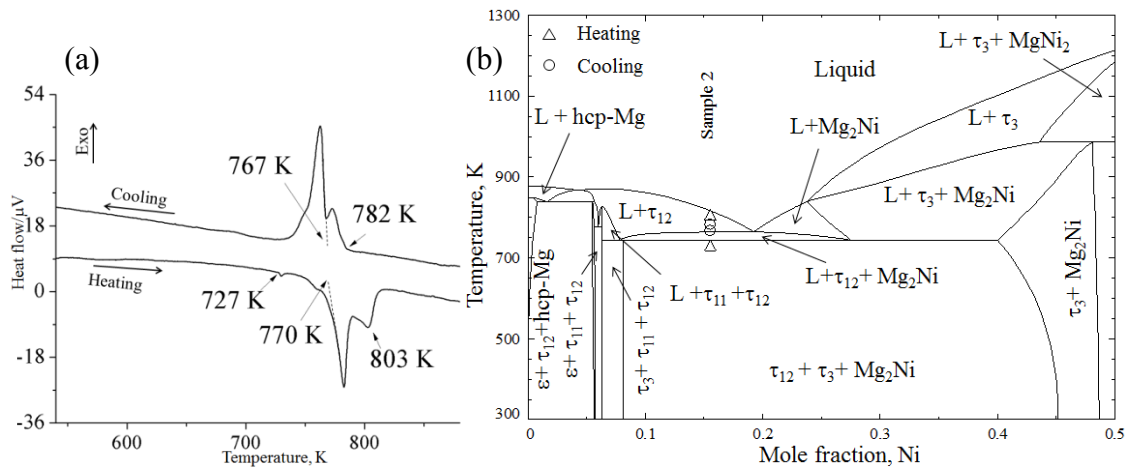
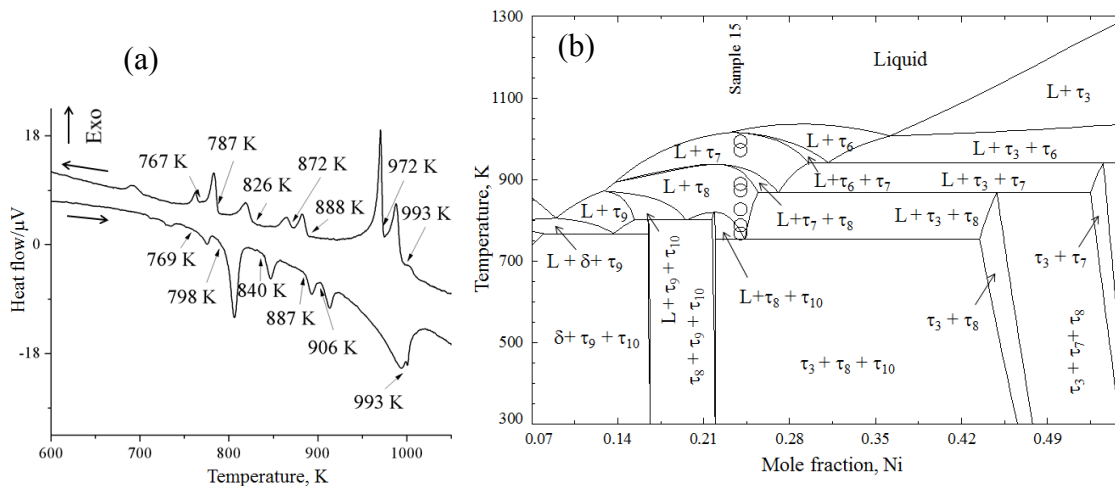


Figure 7-26: (a) DSC spectra during heating and cooling; (b) Calculated vertical section at 6.3 at.% Y with DSC signals of sample 2 (78.2/15.5/6.3 Mg/Ni/Y at.%)

Sample 15 (54.1/24.0/21.9 Mg/Ni/Y at.%) is located in the three-phase field of τ_3 , τ_8 and τ_{10} as is shown in Figure 7-25. The DSC spectra of this alloy are shown in Figure 7-27 (a). The presence of several arrests suggested the occurrence of a rather complex

melting behavior. The complexity arises because of the presence of three incongruent melting compounds (τ_7 , τ_8 and τ_{10}) in close proximity. These compounds decompose in a narrow temperature range as can be seen in the corresponding vertical section in Figure 7-27 (b). τ_6 is a congruent melting compound which has large solubility range. It dominates the liquidus surface in this region. Therefore, during solidification the alloy passes through several phase transformations which resulted in complex DSC spectra. However, an effort has been made to separate these thermal events according to the equilibrium phase transformation which has been listed in Figure 7-27 (c). The experimental results and thermodynamic calculations show reasonable agreement.



(c) Sample	DSC thermal signals, K	Thermodynamic calculation	
		Temperature, K	Reaction or phase boundary
15	993c/993h	1020	L / L+ τ_6
	972c	1013	L+ τ_6 / L+ τ_7
	888c/906h	927	L+ τ_7 / L+ τ_7 + τ_8
	872c/887h	916	L+ τ_7 + τ_8 / L+ τ_8
	826c/840h	-	-
	787c/798h	780	L+ τ_8 / L+ τ_8 + τ_{10}
	767c/769h	751	L+ τ_8 + τ_{10} / τ_3 + τ_8 + τ_{10}

Figure 7-27: (a) DSC spectra during heating and cooling; (b) Calculated vertical section at 21.94 at.% Y with DSC signals; (b) DSC measurements and calculated transformation temperature of sample 15 (54.1/24.0/21.9 Mg/Ni/Y at.%)

Sample 14 is located in the $\tau_3+\tau_6+\tau_7$ phase field as shown in Figure 7-25. The DSC spectra, Figure 7-28 (a), registered three peaks during heating that reoccurred in the cooling curve. The first peak occurred at 1062 and 1059 K in cooling and heating curves, respectively. This represents the liquidus temperature which has been found as 1091 K in the thermodynamic calculation. The next two thermal arrest points occurred at 982 and 883 K during cooling and 990 and 895 K during heating. The DSC signals have been projected on the vertical section at 26.5 at.% Y as shown in Figure 7-28 (b). It shows good agreement.

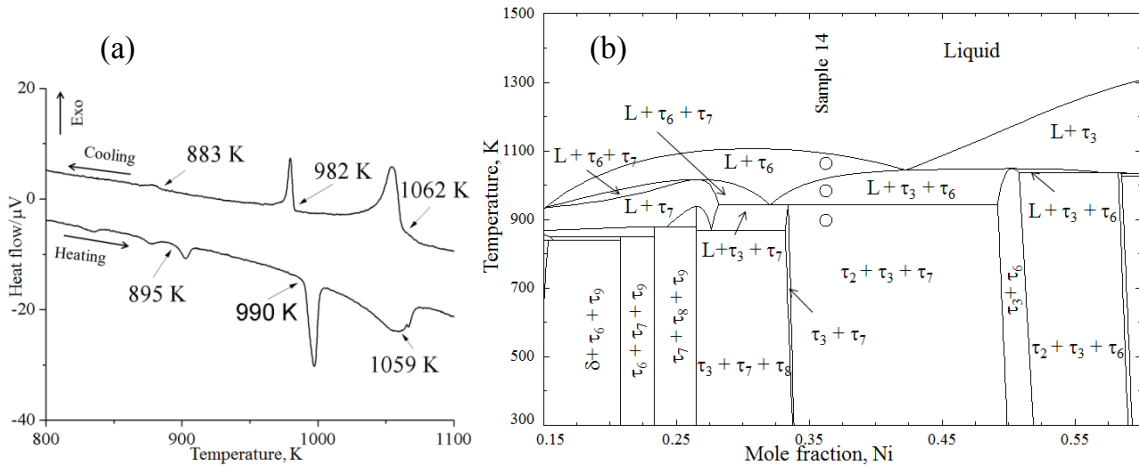
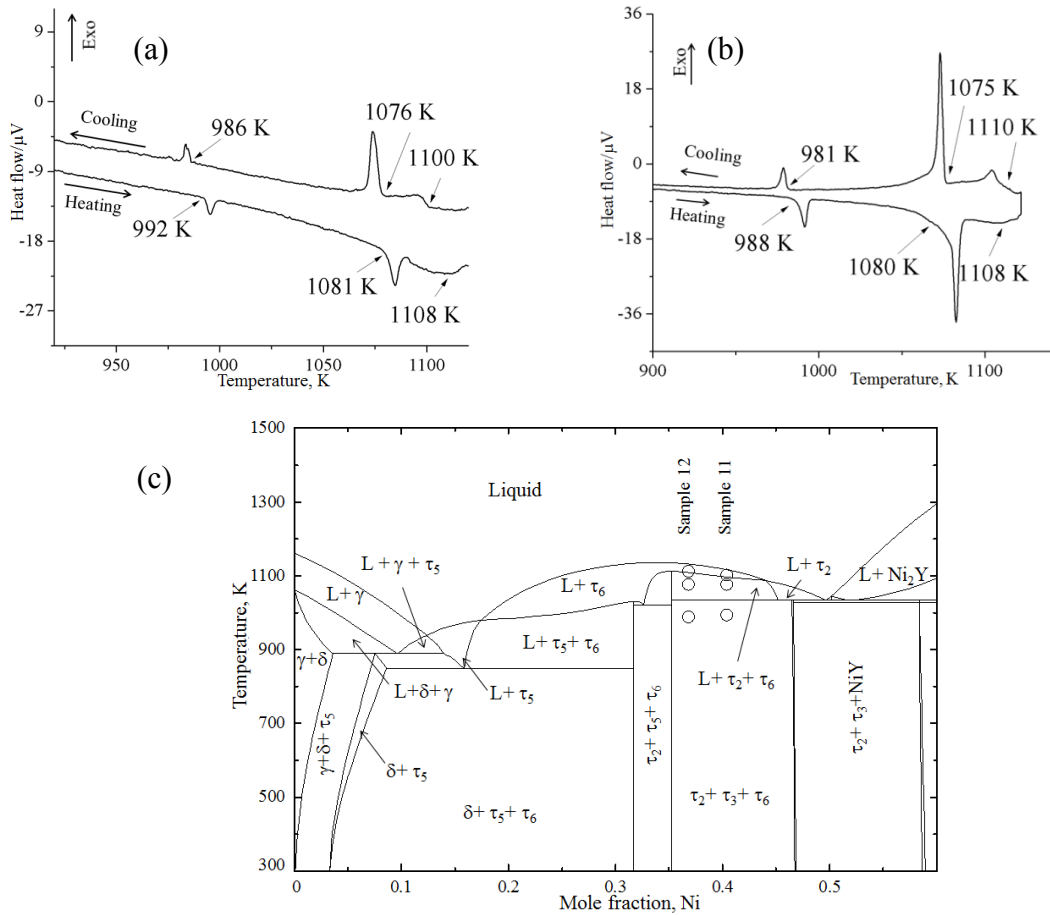


Figure 7-28: (a) DSC spectra during heating and cooling; (b) Calculated vertical section at 26.5 at.% Y with DSC signals of sample 14 (37.2/36.3/26.5 Mg/Ni/Y at.%)

Both samples 11 (23.8/40.4/35.8 Mg/Ni/Y at.%) and 12 (28.0/36.8/35.2 Mg/Ni/Y at.%) are located in the $\tau_2+\tau_3+\tau_6$ phase field as shown in Figure 7-25. The DSC spectra of these alloys are shown in Figure 7-29 (a) and (b) respectively. Sample 11 shows three peaks during heating that were also encountered during cooling. The liquidus temperature has been found to be 1100 K during cooling. The other two signals were observed at 1076 K during cooling and 992 K during heating which occurred due to the transformations: $L+\tau_6$ / $L+\tau_2+\tau_6$ / $\tau_2+\tau_3+\tau_6$. Similar DSC spectra were observed for

sample 12 with slightly higher liquidus temperature at 1110 K during cooling. This demonstrates the repeatability of the experiments since both samples are in close proximity.



(d) Sample	DSC thermal signals, K	Thermodynamic calculation	
		Temperature, K	Reaction or phase boundary
11	1100c/1108h	1114	L / L+ τ_6
	1076c/1081h	1099	L+ τ_6 / L+ τ_2 + τ_6
	986c/992h	1032	L+ τ_2 + τ_6 / τ_2 + τ_3 + τ_6
12	1110c/1108h	1125	L / L+ τ_6
	1075c/1080h	1103	L+ τ_6 / L+ τ_2 + τ_6
	981c/988h	1033	L+ τ_2 + τ_6 / τ_2 + τ_3 + τ_6

Figure 7-29: DSC spectra of (a) sample 11 (26.0/38.2/35.8 Mg/Ni/Y at.%); (b) sample 12 (28.0/36.8/35.2 Mg/Ni/Y at.%); (c) Calculated vertical section at 35.2 at.% Y; (d) DSC measurements and calculated transformation temperature of samples 11 and 12

A vertical section at 35.2 at.% Y has been calculated as shown in Figure 7-29 (c). The DSC thermal arrests for samples 11 and 12 have been superimposed on the vertical section to verify the calculated transformation temperatures along with the associated reactions. It can be observed that the liquidus temperatures are in good agreement with the experimental measurements. A detailed comparison between the experimental and thermodynamic calculation has been shown in Figure 7-29 (d).

Sample 28 (49.9/8.0/42.1 Mg/Ni/Y at.%) is located in the $Mg_2Y(\delta)+MgY(\gamma)+\tau_5$ phase field as shown in Figure 7-25. Three transformation temperatures are registered by DSC spectra of this sample as shown in Figure 7-30 (a). The liquidus temperature was recorded at 1116 K. Two close peaks have been observed at 948 and 940 K during heating which reoccurred at 981 and 974 K during cooling. These findings can be correlated with the vertical section in Figure 7-30 (b). It shows reasonable agreement.

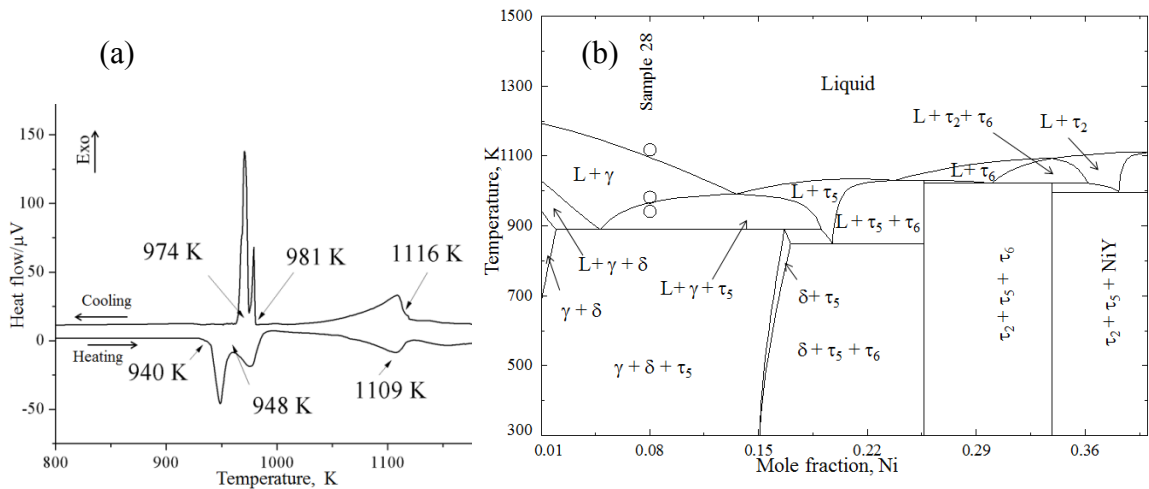


Figure 7-30: (a) DSC spectra during heating and cooling; (b) Calculated vertical section at 42.1 at.% Y with DSC signals of sample 28 (49.9/8.0/42.1 Mg/Ni/Y at.%)

Sample 27 (38.2/15.0/46.8 Mg/Ni/Y at.%) is located in the three-phase region of τ_5 , $MgY(\gamma)$ and $Mg_2Y(\delta)$ as can be seen in Figure 7-25. DSC spectra of this sample

during heating and cooling runs are shown in Figure 7-31 (a). Three peaks appear during heating that reoccurred during cooling. Correspondingly, the liquidus temperature was registered at 980 K. It can be seen that the first two cooling as well as the heating peaks overlapped. This is because of the presence of two close transformations; $L / L + \tau_1 + \tau_5 / L + \text{MgY}(\gamma) + \tau_5$, as can be seen in the calculated vertical section at 15.0 at.% Ni in Figure 7-31 (b). According to the thermodynamic calculation τ_5 starts to form at 1007 K while $\text{MgY}(\gamma)$ and $\text{Mg}_2\text{Y}(\delta)$ begin precipitating at 997 and 888 K, respectively. It demonstrates reasonable agreement with the DSC measurements.

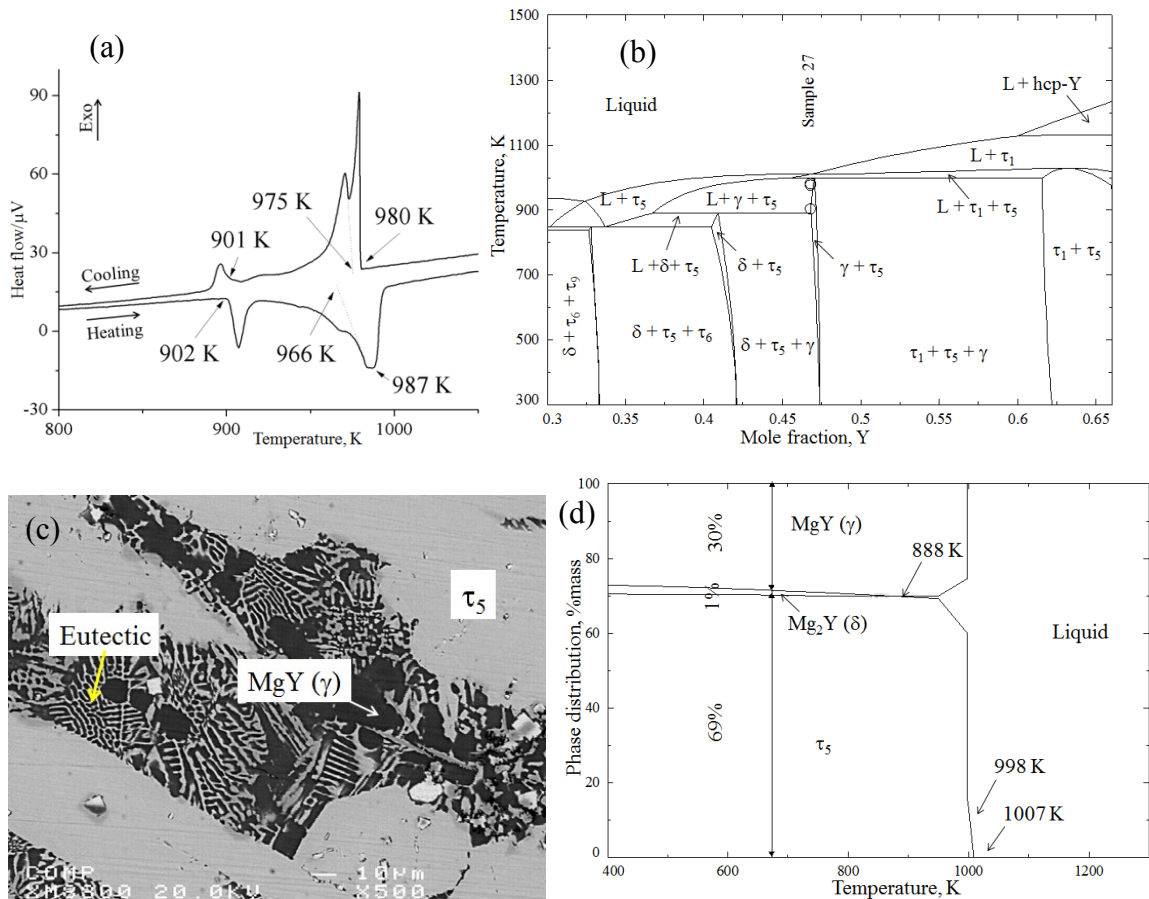


Figure 7-31: DSC spectra during heating and cooling; (b) Calculated vertical section at 46.8 at.% Y with DSC signals; (c) BSE image; (d) calculated phase assemblage diagram of sample 27 (38.2/15.0/46.8 Mg/Ni/Y at.%)

Sample 27 is located at the border of the three-phase region $\tau_5 + \text{MgY}(\gamma) + \text{Mg}_2\text{Y}(\delta)$. Hence, the microstructure is mainly consists of τ_5 and $\text{MgY}(\gamma)$ as can be seen in Figure 7-31 (c). The phase assemblage diagram in Figure 7-30 (d) shows that only 1 wt.% of the total alloy is $\text{Mg}_2\text{Y}(\delta)$ which could not be found in the microstructure. It also shows that about 69 wt.% of the alloy is τ_5 which in agreement with the microstructure. This alloy is located on a univariant valley as can be seen on the liquidus projection in Figure 4-23. For this reason, the eutectic structure clearly occurs in the microstructure as can be seen in Figure 7-31 (c).

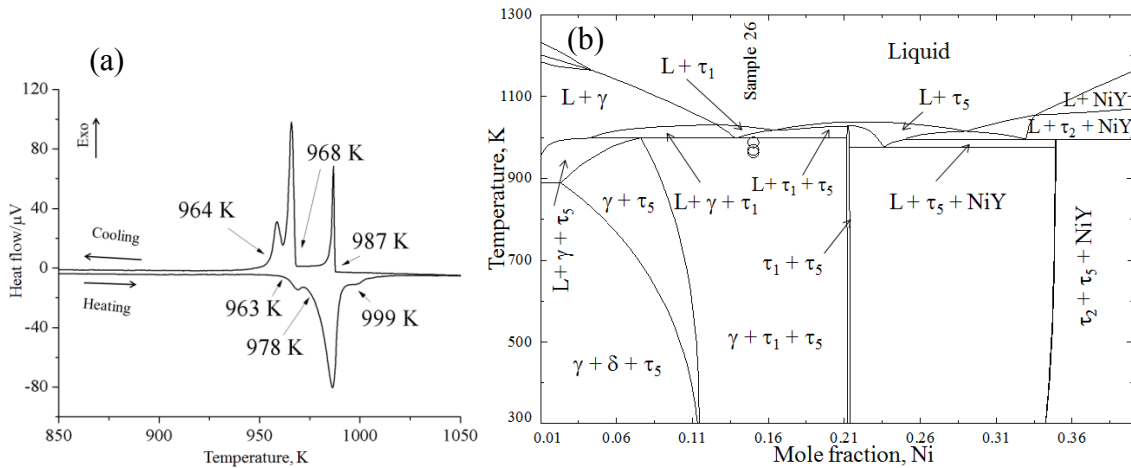


Figure 7-32: (a) DSC spectra during heating and cooling; (b) Calculated vertical section at 48.0 at.% Y with DSC signals of sample 26 (37.0/15.0/48.0 Mg/Ni/Y at.%)

The DSC spectra of sample 26 (37.0/15.0/48.0 Mg/Ni/Y at.%) in Figure 7-32 (a) clearly shows three peaks during heating which reoccurred during cooling. The liquidus temperature of this alloy should be between 987 K and 999 K which is calculated 1023 K using the thermodynamic modeling as can be seen in Figure 7-32 (b). The second peak during cooling was found at 968 K because of $L + \tau_1 / L + \tau_1 + \tau_5$ phase transformation. The solidus temperature from the heating curve was obtained at 963 K compared to 996 K from thermodynamic calculation. The deviation between the experimental results and

calculation is about 33 K. Better agreement with the experimental measurement could not be obtained without sacrificing consistency in other regions of the phase diagram.

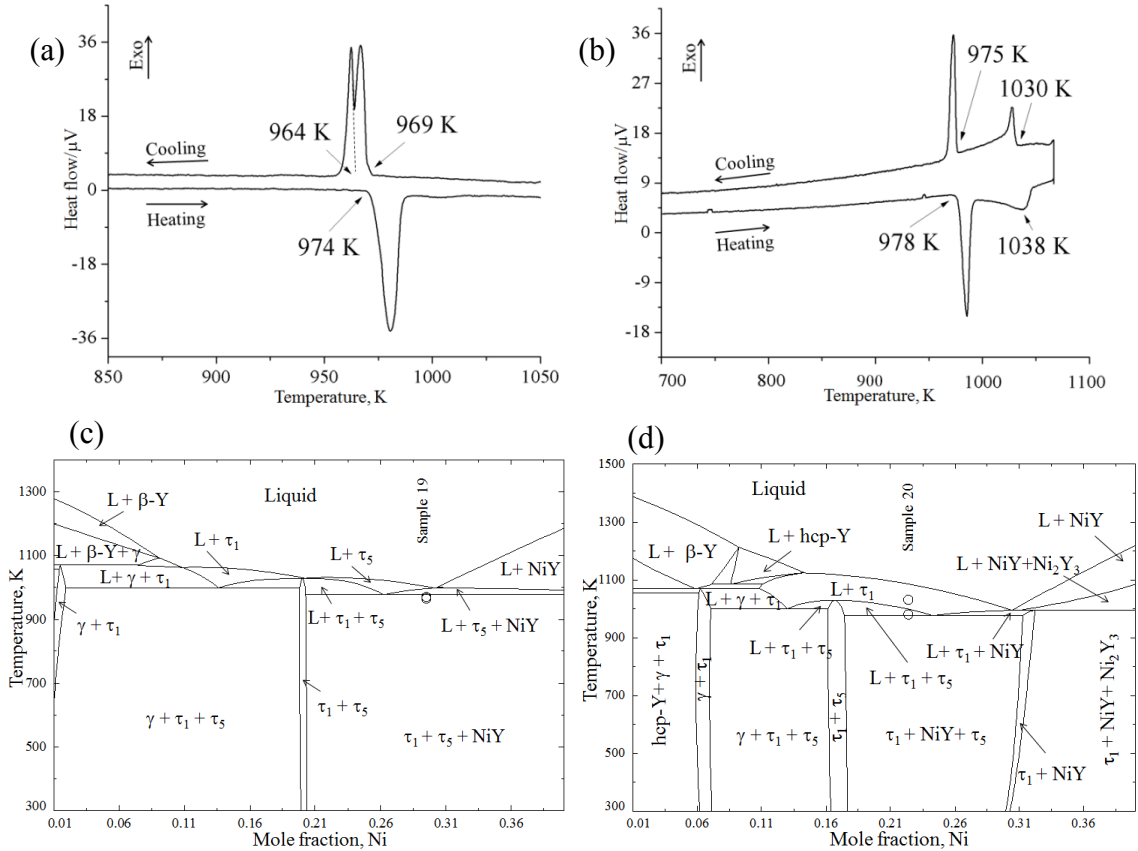


Figure 7-33: DSC spectra of (a) sample 19 (19.5/29.5/51.0); (b) sample 20 (18.5/22.4/59.1 Mg/Ni/Y at.%) during heating and cooling; Calculated vertical section at (c) 51.0 at.% Y; (d) 59.1 at.% Y with DSC signals of sample 20

Samples 19 (19.5/29.5/51.0) and 20 (18.5/22.4/59.1 Mg/Ni/Y at.%) are in the same three-phase region of NiY, τ_1 and τ_5 as can be seen in Figure 7-25. The DSC spectra of these two samples are shown in Figure 7-33 (a) and (b). Sample 19 shows two very close exothermic peaks during the cooling cycle suggesting the presence of small solidification range and the likelihood of an invariant transformation nearby. These two peaks have been overlapped during the heating cycle. Areas under the curve between the cooling (-53.5 J/g) and heating peaks (59.4 J/g) are similar which suggests that the

heating peak is in fact two overlapping peaks. The liquidus temperature has been registered at 969 K. The second thermal arrest has been observed at 964 and 974 K during cooling and heating, respectively. Sample 20 shows two peaks during heating and cooling. The liquidus temperature was found at 1030 K. The other thermal event occurred at 975 and 978 K during cooling and heating, respectively.

Vertical sections of samples 19 and 20 have been calculated as shown in Figure 7-33 (c) and (d). The DSC thermal arrests are projected on them which show reasonable agreement except the liquidus temperature of sample 20. This alloy is located near τ_1 which has a large solubility range as can be seen in Figure 7-25. It was not possible to reproduce the solubility thermodynamically while keeping low liquidus temperature. Hence it is decided to accept a higher liquidus surface. According to the DSC spectra of these two samples an invariant reaction occurs at approximately 974 K which corresponds well with the calculated eutectic reaction ($L \rightleftharpoons \tau_1 + \text{NiY} + \tau_5$) at 977 K. The lamellar structure in the BSE image of sample 19, in Figure 7-34 (a) occurred due to this eutectic reaction. The phase assemblage diagram in Figure 7-34 (b) shows the relative amount of the phases which are in reasonable qualitative agreement with the microstructure.

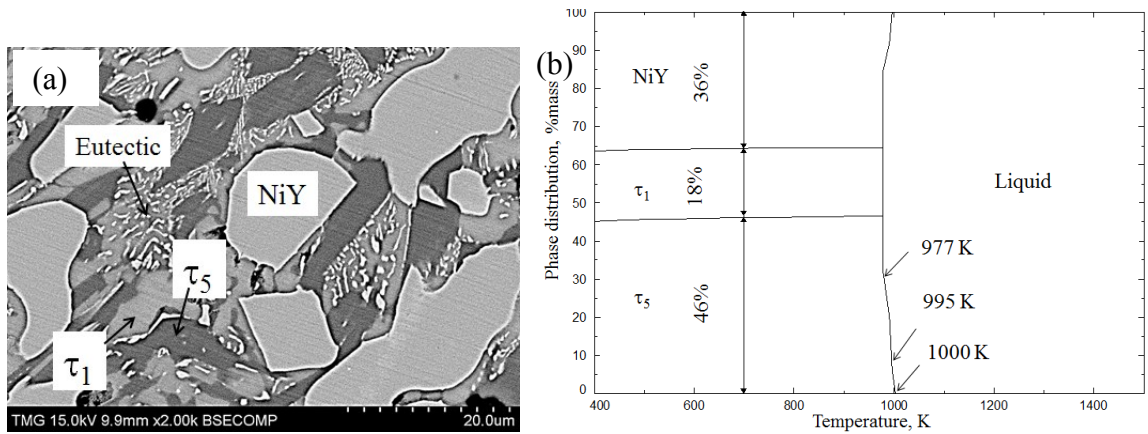


Figure 7-34: (a) BSE image; (b) phase assemblage diagram of sample 19

In order to obtain better understanding of the consistency of the thermodynamic modeling with the experimental data two vertical sections have been calculated as shown in Figure 7-35 and 7-36. These vertical sections contain experimental data of seven key samples allowing overall visualization of the general acceptable agreement with the thermodynamic calculations.

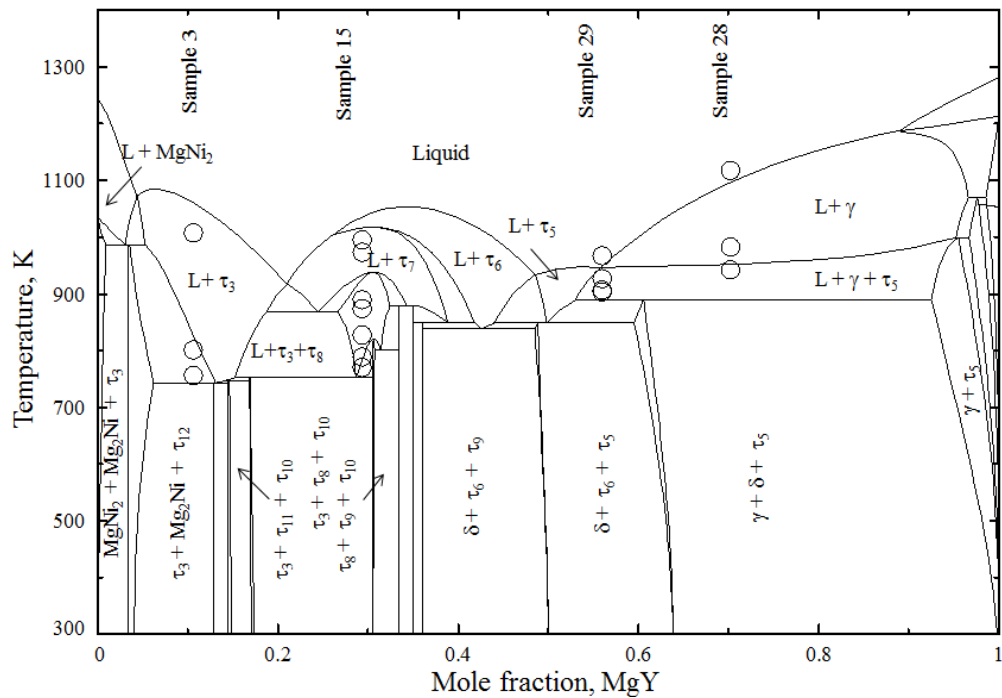


Figure 7-35: Vertical section along $Mg_{56}Ni_{44} - MgY$

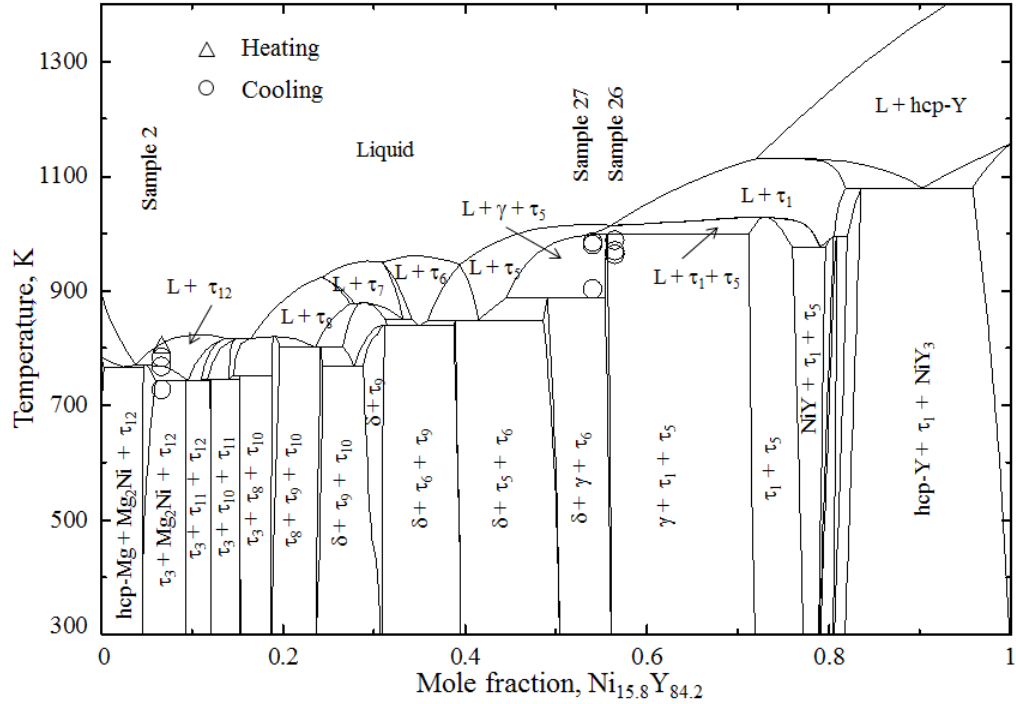


Figure 7-36: Vertical section along $Mg_{84.2}Ni_{15.8} - Ni_{15.8}Y_{84.2}$

Mg-Ni-Y is a promising system due its glass forming ability. This makes it susceptible for super cooling effect. Hence, the liquidus temperatures of the alloys determined in the DSC measurements have been found slightly lower than the calculated one. The liquidus temperature of sample 2 obtained from both the heating and cooling cycle is also projected on the vertical section in Figure 7-36. The difference of the liquidus temperature in the two cycles is due to the super-cooling effect.

The phase relations of this system are very complex which makes it difficult to obtain a very good agreement between the thermodynamic calculation and experimental data. However, the above discussion of the DSC experimental data of the key alloys showed consistency in terms of number of phase transformation with thermodynamic calculations. The maximum deviation between the experimental and calculated temperature is around 45 K. Considering the complexity of the system it is decided to accept this amount of discrepancy.

Chapter 8

Experimental Investigation of the Cu-Ni-Y System

In the following sections the phase equilibrium of the Cu-Ni-Y system will be discussed. The analysis of two solid-solid diffusion couples in section 8.1 will show the existence of the ternary solubility of the binary compounds. Section 8.2 will demonstrate the isothermal section at 973 K of the Cu-Ni-Y system based on the diffusion couple and key sample analysis. The complete mutual solubility of CuY-NiY and Cu₄Y-Ni₄Y will be conferred in sections 8.3 and 8.4 respectively. Also, the partial solubility of Ni₅Y will be discussed in section 8.5. Finally, in section 8.6 an extensive discussion of the key alloys in light of XRD and SEM/WDS analysis will be carried out. Comparison between the thermodynamic modeling and experimental work will also be demonstrated in this section.

8.1 Diffusion couples

Backscatter electron (BSE) images of the solid–solid diffusion couple-1 annealed at 973 K for 6 weeks with gradually increased magnification of the area of interest are shown in Figure 8-1 (a), (b) and (c). The end member 1 (Cu/Ni/Y 80.9/14.1/5.0 at.%) is a two phase region of fcc and Ni₅Y. The other end member (Cu/Ni/Y 15.9/9.1/75.0 at.%) consists of three phases of (CuY), NiY₃ and hcp-Y. Here, (CuY) refers to the solid solution between CuY and NiY. The two end members are closer to the Cu-Y side, one

with high Cu and the other with high Y concentration. They were chosen in order to identify the ternary solubility of the binary compounds of the Cu-Y system.

During heat treatment, extensive inter-diffusion of Cu, Ni and Y took place allowing various equilibrium phases to form. A WDS line scan was used to determine the solubility of Cu_2Y and (CuY) , as shown in Figure 8-1 (a). Spot analysis was carried out to deduce the boundaries of the two-phase $(\text{NiY}_3+\text{CuY})$ region. On the basis of the compositional information, the solid solubility of Ni in the Cu-Y binary compounds was evaluated. Benefitting from the local equilibrium at the interfaces formed between diffusion layers, the sequence of phases along the diffusion path was deduced as:

$\{\text{fcc}(\text{Cu}, \text{Ni})+\text{Ni}_5\text{Y}\}(\text{end member}) \rightarrow \text{Ni}_5\text{Y} \rightarrow \text{Ni}_5\text{Y} + \text{Cu}_2\text{Y} \rightarrow \text{Cu}_2\text{Y} \rightarrow \text{Cu}_2\text{Y} + (\text{CuY}) \rightarrow (\text{CuY}) \rightarrow (\text{CuY}) + \text{NiY}_3 \rightarrow \{(\text{CuY})+\text{NiY}_3+\text{hcp-Y}\}(\text{end member})$. Figure 8-1 (d) shows the estimated diffusion path projected on the Cu-Ni-Y Gibbs triangle.

Figure 8-2 summarizes the results of 1.125 mm WDS line scan across 2 diffusion layers, Cu_2Y and (CuY) , and spot analysis of the other zones. The diffusion layer of Ni_5Y kept breaking during polishing and was difficult to analyze by WDS line scan. However, spot WDS analysis was possible on a few Ni_5Y retained regions. The next layer is very stable and is about 1mm thick. It represents the ternary solubility of Cu_2Y . The line scan of this layer shows almost constant concentration of the three constituents as shown in Figure 8-2. It is probably because of the distinctive location of the end members (a line connecting the two end members is almost perpendicular to the solubility line) which does not allow diffusion path to move horizontally. Therefore, it forms a thick layer with almost constant composition.

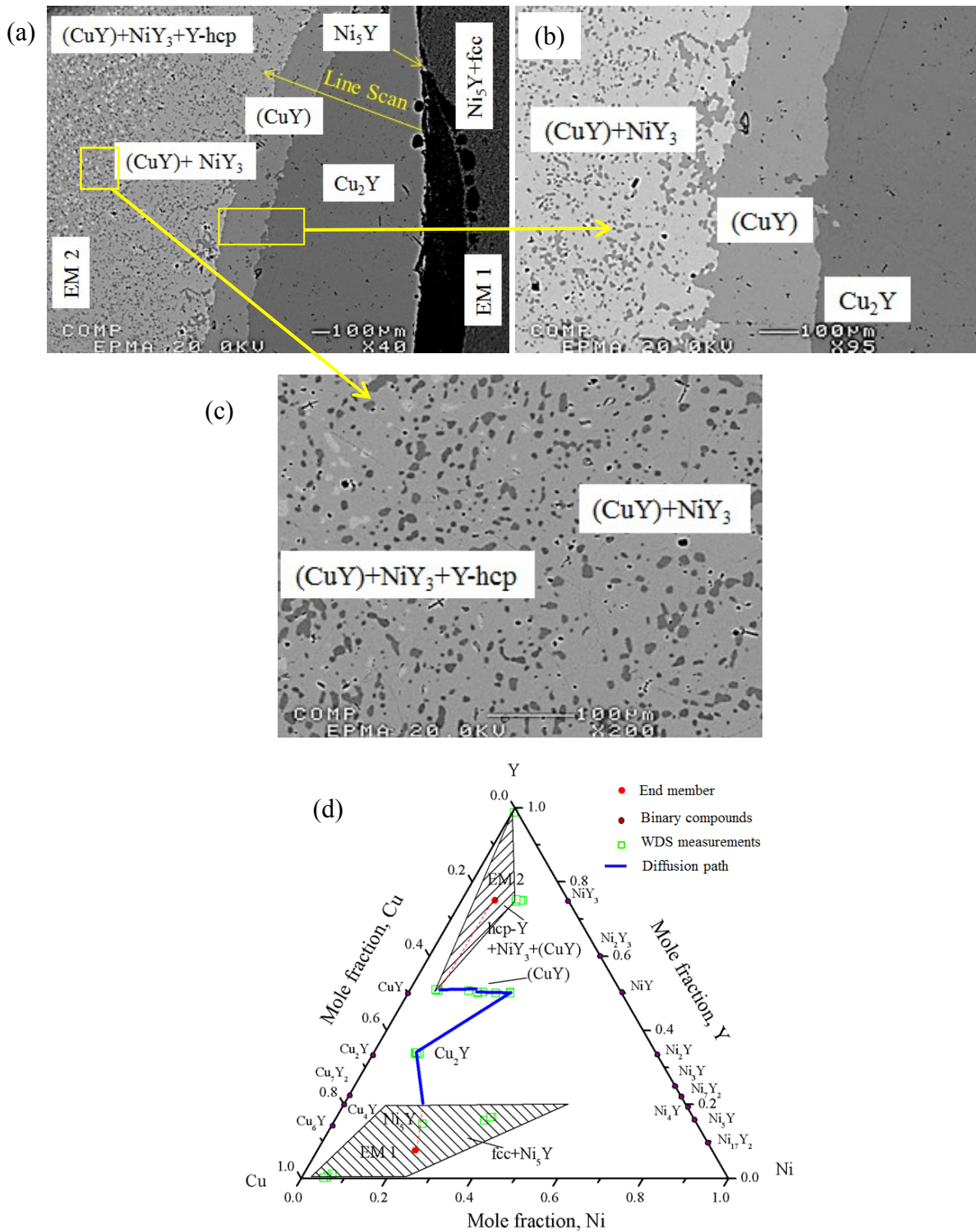


Figure 8-1: (a-c) BSE images of the solid–solid diffusion couple-1 annealed at 973 K for 6 weeks, showing the formation of four intermetallic compounds; (d) diffusion path projected on the Cu-Ni-Y Gibbs triangle.

The layer after this is about 100 μm and represents (CuY). The concentration profile of this layer (Figure 8-2) reveals that the (CuY) forms a substitutional solid solution where Cu substitutes for Ni atoms while the Y content remains constant at ~ 50 at.%. The next layer is a two phase region between (CuY) and NiY_3 phase. The concentration profile in Figure 8-2 for the two-phase region of (CuY)+ NiY_3 has been obtained by spot analysis of the phases taking measurements at approximately equal distances through a line perpendicular to the interface. The profile shows constant Y concentrations of ~ 50 and ~ 75 at.% in (CuY) and NiY_3 , respectively. However, variation in the Cu and Ni concentrations can be observed for (CuY). As can be seen in Figure 8-2 in the NiY_3 +(CuY) region, the concentration of Cu is increasing and that of Ni is decreasing. This reveals the substitution of Ni by Cu for (CuY). After this the three phase region (CuY+ NiY_3 +hcp-Y) of the end member can be seen.

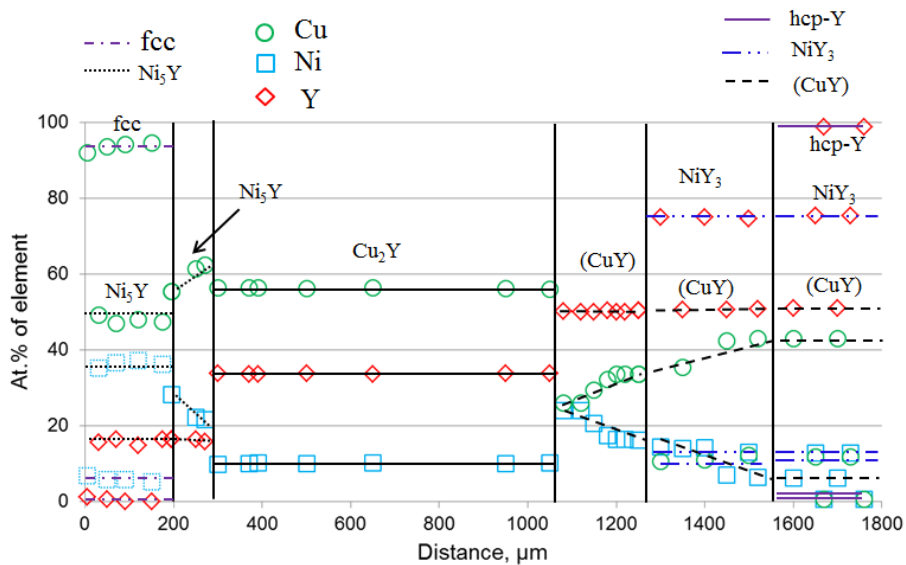


Figure 8-2: Composition profile of the diffusion couple 1 along the line scan shown in figure 1(a). Different phases have been represented by different line type for clear understanding.

No phases can be found between the Ni_5Y and Cu_2Y layer, which is not in agreement with key sample analysis in this region that suggests the presence of (Cu_4Y) phase. This is probably due to the highly stable Cu_2Y phase which hinders the diffusion of Y atoms to the next layer. However, the diffusion couple approach does not always lead to the formation of all possible phases. The possibility of missing phase is a common phenomenon [163]. In order to overcome this uncertainty, a combined investigation with key samples has been followed and will be discussed.

The BSE image of the 2nd solid-solid diffusion couple is shown in Figure 8-3 (a) and (b). The diffusion path is shown in Figure 8-3 (c). The end member 1 (Cu/Ni/Y 30.4/62.2/7.4 at.%) is a two-phase region of fcc and Ni_{17}Y_2 . The other end member (Cu/Ni/Y 22.7/47.1/30.2 at.%) consists of three phases; Cu_2Y , Ni_2Y and Ni_3Y . The end members are chosen close to each other in this fashion in order to force the formation of the intermetallic layers of Ni_5Y , (Cu_4Y) and Ni_3Y . Here, (Cu_4Y) refers to the complete mutual solubility between Cu_4Y and Ni_4Y which will be discussed in section 8.4. Two diffusion layers can be seen clearly in the BSE image. The WDS analysis identifies these two layers as Ni_5Y and Ni_3Y . A line scan has been done through these two layers and the compositional profile is shown in Figure 8-4. A careful observation of the profile shows the presence of (Cu_4Y) in between Ni_5Y and Ni_3Y . The Y content in this layer has been found to be constant at about 20.9 at.% while Ni atoms were substituted by Cu atoms. The solubility of Cu in (Cu_4Y) was observed to be from about 30 to 40 at.% Cu.

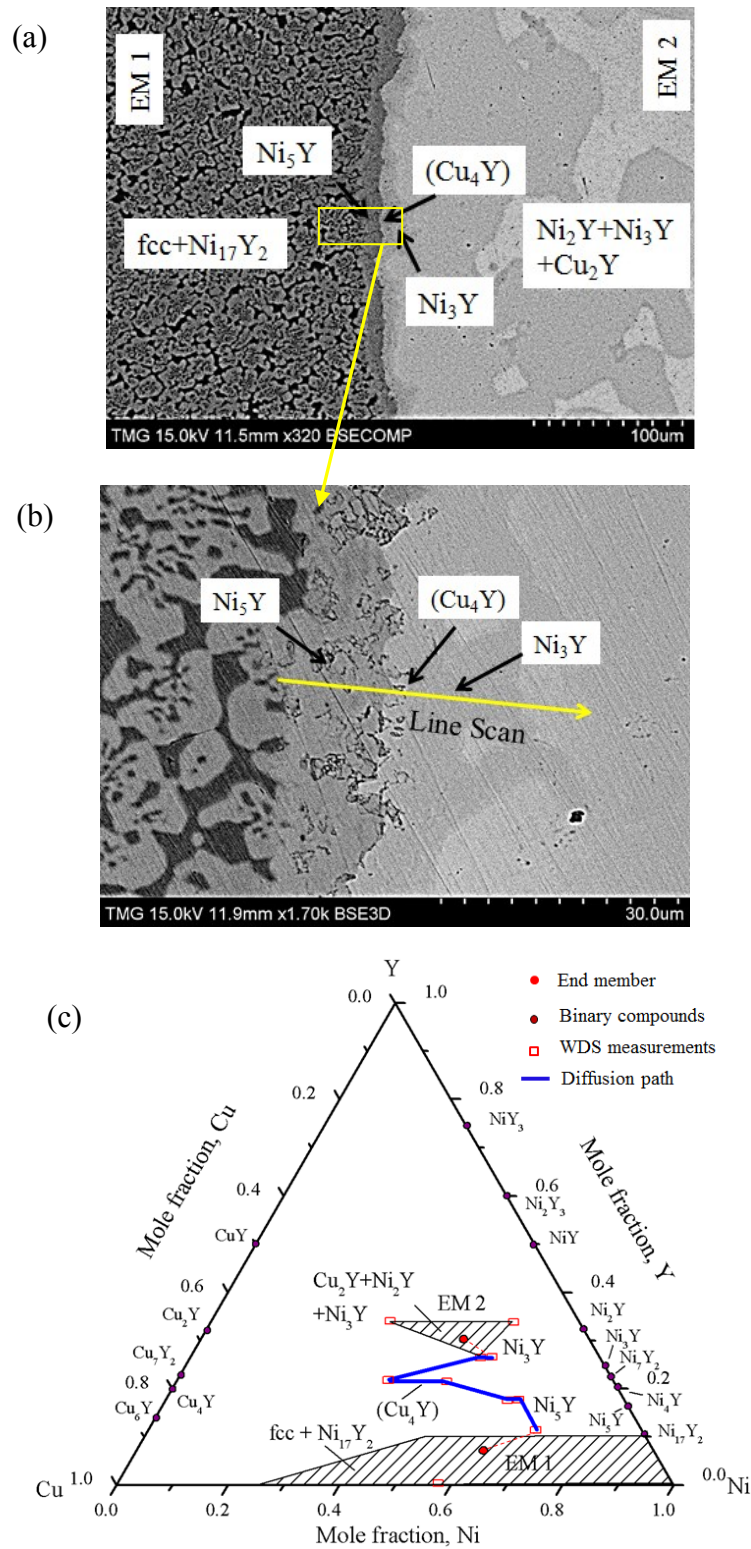


Figure 8-3: (a, b) BSE images of the solid–solid diffusion couple 2 annealed at 973 K for 6 weeks, showing the formation of six intermetallic compounds; (c) diffusion path in the Cu-Ni-Y Gibbs triangle.

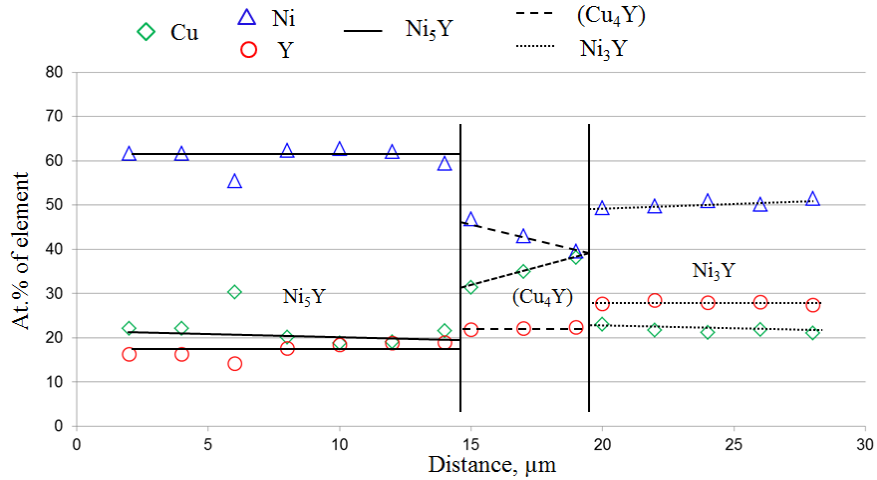


Figure 8-4: Composition profile of the diffusion couple 2 along the line scan shown in figure 3(b). Different phases have been represented by different line types for clear understanding.

The sequence of phases along the diffusion path was deduced as: {fcc+Ni₁₇Y₂} (end member) → Ni₅Y → Ni₅Y + Ni₄Y → (Cu₄Y) → (Cu₄Y)+Ni₃Y → Ni₃Y → {Ni₃Y+Ni₂Y+Cu₂Y} (end member). The first diffusion layer is about 12 μm thick and is identified as Ni₅Y phase. The next layer is very thin about 4 μm representing (Cu₄Y). The subsequent layer is about 12 μm thick and is identified as Ni₃Y. Because of the small contrast between these two layers, (Cu₄Y) and Ni₃Y, it was not possible to visualize them separately in the BSE image. After this layer the diffusion path terminates in the three phase region of the end member, Ni₃Y+Ni₂Y+Cu₂Y.

8.2 Isothermal section based on diffusion couples and key alloys analysis

29 key alloys have been prepared and investigated in order to construct the isothermal section at 973 K. Based on the WDS and XRD analysis of these alloys and two diffusion couples, the isothermal section at 973 K has been constructed as shown in Figure 8-5.

The actual global composition of the key alloys and WDS results are summarized in Table 8-1.

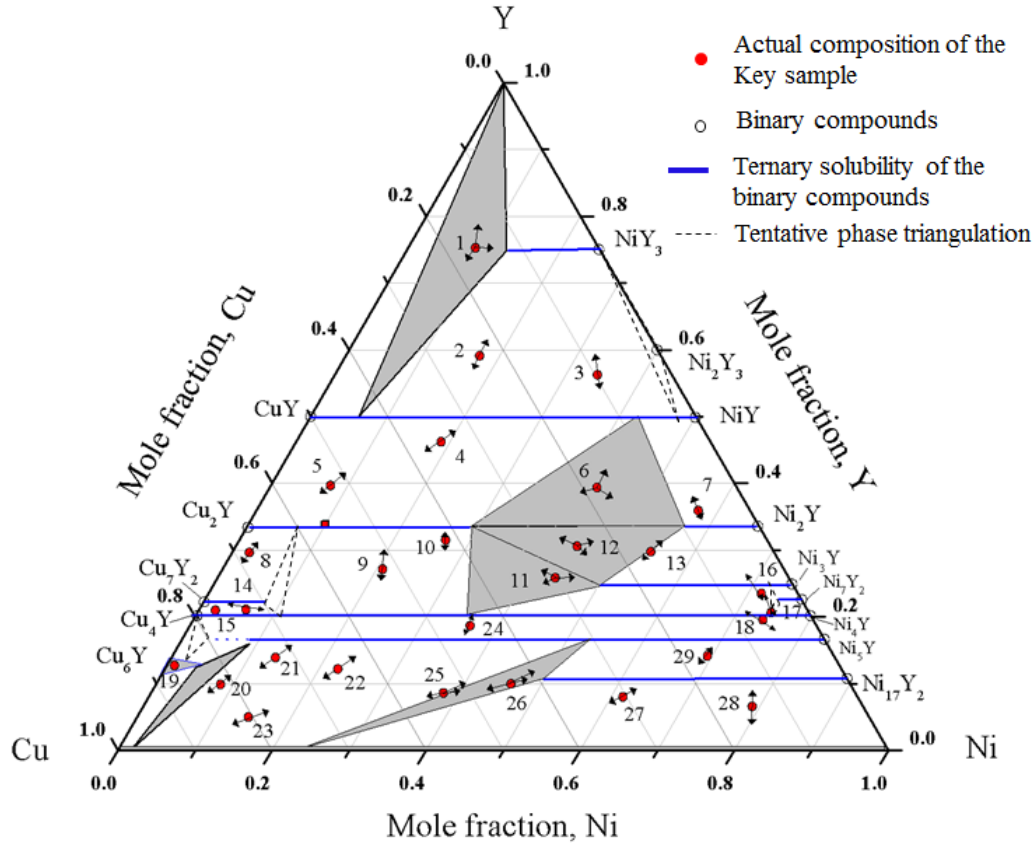


Figure 8-5: Isothermal section of the Cu-Ni-Y system at 973 K. The arrow heads point to the location of the phase composition.

Some of the three-phase regions in the Cu-Ni-Y system could not be identified clearly. They have been constructed based on the tendency of the phase development in the region. These are: $\text{NiY}+\text{Ni}_2\text{Y}_3+\text{NiY}_3$, $\text{Ni}_3\text{Y}+\text{Ni}_7\text{Y}_2+(\text{Cu}_4\text{Y})$, $\text{Cu}_7\text{Y}_2+\text{Cu}_2\text{Y}+(\text{Cu}_4\text{Y})$ and $\text{Cu}_6\text{Y}+(\text{Cu}_4\text{Y})+\text{Ni}_5\text{Y}$. All these three-phase regions are expected to be present in the equilibrium phase diagram as the constituent compounds are stable in the binary systems at this temperature. These regions are very thin and it is very difficult to prepare alloys that lie in them. Therefore, they have been shown by dotted lines on the isothermal section in Figure 8-5. Zheng and Nong [6] reported a three-phase region among Ni_5Y ,

Cu₆Y and fcc phase based on their XRD analysis. This has been accepted in the current work.

Table 8-1: WDS data on the Cu-Ni-Y alloys annealed at 973 K

Actual composition				Identified phases			
No	at. %			Name	Compositions by WDS		
	Cu	Ni	Y		Cu	Ni	Y
1	20.8	9.1	70.1	(CuY)	43.1	6.2	50.7
				NiY ₃	12.0	12.9	75.1
				hcp-Y	0.9	0.5	98.6
2	23.3	17.2	59.5	NiY ₃	8.8	17.0	74.2
				NiY	32.4	17.3	50.3
3	8.4	35.5	56.1	NiY ₃	2.1	22.3	75.6
				(CuY)	12.0	36.6	52.4
4	34.9	18.7	46.4	(CuY)	26.7	22.3	51.0
				Cu ₂ Y	54.9	9.6	35.5
5	50.8	8.7	40.5	Cu ₂ Y	60.5	4.1	35.4
				(CuY)	35.9	12.7	51.4
6	18.2	42.7	39.1	(CuY)	7.4	42.2	50.4
				Ni ₂ Y	10.8	57.4	31.8
				Cu ₂ Y	38.5	28.0	33.5
7	6.2	58.2	35.6	(CuY)	4.7	44.9	50.4
				Ni ₂ Y	7.1	60.7	32.2
8	68.2	2.2	29.6	Cu ₂ Y	61.9	3.2	34.9
				Cu ₇ Y ₂	76.6	1.0	22.4
9	52.1	20.8	27.1	Cu ₂ Y	47.5	17.7	34.8
				(Cu ₄ Y)	55.8	23.0	21.2
10	46.5	24.4	29.1	Cu ₂ Y	40.8	25.6	33.6
				(Cu ₄ Y)	46.7	32.0	21.3
11	30.3	43.8	25.9	Cu ₂ Y	38.2	27.4	34.4
				Ni ₃ Y	25.6	48.5	25.9
				(Cu ₄ Y)	43.5	35.5	21.00
12	25.1	44.2	30.7	Cu ₂ Y	33.4	31.0	35.6
				Ni ₂ Y	12.2	55.6	32.2
				Ni ₃ Y	20.3	53.3	26.4
13	15.9	54.4	29.7	Ni ₂ Y	11.3	55.0	33.7
				Ni ₃ Y	20.4	52.7	26.9
14	72.7	6.0	21.3	Cu ₇ Y ₂	74.5	3.6	21.9
				(Cu ₄ Y)	70.3	8.3	21.4
15	78.0	3.5	18.5	(Cu ₄ Y)	76.8	3.4	19.8
16	4.7	71.8	23.5	Ni ₃ Y	6.2	67.0	26.8
				Ni ₇ Y ₂	5.8	70.6	23.6

Table 8-1 (continued)

Actual composition				Identified phases			
No	at.%			Name	Compositions by WDS		
	Cu	Ni	Y		Cu	Ni	Y
17	5.0	74.9	20.1	(Cu ₄ Y)	3.1	77.6	19.4
				Ni ₇ Y ₂	4.1	74.1	21.8
				Ni ₃ Y	4.5	70.8	24.8
18	6.5	73.9	19.6	(Cu ₄ Y)	8.4	70.7	20.9
				Ni ₅ Y	5.6	75.8	18.6
19	85.6	1.4	13.0	Cu ₆ Y	84.5	1.5	14.0
20	81.8	8.5	9.7	Ni ₅ Y	72.9	11.7	15.4
				fcc	97.9	1.8	0.3
21	72.4	13.1	14.5	Ni ₅ Y	70.3	13.7	16.0
				fcc	97.4	0.0	2.6
22	65.6	22.3	12.1	Ni ₅ Y	52.7	30.6	16.7
				fcc	95.7	4.1	0.2
23	80.9	14.1	5.0	fcc	93.6	5.8	0.6
				Ni ₅ Y	48.2	35.6	16.2
24	45.0	36.3	18.7	Ni ₅ Y	46.1	36.4	17.5
				(Cu ₄ Y)	43.9	36.1	20.0
25	53.4	37.9	8.7	Ni ₅ Y	32.0	51.4	16.6
				Ni ₁₇ Y ₂	40.3	48.5	11.2
				fcc	83.0	16.9	0.1
26	43.9	46.0	10.1	Ni ₅ Y	30.6	52.7	16.7
				Ni ₁₇ Y ₂	38.0	49.4	12.6
				fcc	76.5	23.1	0.4
27	30.3	61.6	8.1	fcc	45.8	53.6	0.6
				Ni ₅ Y	23.8	64.7	11.5
28	14.0	79.6	6.4	Ni ₁₇ Y ₂	13.2	76.3	10.5
				fcc	17.9	81.5	0.6
29	16.7	69.2	14.1	Ni ₅ Y	14.6	69.5	15.9
				Ni ₁₇ Y ₂	19.2	68.4	12.4

(CuY) and (Cu₄Y) refers to the complete solubility between CuY-NiY and Cu₄Y-Ni₄Y

8.3 Complete mutual solubility between CuY and NiY

A complete solid solubility has been detected between CuY and NiY although the room temperature crystal structure of CuY and NiY are CsCl and FeB types, as can be seen in Appendix A-10. Kadumatsu [135] reported that CuY transforms from cubic CsCl to orthorhombic FeB type structure at lower temperature. This transformation temperature showed a large hysteresis during heating (783 K) and cooling (120 K). Since NiY has FeB type structure, Gupta [138] suggested that a continuous solid solution between these

two compounds could exist. Six key samples (1, 3, 4, 5, 6 and 7) have been prepared to investigate the solubility. The WDS measurements of these alloys are listed in Table 8-1. The phase relations are shown on the isothermal section in Figure 8-5. The XRD patterns of these alloys match the FeB not the CsCl structure type. Also, if there is no continuous solubility, a three phase region should be present which could not be found. Therefore, a continuous solubility between CuY and NiY is most likely to exist.

Table 8-2: The chemical compositions and unit cell parameters of (CuY) determined by WDS and Rietveld analysis

Sam ple No.	Composition of (CuY) phase, WDS data			Unit cell parameters and lattice volume				Reliability factors ^a		
	Cu	Ni	Y	a (Å)	b (Å)	c (Å)	V (Å ³)	R _e	R _{wp}	s
1	43.1	6.2	50.7	7.075	4.418	5.416	169.29	4.73	9.02	3.64
4	26.7	22.3	51.0	7.077	4.358	5.446	167.98	4.06	9.71	5.73
5	35.9	12.7	51.4	7.081	4.424	5.423	169.85	6.79	8.07	1.41
6	7.4	42.2	50.4	7.111	4.190	5.490	163.57	9.97	15.12	2.30
7	4.7	44.9	50.4	7.131	4.164	5.511	163.63	9.84	23.08	5.50

^a Reliability factors: *s* is the goodness of fit, *R_{wp}* is the weighted summation of the residuals of the least-squares fit and *R_e* is the statistically expected value

Refinement of the XRD pattern of the alloys containing (CuY) phase has been done using Rietveld analysis. The use of Si as an internal calibration standard enabled the correction for the zero shift and specimen displacement, which are the most serious systematic errors in XRD results. Table 8-2 and Figure 8-6 show the variation of cell parameters with Cu concentration for several samples (1, 4, 5, 6 and 7) where the substitution of Ni by Cu atom decreases the unit cell parameters *a* and *c* but it increases *b*. Table 8-2 lists the refined structural parameters of (CuY) and the reliability factors. The

least-squares approximation is used to establish the relationships between the lattice parameters and Cu concentration. The atomic radii of Cu, Ni and Y are 128 pm, 124 pm and 180 pm, respectively. In the (CuY) ternary solubility region, Y content variation remains constant while substitution of Ni occurs by Cu atoms. According to the normal trend all the lattice parameters should increase with Cu concentration because Cu atoms are slightly larger than Ni which cannot be observed in this case. This can be explained by the increase of the lattice volume as can be seen in Table 8-2 (d). The small reduction in a and c parameters have been compensated by comparatively larger increase in the b parameter.

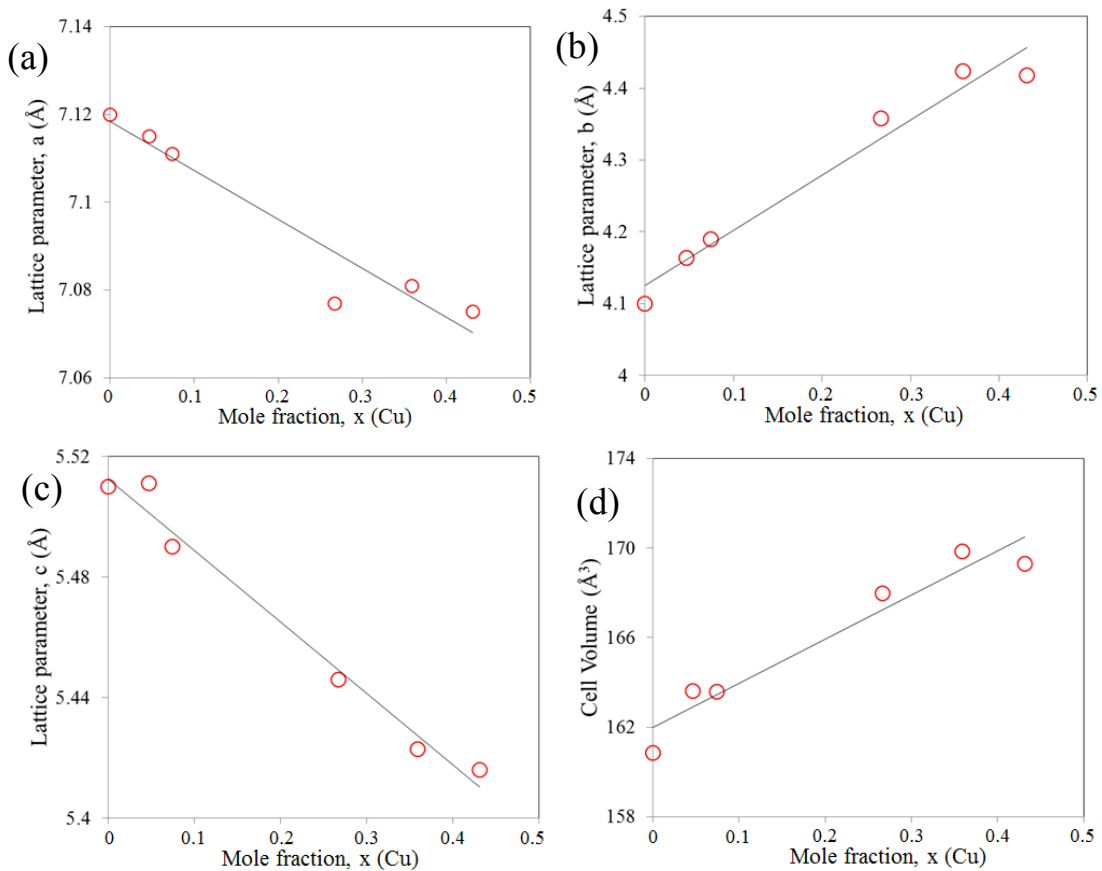


Figure 8-6: Variation of lattice parameters of (CuY) as a function of x for the $\text{Cu}_x\text{Ni}_{1-x}\text{Y}$ ($0 \leq x \leq 1$) alloys (a) lattice parameter a ; (b) lattice parameter b ; (c) lattice parameter c ; (d) cell volume

The coordination sphere and atomic substitution of Ni by Cu has been identified as can be seen in Figure 8-7. The substitution sites have been labeled by M1 (sites of mixing). All the Ni atoms are on the 4c sites. M1 sites can be occupied either by Ni or Cu based on the Cu concentration. There will be no substitution on the Y sites. The bond length has been calculated for the samples 1 (Cu rich) and 7 (Ni rich) as listed in Table 8-3. It can be seen that the maximum change in bond length occurs for the M1-M1 atoms from 2.463 Å to 2.561 Å. This increase of length has been reflected in relatively large increment of the cell parameter b , from 4.164 to 4.418 Å. The bond length for all positions show increment except one of the M1-Y1 bond where it decreases from 2.850 to 2.818 Å. Because of this, cell parameters a and c decreased as can be seen in Figure 8-6 (a and c).

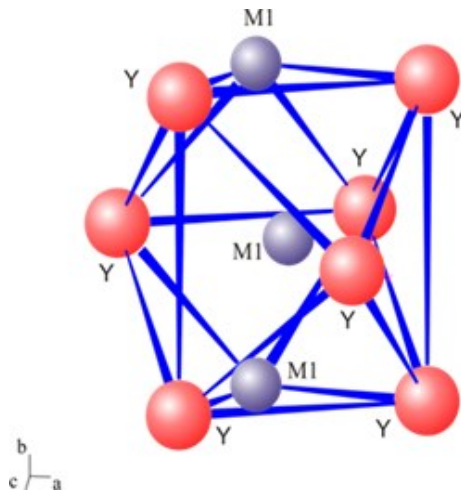


Figure 8-7: The coordination spheres of a Ni atom of the (CuY) compound. The substitution sites of Ni by Cu have been denoted by M1.

Table 8-3: Atomic bond lengths of the (CuY) compound in sample 1 and 7

Sample No.	Atom 1	Atom 2	Distance (Å)	Sample No.	Atom 1	Atom 2	Distance (Å)
7	M1	- M1	2.463	1	M1	- M1	2.561
	M1	- M1	2.463		M1	- M1	2.561
	M1	- Y1	2.850		M1	- Y1	2.818
	M1	- Y1	2.863		M1	- Y1	2.818
	M1	- Y1	2.906		M1	- Y1	2.970
	M1	- Y1	2.906		M1	- Y1	2.987
	M1	- Y1	2.973		M1	- Y1	2.987
	M1	- Y1	2.973		M1	- Y1	3.045
	M1	- Y1	3.018		M1	- Y1	3.045
	Y1	- M1	2.850		Y1	- M1	2.818
	Y1	- M1	2.863		Y1	- M1	2.818
	Y1	- M1	2.906		Y1	- M1	2.970
	Y1	- M1	2.906		Y1	- M1	2.987
	Y1	- M1	2.973		Y1	- M1	2.987
	Y1	- M1	2.973		Y1	- M1	3.045
Y1	- M1	3.018	Y1	- M1	3.045		

8.4 Complete mutual solubility between Cu₄Y and Ni₄Y

Complete solubility between Cu₄Y and Ni₄Y has been observed from the XRD and WDS measurements of several key alloys. The WDS measurements of key alloys 9, 10, 11, 14, 15, 17, 18 and 24 in Table 8-1 show a stable phase with Cu_xNi_{4-x}Y (0 ≤ x ≤ 4) composition. Diffusion couple 2 in Figure 8-4 also shows the presence of this phase from 30 to 40 at.% Cu. All these results indicate a complete solubility between Cu₄Y and Ni₄Y compounds. The primary condition for the formation of this kind of solubility between the constituents is having the same crystal structure. But unfortunately the crystal structure of Ni₄Y phase is not known. Therefore, it is decided to use the reference pattern of Cu₄Y to identify the Ni₄Y compound in the XRD results.

The XRD patterns of three key alloys (15, 17 and 18) have been compared and shown in Figure 8-8. Sample 15 (Cu/Ni/Y 78.0/3.5/18.5 at.%) is a single phase consisting only

of Cu_4Y . Sample 17 (Cu/Ni/Y 5.0/74.9/20.1 at.%) is composed of three phases; Ni_4Y , Ni_3Y and Ni_7Y_2 . Sample 18 (Cu/Ni/Y 6.5/73.9/19.6 at.%) has two phases; Ni_5Y and Ni_4Y . XRD patterns of both samples (17 and 18) show peaks belonging to Cu_4Y . However, Cu_4Y cannot be present in this sample because its composition is very close to the Ni-Y side. This indicates that most probably Ni_4Y has the same crystal structure as Cu_4Y . Further, it can be concluded that a complete solubility between Cu_4Y and Ni_4Y compounds exists. However, more crystallographic investigation needs to be done to verify this observation.

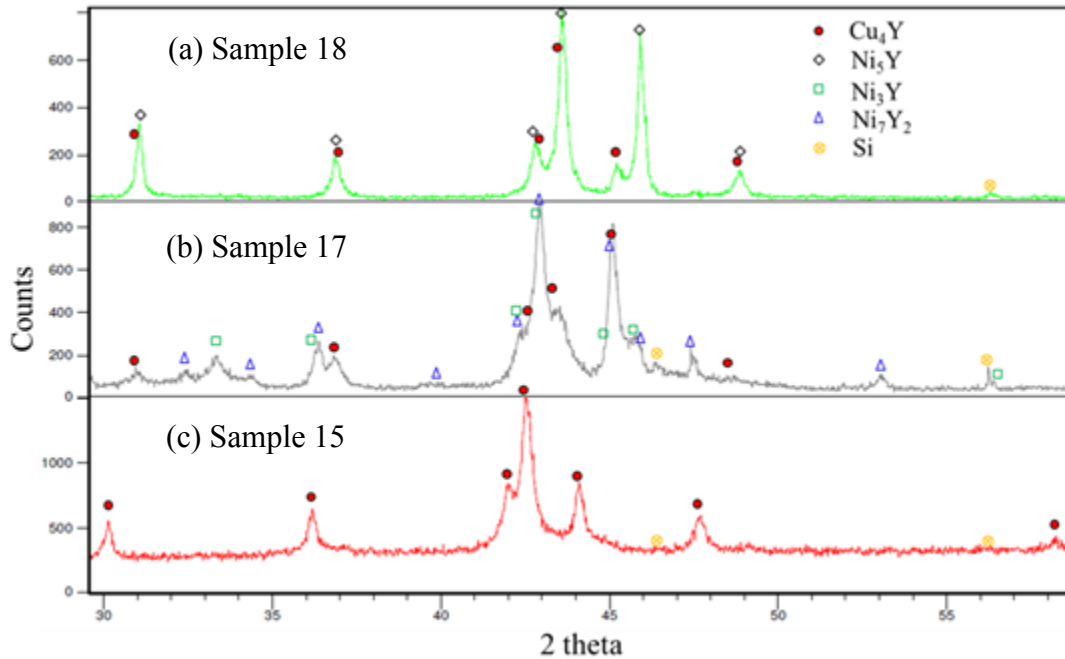


Figure 8-8: XRD patterns of samples (a) 18 (Cu/Ni/Y 6.5/73.9/19.6 at.%; (b) 17 (Cu/Ni/Y 5.0/74.9/20.1 at.%; (c) 15 (Cu/Ni/Y 78.0/3.5/18.5 at.%) showing the effect of Cu_4Y - Ni_4Y extended solubility

8.5 Partial solubility of Ni_5Y phase

The partial isothermal section at room temperature reported by Zheng and Nong [134] shows that Ni_5Y phase is stable until Cu_5Y composition. But Cu_5Y compound does not

exist in the acceptable Cu-Y phase diagram [138]. Thus stability of the Ni₅Y phase upto the Cu₅Y composition is not possible. Dwight [137] examined the crystal structures of several alloys at the Cu_xNi_{5-x}Y (0 ≤ x ≤ 5) compositions. The CaCu₅ type structure was found to be stable from Ni₅Y to Cu₄NiY composition. Most probably Cu₅Y is a metastable phase which was stabilized by the addition of a small amount of Ni. Four key alloys, 20-23, have been prepared in this region to determine the solubility limit of Ni₅Y. All of these alloys contain Ni₅Y and fcc phases as can be seen in the BSE image of sample 20 (Cu/Ni/Y 81.8/8.5/9.7 at.%) in Figure 8-9. Based on the WDS analysis of these alloys as listed in Table 8-1, it can be confirmed that Ni₅Y is stable at least until 72.4 at.% Cu. However, the maximum solubility of Ni₅Y could not be obtained in this work because of the presence of phases very close in composition such as of Cu₆Y and Cu₄Y. One alloy, sample 19 (Cu/Ni/Y 85.6/1.4/13.0 at.%) which has slightly more Cu concentration than sample 20 (Cu/Ni/Y 81.8/8.5/9.7 at.%) shows a single phase of Cu₆Y. The location of this alloy can be seen in Figure 8-5. Therefore, a three-phase region containing Cu₆Y, Ni₅Y and (Cu₄Y) is assumed and drawn with a dotted line in Figure 8-5 indicating that this region is not experimentally confirmed.

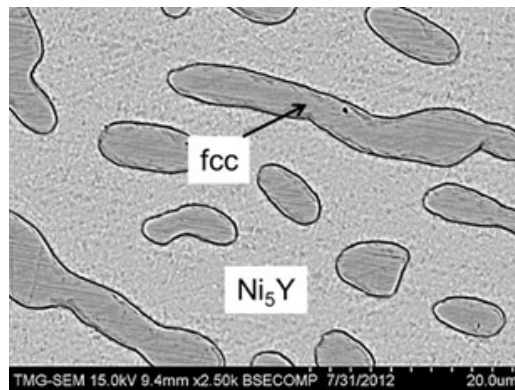


Figure 8-9: BSE image of sample 20 (Cu/Ni/Y 81.8/8.5/9.7 at.%)

8.6 Comparison between experimental results and thermodynamic modeling

The Cu-Ni system is completely miscible below the liquidus until the critical (T_c) temperature below which the immiscibility exists. The paramagnetic to a ferromagnetic transformation also occurs in the immiscibility region. On the other hand, both Cu-Y and Ni-Y systems have several intermetallic compounds and many of the compositions such as CuY-NiY, $\text{Cu}_2\text{Y-Ni}_2\text{Y}$, $\text{Cu}_7\text{Y}_2\text{-Ni}_7\text{Y}_2$ and $\text{Cu}_4\text{Y-Ni}_4\text{Y}$ show resemblance in terms of their stoichiometry and crystal structure to some extent. Therefore, they have a tendency to form ternary solubility along these lines. These compounds basically sectioned the Cu-Ni-Y system into several pseudo-binary zones. To obtain a clear understanding of various phase relationships in the Cu-Ni-Y system, an elaborate discussion on the XRD, WDS and DSC results of the key alloys is given below.

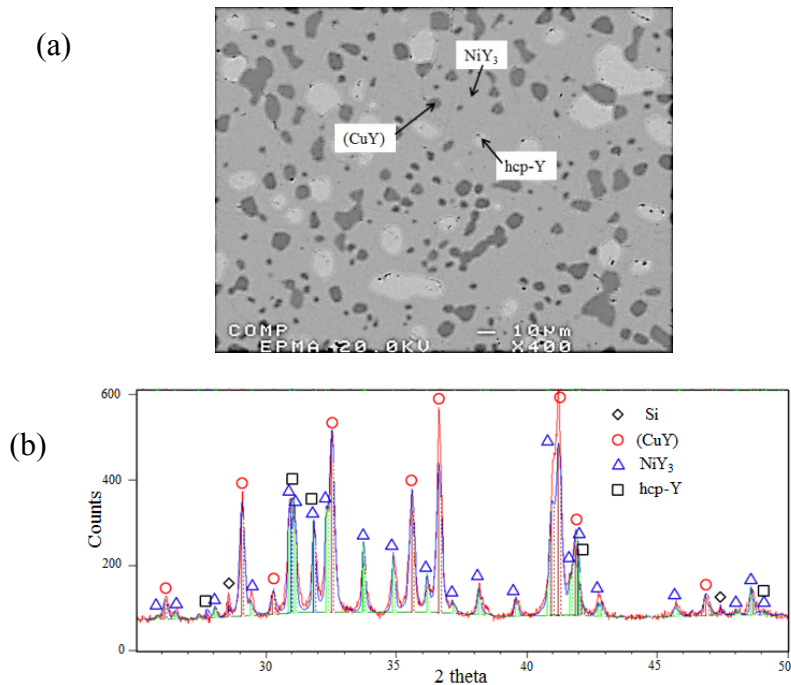


Figure 8-10: (a) BSE image; (b) XRD pattern of sample 1 (20.8/9.1/70.1 Cu/Ni/Y at.%)

A three-phase region has been identified among the hcp-Y, NiY₃ and (CuY). The BSE image and XRD pattern of key sample 1 (20.8/9.1/70.1 Cu/Ni/Y at.%) in Figure 8-10 (a) and (b) clearly show the phase relation. Based on the WDS analysis listed in Table 8-1, the maximum solubility of Cu in NiY₃ is found to be 12.0 at.%. Rietveld refinement of the XRD results reveals the lattice parameters as $a = 6.93 \text{ \AA}$, $b = 9.70 \text{ \AA}$ and $c = 6.39 \text{ \AA}$.

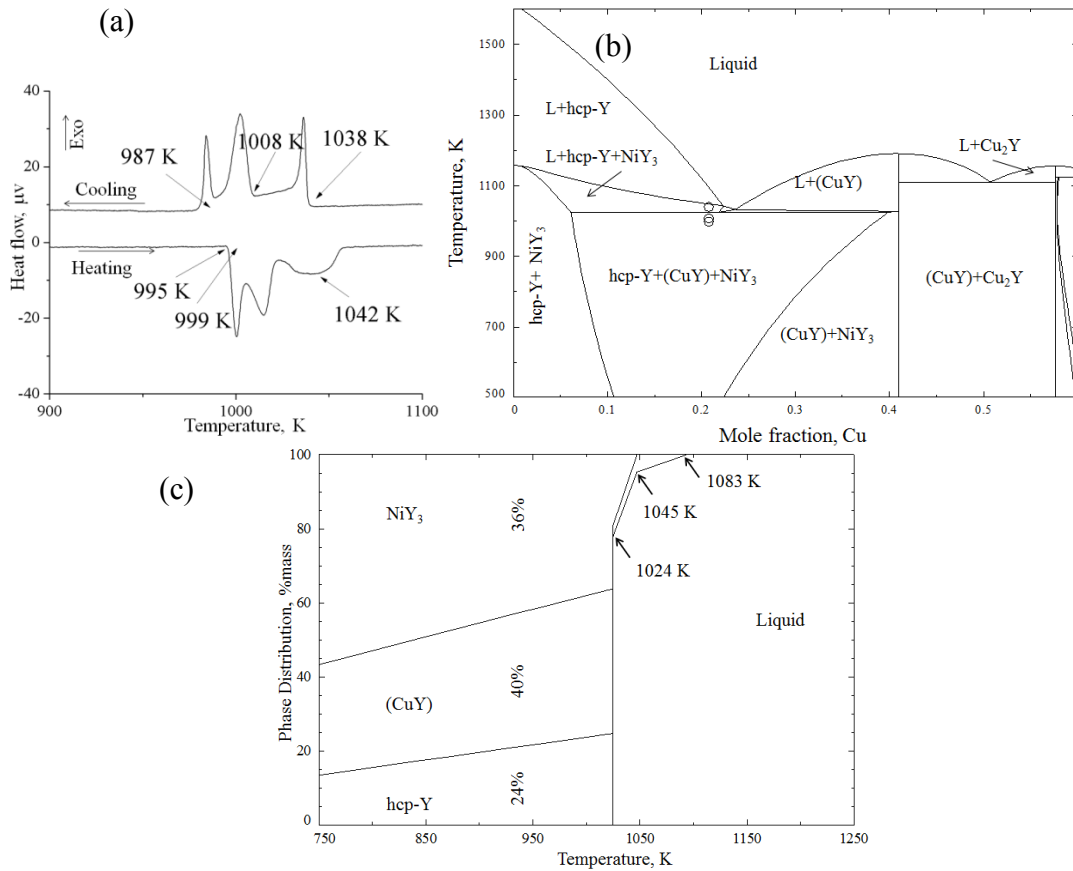


Figure 8-11: (a) DSC spectra; (b) Calculated vertical section at 9.1 at.% Ni with DSC signals; (c) phase assemblage diagram of sample 1 (20.8/9.1/70.1 Cu/Ni/Y at.%)

The DSC spectra of sample 1 are shown in Figure 8-11 (a). The heating profile shows three thermal events at 1042, 999 and 995 K that reoccurred in the cooling at 1038, 1008 and 987 K. These measured temperatures can be correlated to the calculated vertical

section at const. 9.1 at.% Ni in Figure 8-11 (b) which show reasonable agreement. Figure 8-11 (c) shows the calculated phase assemblage diagram for this alloy. According to the calculation the first solid starts to precipitate at 1083 K in the form of hcp-Y. It consumes about 24% of the total liquid. This phase can be seen as the white precipitates in the microstructure in Figure 8-10 (a). Then at 1045 and 1024 K, NiY_3 and (CuY) precipitate forming about 36% and 40% of the overall material.

The BSE image of sample 4 (34.9/18.7/46.4 Cu/Ni/Y at.%) in Figure 8-12 (a) shows a two-phase equilibrium: $(\text{CuY})+\text{Cu}_2\text{Y}$. The grey matrix is (CuY) and the dark network is Cu_2Y . The WDS analysis listed in Table 8-1 and XRD pattern in Figure 8-12 (b) positively identify these compounds.

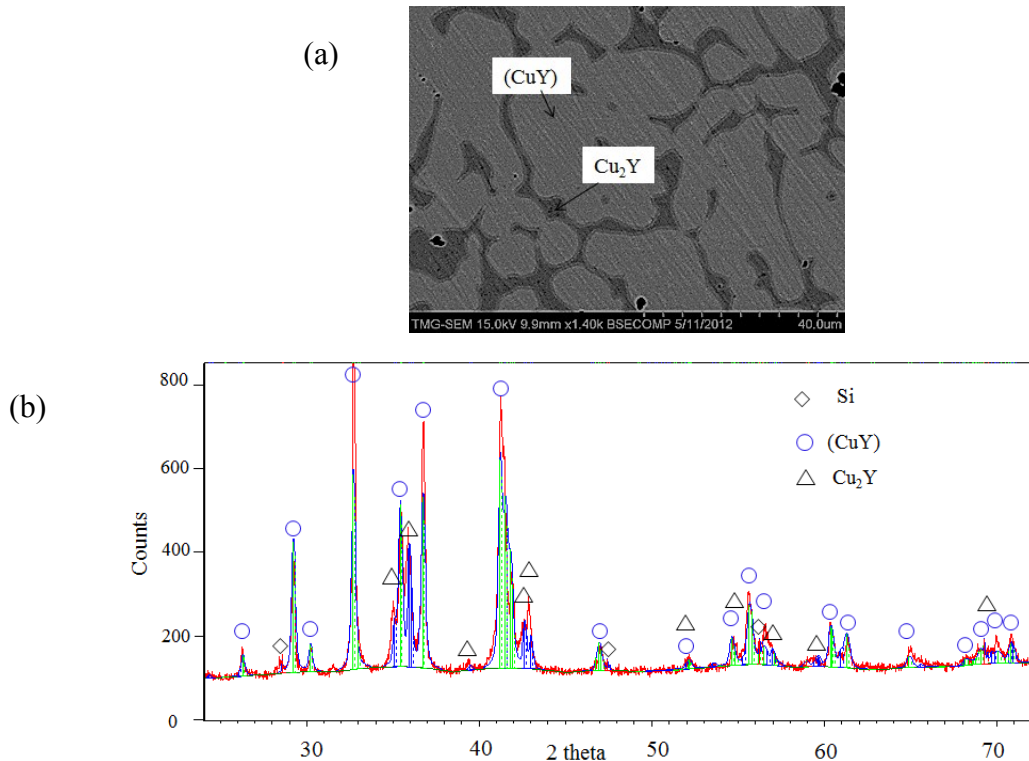


Figure 8-12: (a) BSE image; (b) XRD pattern of sample 4 (34.9/18.7/46.4 Cu/Ni/Y at.%)

Sample 5 (50.8/8.7/40.5 Cu/Ni/Y at.%) is also located in the same two-phase region: (CuY)+Cu₂Y as shown in Figure 8-5. The DSC spectra of these alloys are shown in Figure 8-13 (a) and (b). Both of them show two thermal events during heating which have been reoccurred during cooling. The thermal arrests are projected on the vertical section along Cu₂Y-Ni₂Y₃ in Figure 8-13 (c) which show reasonable agreement.

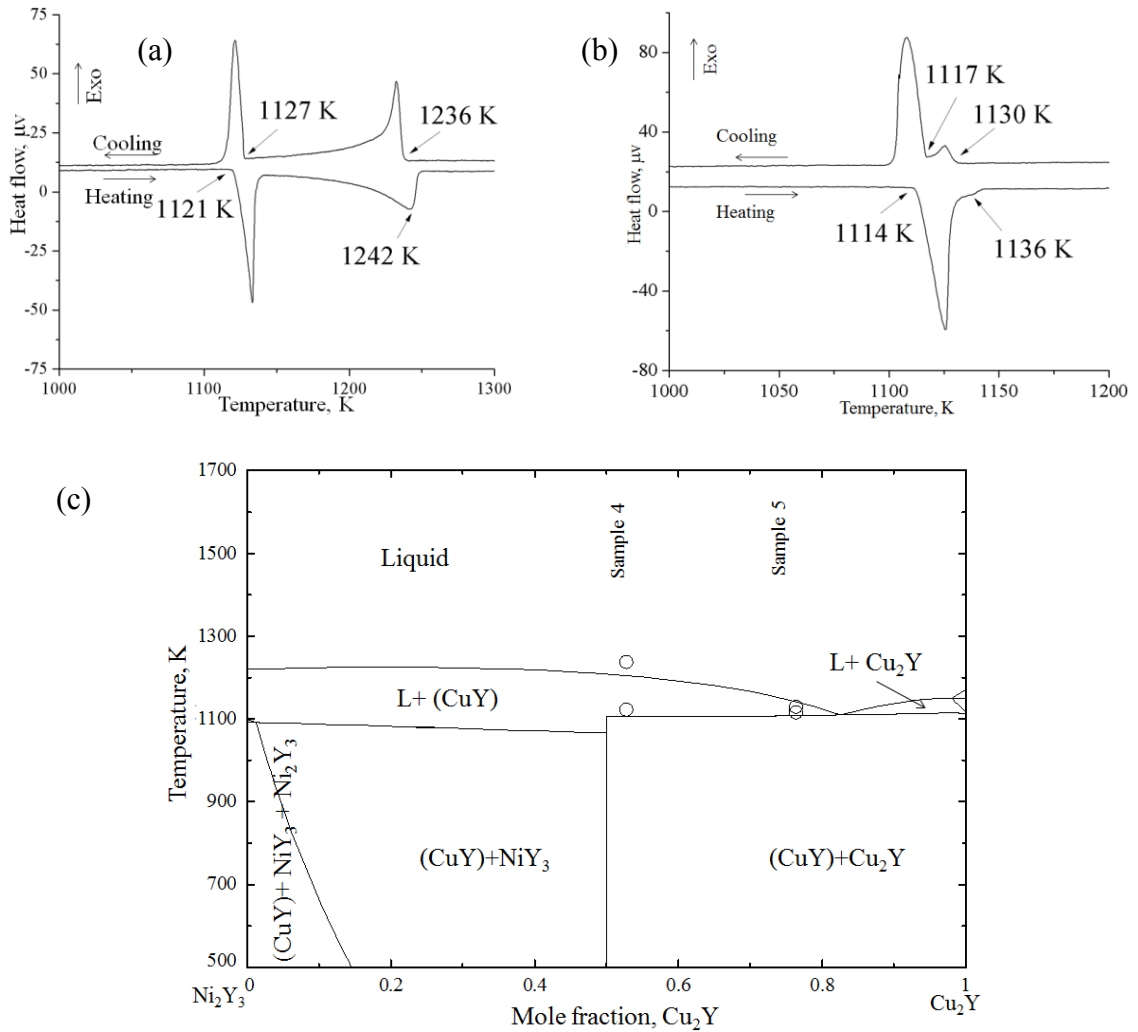


Figure 8-13: DSC spectra of (a) sample 4 (34.9/18.7/46.4 Cu/Ni/Y at.%) ; (b) sample 5 (50.8/8.7/40.5 Cu/Ni/Y at.%) during heating and cooling; (c) calculated vertical section along Cu₂Y-Ni₂Y₃ with DSC signals

Sample 6 (Cu/Ni/Y 18.2/42.7/39.1 at.%) is located in the three-phase region: (CuY)+Cu₂Y+Ni₂Y. The BSE image of this alloy is shown in Figure 8-14 (a) which

shows three different phases in equilibrium. These phases; (CuY), Cu_2Y and Ni_2Y are positively identified in the XRD and WDS analysis as can be seen in Figure 8-14 (b) and in Table 8-1. The maximum solubility of Cu_2Y and Ni_2Y are found to be 28 at.% Ni and 9.7 at.% Cu, respectively. These values are in good agreement with those of Paul-Boncour et al. [136] who reported them as 30.5 at.% and 10.4 at.% Cu.

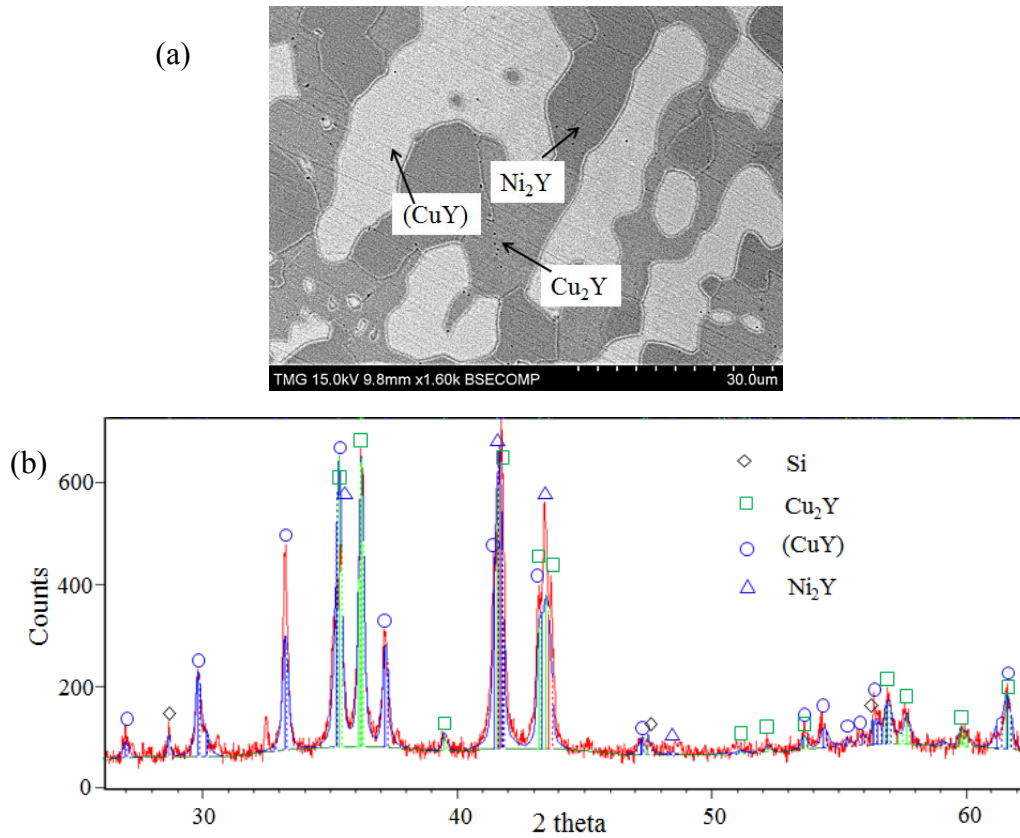


Figure 8-14: (a) BSE image; (b) XRD pattern of sample 6 (18.1/42.0/39.9 Cu/Ni/Y at.%)

Observing the variation in the lattice parameters of Cu_2Y is attempted in this work. Rietveld analysis has been performed for the XRD patterns of the five key alloys (4, 5, 6, 9 and 10) that contain Cu_2Y . The location of these alloys can be seen in Figure 8-5. The change of lattice parameter and cell volume with Ni concentration has been shown in Figure 8-15 (a-d) compared with the values reported by Paul-Boncour et al.

[136] which shows good agreement. The ‘*a*’ parameter decreases significantly with the increase of Ni concentration due to the smaller atomic size of Ni. The cell volume also decreases linearly with the increase in Ni concentration. However, negligible change of the ‘*b*’ and ‘*c*’ parameters can be observed. Paul-Boncour et al. [136] analyzed the crystal structure of the Cu_2Y closely using neutron diffraction and XRD experiments. They reported large anisotropic shifting of the atoms due to the substitution. This explains larger increment of the ‘*a*’ parameter than ‘*b*’ and ‘*c*’.

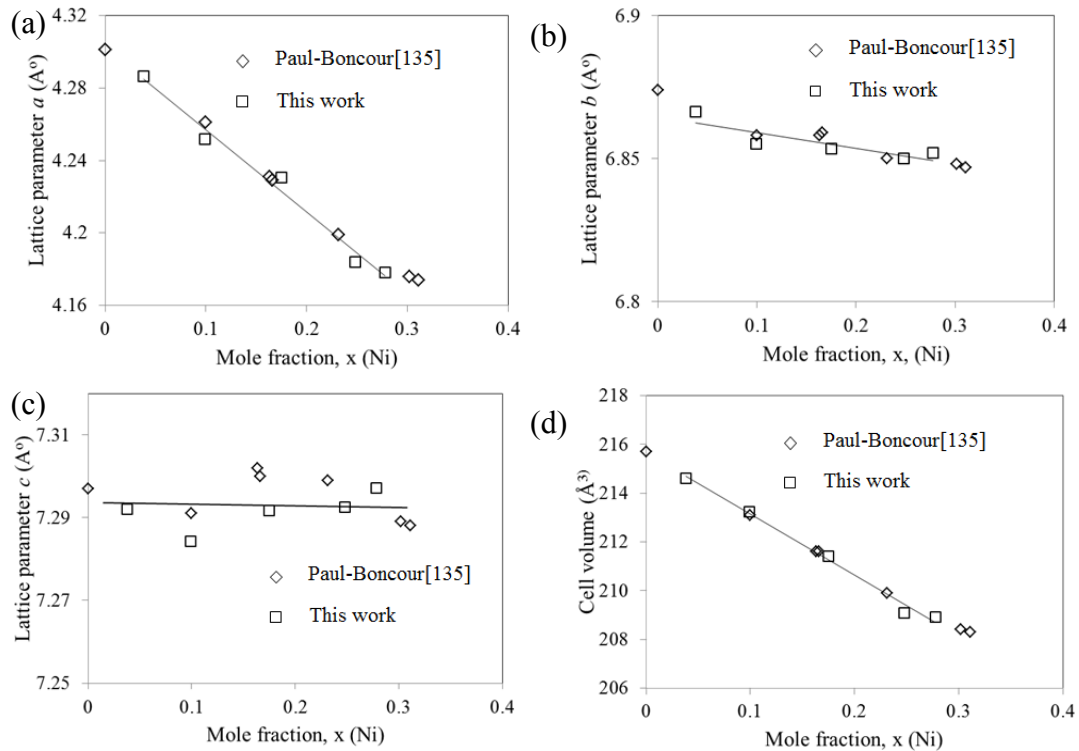


Figure 8-15: Variation of lattice parameters of Cu_2Y as a function of x for the $\text{Cu}_{2-x}\text{Ni}_x\text{Y}$ ($0 \leq x \leq 1.1$) alloys (a) lattice parameter *a*; (b) lattice parameter *b*; (c) lattice parameter *c*; (d) variation of cell volume.

Sample 7 (6.2/58.2/35.6 Cu/Ni/Y at.%) is located in the two phase region of Ni_2Y and (CuY). The BSE image in Figure 8-16 clearly shows these two phases. The grey matrix in the microstructure is Ni_2Y whereas the white phase is (CuY). According to the

WDS measurements as listed in Table 8-1, (CuY) and Ni₂Y dissolve about 4.68 and 7.12 at.% Cu, respectively.

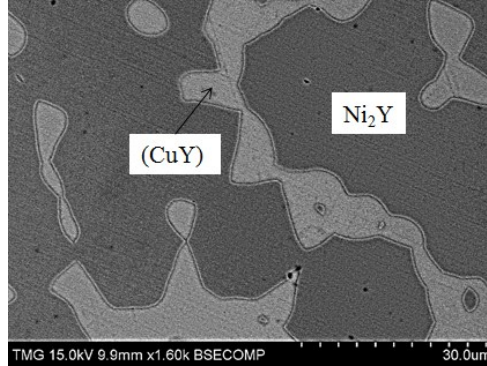


Figure 8-16: BSE image of sample 7 (6.2/58.2/35.6 Cu/Ni/Y at.%)

The DSC spectra of sample 6 (18.2/42.7/39.1 Cu/Ni/Y at.%) with the heating and cooling runs are shown in Figure 8-17 (a). It shows two peaks during heating and three peaks during cooling. It can be seen that the 2nd peak during heating overlapped with the 3rd peak. Areas under the curve between the last two cooling peaks (-125 J/g) and the 2nd heating peak (123 J/g) are similar which confirms that the heating peak is in fact two overlapping peaks. Similar results were observed in all the three heating and cooling cycles. The thermal arrests observed during cooling are at temperatures of 1170, 1118 and 1108 K. While during heating the peaks' temperatures are 1172 and 1110 K. The DSC thermal arrests are projected on the calculated vertical section Ni₂Y-CuY as can be seen in Figure 8-17 (c). The liquidus temperature is found at 1164 K which is in good agreement with the experimental value of 1170 K. The other two thermal events in the DSC spectra are due to the phase transformations; L+Ni₂Y / L+Ni₂Y+(CuY) and L+Ni₂Y+(CuY) / Cu₂Y+Ni₂Y+(CuY). According to the calculation these transformations occur at 1115 and 1076 K.

The DSC heating and cooling spectra of Sample 7 (6.2/58.2/35.6 Cu/Ni/Y at.%) are also shown in Figure 8-17 (b). Two endothermic peaks at 1337 and 1161 K in the heating cycle can be seen. These peaks reoccurred at 1338 and 1166 K in the cooling cycle. The DSC measurements have been projected on the same (Ni₂Y-CuY) vertical section in Figure 8-17 (c) which show good agreement.

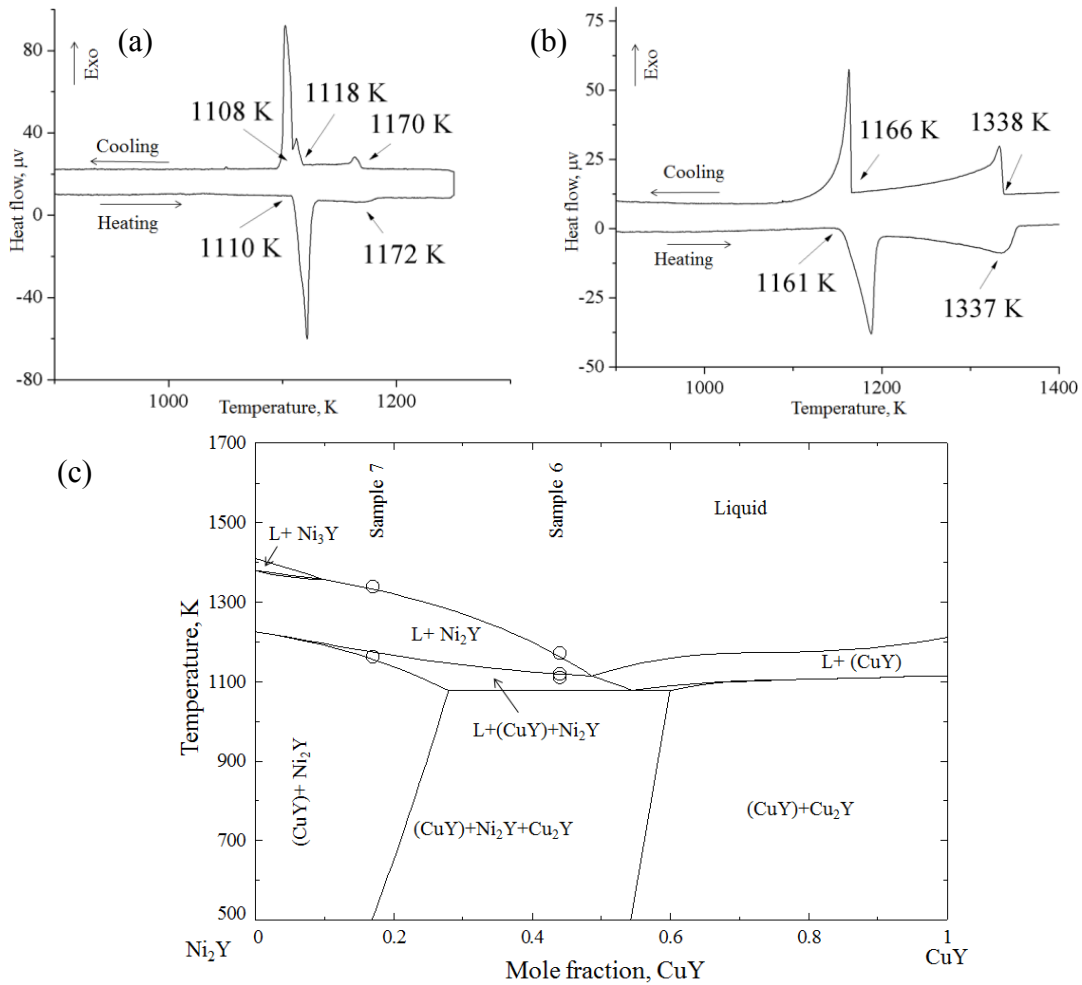


Figure 8-17: DSC spectra of (a) sample 6 (18.2/42.7/39.1 Cu/Ni/Y at.%); (b) sample 7 (6.2/58.2/35.6 Cu/Ni/Y at.%) during heating and cooling; (c) calculated vertical section along Ni₂Y-CuY with DSC signals

Sample 9 (52.1/20.8/27.1 Cu/Ni/Y at.%) and Sample 10 (46.5/24.4/29.1 Cu/Ni/Y at.%) are located in the two phase region of Cu₄Y+Cu₂Y as can be seen in Figure 8-5.

The XRD pattern of sample 9 in Figure 8-18 (a) confirms the existence of the phases. The WDS analysis of these alloys is listed in Table 8-1. DSC spectra of sample 10 during heating and cooling are shown in Figure 8-18 (b). Two thermal events at 1202 and 1169 K have been observed in the heating cycle. These two events reoccurred at 1200 and 1167 K during cooling cycle. The DSC signals have been projected on the calculated vertical section at constant 24.4 at.% Ni as can be seen in Figure 8-18 (c). The deviation between the calculation and experimental measurement is about 55 K. It was not possible to improve consistency with this particular alloy without affecting the other side of the phase diagram. Hence, it is decided to accept this amount of error.

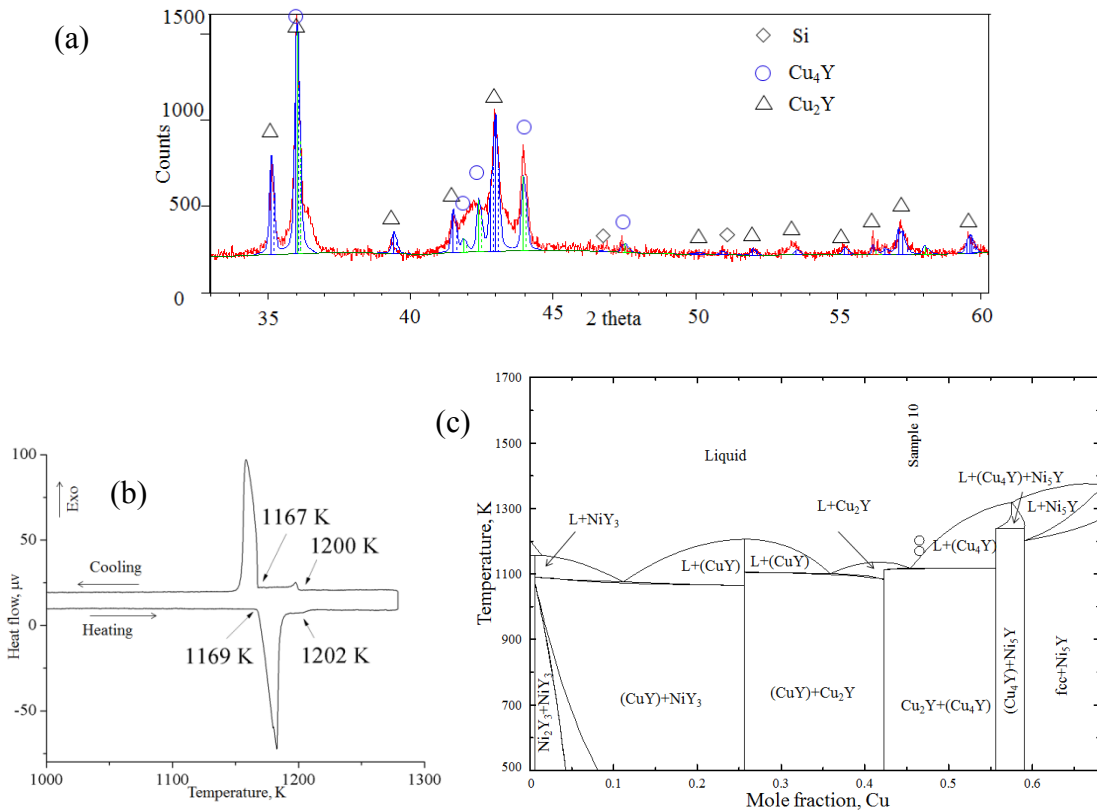


Figure 8-18: (a) XRD pattern of sample 9 (52.13/20.75/27.12 Cu/Ni/Y at.%); (b) DSC spectra of sample 10 (46.5/24.4/29.1 Cu/Ni/Y at.%) during heating and cooling; (c) Calculated vertical section at 24.38 at.% Ni with DSC signals of sample 10

Two three-phase regions: $\text{Ni}_3\text{Y}+\text{Cu}_2\text{Y}+(\text{Cu}_4\text{Y})$ and $\text{Ni}_3\text{Y}+\text{Cu}_2\text{Y}+\text{Ni}_2\text{Y}$ exit in the center of the phase diagram. Two key alloys (11 and 12) have been prepared to identify the phase relations. Their WDS analysis has been summarized in Table 8-1. The BSE image of key alloy 12 (25.1/44.2/30.7 Cu/Ni/Y at.%) is shown in Figure 8-19. One of the common phases in these two regions is Ni_3Y which is promising for the hydrogen storage application. Burnasheva and Tarasov [131], in their hydrogen storage work on the Cu-Ni-Y system, reported that they found one alloy $\text{Cu}_{0.5}\text{Ni}_{2.5}\text{Y}$ to be a single phase with the same crystal structure as that of Ni_3Y . Although this result does not provide the maximum solubility of Cu in Ni_3Y , it proves that the solubility should be equal to or greater than 12.5 at.% Cu which is in accordance with the present work that finds the maximum solubility to be ~25 at.% Cu. There is a possibility for a two phase region ($\text{Cu}_2\text{Y}+\text{Ni}_3\text{Y}$) to exist between these two three-phase regions. But it was not observed in the present work.

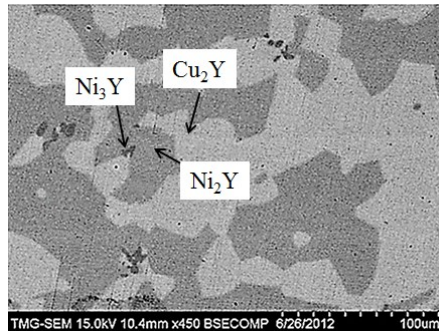


Figure 8-19: BSE image of sample 12 (25.1/44.2/30.7 Cu/Ni/Y at.%)

Key samples 13, 16, 17 and 18 are located between the intermetallic compounds: $\text{Ni}_2\text{Y}-\text{Ni}_3\text{Y}$, $\text{Ni}_3\text{Y}-\text{Ni}_7\text{Y}_2$, $\text{Ni}_7\text{Y}_2-(\text{Cu}_4\text{Y})$ and $(\text{Cu}_4\text{Y})-\text{Ni}_5\text{Y}$, respectively, as can be seen in Figure 8-5. WDS analysis of these alloys is listed in Table 8-1. The XRD pattern of sample 13 (15.9/54.4/29.7 Cu/Ni/Y at.%) in Figure 8-20 (a) positively identified Ni_2Y

and Ni_3Y compounds. Also, in Figure 8-20 (b), the XRD pattern of sample 18 (6.5/73.9/19.6 Cu/Ni/Y at.%) shows the existence of Ni_5Y and (Cu_4Y) .

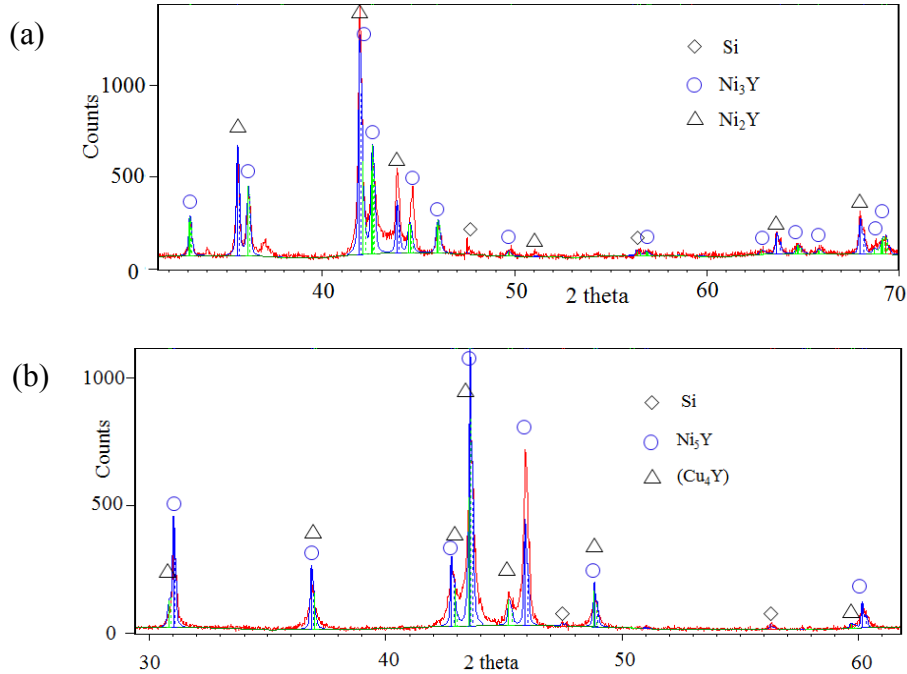


Figure 8-20: XRD pattern of (a) sample 13 (15.9/54.4/29.7 Cu/Ni/Y at.%) (b) sample 18 (6.5/73.9/19.6 Cu/Ni/Y at.%)

DSC spectra of heating and cooling cycles of sample 17 (5.0/74.9/20.1 Cu/Ni/Y at.%) are shown in Figure 8-21 (a). According to the WDS analysis listed in Table 8-1 this alloy is located in the three-phase field: $\text{Ni}_4\text{Y}+\text{Ni}_3\text{Y}+\text{Ni}_7\text{Y}_2$. Also, the solubility of Cu in Ni_7Y_2 has been found ~ 3.1 at.% which could be obtained 0.5 at.% in the current thermodynamic modeling. Because of the experimental uncertainty the lower ternary solubility in Ni_7Y_2 has been accepted as discussed earlier in section 4.2.4. Hence, the composition of this alloy is found in a two-phase region: $\text{Ni}_4\text{Y}+\text{Ni}_3\text{Y}$ during calculation as can be seen in Figure 8-21 (b).

Four thermal events can be seen in the heating spectrum of sample 17. However, only two peaks appear in the cooling cycle. This is probably due to the super cooling effect

which shifts the cooling peaks. Several phase transformations occur in a relatively narrow and sufficiently high temperature range which forces the first three peaks during cooling to overlap and appear as one sharp peak. Similar spectrum has been observed in all three DSC runs of the sample. Therefore, only the heating signals will be considered for this alloy. Figure 8-21 (b) shows the calculated vertical section at 20.1 at.% Y with the DSC signals of this sample. The measured transformation temperatures correspond well to the phase boundaries in the vertical section: L / L+Ni₅Y / L+Ni₅Y+(Cu₄Y) / L+(Cu₄Y) / Ni₃Y+(Cu₄Y) occurring at 1643, 1571, 1550 and 1501 K predicted from thermodynamic calculation, respectively.

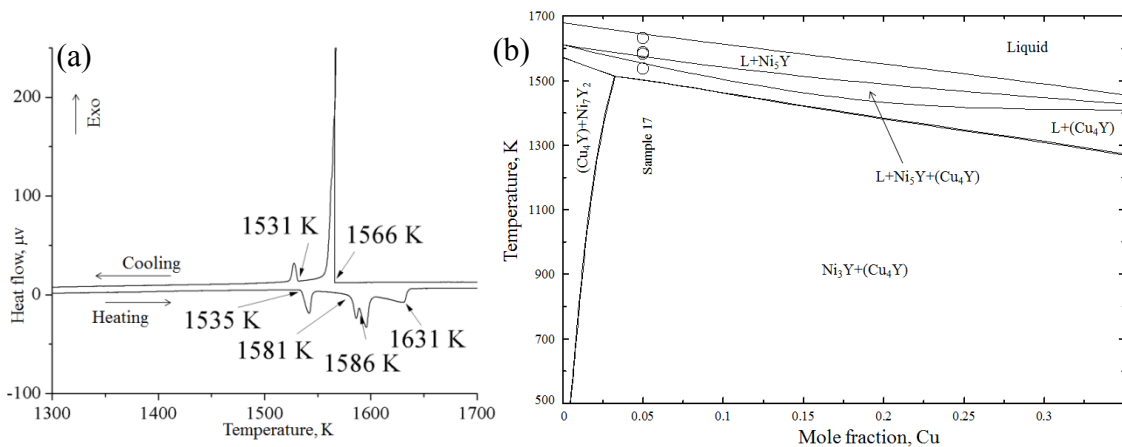


Figure 8-21: (a) DSC spectra; (b) Calculated vertical section at 20.1 at.% Y with DSC signals of sample 17 (5.0/74.9/20.1 Cu/Ni/Y at.%)

Key samples 20-23 have been prepared in the two-phase region of fcc+Ni₅Y. The locations and WDS analysis of these alloys have been shown in Figure 8-5 and Table 8-1 respectively. The WDS analysis confirms the existence of fcc and Ni₅Y in all the alloys. The BSE image and XRD pattern of sample 23 (80.9/14.1/5.0 Cu/Ni/Y at.%) in Figure 8-22 (a) and (b) positively identify the two-phase region. According to the WDS analysis fcc phase dissolves negligible (~ 0.62 at.%) amount of Y.

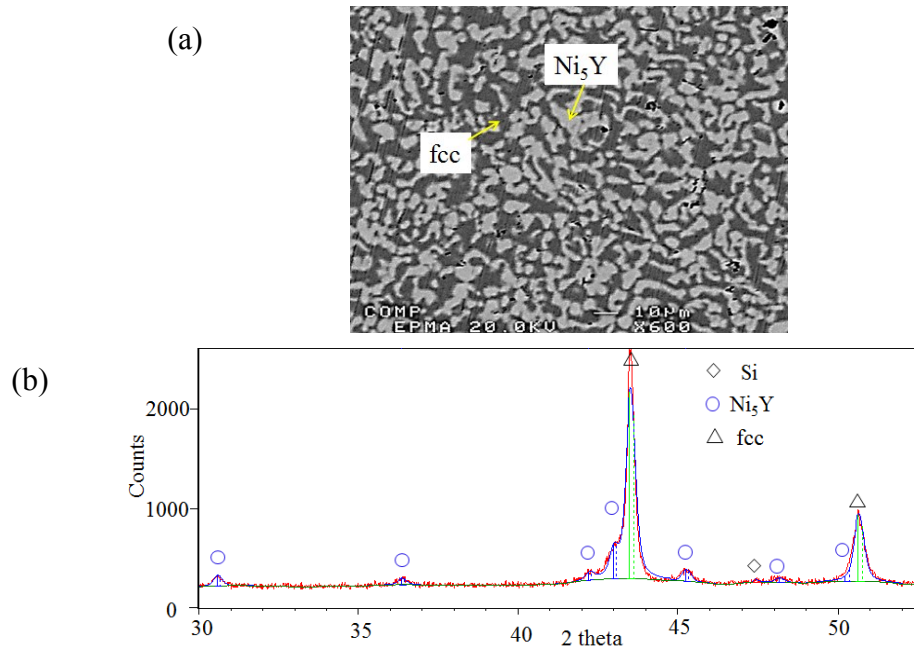


Figure 8-22: (a) BSE image; (b) XRD pattern of sample 23 (80.9/14.1/5.0 Cu/Ni/Y at.%)

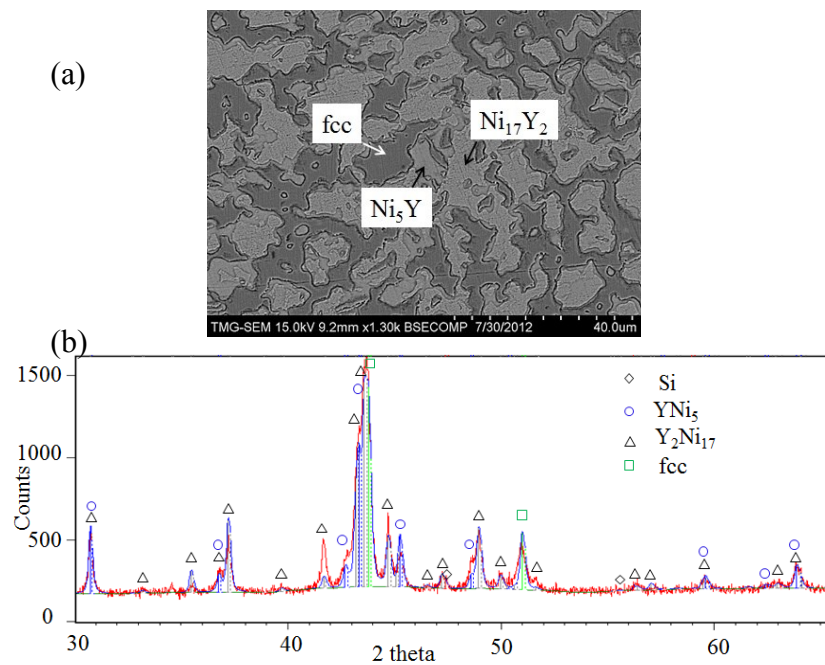


Figure 8-23: (a) BSE image (b) XRD pattern of sample 25 (53.4/37.9/8.7 Cu/Ni/Y at.%)

Sample 25 (53.4/37.9/8.7 Cu/Ni/Y at.%) and 26 (43.9/46.0/10.1 Cu/Ni/Y at.%) confirms the existence of the phase relation: fcc+Ni₅Y+Ni₁₇Y₂. The BSE image and XRD

pattern of sample 25 in Figure 8-23 (a) and (b) positively identifies these phases. It should be mentioned that the sample has to be etched with 3% HNO₃ for 30 seconds to distinguish the phases. The WDS analysis of these alloys is shown in Table 8-1 which reveals that Ni₁₇Y₂ dissolves about 38 at.% Cu which is in good agreement with Zheng and Nong [134]. However, the Ni₅Y triangulation has been found at 31 at.% Cu whereas the fcc phase is found around 80 at.% Cu. The reported values by Zheng and Nong [134] were 39.16 and 67.76 at.% Cu, respectively. However, WDS analysis is more precise in determining the composition than the XRD analysis. Therefore, location of the phase triangulation obtained in this work is more likely.

Sample 27 (Cu/Ni/Y 30.3/61.6/8.1 at.%) is located in the fcc+Ni₁₇Y₂ phase field as shown in Figure 8-5. The BSE image in Figure 8-24 (a) clearly shows the two-phase equilibrium in this alloy. WDS analysis listed in Table 8-1 confirms the phases.

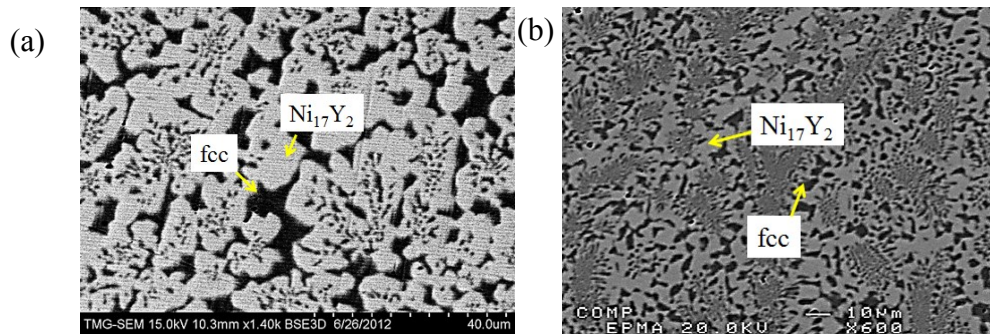


Figure 8-24: BSE image of (a) sample 27 (30.3/61.6/8.1 Cu/Ni/Y at.%; (b) sample 28 (14.0/79.6/6.4 Cu/Ni/Y at.%)

Similar to sample 27, sample 28 (14.0/79.6/6.4 Cu/Ni/Y at.%) is also located in the fcc+Ni₁₇Y₂ phase field as shown in Figure 8-5. The BSE image of the sample in Figure 8-24 (b) shows the two-phase equilibrium. The dark and white phases in the microstructure are fcc and Ni₁₇Y₂, respectively. WDS analysis listed in Table 8-1 confirms these phases. The grey region in the BSE image is not a separate phase but an

alternate layered structure of fcc and Ni_{17}Y_2 . Sample 27 in Figure 8-24 (a) also shows this type of morphology. But the layers there are thicker than sample 28. According to the liquidus projection as shown in Figure 4-26 this alloy is located on a univariant valley. For this reason during solidification this eutectic structure occurs.

The DSC spectra of sample 28 registered two signals in cooling cycle at 1557 and 1544 K as shown in Figure 8-25 (a). During heating these two peaks overlapped and the 1st signal could not be separated. Figure 8-25 (b) shows good agreement between the measured phase transformation temperatures with the calculated vertical section.

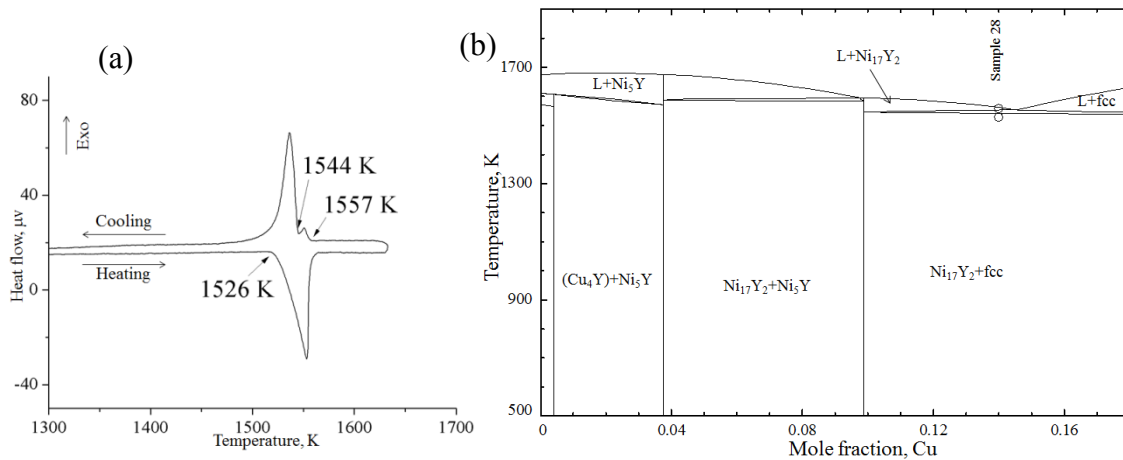


Figure 8-25: (a) DSC spectra of sample 28 (14.0/79.6/6.4 Cu/Ni/Y at.%) during heating and cooling; (b) Calculated vertical section at 79.6 at.% Ni with DSC signals

Some other rare earth containing systems like Gd-Cu-Ni [168], Ho-Cu-Ni [169], La-Cu-Ni [170], and Ce-Cu-Ni [171] show that the compounds of (RE,Cu) or (RE,Ni) form complete or partial but significant solid solutions of Cu in (RE,Ni) or Ni in (RE,Cu) binary compounds. The ternary solid solubilities of these compounds are almost parallel to the Cu-Ni line keeping constant RE concentration. The same tendency has been observed in the Cu-Ni-Y system.

Chapter 9

Concluding remarks, contributions and suggestions for future work

9.1 Concluding remarks

An extensive investigation has been carried out in this work on the three ternary systems Mg-Cu-Y, Mg-Ni-Y and Cu-Ni-Y using both experimental analysis and thermodynamic modeling. The fourth system (Mg-Cu-Ni) has only been studied thermodynamically as sufficient experimental data is available in the literature. A self-consistent set of parameters for all the ternary systems has been obtained. The experimental part of this work is accomplished by diffusion couples and key samples analysis.

In order to obtain a sound thermodynamic description, the liquids of the constituent binary and ternary sub-systems of the Mg-Cu-Ni-Y quaternary have been modeled using the modified quasichemical model which considers the short range ordering in the liquid. To describe the terminal solid solutions, the Bragg-Williams model with Redlich-Kister polynomial has been used. The binary and ternary solubility of the intermetallic compounds have been reproduced thermodynamically using sublattice modeling within the compound energy formalism. The crystallographic information has been considered during modeling. The impact of the end-members on the homogeneity range of the compounds has been identified to reduce the number of parameters of the sublattice model.

Based on the experimental phase diagram and thermodynamic properties available in the literature, optimization of the Mg-Ni, Mg-Y, Ni-Y and Cu-Ni systems has been carried out. Excellent agreement between the current calculations and the experimental data has been obtained. Also, thermodynamic database of the Mg-Cu-Y, Mg-Ni-Y, Mg-Cu-Ni and Cu-Ni-Y ternary systems has been constructed by incorporating the experimental findings of this work and from the literature. Several isothermal sections, vertical sections and phase assemblage diagrams have been constructed to understand the phase relations in these ternary systems.

A combined approach of diffusion couples and key samples analysis has been carried out to establish the isothermal sections of the Mg-Ni-Y and Cu-Ni-Y systems. All the ternary compounds identified in the diffusion couples have been verified using key samples. This effort enabled accurate determination of the phase composition as well as the ternary solubility of the binary compounds. The Mg-Cu-Y system has been investigated using key samples. The homogeneity of the key samples has been ensured by crushing and melting several times in a controlled inert atmosphere.

The experimental investigation on the Mg-Ni-Y system revealed twelve ternary intermetallic compounds. Crystal structure of two of these compounds has been determined. This has been done by comparing several alloys containing the same phase with similar structure type compounds from Pearson crystal structure database. Ternary solubility of the binary compounds; Mg_2Ni , MgNi_2 , $\text{Mg}_{24}\text{Y}_5(\epsilon)$, $\text{Mg}_2\text{Y}(\delta)$, $\text{MgY}(\gamma)$, Ni_{17}Y_2 , Ni_2Y , NiY and NiY_3 have been found to extend in the ternary Mg-Ni-Y system. The existence of eleven ternary compounds has been confirmed in the Mg-Cu-Y system. Also, ternary solubility of ten binary compounds; $\text{Mg}_{24}\text{Y}_5(\epsilon)$, $\text{Mg}_2\text{Y}(\delta)$, $\text{MgY}(\gamma)$, Mg_2Cu ,

MgCu₂, CuY, Cu₂Y, Cu₇Y₂, Cu₄Y and Cu₆Y has been determined. In the Cu-Ni-Y system, it is found that nine binary compounds; NiY₃, Ni₂Y, Ni₃Y, Ni₇Y₂, Ni₅Y, Ni₁₇Y₂, Cu₆Y, Cu₇Y₂ and Cu₂Y dissolve the third component. Also, complete mutual solubility between CuY-NiY and Cu₄Y-Ni₄Y has been established. Based on the current experiments, the isothermal sections of the Mg-Cu-Y and Mg-Ni-Y systems at 673 K and the Cu-Ni-Y system at 973 K are constructed.

The liquidus projections of the four ternary systems are calculated based on the present thermodynamic modeling. The invariant reactions along with their temperatures and compositions are identified. Also, the primary crystallization field of the pertinent phases in the ternary systems are identified.

Thermal analysis is also performed for the Mg-Cu-Y, Mg-Ni-Y and Cu-Ni-Y systems using DSC technique. Experimental phase transformations and liquidus temperatures are compared with the thermodynamic calculations which show reasonable agreement.

None of the commercially available databases possesses these systems for the whole composition range. Hence such an extensive work was needed. The present self-consistent thermodynamic database will provide the most accurate description of the Mg-Cu-Ni-Y quaternary. It can be used for the prediction of the best composition for metallic glass as well as several other applications.

9.2 Contributions

In this work, the Mg-Cu-Ni-Y quaternary, one of the most promising Mg-based alloys, has been studied experimentally and thermodynamically to provide an accurate description of the phase equilibria.

- A self-consistent thermodynamic database for the Mg-Cu-Ni-Y quaternary has been constructed for the first time. Optimizations of the binary systems: Mg-Ni, Mg-Y, Ni-Y and Cu-Ni and, ternary systems: Mg-Cu-Y, Mg-Ni-Y, Mg-Cu-Ni and Cu-Ni-Y have been carried out using the most accurate experimental results of the phase diagram and thermodynamic properties from the current work as well as from the literature.
- The modified quasichemical model has been used for the first time to describe the liquid phase of the constituent binary and ternary systems of the Mg-Cu-Ni-Y quaternary.
- The presence of the ternary compounds in the Mg-Cu-Y system has been confirmed. The isothermal section at 673 K of the Mg-Cu-Y system for the whole composition range has been determined for the first time. Experimental findings of the homogeneity range of the ternary compounds, $\text{MgCu}_4\text{Y}(\tau_2)$, $\text{MgCu}_2\text{Y}_2(\tau_3)$ and $\text{Mg}_x\text{Cu}_y\text{Y}_z(\tau_{11})$ (where $x = 9$ to 18 and $y/z = 1$) have been modeled successfully.
- The present understanding of the Mg-Cu-Y system has been used to explain the solidification behavior of some of the most promising glass forming regions. It

has been found that higher glass forming alloys lies on the valley of the deep eutectic and not exactly on the eutectic point.

- Twelve ternary intermetallic compounds have been identified in the Mg-Ni-Y system. The complex phase relations for the whole composition range of this system have been established for the first time. Ternary solubility of three of the ternary compounds, $\text{MgNiY}_4(\tau_1)$, $\text{MgNi}_4\text{Y}(\tau_3)$ and $\text{Mg}_8\text{NiY}(\tau_{10})$ have been determined and thermodynamically modeled.
- Crystal structures of $\text{MgNiY}_4(\tau_1)$ and $\text{MgNi}_2\text{Y}_2(\tau_2)$ ternary compounds have been determined.
- This is the first attempt to construct a complete isothermal section of the Cu-Ni-Y system at 973 K. The maximum ternary solubility of nine binary compounds in this system has been determined. Complete mutual solubility between CuY-NiY and Cu_4Y - Ni_4Y has been established.
- Rietveld analysis has been carried out for the XRD results and the variation of the lattice parameters has been reported for the NiY and Cu_2Y compounds in the Cu-Ni-Y system.
- The present work has provided a thorough experimental study using thermal analysis and microstructure characterization coupled with thermodynamic calculations for the Mg-Cu-Y, Mg-Ni-Y and Cu-Ni-Y systems.

During the course of the current research work the following publications and presentations have been accomplished:

Journal publications

1. M. Mezbahul-Islam and M. Medraj, "Phase Equilibrium In Mg-Cu-Y" , Scientific reports, Nature publishers (accepted August 2013).
2. M. Mezbahul-Islam and M. Medraj, "Experimental study of the Cu-Ni-Y system at 700°C using diffusion couples and key alloys", Journal of Alloys and Compounds, 2013, Vol. 561 (5) pp. 161-173.
3. M. Mezbahul-Islam and M. Medraj, "A Critical Thermodynamic Assessment of the Mg-Ni, Ni-Y Binary and Mg-Ni-Y Ternary Systems", CALPHAD, 2009, Vol. 33 (3) pp. 478-486.
4. P. Ghosh, M. Mezbahul-Islam and M. Medraj, "Critical assessment and thermodynamic modeling of Mg-Zn, Mg-Sn, Sn-Zn and Mg-Sn-Zn systems", CALPHAD, 2012, Vol. 36 pp. 28-43.
5. A. Mostafa, A. Gheribi, D. Kevorkov, M. Mezbahul-Islam, and M. Medraj, "Experimental Investigation and Thermodynamic Modeling of Mn-Nd Phase Diagram", CALPHAD, 2013, Vol. 42, pp. 27-37.
6. M. Mezbahul-Islam, D. Kevorkov and M. Medraj, "Experimental study of the Mg-Ni-Y system at 673 K using diffusion couples and key alloys" (In preparation)

Conference publications:

1. M. Mezbahul-Islam, D. Kevorkov, E. Essadiqi and M. Medraj, "Ternary intermetallic compounds across the Mg-NiY line at 673 K", Materials Science Forum, 2012, Vols. 706-709, pp. 1134-1139.

2. M. Mezbahul-Islam, E. Essadiqi and M. Medraj, "A Differential Scanning Calorimetric Study of the Mg-Cu-Y System", Materials Science Forum, 2012, Vols. 706-709, pp. 1215-1220.
3. M. Mezbahul-Islam and M. Medraj, "Thermodynamic modeling of the Mg-Cu-Ni ternary system using the modified quasichemical model", COM 2011, Light metals, pp. 241-253.
4. M. Mezbahul-Islam and M. Medraj, "Thermodynamic evaluation of the Mg-Ni-Y Ternary System", Proceedings of the Materials Science & Technology Conference, Pittsburgh, Pennsylvania, USA, Oct 5-9, 2008, pp.1017-1028.

9.3 Suggestions for future work

The present work provides a clear understanding of the phase equilibria in the Mg-Cu-Ni-Y system. However, it can be improved by further experimental studies to refine the thermodynamic modeling. For example the following suggestions can be useful:

- Crystallographic information of the newly discovered ternary intermetallic compounds in the Mg-Ni-Y system needs to be determined. This can be achieved by preparing alloys containing the phase of interest and examining them using single crystal XRD analysis and Transmission Electron Microscopy (TEM) with specimen preparation using Focused Ion Beam (FIB).
- Some of the phase triangulations of the Cu-Ni-Y system could not be confirmed due to difficulty of sample preparation. This needs to be confirmed. Also, crystal structure of Ni_4Y needs to be determined to validate the proposed complete mutual solubility $\text{Cu}_4\text{Y-Ni}_4\text{Y}$.

- Care should be taken while preparing samples especially in the Mg-Ni-Y system. Due to higher melting temperature of Ni and the affinity of Mg to oxygen, it is difficult to obtain homogenous alloy. Therefore it is suggested to prepare the master alloy of Ni-Y and then add Mg in an arc melting furnace. The alloy then can be re-melted in the induction melting furnace to ensure homogeneity.
- Both Mg-Cu-Y and Mg-Ni-Y are glass forming systems. This means these alloys have slow equilibrium kinetics. To obtain complete equilibrium it is advised to heat treat the alloys for at least four weeks.
- Few key samples on the quaternary Mg-Cu-Ni-Y system can be analyzed experimentally to verify the phase relations obtained through thermodynamic modeling.
- Some of the suggested metallic glass samples (ribbons) can be prepared using melt-spinning to study their thermal stability, glass transition and crystallization temperatures as well as mechanical properties.
- Hydrogen sorption properties of some of the Mg-Ni-Y alloys can be tested using PCT (Pressure Composition Temperature) instrument.

References

- [1] D. Salt, Blasting out supermetals, in: *Materials Monthly*, Centre for Science and Engineering of Materials (CSEM), Australian National University, February, 2006.
- [2] R. Hojvat de Tandler, M.R. Soriano, M.E. Pepe, J.A. Kovacs, E.E. Vicente, J.A. Alonso, Calculation of metastable free-energy diagrams and glass formation in the Mg–Cu–Y alloy and its boundary binaries using the Miedema model, *Intermetallics*, 14 (2006) 297-307.
- [3] A. Inoue, A. Kato, T. Zhang, S.G. Kim, T. Masumoto, Magnesium-copper-yttrium amorphous alloys with high mechanical strengths produced by a metallic mold casting method, *Materials Transactions, The Japan Institute of Metals and Materials*, 32 (1991) 609-616.
- [4] A. Inoue, K. Ohtera, K. Kita, T. Masumoto, New amorphous magnesium-cerium-nickel alloys with high strength and good ductility, *Japanese Journal of Applied Physics, Part 2*, 27 (1988) L2248-L2251.
- [5] G. Chen, M. Ferry, Crystallization and thermally induced surface relief effects in a Mg₆₅Cu₂₅Y₁₀ bulk metallic glass, *Journal of Materials Science* 42 (2007) 646-651.
- [6] A. Katz-Demyanetz, H. Rosenson, Z. Koren, M. Regev, Bulk metallic glass formation in the Mg–Cu–Y system, *Materials Science and Technology* 25 (2009) 1227-1233.
- [7] D. Kim, B.-J. Lee, N.J. Kim, Prediction of composition dependency of glass forming ability of Mg–Cu–Y alloys by thermodynamic approach, *Scripta Materialia*, 52 (2005) 969-972.
- [8] S.G. Kim, A. Inoue, T. Masumoto, High mechanical strengths of magnesium-nickel-yttrium and magnesium-copper-yttrium amorphous alloys with significant supercooled liquid region, *Materials Transactions, The Japan Institute of Metals and Materials*, 31 (1990) 929-934.
- [9] Q.F. Li, K.Q. Qiu, X. Yang, Y.L. Ren, X.G. Yuan, T. Zhang, Glass forming ability and reliability in fracture stress for Mg–Cu–Ni–Nd–Y bulk metallic glasses, *Materials Science and Engineering: A*, 491 (2008) 420-424.
- [10] Z.P. Lu, Y. Li, S.C. Ng, Reduced glass transition temperature and glass forming ability of bulk glass forming alloys, *Journal of Non-Crystalline Solids*, 270 (2000) 103-114.
- [11] D. Ma, Y.A. Chang, Competitive formation of ternary metallic glasses, *Acta Materialia*, 54 (2006) 1927-1934.

- [12] H. Ma, Q. Zheng, J. Xu, Y. Li, E. Ma, Doubling the critical size for bulk metallic glass formation in the Mg-Cu-Y ternary system, *Journal of Materials Research*, 20 (2005) 2252-2255.
- [13] B.S. Murty, K. Hono, Formation of nanocrystalline particles in glassy matrix in melt-spun Mg-Cu-Y based alloys, *Materials Transactions, The Japan Institute of Metals and Materials*, 41 (2000) 1538-1544.
- [14] E. Akiba, Hydrogen-absorbing alloys, *Current Opinion in Solid State and Materials Science*, 4 (1999) 267-272.
- [15] M. Hara, S. Morozumi, K. Watanabe, Effect of a magnesium depletion on the Mg-Ni-Y alloy hydrogen absorption properties, *Journal of Alloys and Compounds*, 414 (2006) 207-214.
- [16] N. Cui, J.L. Luo, K.T. Chuang, Nickel-metal hydride (Ni-MH) battery using Mg₂Ni-type hydrogen storage alloy, *Journal of Alloys and Compounds*, 302 (2000) 218-226.
- [17] L. Kaufman, H. Bernstein, *Computer Calculation of Phase Diagrams; With Special Reference to Refractory Metals (Refractory Materials, Vol. 4)*, Academic, 1970.
- [18] U.R. Kattner, The thermodynamic modeling of multicomponent phase equilibria, *JOM*, 49 (1997) 14-19.
- [19] K.K.C. Hari, P. Wollants, Some guidelines for thermodynamic optimisation of phase diagrams, *Journal of Alloys and Compounds*, 320 (2001) 189-198.
- [20] C.W. Bale, P. Chartrand, S.A. Degterov, G. Eriksson, K. Hack, M.R. Ben, J. Melancon, A.D. Pelton, S. Petersen, FactSage thermochemical software and databases, *CALPHAD: Comput. Coupling Phase Diagrams Thermochem.*, 26 (2002) 189-228.
- [21] G. Voss, Alloys of Nickel with Tin, Lead, Thallium, Bismuth, Chromium, Magnesium, Zinc, and Cadmium, *Zeitschrift fuer Anorganische Chemie*, 57 (1908) 34-71.
- [22] J.L. Haughton, R.J.M. Payne, Alloys of magnesium research. I. The constitution of the magnesium-rich alloys of magnesium and nickel, *Journal of the Institute of Metals*, 54 (1934) 275-284.
- [23] P. Bagnoud, P. Feschotte, Binary systems of magnesium-copper and magnesium-nickel, especially the nonstoichiometry of the MgCu₂ and MgNi₂ laves phases, *Zeitschrift für Metallkunde*, 69 (1978) 114-120.
- [24] K. Micke, H. Ipsen, Thermodynamic properties of liquid magnesium-nickel alloys, *Monatsh. Chem.*, 127 (1996) 7-13.

- [25] P.D. Merica, R.G. Waltenberg, Tech. Paper, National Bureau of Standards (U.S), 19 (1925) 155-182.
- [26] J.S. Wollam, W.E. Wallace, Magnetic susceptibility, heat capacity, and third-law entropy of MgNi_2 , *Physics and Chemistry of Solids*, 13 (1960) 212-220.
- [27] K.H.J. Buschow, Magnetic properties of magnesium-cobalt (MgCo_2), magnesium-nickel (MgNi_2), and magnesium-nickel (Mg_2Ni), *Solid State Communications*, 17 (1975) 891-893.
- [28] F. Laves, H. Witte, X-ray determination of structure of MgNi_2 , *Metallwirtschaft, Metallwissenschaft, Metalltechnik*, 14 (1935) 1002.
- [29] K.H. Lieser, H. Witte, The ternary systems Mg-Cu-Zn; Mg-Ni-Zn; Mg-Cu-Ni, *Zeitschrift für Metallkunde*, 43 (1952) 396-401.
- [30] K. Schubert, K. Anderko, Crystal structure of NiMg_2 , CuMg_2 and AuMg_3 , *Zeitschrift für Metallkunde*, 42 (1951) 321-324.
- [31] H. Feufel, F. Sommer, Thermodynamic investigations of binary liquid and solid Cu-Mg and Mg-Ni alloys and ternary liquid Cu-Mg-Ni alloys, *Journal of Alloys and Compounds*, 224 (1995) 42-54.
- [32] I.T. Sryvalin, O.A. Esin, B.M. Lepinskikh, Thermodynamic properties of solutions of magnesium in nickel, lead, and silicon, *Zhurnal Fizicheskoi Khimii*, 38 (1964) 637-641.
- [33] P. Sieben, N.G. Schmahl, Vapor pressure and activity of magnesium in the binary alloy systems with nickel and copper and vapor pressures of some pure metals, *Giesserei, Technisch-Wissenschaftliche Beihefte, Giessereiwesen und Metallkunde*, 18 (1966) 197-211.
- [34] P. Schubel, The heat capacity of metals and metallic compounds between 18 and 600°, *Zeitschrift fuer Anorganische Chemie*, 87 (1914) 81-119.
- [35] J.F. Smith, J.L. Christian, Thermodynamics of formation of copper-magnesium and nickel-magnesium compounds from vapor-pressure measurements, *Acta metallurgica Sinica*, 8 (1960) 249-255.
- [36] R.C. King, O.J. Kleppa, A thermochemical study of some selected Laves phases, *Acta Metallurgica*, 12 (1964) 87-97.
- [37] G.M. Lukashenko, V.N. Eremenko, Thermodynamic properties of alloys in the system magnesium-nickel in the solid state, *zvestiya Akademii Nauk SSSR, Metally*, (1966) 161-164.
- [38] A.A. Nayeb-Hashemi, J.B. Clark, The Mg-Ni system, *Bulletin of alloy phase diagrams*, 6 (1985) 238-244.

- [39] M.H.G. Jacobs, P.J. Spencer, A critical thermodynamic evaluation of the Mg-Ni system, CALPHAD: Computer Coupling of Phase Diagrams and Thermochemistry, 22 (1999) 513-525.
- [40] F. Islam, M. Medraj, The phase equilibria in the Mg-Ni-Ca system, CALPHAD: Computer Coupling of Phase Diagrams and Thermochemistry, 29 (2005) 289-302.
- [41] M. Hansen, K.P. Anderko, Constitution of Binary Alloys. Translated from German, McGraw-Hill Book Co., 1957.
- [42] D.J. Chakrabarti, D.E. Laughlin, S.W. Chen, Phase Diagrams of Binary Copper Alloys, ASM International, Ohio, OH, (1994) 276-286.
- [43] E. Schuermann, E. Schulz, Liquidus and solidus curves of the systems copper-manganese and copper-nickel, Z. Metallk., 62 (1971) 758-762.
- [44] E.A. Feest, R.D. Doherty, Copper-nickel equilibrium phase diagram, Journal of the Institute of Metals 99 (1971) 102-103.
- [45] B. Predel, R. Mohs, Thermodynamic study of molten nickel-copper alloys, Archiv fuer das Eisenhuettenwesen, 42 (1971) 575-579.
- [46] B. Mozer, D.T. Keating, S.C. Moss, Neutron measurement of clustering in the alloy CuNi [copper-nickel], Physical Review 175 (1968) 868-876.
- [47] M.F. Ebel, X-ray measurements on spinodal decomposition in copper-nickel alloys, Physica Status Solidi A, 5 (1971) 91-94.
- [48] J. Vrijen, S. Radelaar, Clustering in copper-nickel alloys: a diffuse neutron-scattering study, Physical Review B, 17 (1978) 409-421.
- [49] T. Tsakalakos, Spinodal decomposition in copper-nickel alloys by artificial composition modulation technique, Scripta Metallurgica, 15 (1981) 255-258.
- [50] R.N. Dokken, J.F. Elliott, Calorimetry at 1100 to 1200°: the copper-nickel, copper-silver, and copper-cobalt systems, Transactions of the American Institute of Mining, Metallurgical and Petroleum Engineers 233 (1965) 1351-1358.
- [51] Y. Tozaki, Y. Iguchi, S. Banya, T. Fuwa, Heat of mixing of iron alloys, in, Iron Steel Inst., 1973, pp. 130-132.
- [52] Y. Iguchi, Y. Tozaki, M. Kakizaki, Calorimetric Examination of Mixing Heats of Nickel and Cobalt Alloys, Journal of the Iron and Steel Institute of Japan, 63 (1977) 953-961.
- [53] U.K. Stolz, I. Arpshofen, F. Sommer, B. Predel, Determination of the enthalpy of mixing of liquid alloys using a high-temperature mixing calorimeter, Journal of Phase Equilibria, 14 (1993) 473-478.

- [54] M.A. Turchanin, S.V. Porokhnya, L.V. Belevtsov, A.V. Kokhan, Thermodynamic properties of liquid copper-nickel alloys, *Rasplavy*, (1994) 8-12.
- [55] C.W. Schultz, G.R. Zellars, S.L. Payne, E.F. Foerster, Activities of copper and nickel in liquid copper-nickel alloys, *Bur. Mines Rep. Invest.*, 6410 (1964) 9 pp.
- [56] A.D. Kulkarni, R.E. Johnson, Thermodynamic studies of liquid copper alloys by electromotive force method. II. Copper-nickel-oxygen and copper-nickel systems, *Metallurgical Transactions*, 4 (1973) 1723-1727.
- [57] V.V. Berezutskii, G.M. Lukashenko, Thermodynamic properties of liquid nickel-copper alloys, *Ukrainskii Khimicheskii Zhurnal (Russ. Ed.)*, 53 (1987) 1029-1032.
- [58] J.S.L. Leach, M.B. Bever, Heats of formation of copper-nickel alloys, *Transactions of the American Institute of Mining, Metallurgical and Petroleum Engineers* 215 (1959) 728-729.
- [59] R.A. Oriani, W.K. Murphy, Heats of formation of solid nickel-copper and nickel-gold alloys, *Acta Metallurgica*, 8 (1960) 23-25.
- [60] L. Elford, F. Mueller, O. Kubaschewski, Thermodynamic properties of copper-nickel alloys, *Berichte der Bunsen-Gesellschaft*, 73 (1969) 601-605.
- [61] A.A. Vecher, Y.I. Gerasimov, Investigation of thermodynamic properties of binary metallic systems by the electromotive force method. VII. Cu-Ni solid solutions, *Zhurnal Fizicheskoi Khimii*, 37 (1963) 490-498.
- [62] R.A. Rapp, F. Maak, Thermodynamic properties of solid copper-nickel alloys, *Acta Metallurgica*, 10 (1962) 63-69.
- [63] I. Katayama, H. Shimatani, Z. Kozuka, Thermodynamic study of solid copper-nickel and nickel-molybdenum alloys by emf. measurements using solid electrolyte, *Nippon Kinzoku Gakkaishi*, 37 (1973) 509-515.
- [64] A. Kontopoulos, Thermodynamic activities in copper-nickel-iron solid solutions, *Praktika tes Akademias Athenon*, 52 (1978) B607-B619.
- [65] S. Srikanth, K.T. Jacob, Thermodynamic properties of copper-nickel alloys: measurements and assessment, *Materials Science and Technology* 5(1989) 427-434.
- [66] M.S. An, Thermodynamic re-evaluation of the copper-nickel system, *CALPHAD: Comput. Coupling Phase Diagrams Thermochem.*, 16 (1992) 255-260.
- [67] M.A. Turchanin, P.G. Agraval, A.R. Abdulov, Phase equilibria and thermodynamics of binary copper systems with 3d-metals. VI. Copper-nickel system, *Powder Metallurgy and Metal Ceramics*, 46 (2007) 467-477.

- [68] B.J. Beaudry, A.H. Daane, Yttrium-nickel system, *Trans. Metall. Soc. AIME*, 218 (1960) 854-859.
- [69] R.F. Domagala, J.J. Rausch, D.W. Levinson, The systems Y-Fe, Y-Ni, and Y-Cu, *Transactions of the American Society for Metals*, 53 (1961) 137-155.
- [70] K.H.J. Buschow, Intermetallic compounds of rare earth and 3d transition metals, *Rep. Prog. Phys.*, 40 (1977) 1179-1256.
- [71] K.H.J. Buschow, Crystal structures of the rare-earth compounds of the form R_2Ni_{17} , R_2Co_{17} , and R_2Fe_{17} , *Journal of the Less-Common Metals*, 11 (1966) 204-208.
- [72] P. Nash, Ni-Y, *Binary Alloy Phase Diagrams*, ASM International, Materials Park, OH, 2nd edition (1991).
- [73] P.R. Subramanian, J.F. Smith, Thermodynamics of formation of yttrium-nickel alloys, *Metallurgical Transactions B: Process Metallurgy*, 16B (1985) 577-584.
- [74] Z. Du, W. Zhang, Thermodynamic assessment of the Ni-Y system, *Journal of Alloys and Compounds*, 245 (1996) 164-167.
- [75] N. Mattern, M. Zinkevich, W. Loeser, G. Behr, J. Acker, Experimental and thermodynamic assessment of the Nb-Ni-Y system, *Journal of Phase Equilibria and Diffusion*, 29 (2008) 141-155.
- [76] Y.Y. Pan, P. Nash, *Binary Alloy Phase Diagrams*, ASM International, Materials Park, OH, 2nd ed. (1991) 2406-2408.
- [77] M. Palumbo, G. Borzone, S. Delsante, N. Parodi, G. Cacciamani, R. Ferro, L. Battezzati, M. Baricco, Thermodynamic analysis and assessment of the Ce-Ni system, *Intermetallics*, 12 (2004) 1367-1372.
- [78] P. Nash, The Ni-Yb (nickel-ytterbium) system, *Bulletin of Alloy Phase Diagrams*, 10 (1989) 129-132, 199-200.
- [79] H. Zhou, X. Ou, X. Zhong, An investigation of the holmium-nickel phase diagram, *Journal of Alloys and Compounds*, 177 (1991) 101-106.
- [80] Y.Y. Pan, P. Nash, *Binary Alloy Phase Diagrams*, ASM International, Materials Park, OH, 2nd ed. (1991) 77.
- [81] D. Gignoux, D. Givord, R. Lemaire, A.N. Saada, A. Del Moral, Field induced magnetic density in the Pauli paramagnet YNi_5 , *Journal of Magnetism and Magnetic Materials*, 23 (1981) 274-278.
- [82] D. Gignoux, D. Givord, A. Lienard, d Magnetism in the amorphous yttrium-cobalt, yttrium-nickel, and yttrium-iron alloys, *Journal of Applied Physics*, 53 (1982) 2321-2323.

- [83] M.H.H. Van, K.H.J. Buschow, A.R. Miedema, Hydrogen absorption of rare-earth (3d) transition intermetallic compounds, *Journal of the Less-Common Metals*, 49 (1976) 473-475.
- [84] A.R. Miedema, On the heat of formation of solid alloys. II, *Journal of the Less-Common Metals*, 46 (1976) 67-83.
- [85] R.E. Watson, L.H. Bennett, Optimized predictions for heats of formation of transition-metal alloys. II, *CALPHAD: Comput. Coupling Phase Diagrams Thermochem.*, 8 (1984) 307-321.
- [86] G.I. Batalin, V.A. Stukalo, N.Y. Neshchimenko, V.A. Gladkikh, O.I. Lyuborets, Enthalpy of formation of molten yttrium-nickel alloys, *Izv. Akad. Nauk SSSR, Met.*, (1977) 44-45.
- [87] M. Mezbahul-Islam, D. Kevorkov, M. Medraj, The equilibrium phase diagram of the magnesium-copper-yttrium system, *The Journal of Chemical Thermodynamics*, 40 (2008) 1064-1076.
- [88] H.D. Zhao, G.W. Qin, Y.P. Ren, W.L. Pei, D. Chen, Y. Guo, The maximum solubility of Y in α -Mg and composition ranges of $Mg_{24}Y_{5-x}$ and Mg_2Y_{1-x} intermetallic phases in Mg-Y binary system, *Journal of Alloys and Compounds*, 509 (2011) 627-631.
- [89] E.D. Gibson, O.N. Carlson, The yttrium-magnesium alloy system, *Transactions of the American Society for Metals*, 52 (1960) 1084-1096.
- [90] Z.A. Sviderskaya, E.M. Padezhnova, Phase equilibria in magnesium-yttrium and magnesium-yttrium-manganese systems, *Izv. Akad. Nauk SSSR, Metal.*, (1968) 183-190.
- [91] D. Mizer, J.B. Clark, Magnesium-rich region of the magnesium-yttrium phase diagram, *Transactions of the American Institute of Mining, Metallurgical and Petroleum Engineers* 221 (1961) 207-208.
- [92] J.F. Smith, D.M. Bailey, D.B. Novotny, J.E. Davison, Thermodynamics of formation of yttrium-magnesium intermediate phases, *Acta Metallurgica*, 13 (1965) 889-895.
- [93] H. Flandorfer, M. Giovannini, A. Saccone, P. Rogl, R. Ferro, The Ce-Mg-Y system, *Metallurgical and Materials Transactions A*, 28A (1997) 265-276.
- [94] R. Agarwal, H. Feufel, F. Sommer, Calorimetric measurements of liquid La-Mg, Mg-Yb and Mg-Y alloys, *Journal of Alloys and Compounds*, 217 (1995) 59-64.
- [95] V. Ganesan, F. Schuller, H. Feufel, F. Sommer, H. Ipsen, Thermodynamic properties of ternary liquid Cu-Mg-Y alloys, *Zeitschrift fuer Metallkunde*, 88 (1997) 701-710.
- [96] V. Ganesan, H. Ipsen, Thermodynamic properties of liquid magnesium-yttrium alloys, *Journal de Chimie Physique et de Physico-Chimie Biologique*, 94 (1997) 986-991.

- [97] I.N. Pyagai, A.V. Vakhobov, N.G. Shmidt, O.V. Zhikhareva, M.I. Numanov, Heats of formation of magnesium intermetallic compounds with yttrium, lanthanum, and neodymium, Dokl. Akad. Nauk Tadzh. SSR, 32 (1989) 605-607.
- [98] P. Bagnoud, P. Feschotte, Binary systems of magnesium-copper and magnesium-nickel, especially the nonstoichiometry of the $MgCu_2$ and $MgNi_2$ laves phases, Zeitschrift fuer Metallkunde, 69 (1978) 114-120.
- [99] R. Sahmen, Alloys of copper with cobalt, iron, manganese and magnesium, Zeitschrift für Anorganische und Allgemeine Chemie, 57 (1908) 1-33.
- [100] G.G. Urazov, Alloys of copper and magnesium, Zhurnal Russkogo Fiziko-Khimicheskogo Obschestva, 39 (1907) 1556-1581.
- [101] W.R.D. Jones, Copper-magnesium alloys. IV. Equilibrium diagram, J. Inst. Metals, Advance copy, No. 574 (1931) 25 pp.
- [102] L. Rogel'berg, Solubility of Mg in Cu and Combined Solubility of Mg and Al in Cu, Trudy Instituta - Gosudarstvennyi Nauchno-Issledovatel'skii Proektnyi Institut Splavov i Obrabotki Tsvetnykh Metallov (Russian), 16 (1957) 82-89.
- [103] U. Abend, H.J. Schaller, Constitution and thermodynamics of Cu-Y alloys, Berichte der Bunsen-Gesellschaft, 101 (1997) 741-748.
- [104] T.B. Massalski, J.L. Murray, L.H. Bennett, H. Barker, Binary Alloy Phase Diagrams: Cu-Y, American Society for Metals, Metals park, Ohio, (1986) 977-978.
- [105] S.G. Fries, H.L. Lukas, R. Konetzki, R. Schmid-Fetzer, Experimental investigation and thermodynamic optimization of the Y-Cu binary system, Journal of Phase Equilibria, 15 (6) (1994) 606-614.
- [106] G. Qi, K. Itagaki, A. Yazawa, High-temperature heat content measurements of copper-RE (RE = yttrium, lanthanum, cerium, praseodymium, neodymium) binary systems, Materials Transactions, The Japan Institute of Metals and Materials, 30 (1989) 273-282.
- [107] K.H. Lieser, H. Witte, The ternary systems Mg-Cu-Zn; Mg-Ni-Zn; Mg-Cu-Ni, Zeitschrift fuer Metallkunde, 43 (1952) 396-401.
- [108] H. Ipser, T. Gnanasekaran, S. Boser, H. Mikler, A contribution to the ternary copper-magnesium-nickel phase diagram, Journal of Alloys and Compounds, 227 (1995) 186-192.
- [109] W. Xiong, Y. Du, W.-W. Zhang, W.-H. Sun, X.-G. Lu, F.-S. Pan, Thermodynamic reassessment of the Cu-Mg-Ni system with brief comments on the thermodynamic modeling of the sub-systems, CALPHAD: Comput. Coupling Phase Diagrams Thermochem., 32 (2008) 675-685.

- [110] K.P. Gupta, The Cu-Mg-Ni (copper-magnesium-nickel) system, *Journal of Phase Equilibria and Diffusion*, 25 (2004) 471-478.
- [111] H.L. Lukas, L. Rokhlin, Landolt-Boernstein., Numerical Data and Functional Relationships in Science and Technology (New Series), Physical Chemistry. Ed. Martiensen, W., in: Ternary Alloys systems. Phase Diagrams, Crystallographic and Thermodynamic Data, Group IV (11A4), Springer-Verlag, Berlin, Heidelberg,, 2006.
- [112] V.I. Mikheeva, G.G. Babayan, Melting diagram of the system magnesium-copper-nickel, *Dokl. Akad. Nauk SSSR*, 108 (1956) 1086-1087.
- [113] V.V. Karonik, V.V. Guseva, A.V. Ivanishchev, V.E. Kolesnichenko, Phase diagrams of the magnesium-nickel-copper and magnesium-nickel-silver systems, *Izv. Akad. Nauk SSSR, Met.*, (1983) 220-224.
- [114] P.J. Fehrenbach, H.W. Kerr, P. Niessen, Constitution of copper-nickel-magnesium alloys, *Journal of Materials Science* 7(1972) 1168-1174.
- [115] T. Gnanasekaran, H. Ipsier, The isopiestic method applied to an investigation of the thermodynamic properties of ternary copper-nickel-magnesium alloys, *J. Chim. Phys. Phys.-Chim. Biol.*, 90 (1993) 367-372.
- [116] T. Gnanasekaran, H. Ipsier, Partial thermodynamic properties of magnesium in ternary liquid copper-magnesium-nickel alloys, *Journal of Non-Crystalline Solids*, 156-158 (1993) 384-387.
- [117] T. Gnanasekaran, H. Ipsier, Thermodynamic properties of ternary liquid Cu-Mg-Ni alloys, *Metallurgical and Materials Transactions B*, 25B (1994) 63-72.
- [118] S. Gorsse, G.J. Shiflet, A thermodynamic assessment of the Cu-Mg-Ni ternary system, *CALPHAD: Comput. Coupling Phase Diagrams Thermochem.*, 26 (2002) 63-83.
- [119] J. Miettinen, Thermodynamic description of Cu-Mg-Ni and Cu-Mg-Zn systems, *CALPHAD: Comput. Coupling Phase Diagrams Thermochem.*, 32 (2008) 389-398.
- [120] R. Busch, W. Liu, W.L. Johnson, Thermodynamics and kinetics of the Mg₆₅Cu₂₅Y₁₀ bulk metallic glass forming liquid, *Journal of Applied Physics*, 83 (1998) 4134-4141.
- [121] M. Palumbo, L. Battezzati, Thermodynamics and kinetics of metallic amorphous phases in the framework of the CALPHAD approach, *Calphad*, 32 (2008) 295-314.
- [122] S. De Negri, P. Solokha, A. Saccone, V. Pavlyuk, The Y-Cu-Mg system in the 0–66.7at.% Cu concentration range: The isothermal section at 400°C, *Intermetallics*, 17 (2009) 614-621.

- [123] P. Solokha, S. De Negri, V. Pavlyuk, A. Saccone, Inhomogeneous 2D linear intergrowth structures among novel Y–Cu–Mg ternary compounds with yttrium/copper equiatomic ratio, *Solid State Sciences*, 11 (2009) 801-811.
- [124] Institute for Materials Research of Tohoku University. KIND Data Base. (Cited on October 30, 2012), http://www-db2.imr.tohoku.ac.jp/kind/11_Amor_Ternary/Cu-Mg-Y.html.
- [125] Q. Yao, H. Zhou, Z. Wang, The isothermal section of the phase diagram of the ternary system Y-Mg-Ni at 673K in the region 50-100 at.% Ni, *Journal of Alloys and Compounds*, 421 (2006) 117-119.
- [126] M. Mezbahul-Islam, M. Medraj, A critical thermodynamic assessment of the Mg-Ni, Ni-Y binary and Mg-Ni-Y ternary systems, *CALPHAD: Comput. Coupling Phase Diagrams Thermochem.*, 33 (2009) 478-486.
- [127] K. Kadir, T. Sakai, I. Uehara, Structural investigation and hydrogen capacity of YMg_2Ni_9 and $(\text{Y}_{0.5}\text{Ca}_{0.5})(\text{MgCa})\text{Ni}_9$: new phases in the AB_2C_9 system isostructural with LaMg_2Ni_9 , *Journal of Alloys and Compounds*, 287 (1999) 264-270.
- [128] K. Kadir, T. Sakai, I. Uehara, Synthesis and structure determination of a new series of hydrogen storage alloys; RMg_2Ni_9 (R = La, Ce, Pr, Nd, Sm and Gd) built from MgNi_2 Laves-type layers alternating with AB_5 layers, *Journal of Alloys and Compounds*, 257 (1997) 115-121.
- [129] K. Kadir, D. Noreus, I. Yamashita, Structural determination of AMgNi_4 (where A=Ca, La, Ce, Pr, Nd and Y) in the AuBe_5 type structure, *Journal of Alloys and Compounds*, 345 (2002) 140-143.
- [130] K. Aono, S. Orimo, H. Fujii, Structural and hydriding properties of MgYNi_4 : a new intermetallic compound with C15b-type Laves phase structure, *Journal of Alloys and Compounds*, 309 (2000) L1-L4.
- [131] V.V. Burnasheva, B.P. Tarasov, Effect of the partial replacement of nickel or yttrium by other metals on hydrogen absorption by yttrium-nickel (YNi_3) compounds, *Zhurnal Neorganicheskoi Khimii*, 29 (1984) 1136-1141.
- [132] P.D. Carfagna, W.E. Wallace, R.S. Craig, Crystallographic and Magnetic Characteristics of the $\text{Y}_2\text{Ni}_{17-x}\text{Cu}_x$ System, *Journal of Solid State Chemistry* 2(1970) 1-5.
- [133] Y.L. Ren, J.H. Zuo, K.Q. Qiu, H.F. Zhang, Z.Q. Hu, Eutectic structure and bulk glass formation in Mg-based alloys, *Intermetallics*, 12 (2004) 1205-1209.
- [134] L. Zheng J. and Nong, A part of room temperature section of phase diagram of Y-Cu-Ni ($\text{Y} \leq 16.7$ at.%) system, *Acta metallurgica Sinica*, 21 (1985) B58-60.
- [135] H. Kadomatsu, Y. Kawanishi, M. Kurisu, Structural Phase Transitions in $\text{YCu}_{1-x}\mu_x$ (M = Ni, Ag, and Ga), *Journal of Less Common Metals*, 141 (1988) 29-36.

- [136] V. Paul-Boncour, A. Lindbaum, E. Gratz, E. Leroy, A. Percheron-Guégan, Structural study of the pseudobinary Y(Ni,Cu)₂ system, *Intermetallics*, 10 (2002) 1011-1017.
- [137] A.E. Dwight, Crystal structure of R.E.-Ni₄Au compounds and unit cell constants in the YCo₅-YNi₅-YCu₅ series, *Journal of Less Common Metals*, 43 (1975) 121-128.
- [138] K. Gupta, The Cu-Ni-Y (Copper-Nickel-Yttrium) System, *Journal of Phase Equilibria and Diffusion*, 30 (2009) 651-656.
- [139] P. Villars, K. Cenzual, *Pearson's Crystal Data—Crystal Structure Database for Inorganic Compounds (on CD-ROM)*, Materials Park, OH: ASM International, (2009).
- [140] M.M. Islam, Thermodynamic modeling of the Mg-Cu-Y system, M.A.Sc thesis, Concordia University, Canada, (2007).
- [141] A.T. Dinsdale, SGTE data for pure elements, *Calphad*, 15 (1991) 317-425.
- [142] W.L. Bragg, E.J. Williams, Effect of thermal agitation on atomic arrangement in alloys, *Proc. R. Soc. London, Ser. A*, 145 (1934) 699-730.
- [143] W.L. Bragg, E.J. Williams, Effect of thermal agitation on atomic arrangement in alloys. II, *Proc. R. Soc. London, Ser. A*, 151 (1935) 540-566.
- [144] O. Redlich, A.T. Kister, Thermodynamics of nonelectrolyte solutions, X–Y–T relations in a binary system, *Journal of Industrial and Engineering Chemistry*, 40 (1948) 341-345.
- [145] M. Hillert, M. Jarl, A model for alloying effects in ferromagnetic metals, *CALPHAD: Comput. Coupling Phase Diagrams Thermochem.*, 2 (1978) 227-238.
- [146] A.D. Pelton, S.A. Degterov, G. Eriksson, C. Robelin, Y. Dessureault, The modified quasichemical model I - binary solutions, *Metallurgical and Materials Transactions B*, 31B (2000) 651-659.
- [147] A.D. Pelton, P. Chartrand, The modified quasi-chemical model: Part II. Multicomponent solutions, *Metallurgical and Materials Transactions A*, 32A (2001) 1355-1360.
- [148] P. Chartrand, A.D. Pelton, The modified quasi-chemical model: part III. Two sublattices, *Metall. Mater. Trans. A*, 32A (2001) 1397-1407.
- [149] A.D. Pelton, P. Chartrand., G. Eriksson, The modified quasi-chemical model: part IV. Two-sublattice quadruplet approximation, *Metallurgical and Materials Transactions A*, 32 (2001) 1409-1416.
- [150] K.H.J. Buschow, Short-range order and thermal stability in amorphous alloys, *Journal of Physics F: Metal Physics*, 14 (1984) 593-607.

- [151] A.W. Weeber, Application of the Miedema model to formation enthalpies and crystallization temperatures of amorphous alloys, *Journal of Physics F: Metal Physics*, 17 (1987) 809-813.
- [152] M. Hillert, The compound energy formalism, *Journal of Alloys and Compounds*, 320 (2001) 161-176.
- [153] F. Kohler, Estimation of the thermodynamic data for a ternary system from the corresponding binary systems, *Monatsh. Chem.*, 91 (1960) 738-740.
- [154] Y.M. Muggianu, M. Gambino, J.P. Bros, Enthalpies of formation of liquid alloys bismuth-gallium-tin at 723.deg.K. Choice of an analytical representation of integral and partial excess functions of mixing, *J. Chim. Phys. Phys.-Chim. Biol.*, 72 (1975) 83-88.
- [155] G.W. Toop, Predicting ternary activities using binary data, *Transactions of the American Institute of Mining, Metallurgical and Petroleum Engineers* 233 (1965) 850-855.
- [156] Z.Y. Qiao, X. Xing, M. Peng, A. Mikula, Thermodynamic criterion for judging the symmetry of ternary systems and criterion applications, *Journal of Phase Equilibria*, 17 (1996) 502-507.
- [157] A.D. Pelton, A general "geometric" thermodynamic model for multicomponent solutions, *Calphad*, 25 (2001) 319-328.
- [158] W. Martienssen, (Editor in Chief) Lehrstuhl für Werkstoffchemie (Ed.), Rheinisch-Westfälische Technische Hochschule Aachen, Thermodynamic Properties of Inorganic Materials compiled by SGTE, Scientific Group Thermodata Europe, 4/19B4, (2006) 123-126.
- [159] Q. Yao, H. Zhou, Z. Wang, The isothermal section of the phase diagram of the ternary system Y-Mg-Ni at 673K in the region 50-100 at.% Ni, *J. Alloys Compd.*, 421 (2006) 117-119.
- [160] J.-C. Zhao, A combinatorial approach for structural materials, *Advanced Engineering Materials*, 3 (2001) 143-147.
- [161] J.-C. Zhao, A combinatorial approach for efficient mapping of phase diagrams and properties, *Journal of Materials Research*, 16 (2001) 1565-1578.
- [162] F.J.J. van Loo, Multiphase diffusion in binary and ternary solid-state systems, *Progress in Solid State Chemistry*, 20 (1990) 47-99.
- [163] A.A. Kodentsov, G.F. Bastin, F.J.J. Van Loo, The diffusion couple technique in phase diagram determination, *Journal of Alloys and Compounds*, 320 (2001) 207-217.
- [164] J.C. Zhao, M.R. Jackson, L.A. Peluso, Determination of the Nb-Cr-Si phase diagram using diffusion multiples, *Acta Materialia*, 51 (2003) 6395-6405.

- [165] W.J. Boettinger, U.R. Kattner, K.W. Moon, J.H. Perepezko, NIST Recommended Practice Guide: DTA and Heat-Flux DSC Measurements of Alloy Melting and Freezing, Elsevier, Kidlington, -1, 2006.
- [166] M. Satta, M. Palumbo, P. Rizzi, M. Baricco, Ternary compounds and glass formation in the Cu-Mg-Y system, *Advanced Engineering Materials*, 9 (2007) 475-479.
- [167] F. Tappe, C. Schwickert, S. Linsinger, R. Poettgen, New rare earth-rich aluminides and indides with cubic Gd₄RhIn-type structure, *Monatsh. Chem.*, 142 (2011) 1087-1095.
- [168] Z. Huaiying, Z. Yinghong, G. Zhengfei, The isothermal section (500°C) of the Gd-Cu-Ni ternary phase diagram, *Journal of Alloys and Compounds*, 221 (1995) 98-101.
- [169] Y. Zhuang, L. Zhang, The isothermal section (500°C) of the phase diagram of the Cu-Ho-Ni ternary system, *Journal of the Less Common Metals*, 170 (1991) 223-229.
- [170] J. Liu, F. Ma, Y. Zhuang, F. Jiao, J. Yan, The isothermal section of the phase diagram of the La-Ni-Cu ternary system at 673 K, *Journal of Alloys and Compounds*, 386 (2005) 174-176.
- [171] J. Wang, A. Pisch, R. Flükiger, J.L. Jorda, Phase equilibrium in the cerium-poor Ce-Ni-Cu system, *Journal of Alloys and Compounds*, 436 (2007) 161-169.
- [172] P. Solokha, V. Pavlyuk, A. Saccone, S. De Negri, W. Prochwicz, B. Marciniak, E. Różycka-Sokołowska, Rare earth-copper-magnesium compounds RECu₉Mg₂ (RE=Y, La-Nd, Sm-Ho, Yb) with ordered CeNi₃-type structure, *Journal of Solid State Chemistry*, 179 (2006) 3073-3081.
- [173] R. Mishra, R.-D. Hoffmann, R. Pottgen, New magnesium compounds RE₂Cu₂Mg (RE = Y, La - Nd, Sm, Gd - Tm, Lu) with Mo₂FeB₂ type structure, *Zeitschrift für Naturforschung B, Chemical Science*, 56 (2001) 239-244.

Appendix

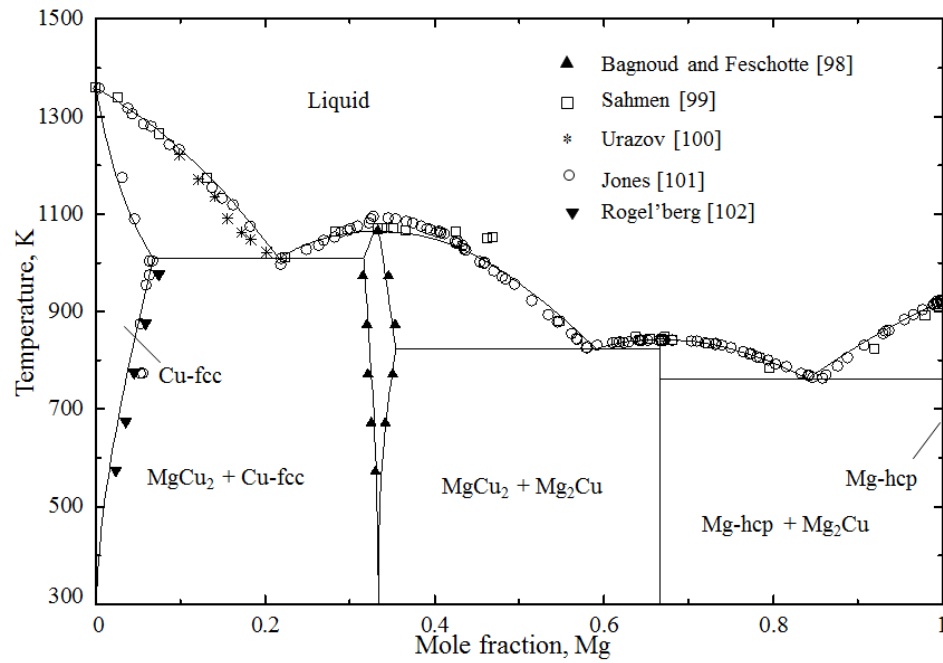


Figure A-1: Calculated Mg-Cu phase diagram [87]

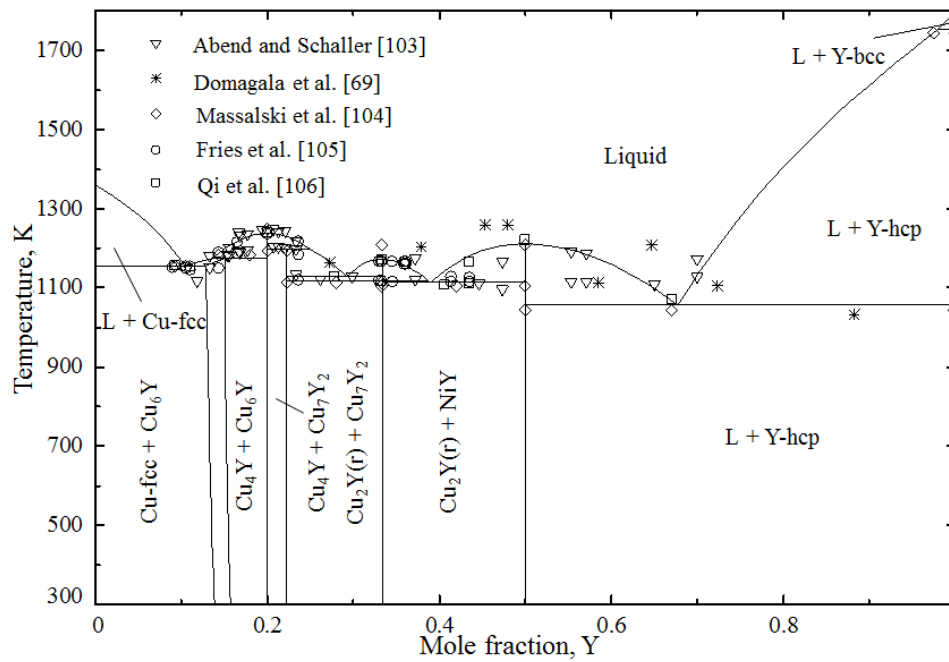


Figure A-2: Calculated Cu-Y phase diagram [87]

Table A-3: Optimized model parameters for the Mg-Cu system.

Phase	Parameters (J/mole)
Liquid	$\Delta g_{\text{MgCu}}^0 = -12\,975.95$; $\Delta g_{\text{MgCu}}^{10} = -6\,153.13 + 1.26T$; $\Delta g_{\text{MgCu}}^{01} = -13\,528.50$
Mg-hcp	${}^0L_{\text{Mg-hcp}} = 30\,012.90$
Cu-fcc	${}^0L_{\text{Cu-fcc}} = -21\,923.39 + 5.37T$
Mg ₂ Cu	$\Delta G_f = -28\,512.22$
MgCu ₂ (Mg%, Cu) (Cu%, Mg) ₂	${}^0G_{\text{Cu:Cu}}^{\text{MgCu}_2} = 16\,743.20$; ${}^0G_{\text{Mg:Cu}}^{\text{MgCu}_2} = -36\,176.48$; ${}^0G_{\text{Cu:Mg}}^{\text{MgCu}_2} = 10\,004.30$; ${}^0G_{\text{Mg:Mg}}^{\text{MgCu}_2} = 14\,766.35$; ${}^0L_{\text{Mg,Cu:Cu}}^{\text{MgCu}_2} = {}^0L_{\text{Mg,Cu:Mg}}^{\text{MgCu}_2} = 13\,011.35$; ${}^0L_{\text{Cu:Mg,Cu}}^{\text{MgCu}_2} = {}^0L_{\text{Mg:Mg,Cu}}^{\text{MgCu}_2} = 6\,599.45$;

Table A-4: Optimized model parameters for the Cu-Y system

Phase	Parameters (J/mole)
Liquid	$\Delta g_{\text{CuY}}^0 = -28718.77 + 6.28T$; $\Delta g_{\text{CuY}}^{10} = -6446.13 + 0.84T$; $\Delta g_{\text{CuY}}^{01} = -6906.57 + 2.09T$;
Cu-fcc	${}^0L_{\text{Cu-fcc}} = 41\,858.00$
Y-hcp	${}^0L_{\text{Y-hcp}} = 40\,221.35$
Cu ₆ Y (Y%, Cu ₂) (Cu) ₅	${}^0G_{\text{Y:Cu}}^{\text{Cu}_6\text{Y}} = -89\,994.70 + 8.37T$; ${}^0G_{\text{Cu:Cu}}^{\text{Cu}_6\text{Y}} = 9\,700.60 + 6.91T$; ${}^0L_{\text{Y,Cu}_2:\text{Cu}}^{\text{Cu}_6\text{Y}} = -117\,977.02 + 7.08T$;
CuY	$\Delta G_f = -42\,124.40 + 3.98T$;
Cu ₂ Y (h)	$\Delta G_f = -52\,248.46 - 4.52T$;
Cu ₂ Y (r)	$\Delta G_f = -65\,997.09 + 7.42T$;
Cu ₄ Y	$\Delta G_f = -89\,479.85 + 8.25T$;
Cu ₇ Y ₂	$\Delta G_f = -168\,977.40 + 15.58T$;

Table A-5: Crystallographic data on the ternary compounds of the Mg-Cu-Y system

Phase	Pearson's symbol	Structure type	Space group	Lattice parameters, Å			Ref.
				a	b	c	
Mg ₂ Cu ₉ Y (τ_1)	hp24	TbCu ₉ Mg ₂	P6 ₃ /mmc	5.004		16.203	[172]
MgCu ₄ Y (τ_2)	cF24	MgCu ₄ Sn	F $\bar{4}$ 3m	7.231			[122]
MgCu ₂ Y ₂ (τ_3)		Mo ₂ FeB ₂	P6/mbm	7.626		3.740	[173]
MgCuY (τ_4)	hp9,3	ZrNiAl	P $\bar{6}$ 2m	7.444	3.995	1.917	[122]
Mg ₈ Cu ₅ Y ₅ (τ_5)	oP36	Mg ₈ Cu ₅ Y ₅	Pmma	26.372	4.006	74.115	[123]
Mg ₁₃ Cu ₅ Y ₅ (τ_6)	oS92,4	Mg ₁₃ Cu ₅ Y ₅	Cmcm	4.097	19.279	25.790	[123]
Mg ₅₇ Cu ₁₈ Y ₂₅ (τ_7)	Not available						
Mg ₁₆ Cu ₅ Y ₅ (τ_8)	oS104,4	Mg ₁₆ Cu ₅ Y ₅	Cmcm	4.136	19.239	29.086	[123]
Mg ₄ CuY (τ_9)	oS48,8	TbCuMg ₄	Cmmm	13.575	20.315	3.906	[123]
Mg ₇₈ Cu ₉ Y ₁₃ (τ_{10})	Not available						
Mg ₉₋₁₈ CuY (τ_{11})	Not available						

Table A-6: Binary phases of the Cu-Ni, Cu-Y and Ni-Y systems and their structure data [138]

Phase	Pearson's symbol	Space group	Type	Lattice parameters, Å		
				a	b	c
fcc (Cu, Ni)	cF4	Fm $\bar{3}$ m	Cu			
α Y	hP2	P6 $_3$ /mmc	Mg			
β Y	cI2	Im $\bar{3}$ m	W			
Cu ₆ Y	h	-	-	6.830	-	4.070
Cu ₄ Y	hp6	P6 $_3$ /mmc	CaCu ₅	4.994	-	4.113
Cu ₇ Y ₂	-	-	-	-		
Cu ₂ Y	oI12	Imma	CaCu ₂	4.305	6.800	7.315
CuY	cP2	Pm $\bar{3}$ m	CsCl	3.477		
CuY*	oP8	Pnma	FeB			
Ni ₁₇ Y ₂	hp38	P6 $_3$ /mmc	Th ₂ Ni ₁₇	8.307		8.040
Ni ₅ Y	hp6	P6/mmm	CaCu ₅	4.883		3.967
Ni ₄ Y	-	-	-	-		
Ni ₇ Y ₂	hR18	R $\bar{3}$ m	Gd ₂ Co ₇	4.924		36.670
Ni ₃ Y	hR12	R $\bar{3}$ m	PuNi ₃	5.000		4.300
Ni ₂ Y	cF24	Fd $\bar{3}$ m	Cu ₂ Mg	7.181	4.100	5.510
NiY	oP8	Pnma	FeB	7.120	4.100	5.510
Ni ₂ Y ₃	tp80	P4 $_2$,2	Ni ₂ Y ₃	7.104		3.659
NiY ₃	oP16	Pnma	Fe ₃ C	6.920	4.470	6.360

Tale A-7: Ternary invariant points of the Mg-Cu-Ni system

Reaction	Type	Temp. (K)	Mg (at.%)	Cu (at.%)	Ni (at.%)	Ref.
Liquid + Ni ₂ Mg ⇌ fcc + Cu ₂ Mg	U ₁	1083	22.66	61.2	16.10	This work
		1081	20.00	65.0	15.00	[108]
		1082	20.70	64.4	14.90	[109]
Liquid + Ni ₂ Mg ⇌ NiMg ₂ + Cu ₂ Mg	U ₂	924	55.97	34.2	9.77	This work
		931	67.00	25.0	0.08	[108]
		928	58.20	36.1	5.70	[109]
Liquid + NiMg ₂ ⇌ CuMg ₂ + Cu ₂ Mg	U ₃	820	59.37	39.8	0.79	This work
		813	68.00	29.0	3.00	[108]
		827	59.50	40.2	0.30	[109]
Liquid ⇌ hcp + NiMg ₂ + CuMg ₂	E	766	83.87	15.5	0.62	This work
		753	84.00	15.0	1.00	[108]
		759	84.00	15.7	0.30	[109]

Table A-8: Ternary invariant points of the Mg-Cu-Y system

Reaction	Type	Temp. (K)	Mg (at.%)	Cu (at.%)	Y (at.%)
Liquid + τ_3 + hcp - Y + Mg ₂ Y (δ)	E ₁	953.32	22.41	22.82	54.77
Liquid \rightleftharpoons τ_1 + fcc - Cu + MgCu ₂	E ₂	987.85	19.05	78.45	2.50
Liquid \rightleftharpoons Mg ₂ Cu + τ_9 + τ_{11}	E ₃	692.62	75.29	15.23	9.47
Liquid + β -Y \rightleftharpoons Mg ₂ Y (δ)+hcp - Y	U ₁	1077.61	32.97	13.15	53.88
Liquid + CuY \rightleftharpoons hcp - Y + τ_3	U ₂	955.21	19.73	24.42	55.85
Liquid + CuY \rightleftharpoons τ_3 + Cu ₂ Y	U ₃	1007.04	14.15	34.52	51.33
Liquid + Cu ₂ Y \rightleftharpoons τ_2 + τ_3	U ₄	970.39	21.05	50.53	28.42
Liquid + Cu ₂ Y ₂ \rightleftharpoons τ_2 + Cu ₂ Y	U ₅	1055.66	8.14	66.37	25.49
Liquid + Cu ₄ Y \rightleftharpoons Cu ₇ Y ₂ + τ_2	U ₆	1087.61	9.76	69.37	20.87
Liquid + Cu ₄ Y \rightleftharpoons Cu ₆ Y + τ_1	U ₇	1031.38	13.41	78.15	8.44
Liquid + Cu ₆ Y \rightleftharpoons fcc + τ_{11}	U ₈	1010.42	13.63	80.77	5.60
Liquid + τ_2 \rightleftharpoons MgCu ₂ + τ_1	U ₉	1027.12	22.57	70.70	6.74
Liquid + MgCu ₂ \rightleftharpoons Mg ₂ Cu + τ_2	U ₁₀	803.65	58.31	38.68	3.00
Liquid + τ_2 \rightleftharpoons τ_7 + Mg ₂ Cu	U ₁₁	731.83	65.24	24.56	10.19
Liquid + τ_5 \rightleftharpoons τ_2 + τ_7	U ₁₂	742.03	64.67	24.57	70.76
Liquid + τ_2 \rightleftharpoons τ_2 + τ_5	U ₁₃	753.19	64.04	24.86	11.09
Liquid + MgY(δ) \rightleftharpoons Mg ₂ Y(δ) + τ_3	U ₁₄	908.19	58.43	14.27	27.30
Liquid + τ_3 \rightleftharpoons τ_4 + Mg ₂ Y(δ)	U ₁₅	840.94	65.03	14.94	20.02

Liquid + $\tau_3 \rightleftharpoons \tau_2 + \tau_2$	U ₁₆	811.37	60.55	27.21	12.24
Liquid + $\tau_6 \rightleftharpoons \text{Mg}_2\text{Y}(\delta) + \tau_7$	U ₁₇	752.17	70.97	14.19	14.83
Liquid + $\tau_7 \rightleftharpoons \tau_8 + \text{Mg}_2\text{Cu}$	U ₁₈	717.45	69.55	20.19	10.26
Liquid + $\tau_8 \rightleftharpoons \tau_9 + \text{Mg}_2\text{Cu}$	U ₁₉	709.40	71.46	18.39	10.15
Liquid + $\text{Mg}_2\text{Y}(\delta) \rightleftharpoons \text{Mg}_{48}\text{Y}_{10}(\varepsilon) + \tau_8$	U ₂₀	714.45	74.92	12.53	12.55
Liquid + $\varepsilon \rightleftharpoons \tau_{11} + \tau_{10}$	U ₂₁	700.25	76.00	13.21	10.78
Liquid + $\tau_{10} \rightleftharpoons \tau_{11} + \tau_9$	U ₂₂	697.07	75.96	13.75	10.29
Liquid + hcp-Mg $\rightleftharpoons \tau_{11} + \text{Mg}_2\text{Cu}$	U ₂₃	717.50	81.74	13.83	4.43
Liquid + $\tau_2 + \text{Cu}_4\text{Y} \rightleftharpoons \tau_1$	P ₁	1036.11	16.11	73.92	9.89
Liquid + $\text{Mg}_2\text{Y}(\delta) + \tau_4 \rightleftharpoons \tau_6$	P ₂	787.32	67.98	15.15	16.87
Liquid + $\tau_4 + \tau_6 \rightleftharpoons \tau_5$	P ₃	784.14	68.00	15.55	16.44
Liquid + $\tau_5 + \tau_6 \rightleftharpoons \tau_7$	P ₄	773.00	68.40	16.22	15.38
Liquid + $\text{Mg}_2\text{Y}(\delta) + \tau_7 \rightleftharpoons \tau_8$	P ₅	734.54	72.42	13.68	13.89
Liquid + $\text{Mg}_2\text{Y}(\delta) + \tau_7 \rightleftharpoons$	P ₆	721.51	73.78	13.10	13.12
Liquid + hcp-Mg + $\text{Mg}_{48}\text{Y}_{10}(\varepsilon) \rightleftharpoons \tau_{11}$	P ₇	699.46	76.35	13.18	10.47
Liquid + $\varepsilon + \tau_{11} \rightleftharpoons \tau_{10}$	P ₈	742.76	83.89	8.56	7.56
Liquid $\rightleftharpoons \text{MgY}(\gamma) + \tau_3$	m ₁	989.72	33.21	22.06	44.73
Liquid $\rightleftharpoons \text{CuY} + \tau_3$	m ₂	1056.50	17.36	41.08	41.56
Liquid $\rightleftharpoons \text{Cu}_4\text{Y} + \tau_2$	m ₃	1094.77	11.41	17.93	70.66
Liquid $\rightleftharpoons \text{MgCu}_2 + \tau_2$	m ₄	1036.71	27.88	66.44	5.68
Liquid $\rightleftharpoons \tau_3 + \tau_4$	m ₅	854.5	63.44	18.98	17.58

Table A-9: Ternary invariant points of the Mg-Ni-Y system

Reaction	Type	Temp	Mg (at.%)	Ni (at.%)	Y (at.%)
Liquid \rightleftharpoons fcc-Ni+ τ_4 + MgNi ₂	E ₁	1369.4	20.05	78.68	1.27
Liquid \rightleftharpoons NiY + τ_2 + τ_3	E ₂	1032.5	14.77	49.77	35.46
Liquid \rightleftharpoons τ_2 + τ_3 + τ_6	E ₃	1034.6	19.53	47.49	32.98
Liquid \rightleftharpoons τ_1 + NiY + τ_5	E ₄	977.1	16.12	29.29	54.59
Liquid \rightleftharpoons δ + τ_5 + τ_6	E ₅	837.76	58.75	12.58	28.67
Liquid \rightleftharpoons Mg ₂ Ni + τ_3 + τ_{12}	E ₆	742.7	69.31	21.42	9.27
Liquid \rightleftharpoons δ + τ_9 + τ_{10}	E ₇	767.66	73.16	8.50	18.34
Liquid \rightleftharpoons Mg ₂ Ni + τ_{12} + hcp-Mg	E ₈	766.2	83.50	14.33	2.17
Liquid + Ni ₁₇ Y ₂ \rightleftharpoons fcc-Ni + τ_4	U ₁	1445.6	10.80	84.37	4.83
Liquid + Ni ₅ Y \rightleftharpoons Ni ₁₇ Y ₂ + τ_4	U ₂	1467.1	10.98	82.68	6.33
Liquid + Ni ₅ Y \rightleftharpoons τ_3 + τ_4	U ₃	1369.5	23.67	62.86	13.48
Liquid + Ni ₄ Y \rightleftharpoons τ_3 + Ni ₇ Y ₂	U ₄	1369.8	15.35	63.59	21.06
Liquid + Ni ₇ Y ₂ \rightleftharpoons τ_3 + Ni ₃ Y	U ₅	1367.4	15.08	63.47	21.45
Liquid + Ni ₃ Y \rightleftharpoons τ_3 + Ni ₂ Y	U ₆	1243.2	10.78	58.70	30.52
Liquid + Ni ₂ Y \rightleftharpoons τ_2 + τ_3	U ₇	1044.7	14.56	50.19	35.24
Liquid + τ_2 \rightleftharpoons τ_5 + NiY	U ₈	997.6	18.94	30.10	50.95
Liquid + τ_6 \rightleftharpoons τ_2 + τ_5	U ₉	1020.6	25.30	28.29	46.40
Liquid + Ni ₂ Y ₃ \rightleftharpoons τ_1 + NiY	U ₁₀	995.2	9.94	30.37	59.69

Liquid + NiY ₃ ⇌ τ ₁ + Ni ₂ Y ₃	U ₁₁	996.8	9.62	30.32	60.06
Liquid + hcp-Y ⇌ τ ₁ + NiY ₃	U ₁₂	1076.1	8.88	24.15	66.97
Liquid + hcp-Y ⇌ τ ₁ + β-Y	U ₁₃	1083.1	35.85	10.74	53.41
Liquid + β-Y ⇌ τ ₁ + γ	U ₁₄	1068.9	37.84	10.34	51.83
Liquid + τ ₁ ⇌ τ ₅ + γ	U ₁₅	998.3	40.49	13.99	45.52
Liquid + τ ₄ ⇌ τ ₃ + MgNi ₂	U ₁₆	1217.1	43.00	51.02	5.98
Liquid + τ ₆ ⇌ τ ₃ + τ ₇	U ₁₇	941.6	50.78	30.51	18.71
Liquid + γ ⇌ δ + τ ₅	U ₁₈	888.8	56.05	11.73	32.22
Liquid + τ ₅ ⇌ δ + τ ₆	U ₁₉	847.6	57.38	12.82	29.80
Liquid + τ ₇ ⇌ τ ₆ + τ ₉	U ₂₀	848.3	59.12	12.83	28.05
Liquid + τ ₇ ⇌ τ ₃ + τ ₈	U ₂₁	867.5	58.30	26.25	15.45
Liquid + τ ₈ ⇌ τ ₃ + τ ₁₀	U ₂₂	752.1	66.13	22.10	11.77
Liquid + τ ₁₀ ⇌ τ ₃ + τ ₁₁	U ₂₃	745.8	67.71	21.73	10.56
Liquid + Mg ₂ Ni ⇌ τ ₃ + τ ₁₂	U ₂₄	743.2	69.41	21.40	9.19
Liquid + MgNi ₂ ⇌ τ ₃ + Mg ₂ Ni	U ₂₅	986.2	62.72	34.17	3.11
Liquid + τ ₈ ⇌ τ ₉ + τ ₁₀	U ₂₆	801.7	71.25	11.32	17.43
Liquid + ε ⇌ τ ₁₀ + δ	U ₂₇	768.6	73.91	8.17	17.92
Liquid + τ ₁₂ ⇌ τ ₁₁ + ε	U ₂₈	776.2	74.88	8.02	17.10
Liquid + hcp-Mg ⇌ τ ₁₂ + ε	U ₂₉	837.6	86.96	3.11	9.93
Liquid + Ni ₅ Y + Ni ₄ Y ⇌ τ ₃	P ₁	1378.9	17.56	63.8	18.64
Liquid + τ ₇ + τ ₈ ⇌ τ ₉	P ₂	878.4	64.28	13.16	22.55

Liquid \rightleftharpoons MgNi ₂ + τ_4	m ₁	1402.4	28.33	69.11	2.56
Liquid \rightleftharpoons Ni ₅ Y + τ_4	m ₂	1500.7	15.09	75.97	8.94
Liquid \rightleftharpoons τ_1 + τ_2	m ₃	1038.5	17.31	48.52	34.16
Liquid \rightleftharpoons τ_3 + τ_6	m ₄	999.3	26.14	44.81	29.05
Liquid \rightleftharpoons τ_2 + τ_6	m ₅	1111.8	22.52	38.79	38.68
Liquid \rightleftharpoons NiY + τ_2	m ₆	1113.5	16.87	42.13	41.00
Liquid \rightleftharpoons τ_5 + τ_6	m ₇	1030.2	32.41	24.63	42.96
Liquid \rightleftharpoons τ_1 + τ_5	m ₈	1028.3	27.38	21.09	51.53
Liquid \rightleftharpoons τ_1 + hcp-Y	m ₉	1139.7	20.27	17.20	62.53
Liquid \rightleftharpoons τ_6 + τ_7	m ₁₀	1017.5	55.06	22.71	22.22
Liquid \rightleftharpoons δ + τ_9	m ₁₁	838.6	60.05	11.99	27.95
Liquid \rightleftharpoons τ_7 + τ_8	m ₁₂	938.1	62.48	19.04	18.48
Liquid \rightleftharpoons τ_8 + τ_{10}	m ₁₃	821.0	71.01	14.01	14.98
Liquid \rightleftharpoons τ_{10} + τ_{11}	m ₁₄	822.8	73.45	12.83	13.72
Liquid \rightleftharpoons τ_{11} + τ_{12}	m ₁₅	826.0	73.89	13.05	13.05
Liquid \rightleftharpoons Mg ₂ Ni + τ_{12}	m ₁₆	773.4	79.35	16.72	3.9
Liquid \rightleftharpoons hcp-Mg + τ_{12}	m ₁₇	870.1	89.88	5.22	4.90

Table A-10: Ternary invariant points of the Cu-Ni-Y system

Reaction	Type	Temp. (K)	Cu (at.%)	Ni (at.%)	Y (at.%)
Liquid \rightleftharpoons hcp-Y + NiY ₃ + NiY	E ₁	1024	24.12	7.92	67.96
Liquid \rightleftharpoons NiY + Ni ₂ Y + Cu ₂ Y (r)	E ₂	1077	24.93	36.27	38.80
Liquid \rightleftharpoons Cu ₂ Y (r) + Ni ₃ Y + Cu _x Ni _{1-x} Y	E ₃	1111	39.48	29.26	31.25
Liquid + Cu ₂ Y (h) \rightleftharpoons Cu ₂ Y (r) + Cu ₇ Y ₂	U ₁	1124	70.53	0.21	29.26
Liquid + Cu ₇ Y ₂ \rightleftharpoons Cu ₂ Y (r) + Cu _x Ni _{4-x} Y	U ₂	1122	64.75	6.97	28.28
Liquid + Cu ₇ Y ₂ \rightleftharpoons Ni ₃ Y + Cu _x Ni _{4-x} Y	U ₃	1513	5.96	67.25	26.78
Liquid + Cu _x Ni _{4-x} Y \rightleftharpoons Cu ₆ Y + Ni ₅ Y	U ₄	1171	82.56	4.21	13.23
Liquid + Ni ₁₇ Y ₂ \rightleftharpoons Ni ₅ Y + fcc	U ₅	1375	68.25	24.92	6.83
Liquid + Ni ₂ Y + Ni ₃ Y \rightleftharpoons Cu ₂ Y (r)	P ₁	1112	36.70	31.13	32.17